Multi-phase Thermal Cavitation Flow in Rough Conforming and Partially Conforming Conjunctions

By

Hamed Shahmohamadi

BSc, MSc

A thesis submitted in partial fulfilment of the requirements for the Degree of Doctor of Philosophy of Loughborough University

Wolfson School of Mechanical and Manufacturing Engineering

Loughborough University

UK

April 2015

Loughborough University

Abstract

The main aim of this research was to investigate the mechanism of cavitation in conforming and partially conforming tribological conjunctions. The effect of cavitation on load carrying capacity and frictional performance of is also investigated. This is important with regards to fuel efficiency in internal combustion (IC) engines. Friction accounts for 15-20% of IC engine losses. The piston-cylinder system contributes to 40-50% of these, with the compression ring(s) being responsible for most of this. This is because the primary function of the ring is to seal the combustion chamber, thus small emerging gaps lead to increased friction. In fact, compression ring(s) expend 3-5% of engine input fuel energy. The share of frictional losses of engine bearings is approximately 20-25%.

Traditionally, prediction of performance of tribological conjunctions has been studied using Reynolds equation. When the effect of cavitation is considered, various cavitation algorithms with associated boundary conditions for lubricant rupture and reformation are proposed. These include Elrod, and Elrod and Coyne algorithms, as well as boundary conditions such as Swift-Stieber, JFO and Prandtl-Hopkins. There are a number of assumptions embodied in these approaches, as well as the use of Reynolds equation itself. These approaches do not uphold the continuity of mass and momentum in multi-phase flow, in cavitation beyond the lubricant film rupture.

A detailed methodology for multi-phase flow, comprising simultaneous solution of Navier-Stokes, energy and lubricant rheological state equations is developed. For multi-phase flow through narrow gaps this approach is supplemented with Rayleigh-Plesset void fraction algorithm, modified in order to limit the growth of cavities within a finite size domain. Furthermore, vapour transport equation is used to underpin the flow of vapour in the cavitation zone. This methodology has not hitherto been reported in literature. It is verified with experimentation using test results, including those from engines. The method and validation process account for the main contributions of the thesis.

There are various findings. Reverse and swirl flows occur at the inlet, culminating in a stagnation boundary. This agrees with the potential flow analysis of Tipei, based on Swift-Stieber boundary conditions, as well as experimental observations. The flow

Main journal publications from this thesis are included in the Appendix.

in the contact is multi-layered thermal streams with change of pressure gradient into the depth of lubricant. This cannot be predicted using Reynolds equation. At the outlet, the separation boundary closely follows the Prandtl-Hopkins boundary, with thermal flow in the presence of retarding friction. This is in line with the observations of Brewe as well as Dowson. Therefore, the main finding of the thesis is that the inlet and outlet boundary conditions can be obtained automatically without a need to specify them.

K**eywords: Control volume CFD, Multi-phase flow, Cavitation, Tribological conjunctions, Friction**

Acknowledgements

The author wishes to express his gratitude to his supervisors; Professors Homer Rahnejat and Colin Garner and Dr. Ramin Rahmani for guidance throughout this research.

The author is grateful to Lloyd's Register Foundation for the financial support extended to this work under the grant made to International Institute for Cavitation Research. Thanks are also due to Capricorn Automotive Limited for the engine testing facility and data, against the results of which some of the numerical analysis is validated.

The author also acknowledges the many technical and scientific discussions with Dr. Nicholas Morris, particularly for his collaboration in journal bearing testing with textured surfaces and Dr. Mahdi Mohammad-Pour for discussion regarding inlet and outlet boundary conditions for lubricant flow through the conjunctions.

I am grateful for the continuing support, encouragement and patience of my family members; mother, father and my wife throughout my research work.

This thesis is dedicated to my parents and my wife; Mahsa

Table of Contents

List of Figures

List of Tables

Nomenclature

A	Apparent contact area
A_a	Asperity contact area
A_p	Piston cross-sectional area
A_v	Area subject to viscous friction
b	Ring axial face-width
C	Centre of mass of the connecting rod
c_{maj}	Contact clearance along the semi-major axis
c_{min}	Contact clearance along the semi-minor axis
c	$c = \frac{c_{maj} + c_{\min}}{2}$
c_p	Specific heat capacity
d	Ring radial width
E	Young's modulus of elasticity
E'	Composite Young's modulus of elasticity of contacting solids $(\frac{1}{E'} = \frac{1-\nu_1^2}{E_1} + \frac{1-\nu_2^2}{E_2})$
e	Eccentricity
F_2, $F_{5/2}$	Statistical functions
F_{in}	Inertial force
F_G	Combustion gas force
F_T	Ring tension force
f	Total friction

f_b	Boundary friction
f_{drag}	Drag function
f_v	Viscous friction
g	Gravitational acceleration
h	Film thickness
h_0	Minimum film thickness
h_t	Coefficient of heat transfer
h_s	Ring axial profile
H	Enthalpy
I	Ring cross-sectional moment of inertia
k	Lubricant thermal conductivity
k_j	Thermal conductivity of the journal
k_b	Thermal conductivity of the bearing
k_{s1}	Thermal conductivity of the liner
k_{s2}	Thermal conductivity of the ring
L	Bearing lateral width
l	Connecting rod length
m_1	Effective mass in translational motion
m_{con}	Equivalent translational mass of the connecting rod
m_g	Gudgeon pin mass
m_p	Piston mass
n_B	Bubble number density
p	Hydrodynamic pressure

p_{atm}	Atmospheric pressure
p_c	Cavitation/Vaporisation pressure
p_g	Combustion gas pressure acting on the ring
p_{in}	Inlet lubricant supply pressure
Q	Frictional heat
$\dot{Q}_1$	Conductive heat flow rate through the liner
$\dot{Q}_2$	Conductive heat flow rate through the ring
$\dot{Q}_{cv}$	Convective heat flow rate
r	Crank-pin radius
r_0	Nominal bore radius
R_l	Conductive thermal resistance for the lubricant layer
R_v	Convective thermal resistance between film and surface
R_b	Bearing radius
R_B	Bubble radius
R_j	Journal radius
T	Temperature
T_a	Ambient temperature
T_{ba}	Bearing outside surface temperature
T_{bl}	Bearing and lubricant interface temperature
T_j	Journal and lubricant interface temperature
T_i	Inlet temperature of the lubricant
t	Time
U	Ring sliding velocity

u_∞	Free stream velocity
U_1, U_2	Surface velocities of contacting bodies
$\vec{V}$	Velocity vector
V_{ch}	Characteristic velocity
$\vec{V}_{dr}$	Drift Velocity
W	Total reaction force from contact
W_a	Load carried by asperities
W_h	Hydrodynamic load carrying capacity
x_c	Oil film rupture point

Greek symbols

α	Thermal diffusivity
α_l	Liquid volume fraction
α_v	Vapour volume fraction
α_0	Pressure–viscosity coefficient
β	Lubricant bulk modulus
β_0	Viscosity-temperature coefficient
ΔT	Lubricant temperature rise
δ	Attitude angle
ε	Eccentricity ratio
ϕ	Connecting rod obliquity angle
φ	Crank angle
θ	Circumferential direction in journal bearing
ζ	Number of asperity peaks per unit contact area

η	Lubricant dynamic viscosity
η_0	Lubricant dynamic viscosity at ambient conditions
κ	Average asperity tip radius
λ	Stribeck's oil film parameter
μ	Pressure coefficient for boundary shear strength of asperities
ν	Poisson's ratio
ρ	Lubricant density
ρ_0	Lubricant density at ambient conditions
σ_r	Liner RMS surface roughness
σ_l	Ring RMS surface roughness
σ_1	Bearing RMS surface roughness
σ_2	Journal RMS surface roughness
σ_s	Surface tension coefficient
τ	Shear stress
τ_0	Eyring shear stress
Γ	Diffusion coefficient
T_e	Average (effective) lubricant temperature
ω	Angular speed of crank shaft (engine speed)

Chapter 1: Introduction

1.1. Background and motivation for research

The science of Tribology focuses on the understanding of lubrication, friction and wear. It is a multidisciplinary subject requiring other key sciences, including but not limited to surface topography, lubricant rheology, heat transfer, dynamic and material science. An important aim is to mitigate friction and wear between two contacting surfaces. This is ideally achieved through the introduction of a low shear strength lubricant film formed between the two surfaces in relative motion.

The internal combustion engine as the source of propulsion, shown in Figure 1.1, is one of the most important systems in the motor vehicle which is employed in passenger vehicles, motorcycles, commercial and construction vehicles, agricultural vehicles, trains and ships.

The lubrication of the piston rings and skirt, valve train and various engine journal bearings has been a topic of importance as these components contribute to the engine frictional power losses. Poor lubrication also results in wear of contacting Therefore, it is essential to be able to accurately predict friction generation and evaluate design concepts in order to minimize the power loss from the contacting conjunctions as well as avoid wear.

The power loss in IC engines can be put into two classes, thermodynamic and parasitic. Thermodynamic losses such as heat expelled from the exhaust and heat losses due to the combustion process account for between 50-60% of the total engine power losses. The parasitic losses are due to friction, pumping of various engine fluids and errant dynamics, such as out-of-balances. Friction is the main

contributory factor in parasitic losses. The piston mechanism is responsible for about half of the total parasitic losses, accounting for 17- 25% of all engine losses [1].

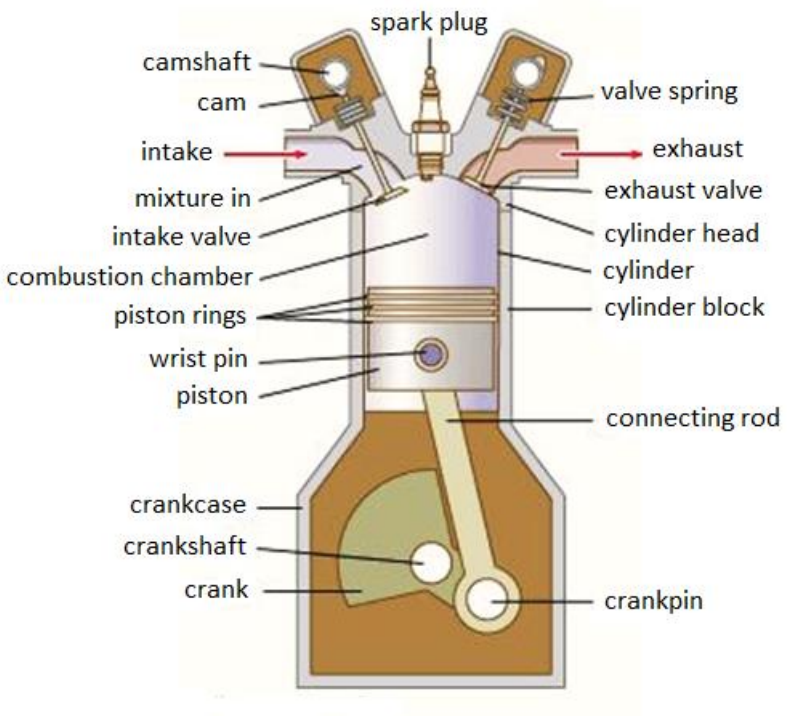

Figure 1.1: Main engine components in an internal combustion engine (The figure reprinted from ENCYCLOPAEDIA BRITANNICA's website)

This thesis is concerned with the analysis of piston top compression ring and engine big-end (i.e. connecting rod) bearing. The top compression ring's main function is to adhere closely to the surface of cylinder liner/bore in order to seal the combustion chamber from the bottom-end. Otherwise, there would be leakage of combustion gasses into the engine bottom-end, thus causing power loss itself. Any significant loss of compression ring sealing function can also result in ingression of lubricant into the combustion chamber during the engine compression and exhaust strokes which can lead to blow-by and thus harmful emissions into the environment. On the other hand close adherence of compression ring to the cylinder wall exacerbates the generated friction. In fact, the top compression ring can account for 4-6% of fuel

consumption [1]. This level of frictional loss from such a diminutive conjunction is unsustainable, requiring in-depth tribological analysis.

The big-end bearing is subjected to high combustion and inertial dynamic loads. Together with the main crankshaft supporting journal bearings, 25% of all the frictional losses (approximately 5% of all IC engine losses) are due to journal bearings. Additionally, journal bearings can develop low pressurised regions where cavitation can occur, which may lead to cavitation bubble burst and erosion of contacting surfaces.

The aforementioned issues form the motivation for in-depth investigation of the compression ring and big-end bearing conjunctions in this thesis.

1.2. Cavitation phenomena

Cavitation plays an important role in the design and operation of fluid machinery and equipment, owing to performance degradation, noise, vibration, and erosion caused by cavitation. Cavitation involves complex phase-change dynamics, large density ratio between phases, and multiple time scales. Considering the classical identification of the mechanism of hydrodynamic pressure generation in lubricating films, Reynolds [2] clearly recognised the possible influence of cavitation on bearing behaviour. The formation of cavities and their disposition have impacts on the generated pressures in a continuous thin film and hence the integrated quantities such as the load capacity of bearings.

Tribological research has resulted in the development of cavitation models which enable the prediction of performance of liquid-film bearings with acceptable accuracy for most engineering applications. However, it should be noted that the physics of cavitation in piston ring conjunction and bearings is not hitherto fully understood.

Two basic forms of cavitation in lubrication films are known as gaseous and vaporous.

1.2.1. Vaporous cavitation

The lubricant may boil at ambient temperature if the pressure within it falls to its vaporisation pressure, creating filled cavities. These cavities/bubbles may later collapse and cause cavitation-induced erosion. The occurrence of vaporous cavitation in bearings is normally restricted to situations in which the loading is dynamic, for instance in the main bearings of diesel engines.

1.2.2. Gaseous cavitation

The most usual mechanism for occurring gas cavities in a lubricant is ventilation from the surrounding atmosphere when sub-ambient pressures occur. However, another evident way of gas cavity generation is the liberation of dissolved gases from a solution when the liquid pressure falls below its saturation pressure. Typically, in many regards ventilation and gas release result in the same behaviour in lubricant films. In operation the appearance of gas streamers, occurring due to such phenomena can be dissimilar, especially under transient conditions.

1.3. Piston rings of IC engines

In an internal combustion engine the piston ring-pack usually consists of three circular rings placed in piston grooves (see figure 1.2). During engine operation, the rings move with the piston, sliding along the cylinder bore. The major function of the rings is to avoid high-pressure gases from leaking through the piston ring-cylinder liner interface, which would result in power loss, blow-by and lubricant degradation. Effective sealing is, therefore, required between the rings and the bore surface. However, close contact between the rings and the bore without lubrication would result in inordinate frictional power losses. Another main function of the piston oil

control ring is the effective distribution of lubricant along the piston ring-cylinder liner interface, without allowing excessive oil flow through the interface and leakage into the combustion chamber. A third function of the piston rings which is mostly essential for the top ring is the heat dissipation from the piston to the cylinder liner.

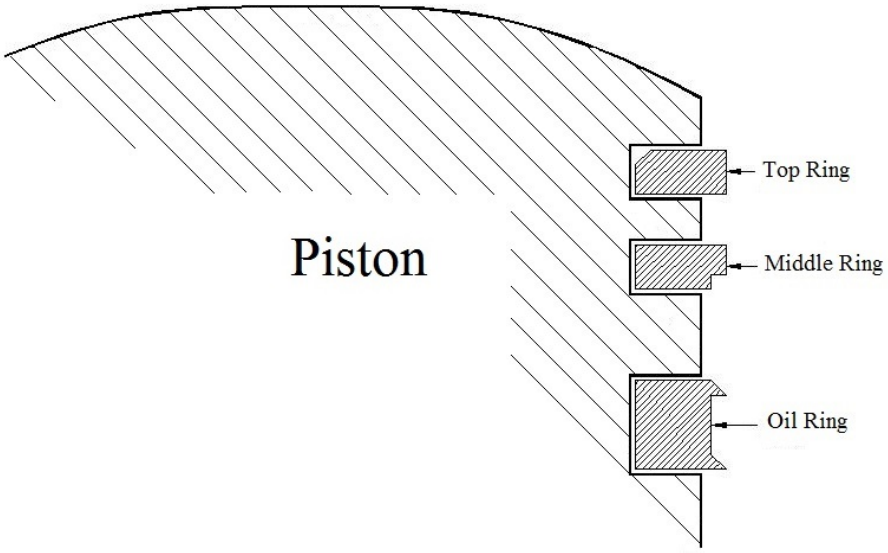

Figure1.2: Piston ring function in an internal combustion engine

For the system to effectively meet these overall objectives, each piston ring has an exclusive role. The top ring seals the piston ring-cylinder liner interface in order to prevent high-pressure gases to escape from the combustion chamber into the lower parts of the engine. The oil control ring adjusts the quantity of oil which passes through the piston ring-cylinder liner interface to lubricate the upper rings. The second ring in most of the engines scrapes down the excessive surface-adhered oil that passes the oil control piston ring-cylinder liner interface and its presence is not critically necessary in all cases. Hence, it may not be used in all types of engines. For example, in racing engines where reduced weight is a critical goal and life expectancy is low, no secondary ring is used, which enables reduced piston height and thus decreasing overall piston weight. However, in large diesel engines where

high pressures are usual and long engine life is desired the secondary rings are used to control oil flow more effectively.

1.4. Cavitation in piston top compression ring

The shape of the surface of the ring is constructed in such a way to create a hydrodynamic wedge at both its extremities in its bi-directional reciprocating motion. However, in practice, hydrodynamic pressures are generated only at the converging inlet wedge, depending in the sense of ring sliding motion. At the diverging outlet the pressures drop and do not contribute significantly to the load carrying capacity. It is difficult to consider negative pressure phenomena. Thus, many assumptions such as the Half-Sommerfeld or Gumbel's condition and Reynolds cavitation condition have been put forward with the assumption that the full width of the ring is covered with oil. However, it has been shown that the entire surface of the ring is not enveloped in the oil film [3], and it has become necessary to establish appropriate new boundary conditions for analysis purposes, which would take into account lubricant film rupture, starvation and cavitation.

Throughout the development process, however, little attention has been paid specifically to the nature of cavitation which occurs in the diverging region of the lubricant film conjunction and the sensitivity of the analysis to the imposition of different film rupture and reformation criteria. The formation of gas cavities in the diverging region of the lubricant film in a converging-diverging wedge, such as that between a piston ring and cylinder liner, influences the shape of the hydrodynamic pressure profile in the entrainment direction. Consequently, this affects the load-carrying capacity of the interface, which is the integral of the pressure distribution. The lubricant film thickness, friction and lubricant flow rate are also affected.

1.5. Journal bearings

Bearings support the applied combustion and inertial loads in an engine. The rotating components of IC engines are furnished with sleeve type sliding bearings. The reciprocating engines can be categorized by cycling loading of their parts as well as their bearing supports. The high loads are a consequence of intermittent combustion gas pressure in the cylinders. Ball bearings, in which a load is shifted by balls to small area of the ring surface, cannot usually withstand the loading conditions of IC engines, except for some racing engine variety operating at lower combustion pressures but smaller strokes. The journal bearings support the applied load over a relatively larger contact area than the rolling element bearings.

1.5.1. Journal bearings in IC engines

Crankshaft bearings support the crankshaft subjected to relatively high inertial oscillating forces begotten by the components transmitted by the connecting rods. These bearings are mounted in the crankcase. A main bearing comprises two parts: upper and lower shells. The upper part of a main bearing normally has an oil supply groove on its inner surface.

The rotating motion of the crank pin within the connecting rod is supplied by connecting rod bearings, which transmit the cyclic loads as the result of combustion loading and piston inertial dynamics. Connecting rod bearings are mounted in the big end of the connecting rod.

1.5.2. Hydrodynamic journal bearings

The engine bearings are commonly hydrodynamic journal bearings (see figure 1.3). In hydrodynamic journal bearing, the bearing surfaces are ideally separated by a film of lubricant generated by the rotation of the journal.

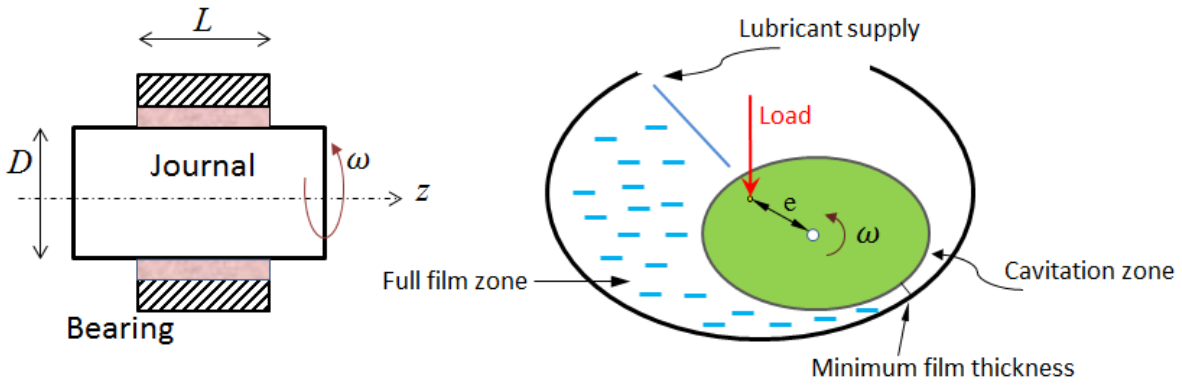

Figure1.3: Schematic of a journal bearing showing lubricant cavitation [4]

The journal position would be concentric with that of the bearing bushing with no applied load (zero load carrying capacity). A loaded journal is displaced from the concentric position and generates a converging gap between the journal and bearing bushing surface. The loaded region is further skewed due to the rotation of the journal, which generates friction torque. A loaded region these results. Figure 1.3 shows a hydrodynamic journal bearing and a journal rotating in an anticlockwise direction.

The viscous lubricant flow in the bearing is entrained by journal rotation in the same direction. The entrainment action squeezes the lubricant due to the converging gap and builds up a pressure distribution. After minimum film thickness in the diverging gap area the pressure drops to the lubricant vaporisation pressure where cavitation occurs. Viscous friction and the lubricant pressure equilibrate the external load. The

equilibrium between these forces determines the instantaneous position of the journal. Big-end bearings of modern IC engines operate at high loads with high eccentricity between the journal and the bushing geometric centres. The resulting thin films can cause the interaction of surface asperities of the counterfaces. Thus, additional friction due to boundary interactions is not uncommon (mixed-hydrodynamic conditions, where mixed refers to some direct interaction of surfaces). Furthermore, because of high applied loads, the big-end bearings are usually of multi-lobed shape, where each lobe carries a certain proportion of applied load. The most common type of such bearings is an elliptic bore bearing (2 loaded lobes). These bearings are also commonly referred to as lemon-shaped bearings.

1.6. Thesis objectives

The overall aim of this thesis is to develop combined analytical and computational fluid dynamic (CFD) models to predict frictional losses in the piston ring conjunction as well as in engine journal bearings.

The specific objectives are:

1. To developing a CFD model to predict mixed hydrodynamics of the compression ring as well as journal bearings
2. To predict film thickness, generated pressures and friction,
3. To determine the global cavitation flow of the compression ring and journal bearing
4. To take into account the generated contact heat and heat transfer.
5. To verify all numerical and analytical methods with reported experimental tests, including with IC engine data.
6. To apply the developed methods to real engine applications with modern emerging technologies such as cylinder deactivation as well as use of surface

engineered textures to encourage micro-hydrodynamics through pressure perturbation.

7. In-depth study of cavitation formation under all reported conditions.

1.7. Structure of the Thesis

Throughout this chapter the general trend and concerns of the automotive industry in relation to cavitation in lubrication of tribological contacts in IC engines, and friction and mechanical losses were discussed. Its current developments and interests were also highlighted, thereby providing necessary motivation for undertaking this research. The thesis is divided into seven chapters including the current chapter.

Chapter 2 reviews the previous research work carried out in this field starting from the basic historical developments and theoretical finding in cavitation phenomena, to the common methods, algorithms and boundary conditions for cavitation flow in lubrication of piston compression ring and journal bearings.

Chapter 3 presents the underlying theory for the numerical analysis presented in this thesis. The theory involves the combined solution of Navier-Stokes equations, together with various forms of energy equation, as well as lubricant rheological state equations. It also includes the use of a vapour transport equation and modified Rayleigh-Plesset equation to take into account the formation of cavitation zones and multi-phase flow.

In Chapter 4, the methodology presented in Chapter 3 is applied to the cases of compression ring-cylinder liner conjunction. The boundary conditions for both pressure and temperature for this case are treated separately in this chapter. An analytical control volume thermal mixing model is also applied for the temperature boundary condition in this chapter. The developed method is validated against experimental results.

Chapter 5 presents a full 3D CFD approach for thermo-hydrodynamic analysis of big-end bearings based on the methodology presented in Chapter 3. The developed model in this chapter is also validated against experimental results. The validated model is then used for analysis of a big-end engine bearing subjected to dynamic loading under normal engine operation as well as with the application of cylinder deactivation (CDA).

In Chapter 6 a combined experimental and numerical approach is employed to investigate the effect of surface modification on the tribological performance of contacting surfaces. Using a partial pad journal bearing test rig, the attitude angle is measured at a constant load while the rotational speed is varied. The introduction of surface texture features to the journal bearing surface caused a reduction in friction generated at an equivalent speed.

Chapter 7 outlines the overall conclusions of the research carried out under this project and included in this thesis. The aims of the research are revisited and the degree of achievement in this regard is gauged. A critical assessment of the thesis is carried out, including the underlying assumptions made in the model used in this project. Finally, Chapter 7 proposes suggestions for future work to be carried out to extend the research and development findings contained in this research.

Chapter 2: Review of Literature

2.1. Preamble

This chapter is devoted to the review of open literature on a number of inter-related topics which affect the cavitation phenomena, specifically in tribological conjunctions. Cavitation also affects the conjunctional load carrying capacity as well as friction and generated heat and transfer of heat away from the contacts. Furthermore, cavitation can lead to erosion of surfaces. The formation of cavitation and its effect particularly upon generated friction in the contact conjunction is of particular interest in this thesis, which is mostly dedicated to energy efficiency within internal combustion engines.

2.2. Previous research on cavitation

Cavitation is an important factor in designing and operating fluid machinery and devices, such as turbo-machinery and internal combustion engines, to name but a few. It can contribute as a source of noise and vibration, a mechanism responsible for erosion of surfaces, degradation of lubricant performance through aeration, and most importantly affect load carrying capacity, friction and heat generation in contacts. Cavitation consists of complex phase-change dynamics, large density ratio between fluid phase, and act in multiple time scales [5]. Navier-Stokes computations of turbulent cavitating flows have been developed due to advances in computational capabilities and the growing physical understanding of the cavitation phenomenon. There are, nevertheless, some remaining challenges regarding the accuracy, efficiency, stability and robustness of predictions, particularly with regard to the complicated unsteady interactions in cavitation dynamics and flow turbulence.

A popular method for cavitation modelling uses the homogeneous flow theory, in which the mixture density concept is introduced and a single set of mass and momentum equations are solved. In this category of cavitation predictive analysis there are differences between the various models due to the relation outlining the variable density field. Delannoy and Kueny [6] suggested a baroscopic state law, which strongly relates the mixture density to the static pressure. This defines the mixture density in the incompressible flow. Chen and Heister [7] derived a time and pressure dependent differential equation for the variation of mixture density. Another common method is the transport equation-based model (TEM), which states the transport equation as a function of either the mass or volume fraction of different phases.

Various researchers have suggested different modelling concepts embodying qualitatively similar source terms with alternate numerical techniques. Kubota et al. [8] combined the Rayleigh-Plesset equation with the flow solver and computed the void fraction, based on the bubble radius. Figures 2.1 and 2.2 illustrate comparison of experimental observations with their computed results for two different cavitation numbers of 1.5 and 1.3, respectively. Merkle et al. [9] and Kunz et al. [10] used the artificial compressibility method with emphasis on the preconditioning formulation. Singhal et al. [11] studied the effect of non-condensable gas in their “full cavitation model”.

Senocak and Shyy [12] developed an Interfacial Dynamics-Based-Cavitation model (IDM), using 3 approaches (noted below). The model proposes direct interpretation of the empirical parameters in the existing transport equation-based models. Quantitative differences are observed in the closure region of the cavity, even though all the considered models provide qualitatively comparable wall pressure distributions in agreement with the experimental data. This is due to different compressibility characteristics of various cavitation models.

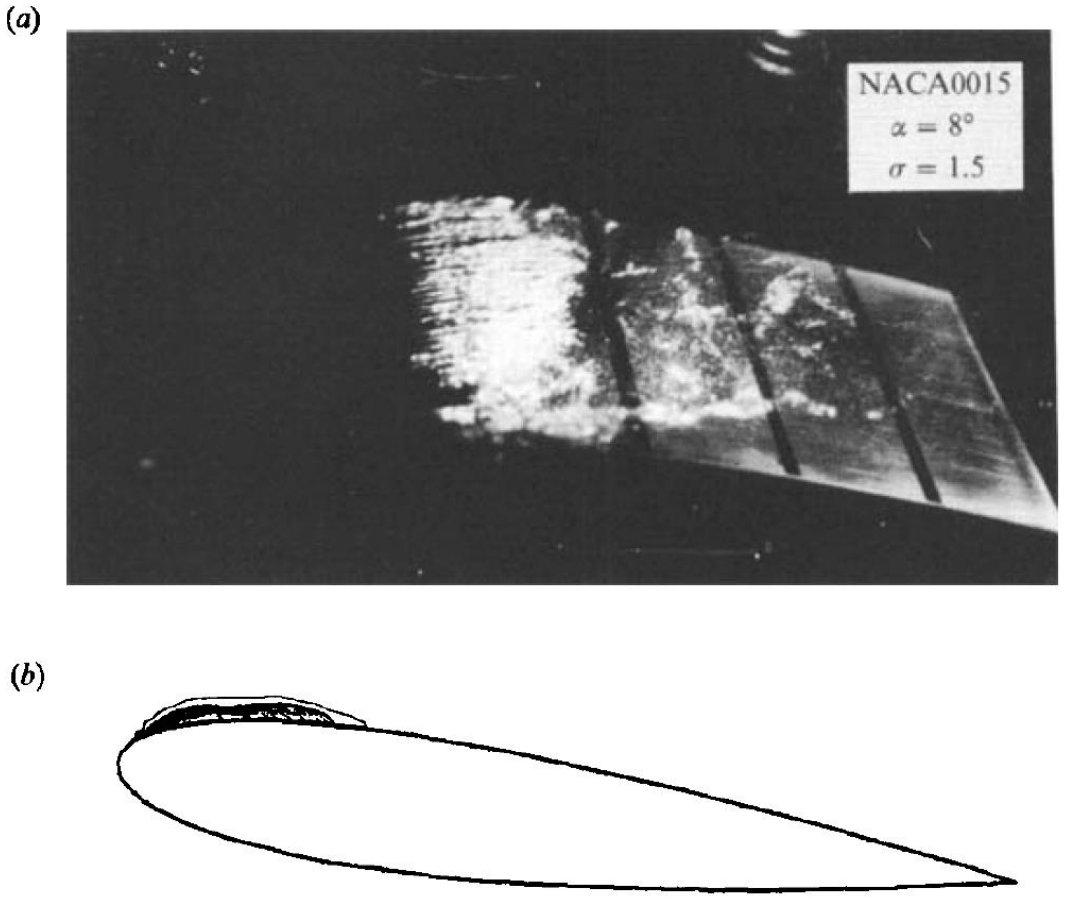

Figure 2.1: Comparison of sheet-type cavity appearance on NACA0015 hydrofoil, Ca=1.5, Re = 3 x 10^5, (*a*) Experimental observation. (*b*) Computed result [8]

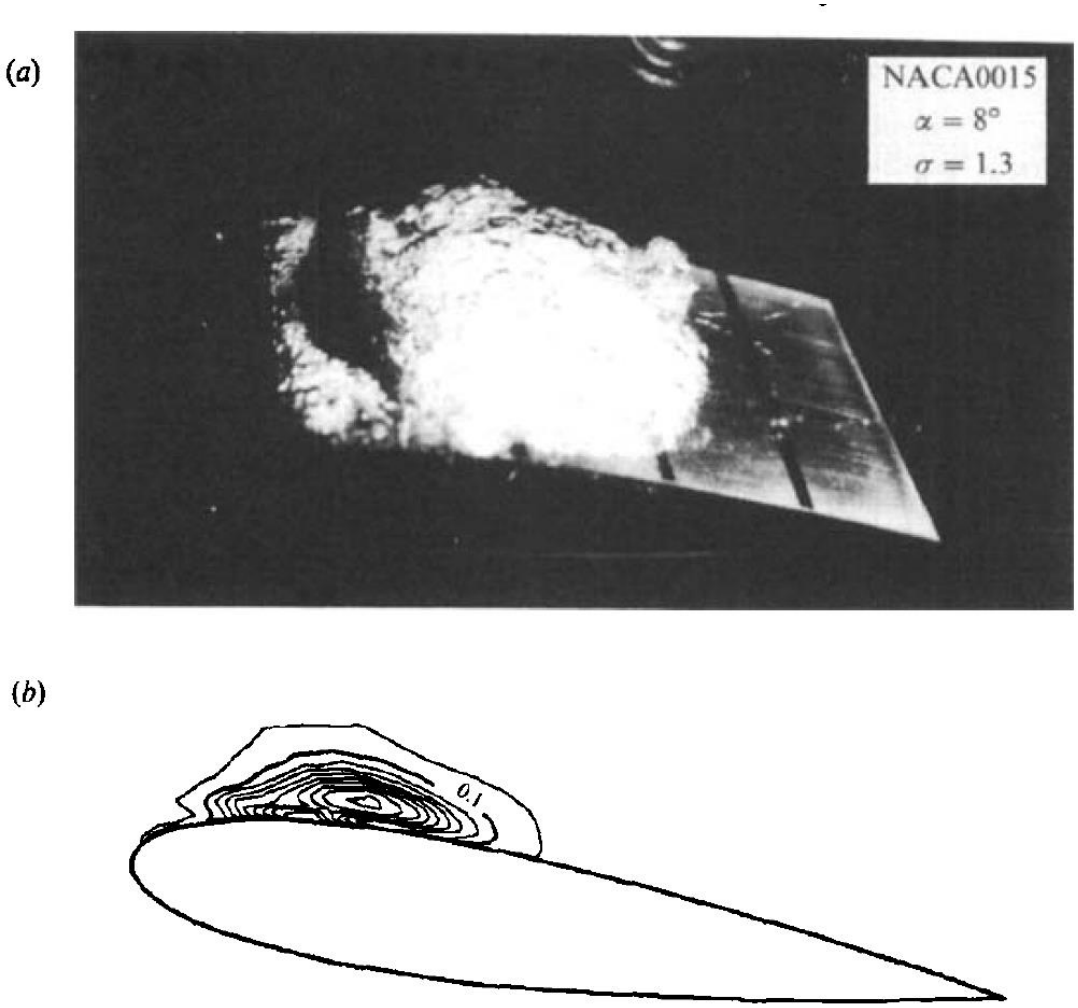

Figure 2.2: Comparison of sheet-type cavity appearance on NACA0015 hydrofoil, Ca=1.3, Re = 3 x 10^5, (*a*) Experimental observation. (*b*) Computed result [8]

The general governing equations for fluid flow to be coupled with one of the following cavitation models in order to include the cavitation phenomenon:

Model 1: Cavitation model is based on the Rayleigh-Plesset equation [8]: The growth and collapse of a bubble cluster is obtained through use of a modified

Rayleigh-Plesset equation. This equation delivers the rate equation controlling vapour generation and condensation:

$$\frac{\partial(\rho_l \alpha_l)}{\partial t} + \nabla.(\rho_l \alpha_l \vec{u}) = (\dot{m}_l^k + \dot{m}_v^k) \tag{2.1}$$

$$\dot{m}_v^k = C_c \frac{3\alpha_v}{R_B}\left(\frac{2}{3}\frac{p-p_c}{\rho_l}\right)^{1/2},\ p > p_c \tag{2.2}$$

$$\dot{m}_l^k = C_e \frac{3\alpha_v \rho_v}{R_B}\left(\frac{2}{3}\frac{p-p_c}{\rho_l}\right)^{1/2},\ p < p_c \tag{2.3}$$

where *p* is the pressure, α_l is the liquid volume fraction, ρ_l is liquid density and ρ_v is vapour density. In this model, the liquid and vapour mass fraction are considered as the dependent variables in the transport equation. Here C_c and C_e are two empirical coefficients, chosen to account for the fact that cavities can form at different rates (condensation is usually much slower than evaporation). Further assumptions regarding the bubble concentration and radius are required in order to obtain an inter-phase mass transfer rate. The Kubota cavitation model [8] employs the following defaults for the model parameters: $R_B = 1\mu\text{m}$, $C_c = 50,\ C_e = 0.01$.

Model 2: This is Interfacial dynamics-based cavitation model (IDM) [12]. A hypothetical interface is assumed to lie in the liquid vapour mixture region. The interfacial dynamics-based cavitation model is as follows:

$$\frac{\partial \alpha_l}{\partial t} + \nabla.(\alpha_l \vec{u}) = \frac{\rho_l Min(p_l - p_c, 0)\alpha_l}{\rho_v (V_v - V_i)^2\ (\rho_l - \rho_v)u_\infty} + \frac{Max(p_l - p_c, 0)(1-\alpha_l)}{(V_v - V_i)^2(\rho_l - \rho_v)u_\infty} \tag{2.4}$$

$$\dot{m}_l^s = \frac{{\rho_l}^2 Min(p_l - p_c, 0)\alpha_l}{\rho_v (V_v - V_i)^2 (\rho_l - \rho_v)u_\infty},\ p < p_c \tag{2.5}$$

$$\dot{m}_v^s = \frac{\rho_l Max(p_l - p_c, 0)\alpha_v}{(V_v - V_i)^2 (\rho_l - \rho_v)u_\infty},\ p > p_c \tag{2.6}$$

where V is velocity, t is the characteristic time scale and u_∞ represent the free stream velocity of the flow problem. The subscripts i, l, v refer to the interface, the liquid phase and the vapour phase, respectively.

Model 3: This is essentially a Density Model: Both the Model-1 and Model-2 are transport equation-based models. Model-1 is able to describe the interaction between the viscous effects such as vortices and cavitation bubbles. In this model, Navier-Stokes equations, including cavitation bubble clusters are solved, where the growth and collapse of a bubble cluster is obtained by a modified Rayleigh's equation. Model-1 can define the mechanism of cavitation cloud generation and larger-scale vortices. These are the same as the feature of cloud-type cavitation shedding from the trailing edge of attached cavities [9]. Model-2 is originated from a theoretical derivation, initiating from conservation of mass and normal momentum at a liquid-vapour interface. Model-2 is developed to alleviate the requirement for empirically adjustment of model parameters with a sound theoretical foundation using the interfacial dynamics directly. A Density Model-3 is developed based on the previous two models in order to determine an interface between the liquid and vapour in front of an attached cavity with relatively high water vapour fraction as well as detailing the process of vortex shedding at the rear of the cavitation region:

$$\dot{m}_l = x(b)\dot{m}_l^k + (1 - x(b))\dot{m}_l^s, \;\; p < p_c \tag{2.7}$$

$$\dot{m}_v = x(b)\dot{m}_v^k + (1 - x(b))\dot{m}_v^s, \;\; p < p_c \tag{2.8}$$

$$x(b) = 0.5 + \tanh[\tfrac{C_1(0.6b - C_2)}{0.2(1-2C_2)+C_2}]/2\tanh(C_1) \tag{2.9}$$

A blending function $x(b)$, given in Eq. 2.9, is employed to combine mass transfer rate of the inner and outer of the cavity, where, $b = \frac{\rho_m}{\rho_l}, C_1 = 4, C_1 = 0.2$. The condensation terms $\dot{m}_v^k$ and $\dot{m}_v^s$ are calculated from Eq. 2.2 and Eq. 2.6. Evaporation

terms $\dot{m}_l^k$ and $\dot{m}_l^s$ are calculated from Eq. 2.3 and Eq. 2.5 respectively. Different transport equation-based cavitation models are summarised as follows: Subsequently a new modified density based closure model is developed for any unsteady characteristics of the cavitating flows. The new modified density based on cavitation models are evaluated for the cavitating flows in comparison to the available experimental data in the open literature. The new model is also employed further to study the flow structures of unsteady cloud cavitation, for example around a hydrofoil.

For tribological conjunctions, Jakobsson and Floberg [13] and Olsson [14] suggested a so-called JFO theory for cavitation region, based on: mass conservation boundary conditions which treat the cavitation region occurring between the lubricant rupture point and the film reformation boundary. Due to the complexity of the JFO theory, however, prediction of the cavitated region is quite complex, using the usual solution of Reynolds equation. Elrod and Adams [3] and Elrod [15] proposed a generalized Reynolds equation valid for both full film and cavitation regions.

2.3. Piston ring-cylinder liner conjunction

In 1984, Hill and Newman [16] initiated a project aimed at reducing piston compression ring friction of internal combustion engines. Based on some simple analysis, they determined five design features that could be altered to reduce friction, which included axial ring contact width, surface pressure, number of rings, effective contacting face profile of the rings and the geometry of the ring and the bore surface. They found that rings with a smaller axial contact width reduced friction, but this friction reduction was accompanied by a reduction in the ring axial stiffness (ring tension). Different materials were investigated to compensate for this effect, but they found that steel rings suffered from side face wear from the aluminum piston grooves. They concluded that surface pressure should be reduced to achieve low

friction, but this would affect the contact load carrying capacity and potentially higher levels of oil consumption. It should be noted that the ring profile is subject to alteration during and after running-in period which produces an asymmetric profile. This can substantially change the lubrication conditions in the ring/liner contact. They developed a simple expression in which conformability was shown to be inversely proportional to radial width cubed, and therefore this factor was deemed most important for the purposes of maximizing ring-bore conformability, reducing applied contact pressures. They left the ring profile, bore macro-geometry, and the ring set design for future investigations.

Jeng [17] developed two models for piston ring lubrication analysis, incorporating realistic boundary conditions and oil transport predictions. He also performed a parametric study to examine the effects of some engine parameters on tribological performance. These included the effect of bore-stroke ratio, surface roughness, ring tension, ring- piston groove interactions, ring offset, ring crown height and ring width on friction. His results were largely qualitative and were not validated experimentally.

Nakada et al. [18] reported on a study that focused on surface treatments to reduce friction and wear. He also suggested removing one ring to reduce friction. As in the previous study, there were no significant quantitative conclusions in this work. Furthermore, the number of compression rings used in an engine is a function of gas flow dynamics, combustion pressure and heat transfer, not merely friction.

Cullen and Frodsham [19] investigated reduced cross-section compression rings made out of steel rather than the traditional cast iron rings. They found that steel rings with a significantly larger free end-gap could be used because of the higher strength of steel compared with cast iron. The larger free end-gap increased ring tension, improving conformability of the ring to the liner surface. They also found that ring radial width should be minimized in order to reduce the ring's moment of inertia and improve its conformability. Friction was reduced by implementing a skewed

barrel profile on the top ring. They measured lower oil consumption and blow-by under several reported test conditions using their new ring designs. They noted that steel could not be used if top ring temperature exceeded 260°C due to higher thermal relaxation resistance of steel compared to that of cast iron.

In 1996, Richardson [20] reviewed several methods for reducing friction that had been investigated by different companies and research institutions. He also reviewed models that were developed and various methods for measuring friction. He specifically investigated the effect of using a skewed barrel profile, a larger barrel drop, reducing the ring contact width and the combination of these parameters on the generated friction. He did not investigate the manufacturing feasibility of barrel drops or skewed barrel profiles. In this work, there were no real quantitative conclusions, as only the reduction of the peak value of friction power loss was given.

Tomanik et al. [21] performed a study in which they reduced the oil ring tension such that unit pressure was decreased from 1.1 to 0.8 MPa. This resulted in a 30% reduction in the friction power losses according to predictions from a Ricardo friction model. Unfortunately, their experimental work focused on a combination of several changes for reduced friction and therefore they did not isolate the effect of the individual parametric changes implemented to reduce friction for the purposes of comparison with their reported model.

From the above discussion, it can be seen that most of the previous work has focused exclusively on reduction of piston ring friction and relatively little emphasis has been placed on ensuring that other adverse effects are minimized, such as reduction in load carrying capacity and oil loss, leading to blow-by and lubricant degradation. There has also been hardly any investigation of cavitation in internal combustion engine ring-packs, particularly as a part of an overall analysis of prediction of friction and generated conjunctional heat. This is due to the complexity of these concomitant effects, which has prevented the development of accurate

models to predict their effects quantitatively.

2.4. Cavitation in piston rings

The passage between the piston ring profile and the cylinder liner is a convergent-divergent gap, suggesting lubricant film rupture and potential cavitation. There are two possibilities for cavitation in piston ring conjunction. These are enclosed and open cavitation [22-24]. Enclosed cavitation assumes that the lubricant film ruptures where in the divergent outlet region and the lubricant film reforms again before the trailing edge of the ring to coincide with the exit pressure boundary condition. On the other hand, open cavitation assumes that lubricant film would separate in the diverging outlet gap instead of reforming. Enclosed cavitation is likely to appear for a fully loaded piston ring. The focus of this thesis is on fully loaded piston ring with enclosed cavitation pattern.

Considerable amount of research has been carried out in this area. The earlier studies regarding piston ring either did not consider cavitation phenomena at all [25-27] or used half-Sommerfeld boundary condition, which does not ensure the continuity of flow conditions. It is known that half-Sommerfeld type boundary condition violates the mass continuity condition at both the cavitation boundaries (rupture and reformation) [28, 29]. Dowson [30] resolved this issue to some extent for a single piston ring using the Reynolds or swift-stieber boundary condition [31, 32]. Dowson assumed that cavitated region commences at the point where the pressure gradient vanishes. However, the assumption of constant flow rate across the ring is debatable when squeeze velocity is not small compared with the change in the Couette flow rate. Jeng [33, 34] employed Dowson's work by introducing a system of two nonlinear equations, which could solve the transient lubrication problem without a constant flow rate assumption. However, he used Reynolds boundary condition, which is correct for describing of the starting point of the cavitated region (film rupture) but states nothing about the ending point of cavitated region (lubricant film reformation).

Many researchers in the past few years [35-38] have alluded to the use of the JFO boundary conditions, coupled with the Elrod cavitation algorithm to find numerical solutions for hydrodynamically lubricated piston rings. There have been several numerical predictions of compression ring-cylinder liner conjunction, where the analyses include a host of parameters which interact with each other, making the tribology of ring-liner conjunction particularly complex. These parameters include the effect of the ring's axial profile along its face-width and its surface topography [39] (figures 2.3-2.5) and the effect of developing wear upon friction and the sealing effectiveness of the ring in an out-of-round bore [40]. These and similar analyses [41-44] have included mixed regime of lubrication, where direct surface interactions can occur at piston dead centre reversals with momentary cessation of lubricant entraining motion into the contact under assumed fully flooded or starved inlet conditions.

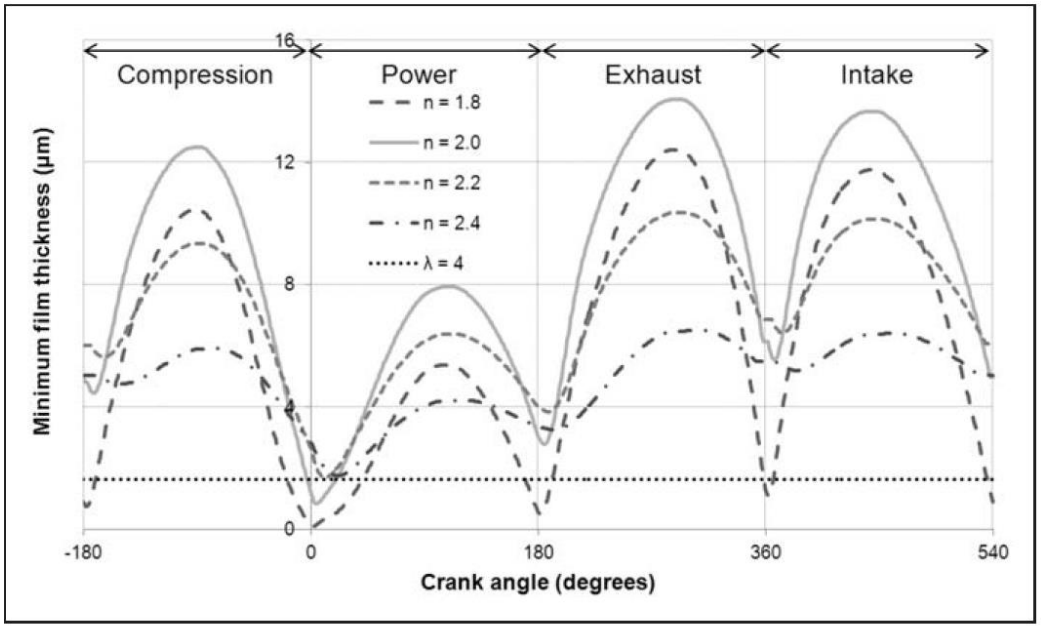

Figure 2.3: Variations of minimum film thickness for different parabolic-type ring profiles during a typical engine cycle [39]

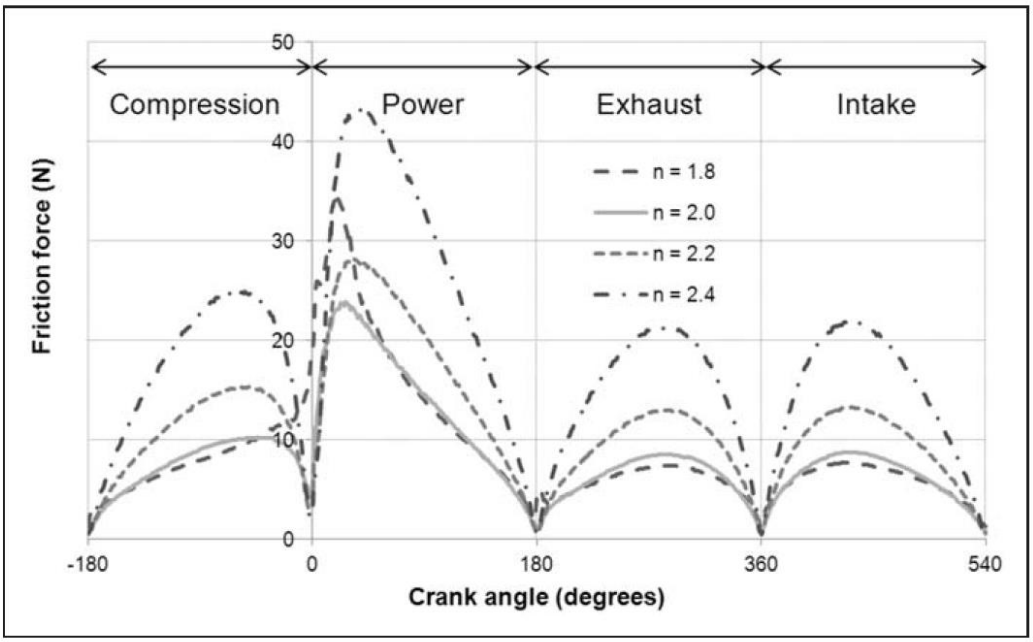

Figure 2.4: Variations of total friction force for different parabolic-type ring profiles during a typical engine cycle [39].

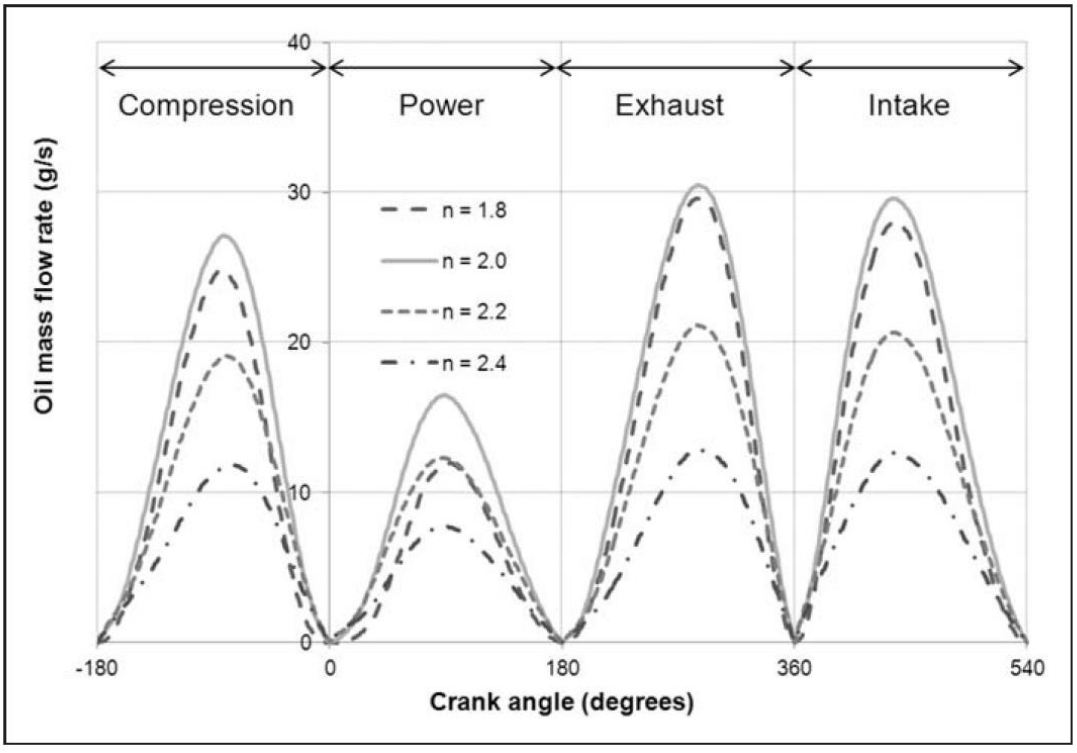

Figure 2.5: Variations of lubricant mass flow rate for different parabolic-type ring profiles during a typical engine cycle [39]

Although ring fitment analysis is taken into account in the works reported in [42, 43] including in some cases with bore out-of-roundness, the ring bore conformability should also take into account the modal behaviour of the ring as, described for example, by Baker *et al* [45]. They showed that ring elastodynamics in fact conforms it to the bore in the high pressure region at low sliding velocities (figures 2.6). This ensures good ring sealing at the expense of increased friction (figures 2.7). However, in some parts of the engine cycle ring elastodynamics as well as ring axial profile can exacerbate the convergent-divergent conjunctional passage and clearance, which suggests lubricant film rupture and the emergence of a cavitation region. This can also affect the compression ring sealing function.

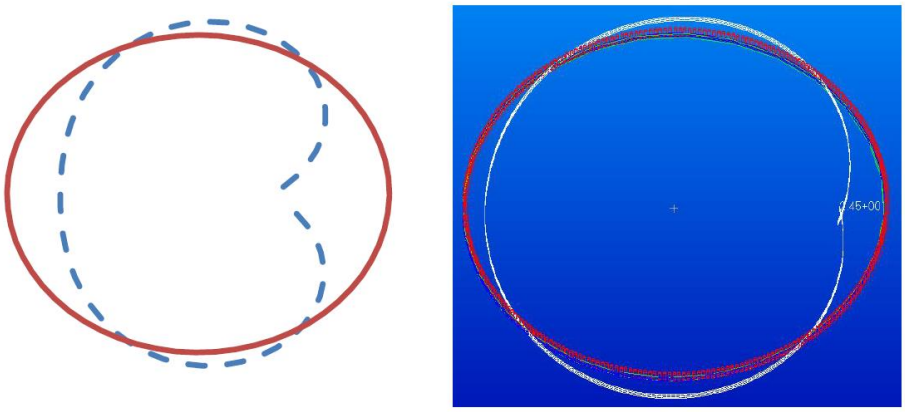

Figure 2.6: Mode shape comparison (a) Analytical (f = 972.06Hz) and (b) FEA (f=969.76Hz) [45].

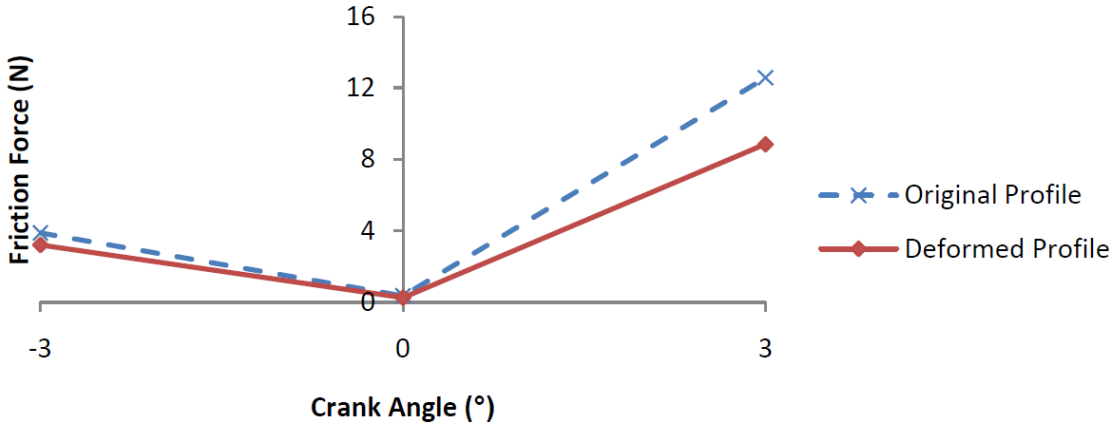

(a)- Transition in reversal at the top dead centre

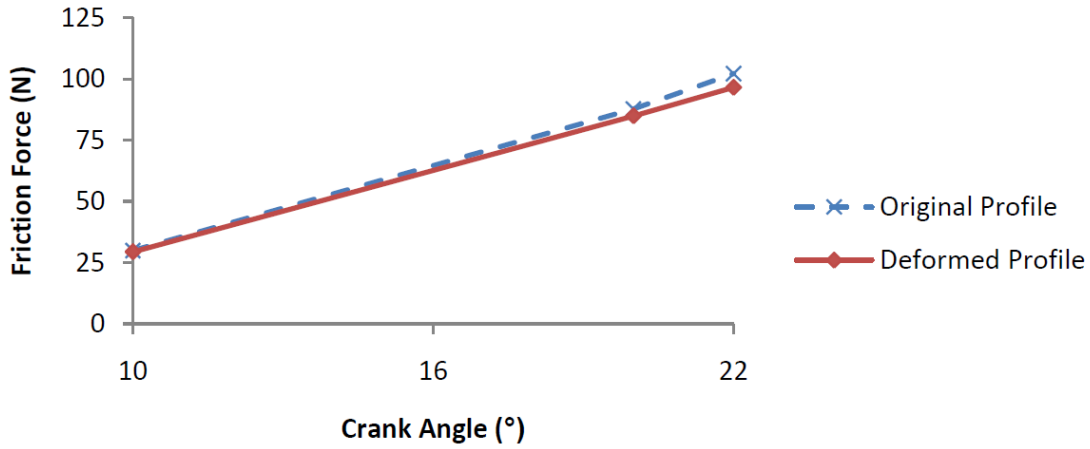

(b)- Transition through maximum combustion pressure

Figure 2.7: Prediction of friction for a rigid and an elastic compression ring [45]

The effect of cavitation was studied by Chong *et al* [46], who used Elrod's approximation [15] to the Jakobsson and Floberg [13] and Olsson [14] JFO cavitation boundary conditions. Chong *et al* [46] showed that cavitation formed at the lubricant film contact exit in the compression stroke reduces the lubricant availability at the TDC reversal, thus causing a starved contact in parts of the power stroke in the vicinity of the TDC (figures 2.8 and 2.9). Therefore, the multi-variate nature of the problem is quite apparent.

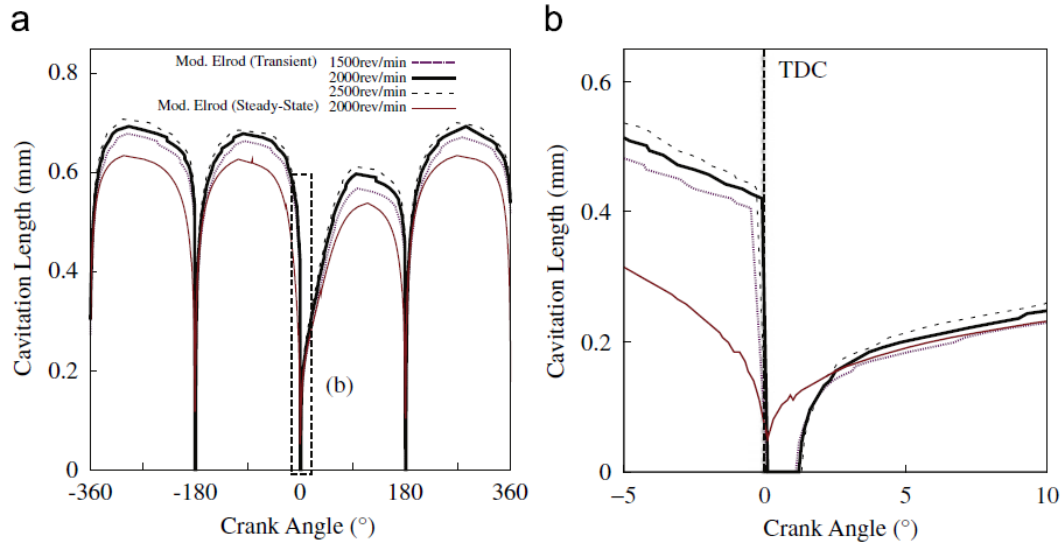

Figure 2.8: Cavitation length (a) Cavitation length for one engine cycle (b) Cavitation length in the vicinity of the power stroke TDC [46]

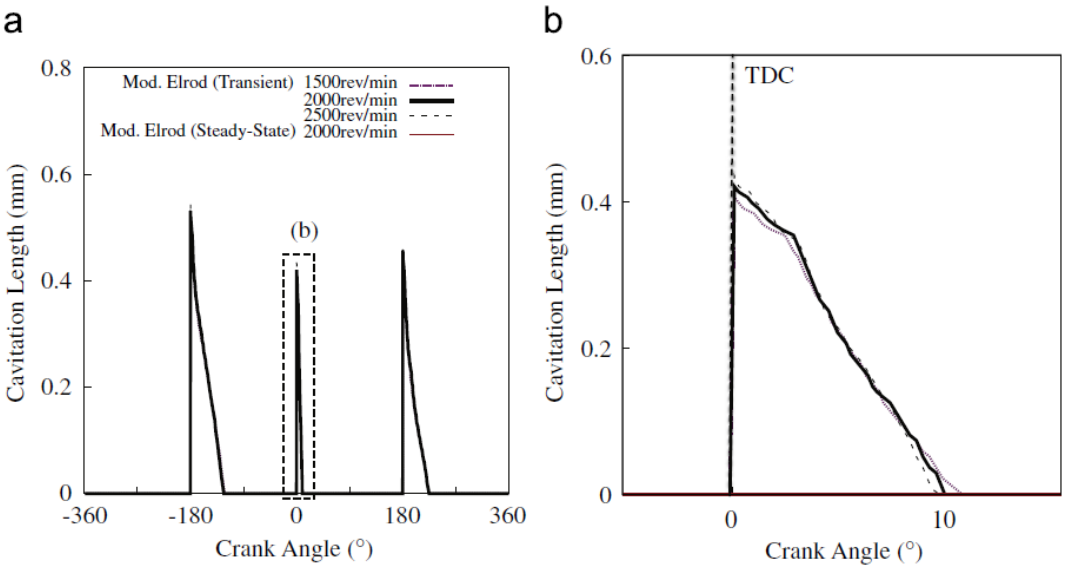

Figure 2.9: Length of the inlet bubble formed by the pre-reversal cavitation (a) Length of the inlet bubble for one engine cycle (b) Length of the cavitation in the vicinity of the power stroke TDC [46]

The analysis in this thesis combines the use of an open free exit boundary condition instead of an imposed cavitation boundary condition. This is achieved by solving the Navier-Stokes equations for multi-phase flow dynamics instead of the usual

Reynolds equation. Additionally, this approach readily enables simultaneous solution with the energy equation. Thus, the effect of surface temperatures, and that caused through viscous shear of the lubricant in the conjunction upon lubricant film formation and viscosity variation into the depth of the film are included in the solution. Unlike Reynolds or Elrod flow equations with Navier-Stokes equations the potential pressure gradient across the film is retained. This enables more accurate prediction of viscous friction due to Poiseuille flow as well as in Couette shear. This approach together with the inclusion of lubricant rheological state and asperity interactions to represent boundary friction has not hitherto been reported in literature.

2.5. Studies on journal bearings: experiments and modelling

According to Richardson [1], friction accounts for 4-15% of total input energy in a fired engine of which 40-55% is due to the losses in the piston skirt and ring-pack. The losses due to the connecting-rod bearings can account for 18-33% of the total parasitic losses as well. In other words, the elliptic bore connecting-rod bearings contribute to around 0.29% to 2.7% of total energy loss from an engine. Obviously, these proportions vary according to engine configuration, such as fuel type, compression ratio, stroke, number of cylinders, etc.

The journal (crank-pin) is usually made of stiff materials with high levels of hardness such as low carbon heat-treated steels or spheroidal graphite irons [47]. The bearing substrate is also made of hard and stiff materials such as nodular cast iron or steel to provide adequate load support mechanism. In addition, overlay materials such as aluminium-tin based alloys (such as Babbitt) are also used to increase the ability to capture the small size wear particles (embeddability property) which are produced when a direct contact between solid surfaces occurs such as under the stop-start conditions or under engine idling [48]. The relatively soft (low elastic modulus overlay, such as Babbitt with a modulus of 60 GPa) encourage localised elastic deformation under load, making the problem elastohydrodynamic. Additionally, a

very thin smooth layer of hard wear-resistant coating is used to reduce friction and wear under boundary or mixed regime of lubrication (such as Indium or Bismuth, with a coated thickness of few micrometres).

Currently minimum film thickness values of around 0.5-1.0μm are expected at parts of the engine cycle (at low speeds and high loads with low-viscosity lubricant) in big end bearings. Therefore, some counterface asperity interaction is expected for the dynamically loaded big-end bearings [49].

Common simplifying assumptions made in the analysis of big end bearings in industry are: short-width bearing assumption, circumferential symmetry, rigid surfaces, no-misalignment, no lubricant recirculation, Newtonian lubricant shear behaviour, no instability induced by vibrations, isothermal conditions [50], no squeeze film effect and idealised circular bore shape.

As it can be noted, as the technology in the IC engine design has advanced, the operating conditions that the engine components such as the main bearings encounter have become harsher. For instance, introduction of start-stop concept has increased the asperity interactions.

The introduction of start-stop system has increased the fuel efficiency of IC engines by 5% through switching off the engine during the engine idle running period [51]. As the driver throttles the engine, the big end bearing is subjected to sudden application of load as well as operating at a higher rotational speed, before any hydrodynamic lubrication film is established. Under these conditions, it is expected that the big end bearing would operate under a mixed or boundary regime of lubrication causing direct asperity contact between opposite surfaces.

According to Adam et al [51], the big end bearings need to be designed for 250,000 to 300,000 stop-starts where the current bearings with aluminium or copper overlays encounter severe wear only after 100,000 such stop-start conditions. This has resulted in many investigations into the lubrication and wear of such bearings in

industry [52] in addition to efforts put into the introduction of various types of polymer-based materials as overlays [53, 54]. To address the complex working conditions encountered in the big end bearings of current (and foreseeable) IC engines, one cannot rely on the results which are predicted by models with the aforementioned simplifying assumptions.

From the early studies on the journal bearings [55, 56] it was evident that inclusion of thermal effect in real applications is essential. For instance, the isothermal models show significant differences between the theoretical and experimental results. Therefore, the investigations were focused on the thermohydrodynamic (THD) study of the journal bearings. The first THD model for journal bearings was introduced by Dowson and March [57]. Using Finite Difference Method (FDM), they solved the 1D Reynolds' equation in the conjunction together with the simplified 2D energy equation to determine the temperature distribution in the lubricant. They considered simplified thermal boundary conditions at the journal and bushing surfaces. They found "encouraging agreement" between their model predictions and experimental findings of Dowson et al [56]. The study of Dowson and March [57] opened new inroads into the THD analysis of journal bearings. For example, Suganami and Szeri [58] employed an FEM (Finite element method) approach to solve the THD problem and modelled the turbulent (or "super-laminar") flow of the lubricant in high speed journal bearings. They found that the isothermal boundary condition for the shaft in the laminar regime was appropriate when at the "super-laminar" regime, where the adiabatic boundary conditions provided more suitable predictions.

Another investigation using FEM was reported by Medwell et al [59] in which they solved the Navier-Stokes equations for high speed cases, where the inertial (advection) terms were suspected to have a significant influence on the bearing performance. It was found that the lubricant advection distorts the axial velocity profile from the assumed parabolic form. The main shortcoming of their research was neglecting the thermal effects. The most important parameter in such studies

was the treatment of the thermal boundary conditions for instance, assuming that the heat transfer in the bearing (sleeve) takes place in the radial direction only and conduction in the circumferential direction was ignored [58]. In addition, for the journal surface Medwell et al [59] assumed an adiabatic or isothermal boundary condition. This is known as ISOADI (isothermal condition at the oil-shaft interface and the adiabatic condition at the oil-bushing interface) boundary conditions [60]. It was shown that the bearing temperature varies considerably depending on the type of boundary conditions used.

In a combined numerical and experimental study by Ferron et al [61], they employed a 2D form of Reynolds equation under steady-state conditions. The thermal boundary conditions at the outside of the bearing were assumed to be partly isothermal and partly under free convention. They imposed heat flux continuity at the lubricant-bushing and lubricant-journal interfaces. They also assumed a constant shaft temperature in the circumferential direction. This was in line with Dowson et al [56] observations that the variation of the journal temperature in the circumferential direction was negligible and therefore, it could be considered as isothermal.

An important parameter introduced through a set of experimental and analytical studies by Mitsui et al [62-64] was the effect of the cooling as the result of the flow of supply oil. This required the introduction of a mixing coefficient into the analysis, which needed to be determined through experiments. In another set of studies, to accelerate the solution procedure, a polynomial temperature distribution was assumed in order to solve the energy equation [65, 66]. However, this method is considered to be quite approximate.

Lund and Hansen [67] also found that their analytical model was inadequate in addressing the film rupture since it was observed through experiments that there exists a backflow of cold supply oil from the grooves into the ruptured film zone which cools the wall of the sleeve. Mitsui [64] also pointed out that the relatively poor

agreement between the experimental and numerical results for THD of journal bearings was due to their lack of addressing the THD in the ruptured film region.

Boncompain et al [68] took into account the reverse flow at the contact inlet and the recirculating heat flux across the cavitation zone, as well as the thermo-elastic displacements of the journal and the bearing bushing. They concluded that most of the heat generated is carried away by the fluid flow.

The subject of thermal behaviour of lubricant in the cavitation region has also been studied by Knight and Niewiarowski [69]. They considered a two-axial-groove journal bearing. They compared two models to treat the thermal behaviour of the lubricant in the cavitation region. They used the traditional effective length (EL) approach [65, 68] as well as an effective density model which took into account the liberation of air from the lubricant in the cavitation zone, called the gas bubble (GB) model. However, they employed the approximate solution method for the energy equation similar to that of Lund and Hansen [65] in which a temperature profile was assumed. The results from the employed GB model showed better agreement with the experimental results in the cavitation region while the predictions from the EL model conformed well to the experimental data in the full-film region.

In the work conducted by Ma and Taylor [70], the contribution from the lubricant back-flow into the cavitated zone (from oil feed grooves) which was expected to induce a ‘temperature fade’ phenomenon in the cavitation region was investigated experimentally. The “temperature fade” phenomenon in the cavitation region observed in several experiments is defined as the gradual decrease in the measured bearing overlay temperature in the cavitation region near to the bearing exit constriction which shows an opposite trend to that of the full-film region. Ma and Taylor [70] showed that the temperature fade is more pronounced for the multi-lobe or elliptical bore bearings.

From the previous theoretical researches which have employed the EL cavitation model it is evident that the model predicts a temperature rise in the cavitation zone, which is not in line with the experimental observations. As discussed previously, the GB model described by Knight and Niewiarowski [69] provides better predictions for this zone due to the fact that it takes into account the reduction in the heat dissipation in the cavitation region by taking into account a mixture of gas and liquid there.

There would be some contribution of cooling effect due to any back-flow (reverse flow) into the cavitated region. This is described by Ma and Taylor [70] who considered this effect as an additional contributor to the temperature fade effect in the cavitation region.

It is noteworthy that a combined experimental and numerical work by Syverud [71] was dedicated specifically to the study of the temperature fade effect in the cavitation zone of a full journal bearing. It was found that the temperature drop in the cavitation zone is highly likely to be due to the evaporation of oil (which requires higher enthalpies) since pressures higher than ambient pressure were observed there when the bearing was operating at sub-ambient pressures. In addition, this drop in temperature was observed to be independent of the total working temperature of the bearing. Here it should be noted that according to Heshamt [72] some experiments suggest that the temperature in the cavitation region should remain constant.

Gethin and El-Deihi [73] also studied the twin-axial-groove journal bearings both experimentally and analytically under extreme transient loading and speed varying conditions. They concluded that the cooling effect of the supplied oil was minimal if the groove fell into the highly loaded zone of the bearing.

More recently, Kuznetsov et al [74] considered the local deformation in the PTFE type overlay of the bearing bushing and solved the THD problem, including the use of column method for localised deformation of the soft overlay. This method is a

simple approximation and provides a linear relationship between the contact pressure and the corresponding local deformation.

To solve the resulting set of governing equations (either Reynolds or Navier-Stokes for flow field and energy equation for temperature distribution), most of the numerical methods have used FDM (to a large extent) or FEM (to a smaller extent). Advances in the FVM (Finite Volume Method) have enabled 3D solution of the THD of the journal bearings. The work reported by Han and Paranjpe [75] were amongst the first using the FVM. They solved the generalised Reynolds equation introduced by Dowson [76] in conjunction with an Elrod type boundary condition to treat the occurrence of cavitation. The advantage of FVM is that the occurrence of reverse flow is automatically taken into account. Han and Paranjpe [75] used adiabatic thermal boundary conditions at the bushing surface, whilst isothermal or adiabatic thermal conditions were imposed at the surface of the journal. However the study was limited to the steady-state case with a specified value for the eccentricity ratio. In addition, the authors noted that some of these boundary conditions have little correspondence to the real physical working conditions of most journal bearings, especially those used in IC engines. They also noted that the choice of thermal boundary conditions would influence the solution quite significantly.

The THD of non-circular or multi-lobe bearings is of great practical importance as in reality and in most applications such as those related to engine connecting rod bearings, this is often the case. Big-end bearings are often “lemon-shaped” (i.e. with an elliptic bore/bushing). In some applications multi-lobed bearings are used. The main advantage of non-circular multi-lobed bearings is the formation of many converging wedges, thus increased load carrying capacity. Clearly, there would be many diverging regions as well which can lead to dispersed regions of cavitation. Hussain et al [77] studied THD of circular, elliptical and multi-lobe journal bearings. They solved Reynolds equation in the conjunction with the energy equation using FDM. The two main findings of the study were that as a higher temperature rise was

observed for the two-lobe bearing than the elliptic bore bearing. In addition, the way that the cavitation phenomenon is treated can have significant effect on the final temperature profile. In addition, it was found that the load capacity was highly influenced by the ellipticity ratio rather than the eccentricity ratio in the case of elliptic bore bearings. The same finding was also noted by Mishra et al [43], who also included the effect of asperity interactions for different asperity patterns on the bearing bushing.

Based on the established THD analysis methods for journal bearings, Khonsari et al [78] and Jang and Khonsari [60] provided a generalised THD study of such bearings. Khonsari et al [78] devised design charts based on the extensive simulations carried out on their THD studies, which provided the maximum and effective bearing temperature for various working conditions.

Another important aspect which most of the previous research have overlooked is the asperity interaction which exists with thin films, resulting in mixed regime of lubrication. Most of the investigations were focused on the cases with low eccentricity ratios whereas under high loading conditions large eccentricity ratios may be unavoidable. Therefore, as the working conditions became harsher, there is a greater tendency for the journal bearings to operate under mixed or even boundary regimes of lubrication for at least short periods of their operational cycle. Such conditions are now prevalent in the big end bearings of IC engines due to ever increasing combustion power.

Shi and Wang [79] and later Wang et al [80] were amongst the first who addressed the THD problem in journal bearings in conjunction with the effect of asperity interactions, the so-called mixed-THD model. Instead of the conventional Reynolds equation, they used average flow model initially developed by Patir and Cheng [81]. They also included the effect of heat generated by asperity contact in the heat source term of the energy equation. However, Shi and Wang [79] did not include the load supported by the asperities. They used the aforementioned GB model for

treating the cavitation phenomenon. They also considered inlet temperature adjustment due to mixing with the recirculating hot lubricant. They found that surface roughness can have a profound effect when the film thickness approaches the same order of magnitude as the surface roughness.

San Andrés [4] reviewed some very important works [82-86] about cavitation in fluid film bearings. He concluded that a film rupture model, based on mass flow continuity through the cavitation region, gives boundary conditions for the inception of the cavitation and subsequent film reformation. San Andrés [4] represented the possible formations of the fluid flow through the cavitation area as observed experimentally. As figure 2.10 shows streamers attached to the moving surface carry the lubricant flow downstream of the cavitation inception point. In another word, the whole moving surface appears wetted by a film of lubricant with the cavitation area connected to the stationary surface. Figure 2.11 shows a schematic of the rupture boundary of the cavitation region which is surrounded by a film of lubricant moving with the journal.

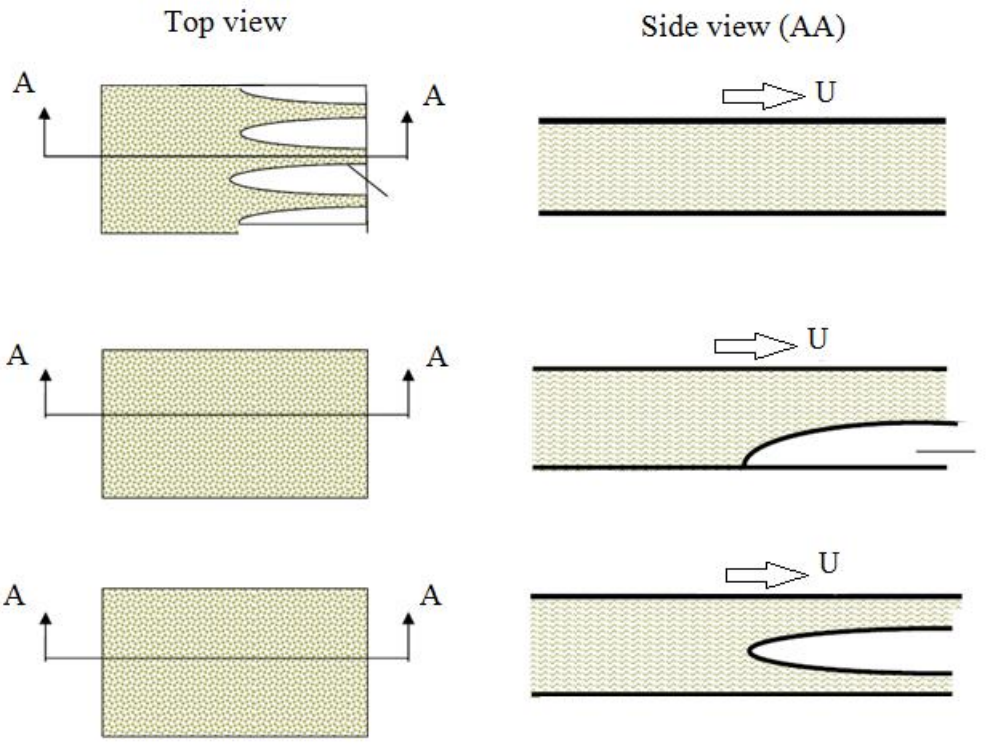

Figure 2.10: Fluid flow through cavitation zone [4]

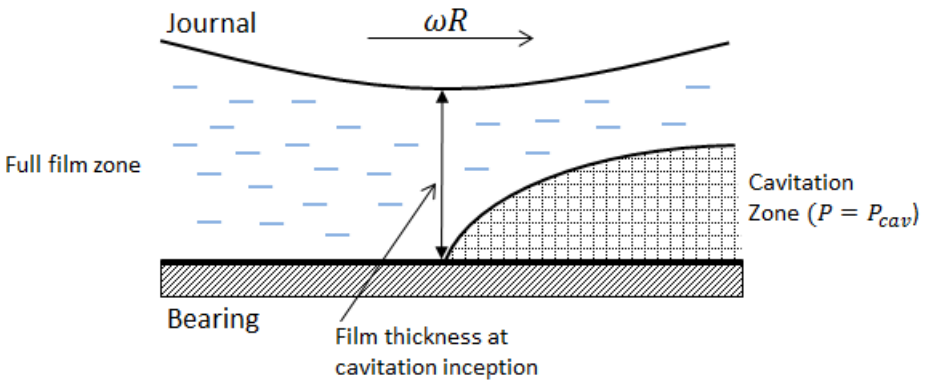

Figure 2.11: Cavitation inception in a thin film

With the advances in numerical methods for fluid flow analysis, particularly those stemming from FVM in CFD, some researchers have focused on solving the full Navier-Stokes and energy equations in 3D for the case of journal bearings. An important contribution is that of Tucker and Keogh [86] who employed a full 3D CFD approach for the THD analysis of steady-state motion of journal bearings. They used an Elrod-type cavitation model which allowed for the existence of sub-ambient pressures. In this method the vapour fraction becomes a function of the film thickness [87]. However, as Tucker and Keogh [86] have mentioned for non-Couette or unsteady flows a time-dependent continuity equation should be used to determine the vapour fraction. They also solved the heat condition equations for the stationary bearing and the rotating journal with convection boundary conditions at the outer surfaces. For the solid-fluid interface continuity of heat flux and compatibility of temperature was assured. The comparison of the numerical results with those from experiments showed fairly good agreement although higher journal temperatures were found to be insensitive to the variation in the circumferential direction unlike the experimental findings. They acknowledged that an appropriate cavitation model should make it possible to predict differentials in the shaft temperature.

In a set of numerical analyses using CFD methods, Nassab and Moayeri [88] and Nassab [89] studied 3D THD of axially grooved journal bearings. The inertial effects as well as the effect of various cavitation models on THD predictions were studied. Nassab and Moayeri [88] solved the 3D Navier-Stokes and energy equations using FVM. They employed liquid fraction to address the properties in the cavitation region and used the mean values of properties of the mixture in this region. However, they set the sub-ambient pressures in the cavitation region equal to the atmospheric pressure in each iteration step, thus the generation of sub-ambient pressures were restricted unlike the method used by Tucker and Keogh [86]. Later, Nassab [89] also found that even at lower Reynolds numbers of order of 10, the fluid inertial terms can have substantial effect on THD characteristics of the journal bearings, especially at low load and high speeds (hence, low eccentricities) running conditions.

The cavitation phenomenon itself and use of and an appropriate model which can exactly describe it and predict its occurrence has been and still remains the subject of investigation by many research workers. The study of cavitation phenomenon in tribology and an attempt to provide a phenomenological model for it dates back to as early as early 1900s [90]. In addition to the most common Reynolds or Swift-Stieber [31,32] cavitation boundary conditions, the most accepted boundary conditions to treat the cavitation phenomenon is the mass-conserving cavitation boundary conditions, originated through the works of Jakobsson-Floberg-Olsson known as the JFO cavitation boundary conditions (Floberg and Jakobsson [13], Olsson [14]). A computationally-friendly version of this model, sometimes referred to as: “the universal cavitation algorithm” was developed by Elrod and Adams [3] and Elrod [15]. This has since been the most popular cavitation model in the literature especially for those who use Reynolds-type equations to obtain the pressure distribution in the contact. A comprehensive review of early works on modelling the cavitation phenomenon in the bearings is given by Dowson and Taylor [91].

The experimental evidence indicates that a cavitation model should allow for the development of sub-ambient pressures as negative pressures of around 1.2MPa absolute have been observed in the cavitated region through experimentation [92]. In addition, various pressure distribution patterns may exist under dynamic loading conditions [91]. In addition, according to Jacobson [93] the experimental investigations suggest that in non-stationary bearings it is the vapour cavitation which is dominant and it is a direct result of breakage in oil-bearing interface, caused by tensile stresses in the lubricant.

Dowson et al [94], in a numerical study, implemented the cavitation algorithm of Elrod and Adams [3] and Elrod [15] in order to predict and locate the rupture and reformation points in a plain journal bearing. Then, they conducted an experimental study [95] in order to investigate the validity of their numerical analysis. Their tests included the study of the effect of varying eccentricity ratio, supply pressure and shaft rotational speed on the rupture and reformation loci. They noticed that the inclusion of film reformation through using Elrod and Adams cavitation algorithm is vital for an accurate prediction of the side leakage from the journal bearings. The predictions, eliminating film reformation such as those of Swift-Stieber [31,32] boundary conditions lead to significant errors. They also found that at lower eccentricity ratios (<0.6) and supply pressures a significant difference between the experimental results and the numerical predictions was observed. In addition, there was not a good quantitative correlation between the numerical predictions and the experimental results for the location of the film reformation point although the trend in the variations was close. They attributed this to the inadequacy in the utilised rupture process model which does not allow for the negative gauge pressures in the lubricant film.

The “universal cavitation model” of Elrod was later modified and refined further to increase the computational stability and efficiency through the work of Vijayaraghavan and Keith [96], Paydas and Smith [97] and Hirani et al [98]; the last

one for journal bearings with high dynamic loads. Alternative models which also consider mass-conserving aspect were also developed later such as that of Giacopini et al [99]. However, it must be noted that some extensive experimental works such as those by Etsion and Ludwig [100] have indicated that the JFO boundary condition is not strictly accurate in predicting the cavitation zone. In addition, they found that the pressure in the cavitation zone does not remain constant and occurrence of sub-ambient pressures and flow reversal can be significant and should not be neglected.

Later studies by Groper and Etsion [101, 102] found that cavitation shape could well be predicted by the shear mechanism while the generated pressures in the cavitation zone using this method was lower than those measured. On the other hand, gas transport through liquid-vapour boundary hypothesis was unable to either predict the cavitation region shape or the observed pressure levels. In fact, they concluded that the reverse flow phenomenon observed in the cavitation zone is accountable for the observed pressure build-up in this region.

As already noted, with advances in the CFD approach, it has been possible to devise models that can address cavitation as a full 3D multi-phase flow phenomenon. Tucker and Keogh [86] used an Elrod type boundary condition in which the ratio of vapour to liquid in the mixture inside the cavitation zone was proportional to the ratio of film thickness at that specific point to the gap at the rupture point. In Nassab and Moayeri [88] and Nassab [89] the vapour-liquid ratio was obtained by assuming linear and parabolic velocity distributions in the circumferential and axial directions in the cavitation zone and using control volume approach for the mass flow continuity. Nassab and Maneshian [103] also investigated the effect of the employed cavitation model on predicting the THD lubrication of finite length journal bearings under steadily loaded conditions. They used vapour-liquid mixture properties for the cavitation zone. The only difference between the three models was the method by which the vapour-liquid ratio in the mixed zone was calculated or the viscous

dissipation was considered. They concluded that the method used in their previous studies [88,89] to calculate the properties in the mixed zone was the most appropriate model amongst the studied cases and the viscous dissipation should be calculated based on the mixed-phase flow properties.

The current study, highlighted in this thesis, uses a full 3D CFD approach into the THD analysis of the big-end bearings in a typical IC engine. The model is validated against experiments and is then adapted to investigate tribological conditions in big-end bearings subjected to cylinder deactivation conditions.

Chapter 3: Numerical Modelling

3.1. General Navier-Stokes and energy equations

This chapter presents the underlying theory for the numerical analysis presented in this thesis. The theory involves the combined solution of Navier-Stokes equations, together with various forms of energy equation, as well as lubricant rheological state equations. It also includes the use of vapour transport equation and modified Rayleigh-Plesset equation to take into account the formation of cavitation zones and multi-phase flow. The methodology presented here is applied to the cases of compression ring-cylinder liner conjunction and journal bearings in general. The boundary conditions for both pressure and temperature are different in these cases and are treated separately in chapters 4, 5 and 6. In the case of the ring-liner conjunction an analytical control volume thermal mixing model is applied as described in section 4.4.

The general continuity and Navier-Stokes momentum equations for compressible viscous fluid flow can be described as [104]:

$$\frac{D\rho}{Dt} + \rho\nabla.\vec{V} = 0 \tag{3.1}$$

$$\rho\frac{D\vec{V}}{Dt} = -\nabla p + \nabla.(\bar{\tau}_{ij}) + \vec{F} \tag{3.2}$$

where $\frac{D}{Dt}$ is the covariant derivative operator, ρ is the lubricant density, p is the pressure, $\bar{\tau}_{ij}$ is the viscous stress tensor and $\vec{F}$ is the body force field vector. In addition, $\vec{V} = U\hat{i} + V\hat{j} + W\hat{k}$ is the velocity vector in which U is the component of velocity in the direction of axial lubricant flow entrainment, V is that in the side-

leakage direction; along the y-axis (which may reasonably be discarded as there is negligible side-leakage in the case of thin film in the ring-bore conjunction, but not in the case of the big end bearing), and W is the squeeze film velocity, $\frac{\partial h}{\partial t}$. This represents the mutual convergence and separation of the conjunctional solid boundaries. The viscous shear stress tensor is:

$$\bar{\tau}_{ij} = \eta\left(\frac{\partial U_i}{\partial x_j} + \frac{\partial U_j}{\partial x_i} - \delta_{ij}\frac{2}{3}\nabla.\vec{V}\right) \tag{3.3}$$

where, η is the effective lubricant dynamic viscosity, δ_{ij} is the Kronecker delta and it is defined as:

$$\delta_{ij} = \begin{cases} 0 & \text{if } i \neq j \\ 1 & \text{if } i = j \end{cases} \tag{3.4}$$

One possibility in a CFD model is to evaluate the fluid viscosity as a function of pressure and temperature along the liner and into the depth of the lubricant film. The latter is neglected in the conventional hydrodynamic lubrication approaches, which are based on Reynolds equation, where it is assumed that for thin films: $\frac{\partial p}{\partial z} = 0$. Finally, the energy equation can be stated as [104]:

$$\rho\frac{DH}{Dt} = \frac{Dp}{Dt} + \nabla.(k\nabla T) + \bar{\tau}_{ij}\frac{\partial U_i}{\partial x_j} \tag{3.5}$$

where, H is the fluid enthalpy, T is the temperature and k is the thermal conductivity of the fluid.

3.1.1. Mixture Model

The mixture model [105] is a simplified multi-phase model. It can be used to model multi-phase flows where the phases move at different velocities, but assume local

equilibrium over short spatial length scales. It can be used to model multi-phase flows with very strong coupling and phases moving at the same velocity.

3.1.1.1. Continuity Equation

The continuity equation for the mixture is:

$$\frac{\partial}{\partial t}(\rho_m) + \nabla.(\rho_m \vec{V}_m) = 0 \tag{3.6}$$

where, $\vec{V}_m$ is the mass-averaged velocity:

$$\vec{V}_m = \frac{\alpha_v \rho_v \vec{V}_v + (1-\alpha_v)\rho_l \vec{V}_l}{\rho_m} \tag{3.7}$$

and ρ_m is the mixture density:

$$\rho_m = \alpha_v \rho_v + (1-\alpha_v)\rho_l \tag{3.8}$$

where, α_v is the vapour volume fraction.

3.1.1.2. Momentum Equation

By summing the individual momentum equations for all the phases, the momentum equation for the mixture can be obtained as:

$$\frac{\partial}{\partial t}(\rho_m \vec{V}_m) + \nabla.(\rho_m \vec{V}_m \vec{V}_m) = -\nabla p + \nabla.\left[\eta_m \left(\nabla \vec{V}_m + \nabla \vec{V}_m^{\,T}\right)\right] + \nabla.\left(\alpha_v \rho_v \vec{V}_{dr,v} \vec{V}_{dr,v} + (1-\alpha_v)\rho_l \vec{V}_{dr,l} \vec{V}_{dr,l}\right) + \vec{F} \tag{3.9}$$

where, $\vec{F}$ is a body force, and η_m is the viscosity of the mixture:

$$\eta_m = \alpha_v \eta_v + (1-\alpha_v)\eta_l \tag{3.10}$$

$\vec{V}_{dr,v}$ is the drift velocity for vapour phas:

$$\vec{V}_{dr,v} = \vec{V}_v - \vec{V}_m \tag{3.11}$$

3.1.1.3. Energy Equation

The energy Eq. (3.5) is modified for the mixture is expressed in the following form:

$$\begin{aligned} &\frac{\partial}{\partial t}\left(\alpha_v \rho_v E_v + (1-\alpha_v)\rho_l E_l\right) + \\ &\quad \nabla.\left(\alpha_v \vec{V}_v(\rho_v E_v + p) + (1-\alpha_v)\vec{V}_l(\rho_l E_l + p)\right) = \nabla.\left[(\alpha_v k_v + (1-\alpha_v)k_l)\nabla T\right]\nabla T) + S_E \end{aligned} \tag{3.12}$$

The first term on the right-hand side of *Eq. (3.12)* denotes energy transfer due to conduction. k is the thermal conductivity of the fluid and S_E includes any other volumetric heat source. For a compressible flow:

$$E_n = H_n - \frac{p}{\rho_n} + \frac{V_n^2}{2} \tag{3.13}$$

where, H_n is the enthalpy for phase n.

3.1.1.4. Relative (Slip) Velocity and the Drift Velocity

The relative velocity between the liquid lubricant and the vapour phase is defined as the velocity of a secondary phase (v) relative to the velocity of the primary phase (l), thus:

$$\vec{V}_{vl} = \vec{V}_v - \vec{V}_l \tag{3.14}$$

For any phase (n), the mass fraction is defined as:

$$f_n = \frac{\alpha_n \rho_n}{\rho_m} \tag{3.15}$$

The relative velocity $\vec{V}_{vl}$ and the drift velocity are related as:

$$\vec{V}_{dr,v} = \vec{V}_{vl} - f_v \vec{V}_{lv} \tag{3.16}$$

In the current mixture model, an algebraic slip formulation is used. The basic assumption of the algebraic slip mixture model is that to assign an algebraic relation for the relative velocity. It means a local equilibrium between the phases should be reached over a short spatial length scale. Following Manninen et al. [105], the form of the relative velocity is given by:

$$\vec{V}_{vl} = \frac{\tau_v}{f_{drag}} \frac{(\rho_v - \rho_m)}{\rho_v} \vec{a}_v \tag{3.17}$$

where, τ_v is the vapour bubble relaxation time which is defined as:

$$\tau_v = \frac{\rho_v d_v^2}{18 \eta_l} \tag{3.18}$$

d is the average diameter of the bubbles of vapour and $\vec{a}_v$ is the acceleration of the vapour bubbles. The default drag function f_{drag} is taken from Schiller and Naumann [106] as:

$$f_{drag} = \begin{cases} 1 + 0.15 \mathrm{Re}^{0.687} & \mathrm{Re} \le 1000 \\ 0.0183 \mathrm{Re} & \mathrm{Re} > 1000 \end{cases} \tag{3.19}$$

$\vec{a}_v$, the average acceleration, is defined as:

$$\vec{a}_v = -(\vec{V}_m . \nabla)\vec{V}_m - \frac{\partial \vec{V}_m}{\partial t} \tag{3.20}$$

The simplest algebraic slip formulation is the so-called drift flux model, in which the acceleration of the bubble is given by a centrifugal force.

3.1.1.5. Vapour Volume Fraction Equation

From the continuity equation for vapour phase the volume fraction equation for vapour phase can be obtained as:

$$\frac{\partial}{\partial t}(\alpha \rho_v) + \nabla.(\alpha \rho_v \vec{V}_m) = -\nabla.(\alpha \rho_v \vec{V}_{dr,v}) + (\dot{m}_{lv} - \dot{m}_{vl}) \tag{3.21}$$

where $\dot{m}_{lv}$ is the mass transfer from phase l to phase v and, $\dot{m}_{vl}$ is the mass transfer from phase v to phase l.

3.1.2. Continuum Surface Force (CSF) model

The surface tension model used in Chapter 4 in the current analysis is the Continuum Surface Force (CSF) model proposed by Brackbill et al [107]. The CSF model tracks the boundaries between two or more immiscible fluids by solving a single set of momentum equations for each phase and tracking the volume fraction of each phase accordingly. With this model, the surface tension can be calculated and added to the source term (body force) in the momentum equation (Eq. (3.9)). Based on the model, the surface tension force source $(\vec{F})$ in the momentum equation is expressed as:

$$\vec{F} = \sigma_s \kappa \hat{\mathrm{n}} \tag{3.22}$$

where σ_s is the interfacial tension between the liquid and vapour phase. The interface unit normal ($\hat{\mathrm{n}}$) and the curvature (κ) can be calculated using the following:

$$\hat{\mathrm{n}} = \frac{\nabla \alpha_v}{|\nabla \alpha_v|} \quad \text{and} \quad \kappa = -(\nabla . \hat{\mathrm{n}}) \tag{3.23}$$

where, α_v is the vapour volume fraction. Based on the governing equations described above, the interfacial tension between the liquid and vapour phases and the viscosities of both liquid and vapour phases are taken into account in the simulation analysis.

3.2. Cavitation Model

3.2.1. Vapour transport equations

With cavitation, the liquid-vapour mass transfer (evaporation and condensation) is governed by the vapour transport equation as [11]:

$$\frac{\partial}{\partial t}(\alpha_v \rho_v) + \nabla . (\alpha_v \rho_v \vec{V}_v) = R_e - R_c \tag{3.24}$$

where ρ_v is the vapour density, $\vec{V}_v$ is the velocity vector of the vapour phase, R_e and R_c are mass transfer source terms related to the growth and collapse of the vapour bubbles respectively. The growth and collapse of a bubble cluster are modelled based on the Rayleigh-Plesset equation, describing the growth of a single vapour bubble in a liquid, which provides the rate equation, controlling vapour generation and condensation.

3.2.2. Consideration of Bubble Dynamics

In most engineering applications it is assumed that there are plenty of nuclei for the inception of cavitation. Thus, the proper accounting of bubble growth and collapse is very important. The bubble dynamics equation can be derived from the generalised Rayleigh-Plesset equation as [108]:

$$R_B \frac{D^2 R_B}{Dt^2} + \frac{3}{2}\left(\frac{DR_B}{Dt}\right)^2 = \left(\frac{P_B - P}{\rho_l}\right) - \frac{4\upsilon_l}{R_B}\frac{DR_B}{Dt} - \frac{2\sigma_s}{\rho_l R_B} \tag{3.25}$$

where, R_B is the bubble radius, σ_s is the liquid surface tension coefficient, ρ_l is the liquid density, P_B is the bubble surface pressure, P is the local far-field pressure and υ_l is the liquid kinematic viscosity. Neglecting the second-order terms, kinematic viscosity and the surface tension force, Eq. (3.25) simplifies to:

$$\frac{DR_B}{Dt} = \sqrt{\frac{2}{3}\frac{P_B - P}{\rho_l}} \tag{3.26}$$

This equation provides a physical approach to introducing the effects of bubble dynamics into the cavitation model.

3.2.3. Full cavitation model

In the current analysis the “full cavitation model” introduced by Singhal et al [11] is used. In this model, all the first-order effects (i.e., phase change, bubble dynamics) only are retained. The model is able to account for multi-phase flows with the slip velocities between the liquid and the gaseous phases. Thermal effects and compressibility of both liquid and gas phases are included. Singhal et al. [11] uses the following two-phase continuity equations to derive an expression for the net phase change rate:

Liquid phase:

$$\frac{\partial}{\partial t}\left[(1-\alpha_v)\rho_l\right]+\nabla.\left[(1-\alpha_v)\rho_l\vec{V}\right]=-R \tag{3.27}$$

Vapour phase:

$$\frac{\partial}{\partial t}(\alpha_v\,\rho_v)+\nabla.(\alpha_v\,\rho_v\vec{V})=R \tag{3.28}$$

The mixture:

$$\frac{\partial}{\partial t}(\rho_m)+\nabla.(\vec{V})=0 \tag{3.29}$$

where, R is the net phase change rate (R_e-R_c), ρ_m is the mixture density (function of phase volume fraction and density) and it is defined as:

$$\rho_m=\alpha_v\,\rho_v+(1-\alpha_v)\rho_l \tag{3.30}$$

Combining Eqs. (3.27)-(3.29) results in a relationship between the mixture density and vapour volume fraction as:

$$\frac{D\rho_m}{Dt}=-(\rho_l-\rho_v)\,\frac{D\alpha_v}{Dt} \tag{3.31}$$

The vapour volume fraction α_v is related to the bubble number density n_B and the radius of a bubble R_B as:

$$\alpha_v=n_B\times\left(\frac{4}{3}\pi\,{R_B}^3\right) \tag{3.32}$$

Substituting Eq. (3.32) into Eq. (3.31) yields the following:

$$\frac{D\rho_m}{Dt} = -(\rho_l - \rho_v)\,(4\pi n_B)^{\frac{1}{3}}\,(3\alpha_v)^{\frac{2}{3}}\,\frac{DR_B}{Dt} \tag{3.33}$$

Using Eq.(3.26), and combining Eq. (3.27), Eq. (3.28), Eq. (3.31), and Eq. (3.33), the expression for the net phase change rate R is obtained as:

$$R = (4\pi n_B)^{\frac{1}{3}}\,(3\alpha_v)^{\frac{2}{3}}\,\frac{\rho_v\,\rho_l}{\rho_m}\left[\frac{2}{3}\left(\frac{P_B - P}{\rho_l}\right)\right]^{\frac{1}{2}} \tag{3.34}$$

in which R represents the vapour evaporation rate. All the terms, except n_B are known constants or dependent variables. The phase change rate can be rewritten in terms of the bubble radius; R_B, since there is no general model for the estimation of the bubble number density. Thus:

$$R = \frac{3\alpha_v}{R_B}\,\frac{\rho_v\,\rho_l}{\rho_m}\sqrt{\frac{2}{3}\left(\frac{P_B - P}{\rho_l}\right)} \tag{3.35}$$

The above equation shows that the unit volume mass transfer rate is not only related to the vapour density; ρ_v, but it is also a function of the liquid density ρ_l as well as the mixture density ρ_m.

Eq. (3.35) is exact since it is derived from volume fraction equations directly and it represents the mass transfer from liquid to vapour phase through mechanism of cavitation. It is worth noting that in practical cavitation models, the local pressure is usually assumed to be the same as the cell centre pressure. The bubble pressure P_B is equal to the saturation vapour pressure in the absence of mass transport and any viscous damping ($P_B = p_c$). Based on Eq. (3.35), a model is suggested by

Singhal et al. [11], where the vapour mass fraction is the dependent variable in the transport equation, thus:

$$\frac{\partial}{\partial t}(\rho_m f) + \nabla.(\rho_m \vec{V}_\upsilon f) = \nabla.(\Gamma \nabla f) + R_e - R_c \tag{3.36}$$

where, Γ is the diffusion coefficient.

The rates of mass exchange are derived from the Rayleigh-Plesset equations with limiting bubble size considerations (interface surface area per unit volume of vapour) using the following equations. For simplicity, in Eq. (3.35), the typical bubble size R_B is taken to be the same as the limiting (maximum) bubble size, then, R_B is determined by the balance between hydrodynamic drag and surface tension forces. A commonly used formula in the nuclear industry is [109]:

$$R_B = \frac{0.061 \mathrm{We}\, \sigma_s}{2\rho_l {V_{vl}}^2} \tag{3.37}$$

For bubble flow regime, V_{vl} is normally fairly small (5-10% of the bulk liquid velocity). By using various limiting arguments, e.g., $R_B \to 0$ as $\alpha_v \to 0$, and the fact that the per unit volume phase change rates should be proportional to the volume fractions of the transferor phase, the following expressions for vapour generation rates are obtained in terms of the vapour mass fraction f:

$$R_e = C_e \frac{V_{ch}}{\sigma_s} \rho_l \rho_\upsilon \sqrt{\frac{2(p_c - p)}{3\rho_l}} (1 - f), \qquad \text{for} \quad p < p_c \tag{3.38}$$

$$R_c = C_c \frac{V_{ch}}{\sigma_s} \rho_l \rho_\upsilon \sqrt{\frac{2(p - p_c)}{3\rho_l}}\, f, \qquad \text{for} \quad p > p_c \tag{3.39}$$

where, V_{ch} is a characteristic velocity, which denotes the effect of the local relative velocity between the liquid and the vapour phases. p_c is the liquid cavitation/vaporisation pressure at a given temperature and C_e and C_c are empirical constants and are considered to be 0.02 and 0.01 respectively according to Singhal et al [11].

3.3. Conventional hydrodynamic cavitation model (Elrod's method)

For the engine under investigation, the ring length-to-width ratio is over 100. Therefore, as a first approximation, the piston ring/liner conjunction can be viewed as an infinitely long sliding bearing [33]. The Elrod cavitation algorithm [15] is only used for the case of ring-liner contact in this thesis. Although, this assumes uniform radial loading and neglects piston secondary motion as well as ring dynamics, the final results can provide a valuable insight. Nevertheless, those can have significant effect in determining the tribodynamics of the ring and the subsequent tribological performance. If the flow is laminar, the behaviour of most lubricated conjunctions can be predicted using 1D Reynolds equation:

$$\frac{\partial}{\partial x}\left(\frac{\rho h^3}{6\eta}\frac{\partial p}{\partial x}\right)=\frac{\partial}{\partial x}(\rho h U)+2\frac{d}{dt}(\rho h) \tag{3.40}$$

Elrod's [15] modification provides an acceptable solution if the cavitation is present: In the full film section of the contact both of the Couette and Poiseuille flow terms are considered, while in the cavitation region the Couette term only is considered. To account for this, a switching term; g_s is defined by Elrod [15] as:

$$g_s=\begin{cases}1 & \text{if } \xi\geq 1 \quad \text{(full film region)}\\ 0 & \text{if } 0<\xi<1 \quad \text{(cavitation region)}\end{cases} \tag{3.41}$$

in which ξ is defined as fractional film content. This allows defining the contact pressure distribution as follows:

$$p = g_s \beta \ln \xi + p_c \tag{3.42}$$

where, p_c is cavitation pressure and β is the lubricant bulk modulus. Reynolds equation is now modified using Eqs. (3.40) and (3.42) as:

$$\frac{\partial}{\partial x}\left(\frac{\rho h^3}{6\eta} g_s \beta \frac{\partial \xi}{\partial x}\right) = U \frac{\partial}{\partial x}(\xi \rho h) + 2\frac{d}{dt}(\xi \rho h) \tag{3.43}$$

in which lubricant viscosity and density can change with the contact pressure and temperature

3.4. Lubricant rheology

The lubricant bulk rheological properties including density and viscosity are affected by pressure and temperature [40]. The density–pressure relationship is [110]:

$$\rho = \rho_0 \left(1 + \frac{6.0\times10^{-10}(p - p_{atm})}{1 + 1.7\times10^{-9}(p - p_{atm})}\right)\left[1 - 0.65\times10^{-3}(T - T_0)\right] \tag{3.44}$$

in which p_{atm} is the atmospheric pressure and T_0 is temperature in K. Variations of lubricant dynamic viscosity with pressure and temperature can be expressed based on Roelands' equation [111] which was further developed by Houpert [112], as follows:

$$\eta = \eta_0 \exp\left\{(\ln(\eta_0) + 9.67)\left[\left(\frac{T - 138}{T_0 - 138}\right)^{-S_0}\left(1 + \frac{p - p_{atm}}{1.98\times10^8}\right)^Z - 1\right]\right\} \tag{3.45}$$

in which, η_0 is the lubricant dynamic viscosity at atmospheric pressure and temperature, and Z and S_0 are constants:

$$Z = \frac{\alpha_0}{5.1\times10^{-9}[\ln(\eta_0)+9.67]} \quad \text{and} \quad S_0 = \frac{\beta_0(T_0-138)}{\ln(\eta_0)+9.67} \tag{3.46}$$

where α_0 and β_0 are constants at atmospheric temperature and pressure. It should be noted that the rheological parameters are for a fresh lubricant. In practice, the lubricant is subject to shear thinning, oxidation and contamination [113].

3.5. Load supported through Asperity contact

Ideally, the applied load is carried by a lubricant film formed in the conjunction (i.e. the hydrodynamic reaction). However, a coherent film of lubricant is not always assured due to the transient nature of engine operations (load-speed combination as well as stop-start conditions). Hence, some of the applied load is carried by the direct contact of surfaces (see figure 3.1), usually a small portion of the rough topography of the crank-pin and the bushing surface (i.e. the asperity load). The latter is usually overlaid with a sandwich of soft and hard layers which also deform locally as the result of conjunctional pressures, conditions which are referred to as elastohydrodynamic. Therefore:

$$W = W_h + W_a = F \tag{3.47}$$

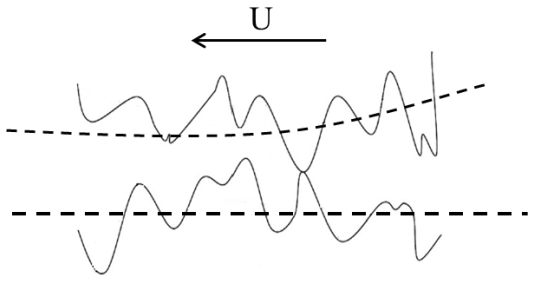

Figure 3.1: Surface asperities contact

where, the elastohydrodynamic reaction is obtained as:

$$W_h = \int \int pdA \tag{3.48}$$

The asperity or boundary load is a function of surface roughness. For an assumed Gaussian distribution of asperities [114]:

$$W_a = \frac{16\sqrt{2}}{15}\pi(\xi\beta\sigma)^2\sqrt{\frac{\sigma}{\beta}}E'AF_{5/2}(\lambda) \tag{3.49}$$

where, the statistical function $F_{5/2}(\lambda)$ is a function of Stribeck oil film parameter $\lambda = \frac{h}{\sigma}$, where σ is the composite root mean square roughness of the contiguous surfaces. The statistical function can be represented by a polynomial-fit function as [115]:

$$F_{5/2}(\lambda) = \begin{cases} -0.004\lambda^5 + 0.057\lambda^4 - 0.296\lambda^3 + 0.784\lambda^2 - 1.078\lambda + 0.617; & \text{for } \lambda \leq \lambda_{cr} \\ 0 \quad ; & \text{for } \lambda > \lambda_{cr} \end{cases} \tag{3.50}$$

where, for the current analysis a critical film ratio of $\lambda_{cr} \approx 3$ is assumed, below which mixed regime of lubrication (including asperity interactions) is deemed to occur. This value of critical Stribeck oil film parameter depends on the surface topographical asperity distribution and the chosen statistical parameter. Some researchers have used lower or slightly higher values for the transition boundary between mixed and full fluid film regimes of lubrication. In particular, Guanteng and Spikes [116] used thin film interferometry and showed that full film lubrication is only realised when λ>2. They noted that there is no clear-cut demarcation boundary between mixed and boundary regimes of lubrication, based on the Stribeck's oil film parameter. As already noted above, $\lambda_{cr} > 3$ is assumed for fluid film lubrication in the current analysis.

According to [114,117], the roughness parameter ($\xi\beta\sigma$) is reasonably constant with a value in the range of 0.03 to 0.05 for steel surfaces. The ratio σ/β is a representation of the average asperity slope [110] and is in the range 10^{-4} to 10^{-2} according to Teodorescu et al [115]. In the current study it is assumed that: $\sigma_1 = \sigma_2$, and the Tabor parameters: $\xi\beta\sigma$= 0.05 and σ/β=0.001. In the case of tilting partial journal bearing, the same values were assumed for the aluminium journal surface in chapter 6. Since a thin smooth hard layer of bismuth is applied as the outer layer of the shell overlay, the boundary friction is assumed to largely depend on the rougher surface of the steel crank pin.

3.6. Friction force

The total friction force in mixed regime of lubrication is obtained as:

$$f_t = f_{vis} + f_b \tag{3.51}$$

where, the viscous friction, f_{vis}, is obtained by integrating the generated shear stress over the lubricant-surface interface as:

$$f_{vis} = \iint \tau dA \tag{3.52}$$

at any instant of time, viscous shear of a film of lubricant, *h*, is obtained as [40]

$$\vec{\tau} = \left| \pm \frac{h}{2} \nabla p - \Delta \vec{V} \frac{\eta}{h} \right| \tag{3.53}$$

The boundary component of friction takes into account the direct dry asperity contact as well as the non-Newtonian shear of pockets of lubricant entrapped between the asperity tips, as (Teodorescu et al [115]):

$$f_b = \tau_0 A_a + \varsigma W_a \tag{3.54}$$

where, the parameter ς is the pressure coefficient for boundary shear strength of asperities on the softer counterface. In the case of the big-end bearing this is the steel surface of the journal. A value of ς=0.17 is obtained using an atomic force microscope [115]. For the case of the aluminium journal the same value was used in Chapter 6. The procedure followed is the same as that described by Buenviaje et al [118] and Styles et al [119]. In addition, limiting Eyring shear stress [120] for the engine oil is τ_0=2MPa.

The underlying hypothesis in the use of Eq. (3.54) is that the asperities are wetted by adsorption of an ultra-thin film of boundary active molecules within the lubricant. Briscoe and Evans [121] assume that a thin Langmuir-Blodgett [122] layer of adsorbed boundary active lubricant species are formed at the tip of asperities and entrapped in their inter-spatial valleys. This layer is subject to non-Newtonian Eyring shear [120]. An alternative hypothesis would be that the opposing asperities form adhesive junctures which are submerged in the menisci formed between them. Therefore, boundary friction may be considered as the effort required to break such meniscus bridges (Bowden and Tabor [123]) in addition to overcoming the adhesion of cold welded asperity junctures themselves. Such an approach is reported by Teodorescu et al [115]. A shortcoming of the approach reported in [122] is the need to specify the proportion of contact in dry contact of asperities. On the other hand the approach in [115] makes use of asperity contact area A_a, based on the assumption of asperity distribution, which is considered to follow a Gaussian distribution as in [114].

The cumulative area of asperity tips, A_a, is found as (Greenwood and Tripp [114]):

$$A_a = \pi^2 (\zeta \kappa \sigma)^2 A F_2(\lambda) \tag{3.55}$$

where $F_2(\lambda)$ is a function representative of the Gaussian distribution of asperities in terms of λ as:

$$F_2(\lambda) = \begin{cases} -0.0018\lambda^5 + 0.0281\lambda^4 - 0.1728\lambda^3 + 0.5258\lambda^2 - 0.8043\lambda + 0.5003; & \text{for } \lambda \le \lambda_{cr} \\ 0; & \text{for } \lambda > \lambda_{cr} \end{cases} \quad (3.56)$$

The total frictional power loss, due to both viscous and boundary contributions to the overall friction, is calculated as follows: $P_f = P_{fb} + P_{fv}$.

3.7. Dynamic Mesh

A dynamic mesh model is used in the current analysis to model flows where the extent of the domain is changing with time due to motion of the solid boundary, such as the compression ring or the journal. The generic transport equation applies to all applicable model equations, such as momentum, energy, phases, etc. The motion of the moving boundary is in the direction of film depth (squeezing velocity) which is determined, based on the solution at the current time for each crank angle (for example in the piston ring case, the minimum film thickness is calculated from the force balance on the ring). The update of the volume mesh is handled automatically by ANSYS FLUENT at each time step based on the new positions of the moving wall. To use the dynamic mesh model, one needs to provide a starting volume mesh and the description of the motion of any moving zone in the model. ANSYS FLUENT allows the description of the motion using either boundary profiles or any user-defined functions (UDFs). ANSYS FLUENT expects the description of the motion to be specified on either face or cell zones.

3.7.1. Dynamic mesh theory

With respect to dynamic meshes, the integral form of the conservation equation for a general scalar ϕ, on an arbitrary control volume, $\overline{V}$, whose boundary is moving can be written as:

$$\frac{d}{dt}\int_{\overline{V}} \rho\phi\, d\overline{V} + \int_{\partial\overline{V}} \rho\phi(\vec{u}-\vec{u}_m)\, d\vec{A} = \int_{\partial\overline{V}} \Gamma\nabla\phi\, d\vec{A} + \int_{\overline{V}} S_\phi\, d\overline{V} \tag{3.57}$$

where ρ is the fluid density, $\vec{u}$ is the flow velocity vector, $\vec{u}_m$ is the mesh velocity of the moving mesh, Γ is the diffusion coefficient, S_ϕ is the source term of ϕ and, $\partial\overline{V}$ is used to represent the boundary of the control volume $\overline{V}$.

By using a first-order backward difference formula, the time derivative term in Eq. (3.57) can be written as:

$$\frac{d}{dt}\int_{\overline{V}} \rho\phi\, d\overline{V} = \frac{(\rho\phi\overline{V})^{n+1} - (\rho\phi\overline{V})^{n}}{\Delta t} \tag{3.58}$$

where n and $n+1$ denote a given quantity at the current and next time step, respectively. Thus, for example, the $(n+1)^{\text{th}}$ time level volume, $\overline{V}^{n+1}$, is computed from:

$$\overline{V}^{n+1} = \overline{V}^{n} + \frac{d\overline{V}}{dt}\Delta t \tag{3.59}$$

where $\frac{d\overline{V}}{dt}$ is the volume time derivative of the control volume. In order to satisfy the mesh conservation law, the volume time derivative of the control volume is computed from:

$$\frac{d\overline{V}}{dt} = \int_{\partial\overline{V}} \vec{u}_m\, d\vec{A} = \sum_{i}^{n_f} \vec{u}_{m.i}\,.\,\vec{A}_i \tag{3.40}$$

where n_f is the number of faces on the control volume and $\vec{A}_i$ is the i face area vector. The $\vec{u}_{m.i}.\vec{A}_i$ on each control volume face is calculated from:

$$\vec{u}_{m.i}.\vec{A}_i = \frac{\delta\vec{V}_i}{\Delta t} \tag{3.41}$$

where $\delta\vec{V}_i$ is the volume swept out by the control volume face i over the time step Δt.

The methodology highlighted above is generic and is applied for compression ring-cylinder liner contact as well as the journal bearing in Chapters 4, 5 and 6. In all cases the boundary conditions are described there as these are quite different for these conjunctions.

Chapter 4: Piston Compression Ring Conjunction

4.1. Introduction

The primary function of the piston compression ring is to seal the combustion chamber. This prevents the escape of high-pressure gases from the combustion chamber and conversely any lubricant leakage into the chamber. However, effective sealing function of the compression ring can result in increased friction and thus parasitic losses [110].The piston assembly accounts for approximately 35-45% of engine frictional losses [1, 124]. Therefore, in order to improve engine performance as well as reducing emission levels, it is important to have a deeper understanding of frictional behaviour of piston-cylinder system as a prerequisite. The current work addresses these issues with regard to the piston compression ring.

4.2. Problem description of piston ring-liner

Figure 4.1 is a schematic representation of ring-liner conjunction along the ring axial face-width. The ring profile $h_s(x)$ is assumed to be parabolic with a maximum crown height of c and a face-width of b:

$$h_s(x) = \frac{cx^2}{(b/2)^2} \tag{4.1}$$

The current analysis assumes good conformance of the ring to the liner surface in the circumferential direction of the bore. This simplifies the problem to a one dimensional contact, which is valid for ring-bore contact for bore diameter-to-ring face-width ratio: $2\pi r_0 / b \geq 30$ as shown by Haddad and Tjan [125], which is applicable to the engine studied here. The engine studied here is a high performance V12 4-stroke naturally aspirated engine (see table 4.1).

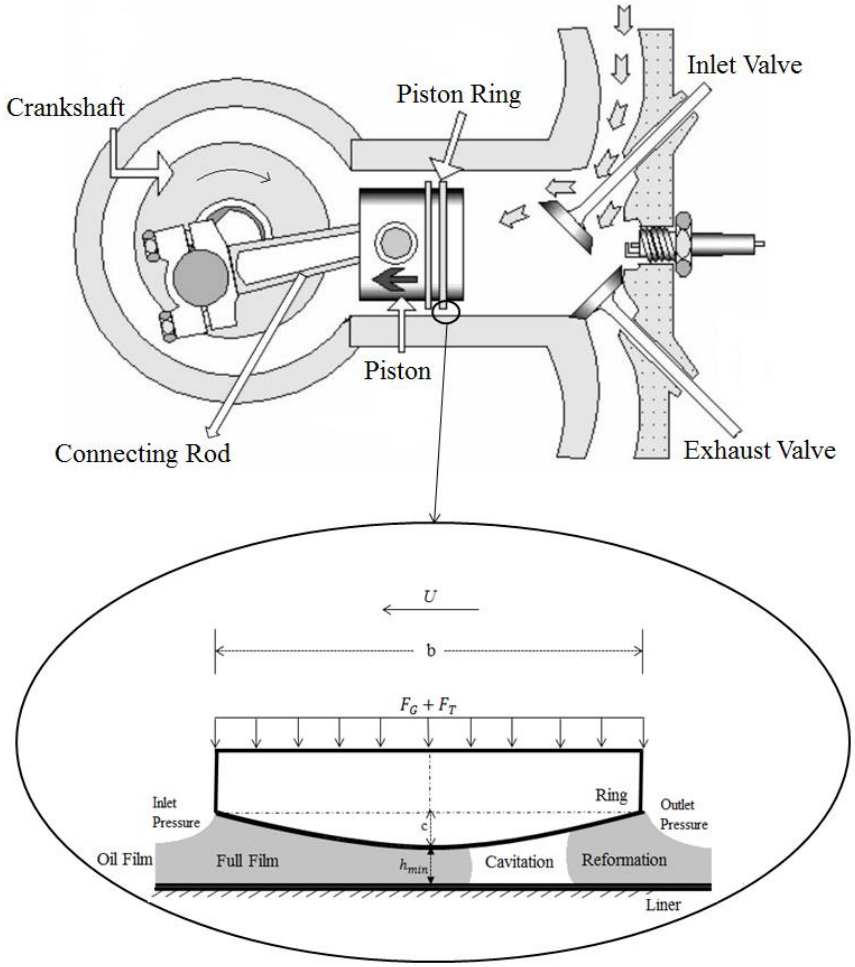

Figure 4.1: 2D Diagram of piston ring-liner conjunction

Table 4.1: Engine data

Parameters	Values	Units
Crank-pin radius, r	39.75	mm
Connecting rod length, l	138.1	mm
Bore nominal radius, r_0	44.52	mm
Ring crown height, c	10	μm
Ring axial face-width, b	1.15	mm
Ring radial width, d	3.5	mm
Ring free end gap, g	10.5	mm

It is assumed that the ring does not undergo any relative motion with respect to the piston sliding at the velocity *U*. In practice, the ring may be subject to axial motion within its retaining groove; a motion termed as ring flutter. Thus, according to Rahnejat [126]:

$$U(\varphi) = -r\omega \sin\varphi \left\{ 1 + \cos\varphi \left[\left(\frac{l}{r} \right)^2 - \sin^2 \varphi \right]^{-\frac{1}{2}} \right\} \tag{4.2}$$

where φ is the crank angle, l is the connecting rod length, r the crank pin radius and ω is the engine rotational speed. Figure 4.2 shows the piston sliding speed variation for the engine speeds of 1500 and 6000 rpm respectively.

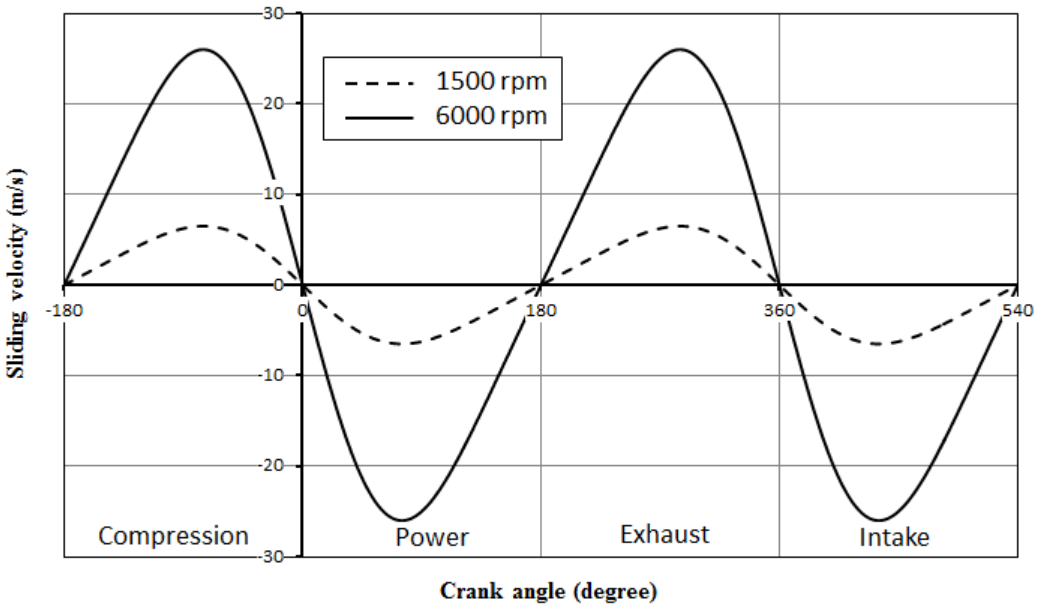

Figure 4.2: piston sliding speed for engine speeds of 1500 and 6000 rpm

Forces acting on the ring are considered as radial in-plane forces. In its radial plane, the ring is subjected to two outward forces; ring elastic tension force F_T and the gas force F_G, both acting on the inner rim of the ring. These forces strive to conform the

ring onto the bore surface. Thus, the total outward force (towards the liner interface), acting on the ring is: $F = F_T + F_G$. The ring tension force, F_T, is obtained as [127]:

$$F_T = p_e\, b\, r_0 \qquad (\text{where } p_e = \frac{gEI}{3\pi b r_0^4}) \tag{4.3}$$

where, p_e is the elastic pressure, r_0 is the bore nominal radius and g is the ring end gap in its free (unfitted) state. The gas force acting on the back of the ring varies according to the chamber pressure in an engine cycle, thus:

$$F_G(\varphi) = 2\pi b r_0\, p_g(\varphi) \tag{4.4}$$

A gas blow-by analysis is required to obtain the exact value of gas pressure acting behind the ring. In the current analysis it is assumed that the gas pressure behind the ring is equal to the in-cylinder gas pressure.

These outward forces (ring elastic tension and the gas force) are opposed by the contact force generated as the result of combined actions of generated conjunctional hydrodynamic pressures and the load share carried by any direct contact of surfaces themselves. The latter is often the load shared by a small portion of asperities on the opposing surfaces. Thus, the instantaneous contact load is determined as $W(\varphi) = W_a(\varphi) + W_h(\varphi)$, where the load carried by any film of lubricant is the integrated pressure distribution as:

$$W_h(\varphi) = 2\pi\, r_0 \int_{-b/2}^{b/2} p_h(\varphi) dx dy \tag{4.5}$$

As shown in Figure 4.1, in general, the contact region may be considered as comprising of three distinct regions: (i) full film (a coherent lubricant film region), (ii) film rupture and cavitation, and (iii) lubricant film reformation. The Elrod cavitation model is the usual basis for the tribological analysis, taking into account these various conjunctional regions. To describe the physics of fluid flow in the cavitated region, in which at least these various states of lubricant film co-exist. A suitable two-phase flow model needs to be employed alongside the use of the Navier-Stokes equations. This would be an elegant approach which for moderately and heavily

loaded conditions represents a reasonable compromise between computational speed and predictive accuracy [128]. However, it can be fairly complex to implement.

4.3. Boundary conditions

In this model, the operating and vaporization (cavitation) pressures are set to be at atmospheric pressure of 101.3 kPa. Since the occurrence of cavitation is treated through solution of the vapour transport equation, there is no need to impose any particular boundary conditions for prediction of lubricant film rupture or subsequent reformation boundaries similar to those employed by Swift-Stieber or Elrod cavitation models. Furthermore, the lubricant-solid interface is assumed to follow no-slip conditions and the solid boundaries were considered to be impermeable.

For the case of the piston ring, pressure inlet and outlet boundary conditions are used for the leading and trailing edges of the ring/liner contact. Therefore, when the piston undergoes upstroke motion, the inlet pressure is that of the chamber given in Figure 4.3, whilst at the exit the crank-case pressure is assumed, which also is assumed to be at atmospheric pressure. On the other hand, for the down-stroke sense of the piston, the inlet pressure is set to that of the crank-case (atmospheric) pressure, whilst the outlet pressure is that of the combustion chamber. The chamber (combustion) pressure varies with engine stroke, speed and throttle demand. Figure 4.3 shows the in-cylinder pressure for the engine speeds of 1500 and 6000 rpm with 63% applied throttle.

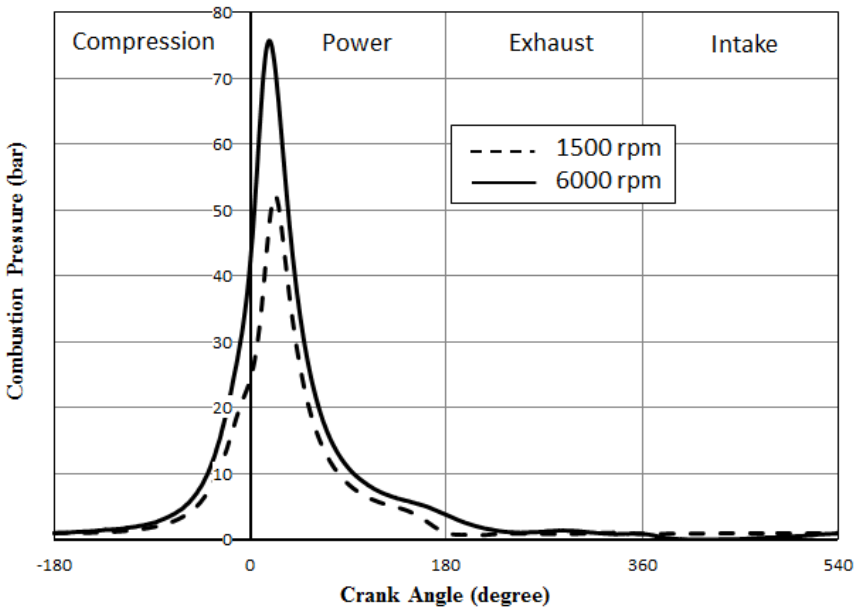

Figure 4.3: Variation of chamber pressure with crank angle for engine speeds of 1500 and 6000 rpm

Thus, the following pressure-based boundary conditions are used along the axial x-direction of the contact (i.e. along the ring face-width, direction of entraining motion).

$$\begin{cases} p_h(-b/2) = p_L \\ p_h(+b/2) = p_U \\ p_h(x_c) = p_c \end{cases} \tag{4.6}$$

No exit boundary condition such as the Swift-Stieber or Prandtl-Hopkins boundary conditions need to be stated with the Navier-Stokes' approach.

4.4. Heat generation and thermal boundary conditions

Lubricant temperature rises due to internal friction. In the Navier-Stokes approach, solving the energy Eq. (3.5) with the appropriate boundary conditions provides a prediction of heat generated in the contact conjunction due to viscous shear of the lubricant film. However, temperatures of contacting surfaces also increase with the

rising contact temperature of the lubricant. Therefore, temperature boundary conditions are themselves a function of internal heat. To obtain the temperature rise of the bounding surfaces, a thermal heat transfer partitioning model needs to be used which takes into account the transferred heat to the contacting surfaces (boundaries) as well as the heat carried away by the lubricant flow though the contact. Morris et al [39] described an analytical model, based on a control volume approach which takes into account the local temperature rise on the contacting surfaces due to conduction from the lubricant and also direct asperity contacts. The method described by Morris et al [39] is adopted here in conjunction with the Navier-Stokes analysis.

In the thermal heat transfer model, at any instant of time, corresponding to a crank angle position, the equality of inlet and outlet flows is upheld. This is an outcome of the instantaneous quasi-static equilibrium at any given crank angle. However, the flow rate is subject to change between subsequent crank angle positions as the variations of the film thickness with time $\left(\frac{\partial h}{\partial t}\right)$ is taken into account. In addition, there is a convection thermal flux at the inlet nib to the conjunction from the solid boundaries to the entrant lubricant supply at a lower temperature of T_{in}. This raises the inlet lubricant temperature to T_0 , from its assumed bulk flow temperature (i.e. inlet heating):

$$T_0 = \frac{T_{s1}U_1 + T_{s2}U_2}{U_1 + U_2} \tag{4.7}$$

where T_{s1} and T_{s2} are the initial surface temperatures of the bore/liner and ring surfaces. Since one of the surfaces is stationary, therefore from Eq. (4.7), $T_0 = T_{s1}$ at the inlet due to the convective thermal flux. The liner temperature is measured from the engine liner surface and, therefore, is known at any given crank angle location (see Figure 4.4).

The lubricant temperature distribution, obtained through solution of energy Eq. (3.5), is based upon an initially assumed temperature for the ring surface. Therefore, the heat partitioning method described by Morris et al [39] can predict the quantity of heat transfer from the ring, contributing to the rise in its temperature when considering the heat removal through convection cooling by lubricant flow (see Figure 4.5).

Figure 4.4: Input conditions as liner temperature

Since the thermal model is a control-volume based approach, the effective temperature of the lubricant, obtained by solving Eq. (3.5) is averaged throughout the contact as:

$$T_e = \frac{\int_{-b/2}^{b/2}\int_0^{h(x)} T(x,z)\,dzdx}{\int_{-b/2}^{b/2}\int_0^{h(x)} dzdx} \tag{4.8}$$

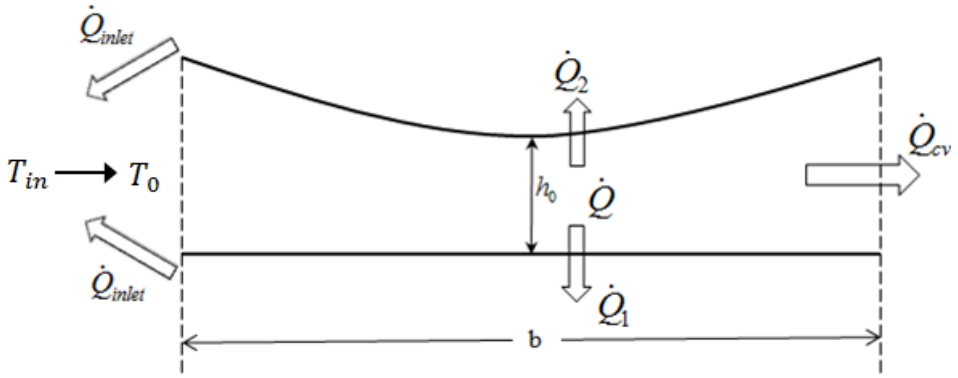

Figure 4.5: Thermal flow within the contact (Morris et al [39])

Table 4.2: Material properties and surface topographical parameters

Parameters	Values	Units
Liner material	Grey cast iron	-
Modulus elasticity of liner material	92.3	GPa
Poisson ratio for liner material	0.211	-
Density for liner material	7200	Kg/m^3
Thermal conductivity for liner material	55	W/m.K
Specific heat capacity for liner material	460	J/Kg.K
Ring material	Steel SAE 9254	-
Modulus elasticity of ring material	203	GPa
Poisson ratio for ring material	0.3	-
Roughness parameter $(\zeta\kappa\sigma)$	0.04	-
Measure of asperity gradient (σ/κ)	0.001	-
Density for ring material	7700	Kg/m^3
Thermal conductivity for ring material	25	W/m.K
Specific heat capacity for ring material	460	J/Kg.K

The rise in the ring surface temperature is obtained from the following relationship (Morris et al [39]):

$$\Delta T_{s2} = \frac{R_f}{R_l + R_v + R_f}(T_e - T_{s2}) \tag{4.9}$$

in which, T_{s2} is the initial ring surface temperature and R_l, R_v and R_f are the thermal resistances associated with conduction through the lubricating film, convective heat transfer through the boundary layer and the rise in the solid surface flash temperature respectively. These parameters are calculated according to the given relationships in Morris et al [38] ($R_l = \frac{h_0}{2kA}$, $R_v = \frac{1}{h_t A}$, $R_v = \frac{S_f}{k_{s2} A}$). The ring and liner mechanical/thermal properties are provided in Table 4.2.

4.5. Grid (Mesh) structures and solution procedures

A 2D simulation model is developed using the CFD package FLUENT 14.5. The pre-processor ANSYS Design Modeller and Meshing is used for generation of computational grid. The geometrical nature of the problem examined here (the film thickness is very small compared with the bore radius) imposes the use of only quadrilateral computational cells. After conducting a grid sensitivity analysis on the accuracy of predictions, 40 divisions were employed across the film thickness and 1,500 divisions along the ring face-width, thus a mesh of 60,000 cells are used. Calculation of Reynolds number for the studied conditions showed that the flow is well within the laminar region. The operating pressure and vaporization (cavitation) pressure are set to the atmospheric pressure of 101.3 kPa.

The pressure-based mixture model [105] is chosen for the CFD analysis. The velocity–pressure coupling is treated using the Semi-Implicit Method for Pressure Linked Equations (SIMPLE) algorithm and the second-order upwind scheme is used for the momentum to reduce the discretisation-induced errors in the calculations. For greater accuracy, a value of 10^{-6} is used for convergence of all the parametric residual terms.

An alternative approach is also undertaken, based on solution of Elrod's cavitation model analytically as described by Sawicki and Yu [87]. However, the method is modified to include the variations of viscosity and density/bulk modulus with pressure and temperature, using the equations given in Section 3.4. Once the pressure distribution is obtained either from CFD analysis or the Elrod's method, it is integrated over the contact area to obtain the hydrodynamic reaction (see Eq. (4.5)).

The solution procedure is as follows:

Step 1: At a given crank angle, calculate the total force exerted on the ring due to combustion gas pressure and ring elastic force (Eqs. (4.3) and (4.4)).

Step 2: Assuming an initial value for the minimum film thickness, lubricant film temperature and pressure distribution, and the lubricant bulk rheological properties are calculated (Lubricant properties in atmospheric pressure and 40° C are presented in Table 4.3). In addition, an initial value for the ring surface temperature is assumed.

Step 3: The contact pressure distribution is obtained using two-phase flow CFD analysis described in Sections 3.1 and 3.2, or the Elrod's cavitation model described in Section 3.3.

Step 4: The predicted pressures are used to update the rheological properties and Step 3 is repeated until the pressure in the Elrod's method in two successive iteration steps remains within the stated convergence criterion. It is noted that in the CFD approach the lubricant rheological properties are updated internally for the generated pressure and temperature distributions as the solution proceeds. In addition, using the heat partitioning model described in Section 4.4, the rise in the ring surface temperature is also calculated.

Step 5: The load carried by asperities is calculated using Eq. (3.49).

Step 6: The pressure distribution is used to obtain the hydrodynamic reaction. Since the method of solution is quasi-static, this conjunctional reaction together with the asperity- carried load should support the total applied load exerted by the gas and

ring elastic forces at each crank angle. The quasi-static balance of applied forces on the ring is sought through:

$$Err_{load} = \frac{|F(\varphi) - W(\varphi)|}{F(\varphi)} \leq 1.0 \times 10^{-3} \tag{4.10}$$

If this criterion is not met, then, the minimum film thickness is updated using the following equation:

$$h_m^n = (1 + \delta \mathrm{X}) h_m^o \tag{4.11}$$

where X is an adjusting parameter, $\mathrm{X} = F(\varphi) - W(\varphi) / \max\{ F(\varphi), W(\varphi)\}$. Superscripts n and o denote new and old steps in the iteration process. A damping coefficient $\delta = 0.05$ is used to achieve faster load convergence, whilst maintaining numerical stability. It is noted that the 'dynamic mesh' concept [129] is employed for variations in the minimum film thickness in the CFD analysis. In this method, the corresponding user-defined function (UDF) determines the desired position of the ring using the dynamic mesh technique. To achieve this, a smoothing mesh method is used with a convergence tolerance of 10^{-5}.

With a new value for the minimum film thickness, the Steps 2 to 6 are repeated until the convergence criterion in Step 6 is met.

Step 7: Calculate the corresponding viscous and boundary friction contributions, and hence the total friction, using Eqs. (3.52), (3.54) and (3.51). Then, proceed to the next crank angle, repeating all the above steps.

Table 4.3: Lubricant properties in atmospheric pressure and 40° C

Parameter	Value	Units
Lubricant viscosity, η_0	0.05	kg/m.s
Lubricant density, ρ_0	833	kg/m^3
Lubricant specific heat, C_p	1968	J/kg-K
Lubricant thermal conductivity, k	0.145	w/m-K
α_0	1×10^{-8}	m^2/N
β_0	4×10^{-2}	-

4.6. Results and Discussion

4.6.1. Pressure distribution of the ring face

Initially, it would be interesting to note the comparison between the predictions of CFD approach developed here with those using the Elrod's approach, which is traditionally used for such tribological contacts. Furthermore, an isothermal analysis somewhat simplifies the problem. Figure 4.6 shows the axial pressure distribution at the crank angle of $+21°$, which is in the power stroke at maximum pressure, where combustion occurs (see figures 4.2 and 4.3).

Figures 4.7-4.9 present the results for axial pressure profiles along the ring face-width at crank-angles: $\pm1°$ (in TDC transition from the compression to the power stroke), $\pm21°$ and $\pm90°$ (at piston mid-span positions in the compression and power strokes) under assumed isothermal conditions. The predictions are made by two different methods: (I) Two-phase flow Navier-Stokes equations and (II) the Elrod's modified approach to Reynolds equation. Good agreement is observed in all the

cases. Note that the crank-angle of 0° corresponds to the position of TDC in transition from the compression to the power stroke. The region bounded by the crank-angles $\pm 1^\circ$ corresponds to quite low speeds of entraining motion of the lubricant. Inlet reversals can be noted as the piston sense of motion alters (Figure 4.7a and b). Figure 4.8b corresponds to the detonation point, where the maximum combustion pressure occurs. The differences between the two methods of analysis emerge in Figures 4.8a, and 4.9a and b. These correspond to relatively lightly loaded contact conditions with higher speeds of entraining motion of the lubricant into the conjunction. These differences are as the result of outlet boundary conditions, which are clearly based on the film rupture point, beyond which cavitation region occurs. With the Elrod's approach there are prescribed contact outlet boundary conditions, which are based on the value of film ratio $\xi < 1$. The CFD approach is based on open boundary conditions (i.e. there is no prescriptive outlet boundary condition for the lubricant film rupture location). Since lightly loaded conditions with higher lubricant entraining velocity (in cases of $\varphi = \pm 90^\circ$, mid-span piston position) lead to film rupture and cavitation any prescriptive outlet conditions may be regarded as somewhat artificial. The difference is more significant in terms of friction than pressure distribution (see later).

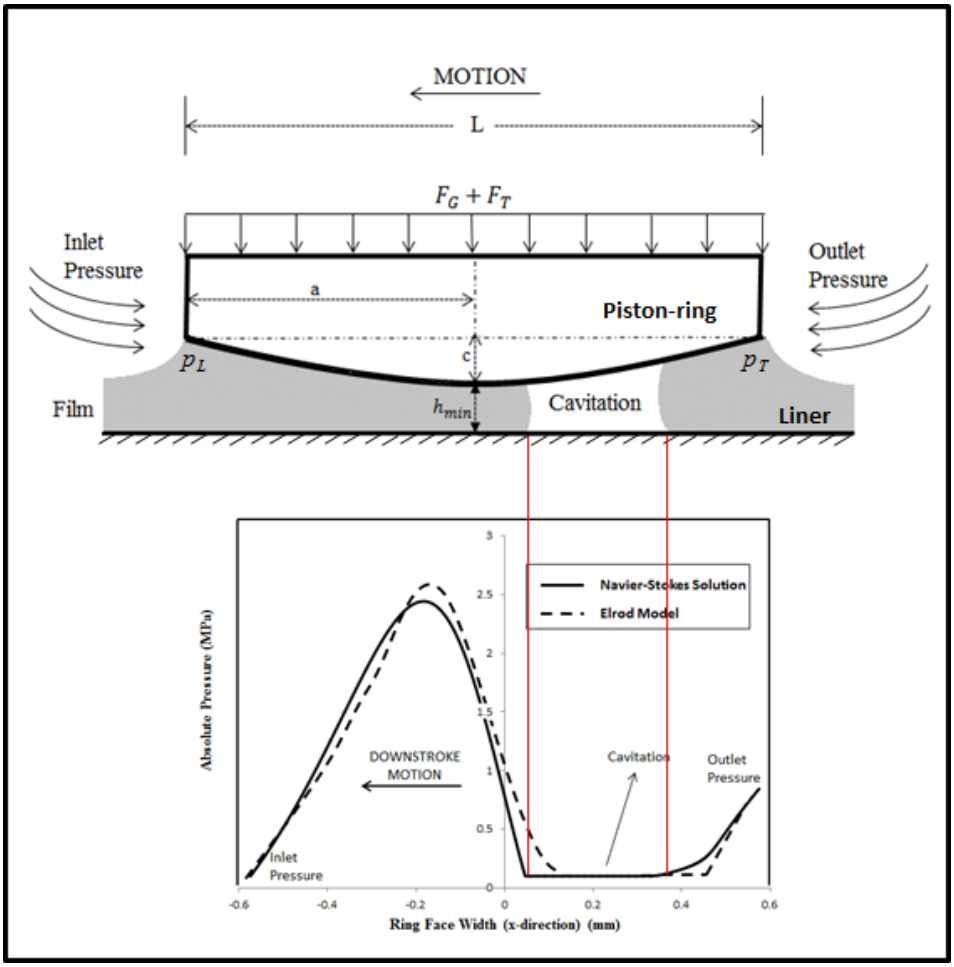

Figure 4.6: Comparison of Navier-Stokes equations to Elrod model for pressure distribution at +21 degree of crank angle

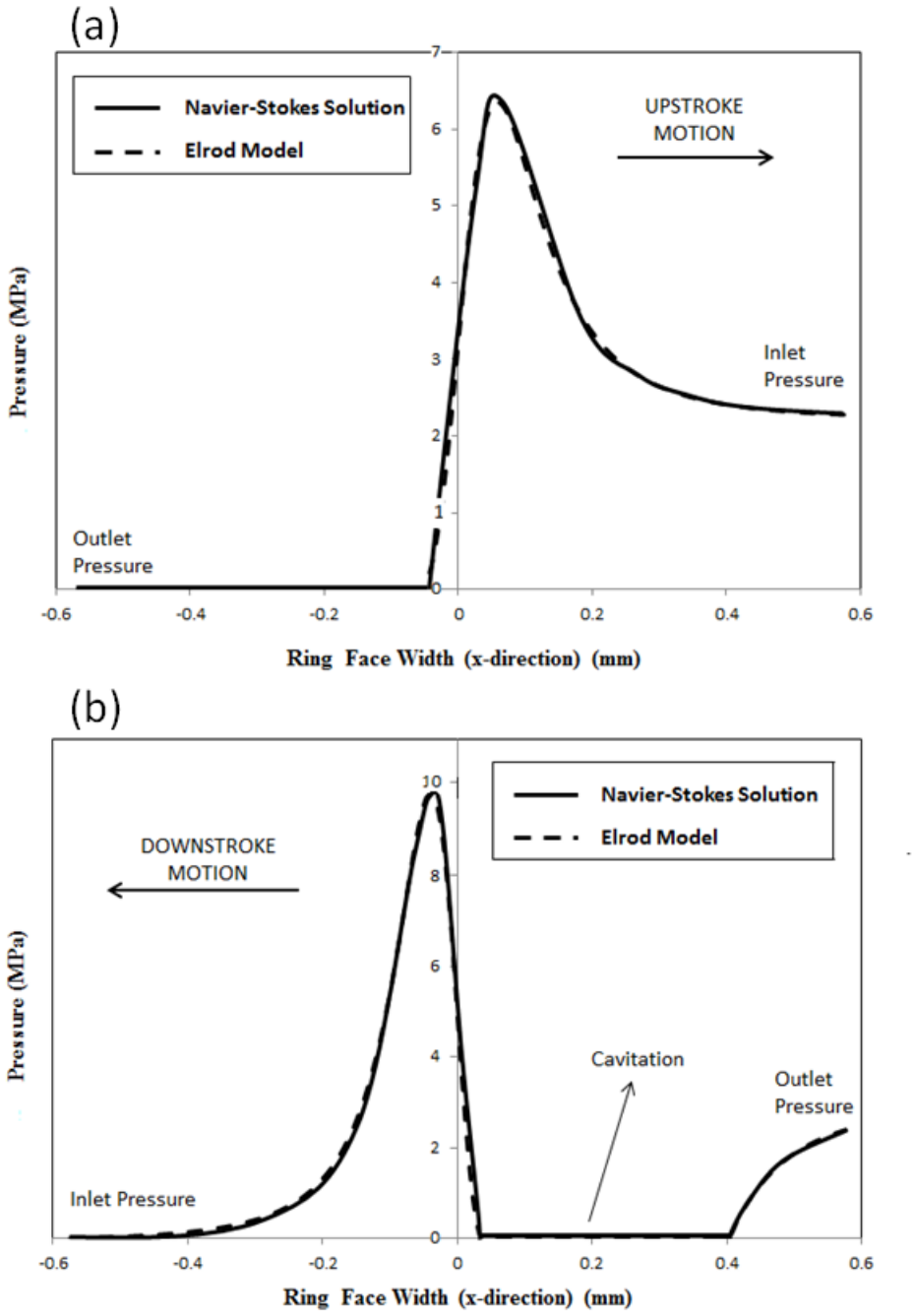

Figure 4.7: Pressure distribution along the ring face-width (x-direction) for (a) $\varphi = -1°$ and (b) $\varphi = +1°$, at engine speed of 1500 rpm

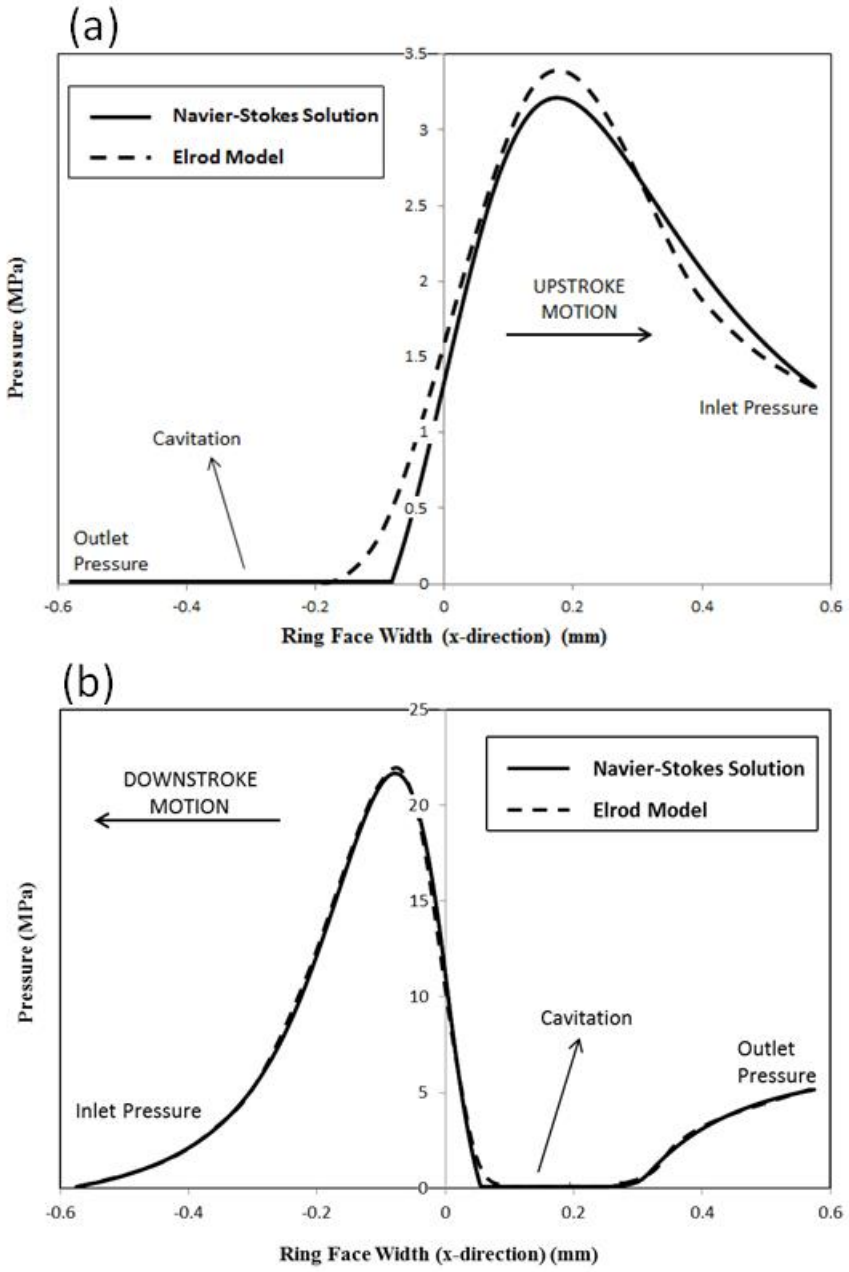

Figure 4.8: Pressure distribution along the ring face-width (x-direction) for (a) $\varphi = -21°$ (*compression stroke prior to TDC*) and (b) $\varphi = +21°$ (*detonation in power stroke*), at engine speed of 1500 rpm

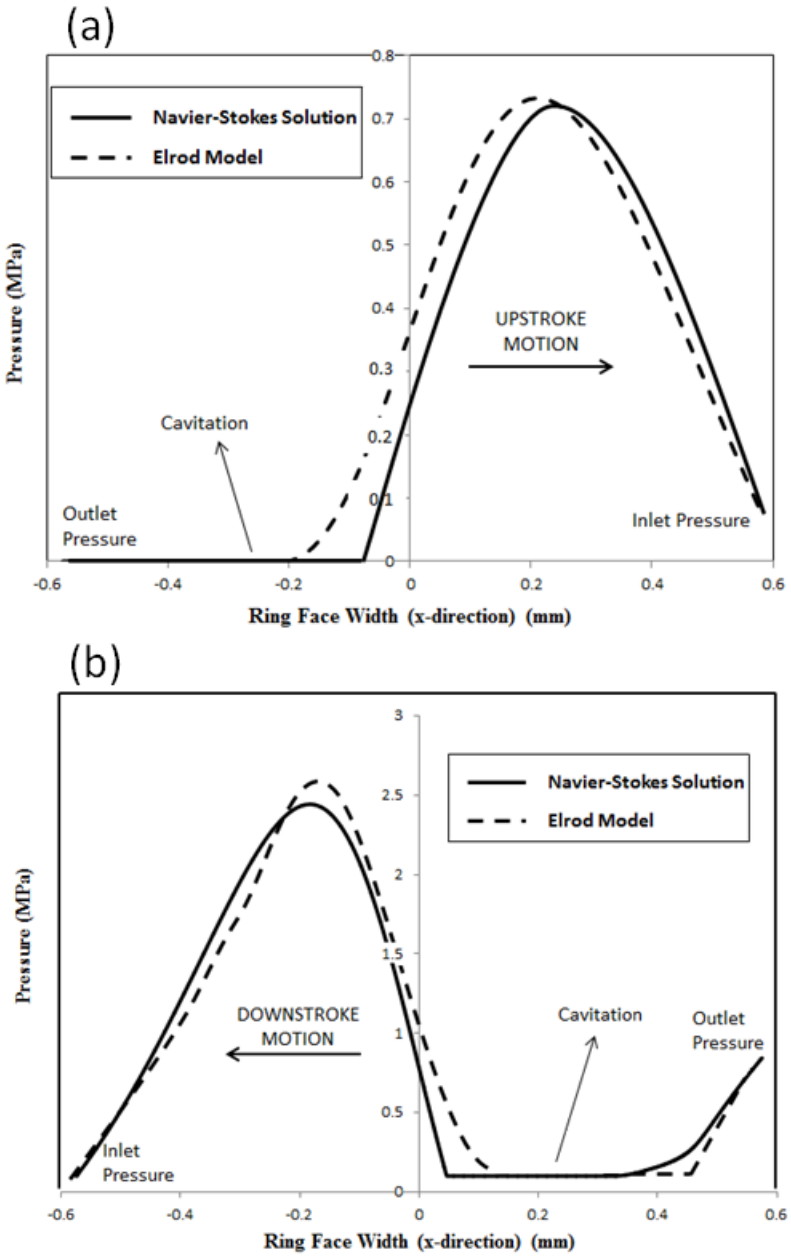

Figure 4.9: Pressure distribution along the ring face-width (x-direction) for (a) $\varphi = -90°$ (*mid-compression stroke*) and (b) $\varphi = +90°$ (*mid power stroke*), at engine speed of 1500 rpm

4.6.2. Lubricant film thickness

The key parameter predicted by the lubrication model is the cyclic variation in the minimum film thickness. There is a direct correlation between film thickness and friction. Therefore, it is particularly interesting to investigate the regions where the film is quite thin. Fig. 4.10 shows the CFD predicted minimum film thickness variations for the parabolic ring at engine speeds of 1500 r/min in comparison to the minimum film thickness predicted by the Elrod model under isothermal conditions. The results are very close together. Both solutions exhibit the expected characteristic shape of curve with small film thicknesses around the dead centre positions, where the entrainment velocity is low, and large film thicknesses at the mid-stroke positions, where the entrainment velocity is relatively high. Film thicknesses on the power strokes, are generally thinner owing to the higher gas loading on the ring. The figure also includes the CFD predicted minimum film thickness variations for thermal condition at the same engine speed.

With thermal effects taken into account, the film thickness is considerably reduced and the ring-bore conjunction resides in mixed and boundary regimes of lubrication for a significant proportion of the engine cycle. Therefore, the assertion of significant differences between isothermal and thermal analyses by Gosh and Gupta [130] is justified, but not often noted in much of the reported studies.

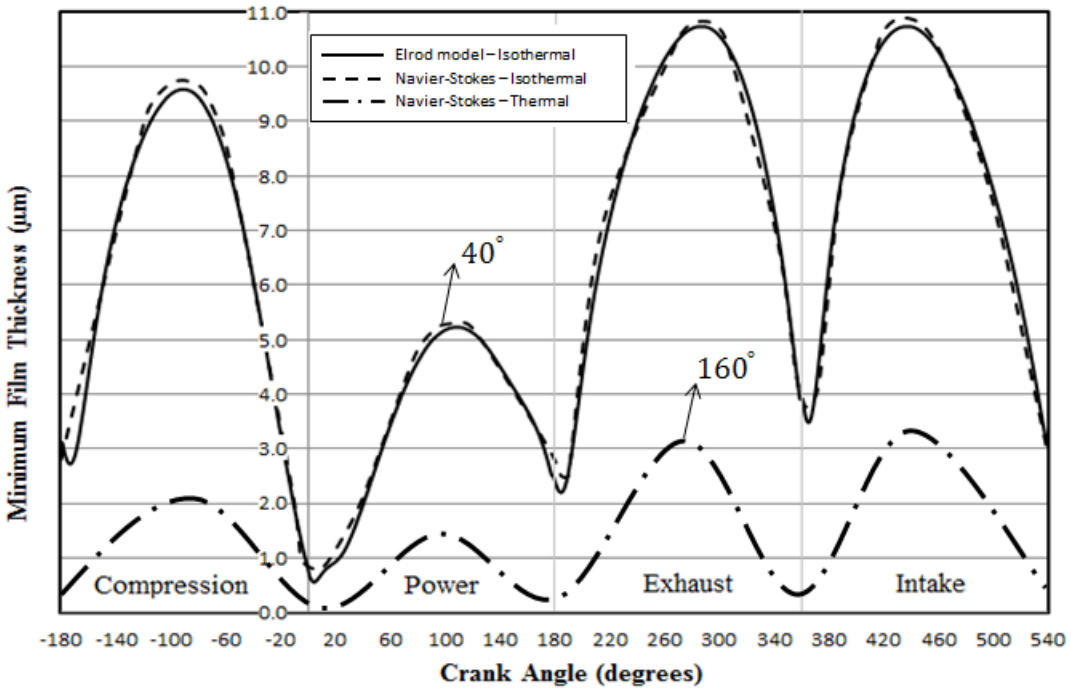

Figure 4.10: Minimum film thickness at engine speeds of 1500 r/min

4.6.3. Fluid properties and flow parameters changes in depth of film

In the other existing models [131], the onset of cavitation is determined without resolving the shape of the cavities. In the middle of the cavitation region, the pressure gradient in the transverse direction is considered be zero (*dp/dz=0*). Thus, no changes would be seen in fluid properties or flow parameters across the film. Unlike other models, in the present CFD model it can be shown that all parameters change into the depth of the lubricant film. The changes of lubricant properties and flow parameters in the *z* direction (film depth) for crank angle of 90° at engine speed of 6000 rpm, in high pressure zone ($x = -0.1mm$) are plotted in Figures. 4.11 and 4.12, respectively.

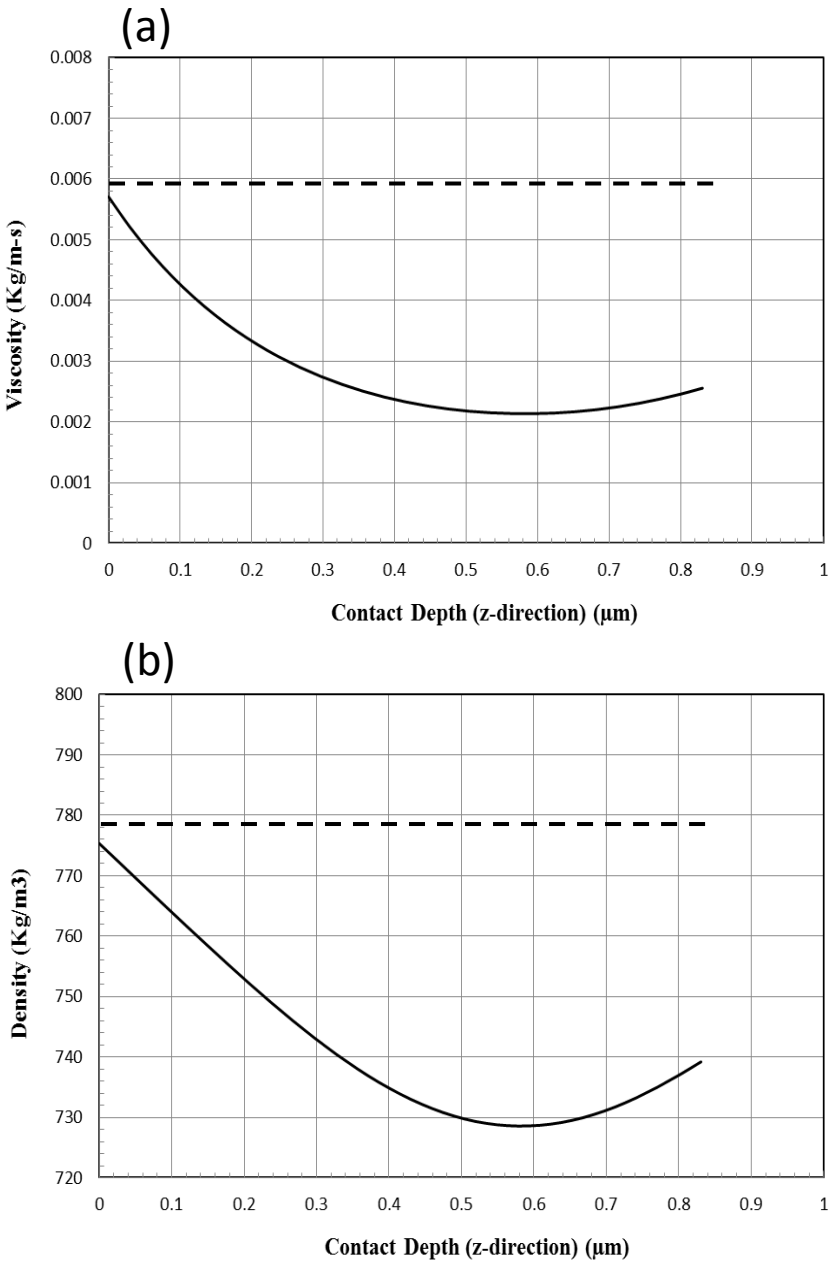

Figure 4.11: The changes of lubricant viscosity (a) and density (b) in z direction (film depth) for crank angle 90 at engine speed 6000 rpm, in high pressure zone ($x = -0.1\,mm$)

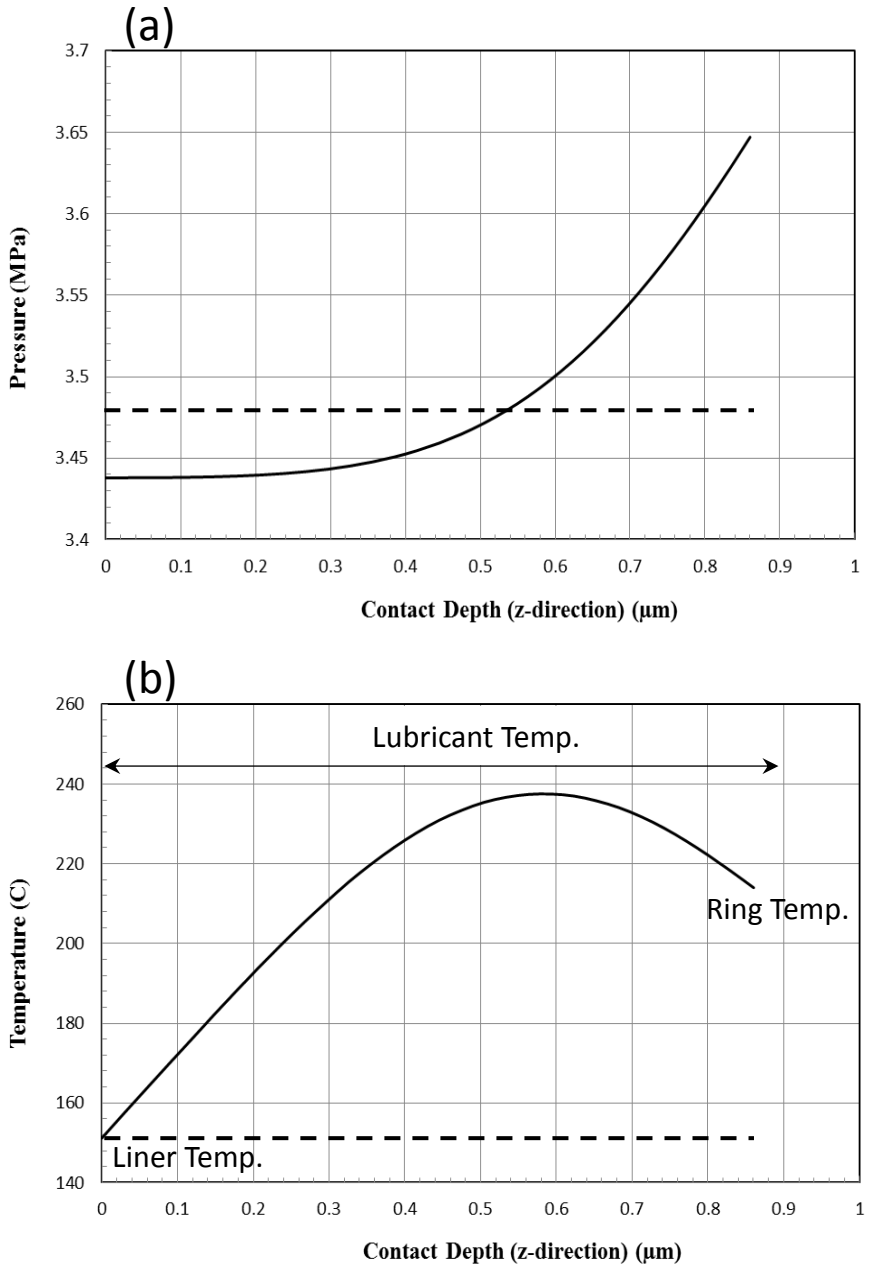

Figure 4.12: The changes of pressure (a) and temperature (b) in z direction (film depth) for crank angle 90 at engine speed 6000 rpm, in high pressure zone ($x = -0.1\,mm$)

Figure 4.13 illustrates changes of vapour volume fraction in the cavitation zone ($x = 0.2\,mm$) and also changes of lubricant viscosity in the high pressure zone ($x = -0.15\,mm$) in the *z* direction (film depth) layer by layer for the same crank angle and engine speed under isothermal conditions.

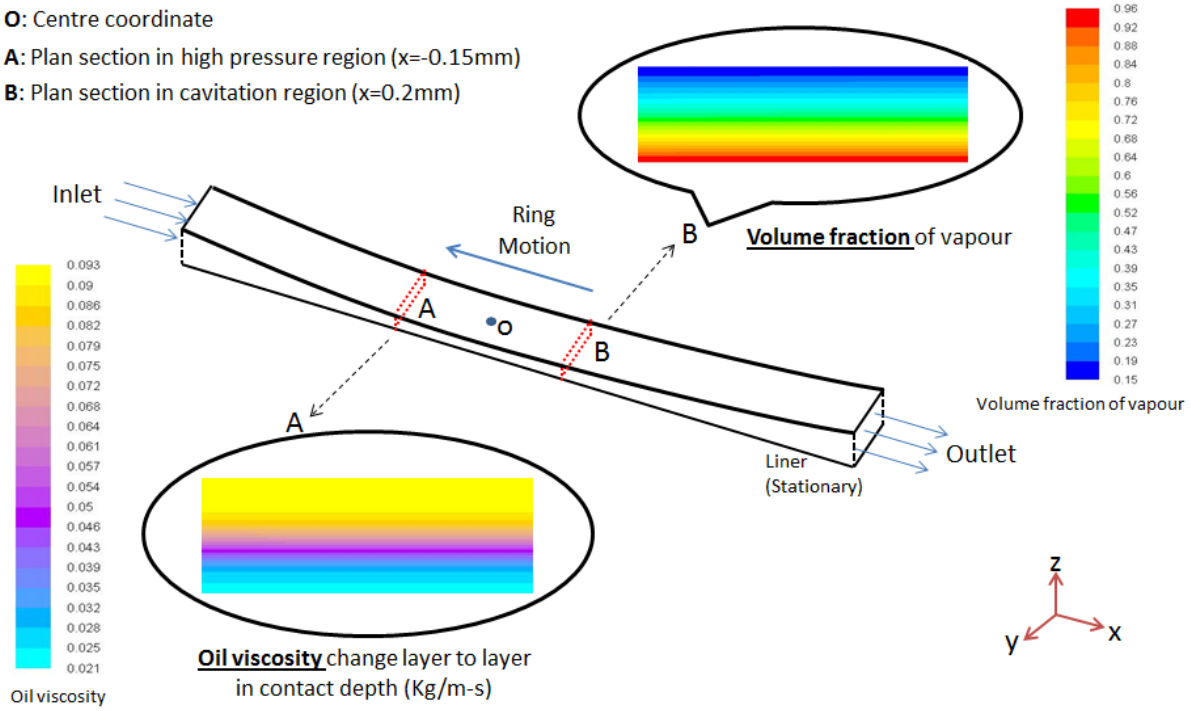

Figure 4.13: The changes of vapour volume fraction in cavitation zone ($x = 0.2\,mm$) and also changes of oil viscosity in high pressure zone ($x = -0.15\,mm$) in z direction (into the film depth)

4.7. Model Validation

4.7.1. Friction

Piston-cylinder friction is a dominant source of parasitic mechanical losses in IC engines, accounting for nearly 9% of the input fuel energy expended. Therefore, one of the overriding industrial objectives is to predict frictional losses from all the conjunctions of the piston-cylinder system. Figure 4.14 shows the CFD predicted friction compared with the experimental measurements by Furuhama and Sasaki [132] for a 2 cylinder rig made from an 8-cylinder Chevrolet engine running at the engine speed of 1200 rpm, under motorised condition. The other predictions in the

figure are those by Mishra et al. [43]. The CFD predictions conform well to the experimental results and show an improvement compared with those predicted by Mishra et al [43] which are isothermal and use Reynolds equation with Swift-Stieber exit boundary condition for the hydrodynamic contribution. The agreement is particularly striking for the power stroke and for the later stages of the compression stroke. There are some differences at mid-span in the power stroke. There seems to be more boundary interactions in the experimental results. This may well be because of bore out-of-roundness, thus some reduced clearance, which would be expected of all cylinder bores in practice. However, such data is not provided in [43]. The current analysis assumes a right circular cylindrical bore with circumferentially conforming ring-bore contact.

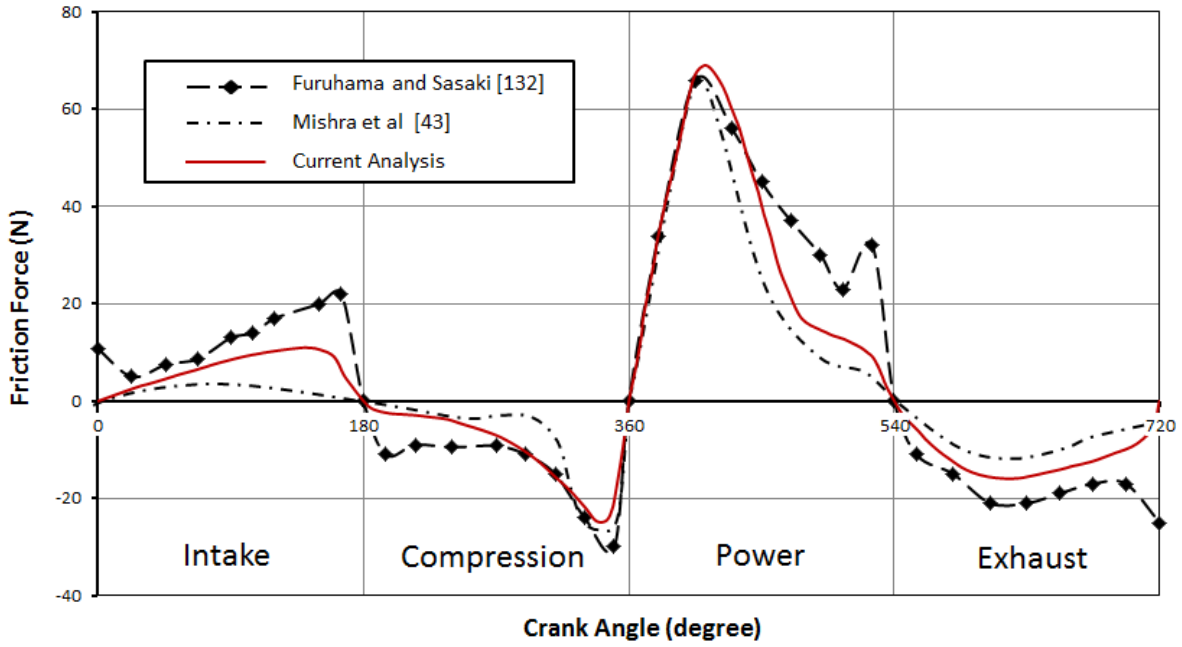

Figure 4.14: Comparison of current work with experimental measurements for friction force

Comparison of friction for isothermal and thermal cases is demonstrated in Figure 4.15. Note that the isothermal analysis would be representative of cold steady state conditions, for example, similar to those at low engine speed emission tests defined

by the NEDC (New European Drive Cycle) [133], where the lubricant viscosity used in the analysis corresponds to the temperature of 40°C. Various regions of predicted engine cycle frictional characteristics are marked on the figure. Under isothermal (cold engine condition) viscous friction is generally higher because of a higher lubricant viscosity. Furthermore, the dominant source of viscous shear is Couette flow, which follows the piston sliding speed (second term in Eq. (3.53)). The exception is the region in transition from compression to the power stroke and extending past the detonation point. Under cold engine condition, it can be seen that the pure proportionality $\tau_v \propto U$ is lost in this region, because there is significant pressure loading of the ring conjunction (combustion curves in Figure 4.3). In this region lubricant action is dominated by Poiseuille shear (the first term in Eq. (3.53)).

The important point to note is that viscous friction, in general, is lower in the thermal case due to reduced lubricant viscosity. However, at the dead centre reversals, because of low entraining velocity the film thickness is significantly reduced (Figure 4.10), which leads to boundary interactions in the case of thermal case. This can be representative of hot steady state portion of the NEDC emission cycle [133]. The sharp rise rate in friction characteristics at dead centre reversals, due to mixed or boundary regime of lubrication, are also marked on Figure 4.15. In particular, the results show that friction at TDC reversal in transition from compression to the power stroke corresponds to a significant proportional of all cyclic frictional losses.

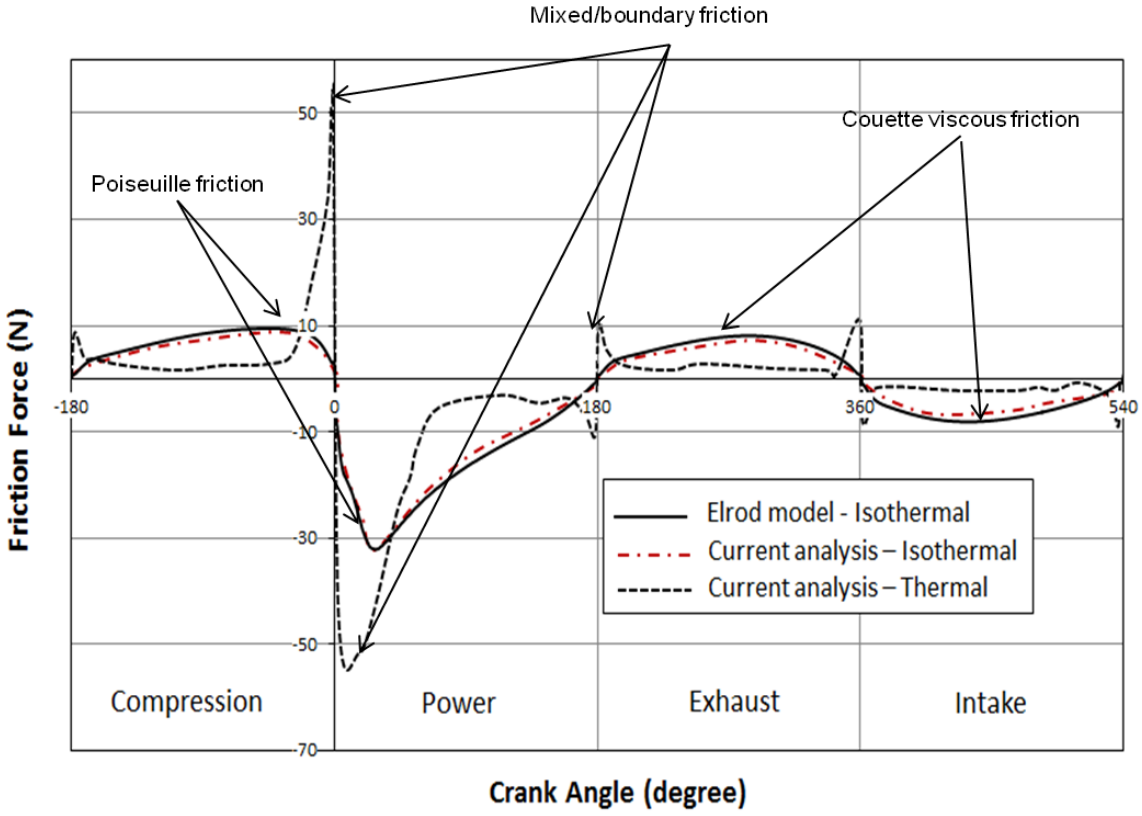

Figure 4.15: Predicted friction under isothermal and thermal conditions with CFD and Elrod-type analyses

4.7.2. Comparison of model predictions with measurements of a floating liner

Gore et al [134] chose a Honda CRF450R motocross motorcycle 4-stroke engine for their experimental measurement of friction in in-situ conditions because of its high power and torque characteristics (41 kW, 50 Nm) with maximum speed of 11000 rpm. The load-speed combination envelopes a wide range of engine technology, and representative of a broad spectrum of tribological conditions. In fact, this engine is representative of the highest performing naturally aspirated single cylinder engine technology (i.e. over 90 kW/Ltr and 110 Nm/Ltr). The engine's OEM barrel was replaced by a wet barrel, containing the floating liner. Gore et al [134] noted that because of the differential operating temperature, there is a need to control the

clearance between the cylinder liner and the housing, and thus minimise the induced stresses in the OEM aluminium structure. The choice of housing material was restricted to materials with a coefficient of thermal expansion between 16 and 18 ppm/K, and yield strength significantly higher than the original donor engine barrel. Thus, austenitic stainless steel grade 304 was used as the floating liner material (Figure 4.16).

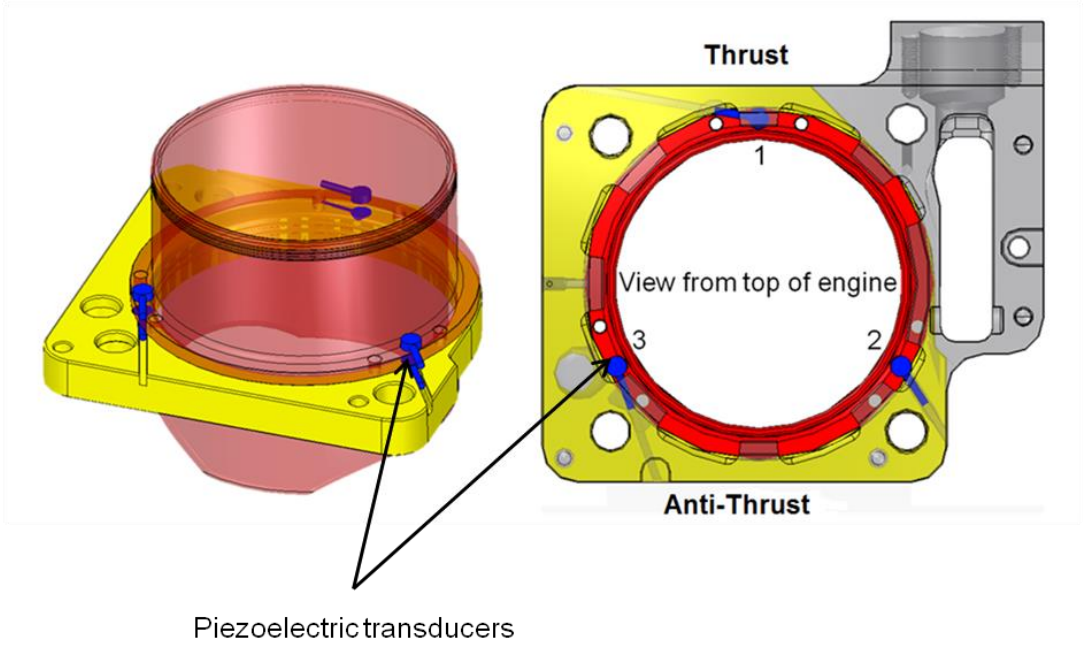

Figure 4.16: The floating liner (Gore et al [134])

The working surface of the liner is coated with a $60\mu m$ thick Ni-SiC layer. As shown, the floating liner is suspended in such a way that any point of contact between the liner and any rigidly mounted components are intervened by a number of piezoelectric load cells [134,135]. The load cells are preloaded whilst *in situ* and at rest, including the weight of the liner itself. The preload value is obtained and recorded prior to any testing. The nominal piston-liner clearance is $50\mu m$. The infinitesimal movement of the liner is such that the load cells remain perpetually in

compression. The total load cell readings equate the inertial force of the liner, dragged by the motion of the piston. The net applied force is due to gas pressure loading on the upper rim of the liner, P_s which is sealed by a labyrinth seal and liner-piston friction. Thus, friction is measured directly as (depending on the sense of liner motion):

$$\pm f = Ma_l - P_s \tag{4.12}$$

The engine was mounted onto an Oswald 250kW transient dynamometer. All standard engine testing parameters (chamber pressure, air fuel ratio, test cell humidity, test cell temperature, input temperature of fuel and coolant, etc) were logged as well as friction to ensure reliability and consistency of all test measurements. The basic setup is shown in Figure 4.17.

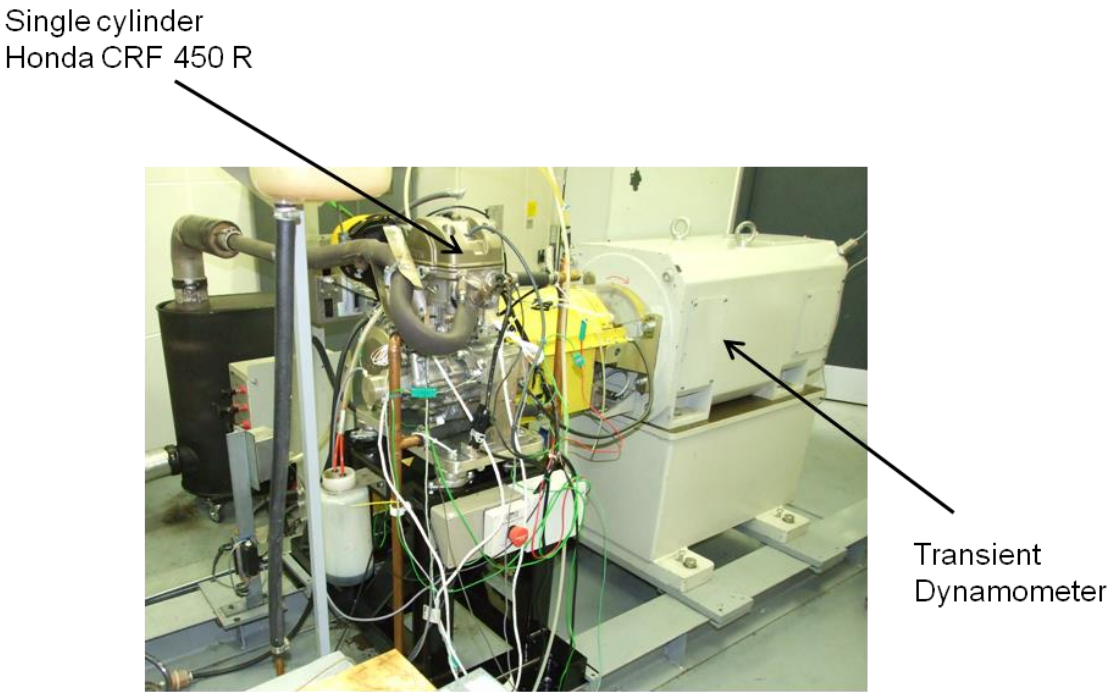

Figure 4.17: The engine test-bed [134]

Figure 4.18(a) shows the measured friction using the floating liner's piezo-electric transducers. The changes of sign in friction represent piston reversals. The gap between the two traces constitutes the frictional contribution of the compression ring.

The results show that the main contribution to friction in the case of this engine set up and running conditions is due to the piston skirt. For the test conditions reported here (Table 4.4), the compression ring friction contribution is approximately 10-15% of the total. Figures 5(b) and (c) show compression ring-liner friction contributions in two regions. One region is in the compression part of the cycle, prior to the TDC reversal at crank angle of 0° and the other is in the early stages of the intake stroke post the same TDC reversal. An average value for each region is calculated from measurements and predictions. These are shown in Figures 4.18(b) and (c).

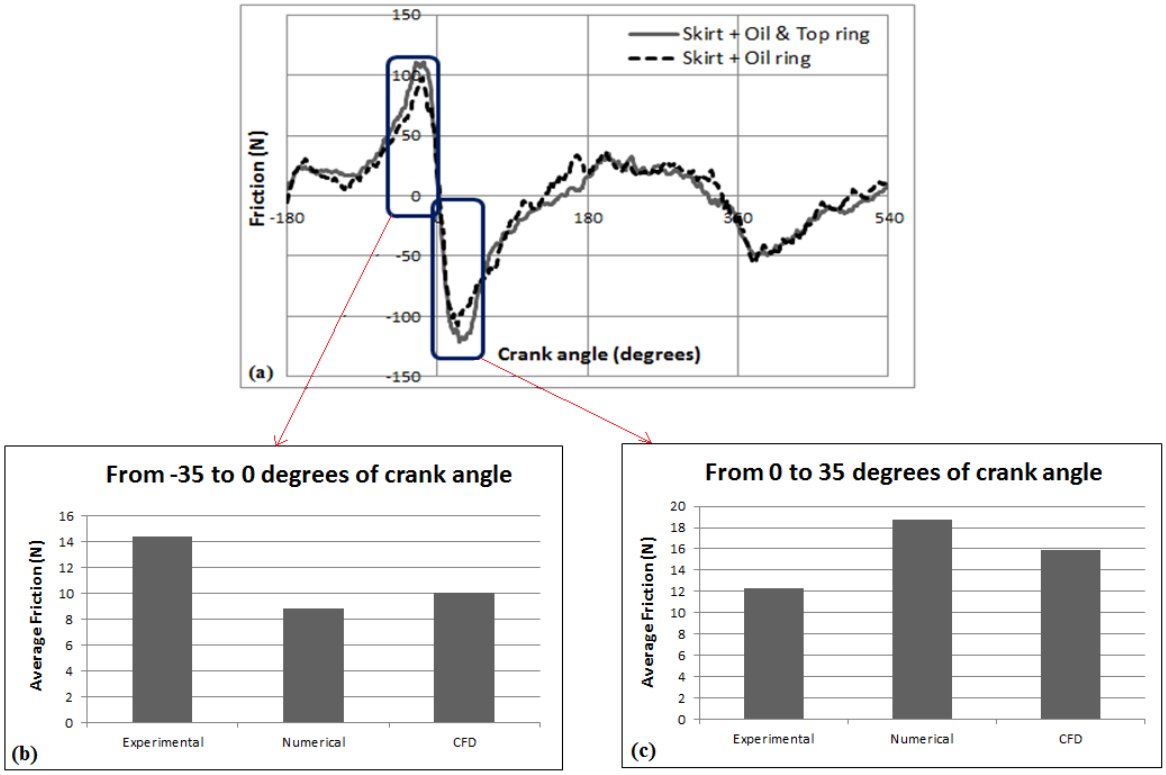

Figure 4.18: Comparison of measured and predicted ring-liner friction

The differences between numerical models (CFD and Elrod) and measurements can be as the result of some assumptions in the models, such as the assumed ring-liner circumferential conformity, a right circular cylindrical bore shape and isothermal conditions. From figure 4.18 a better agreement is found between the CFD results and measurements rather than those using the Elrod cavitation algorithm.

Table 4.4: List of engine specification and analysis data

Parameter	Value	Unit
Engine speed	3000	*rpm*
Connection rod length	107	*mm*
Engine stroke	62.1	*mm*
Liner material	Steel	-
Bore nominal radius	48	*mm*
Top ring	Steel	-
Liner Elasticity Modulus	203	GPa
Liner Poisson ratio	0.3	-
Ring Elasticity Modulus	203	GPa
Ring Poisson ratio	0.3	-
Ring end gap	10.92	*mm*
Ring face width	0.72	*mm*
Pressure coefficient of boundary shear strength	0.22	-
Rq for liner surface	0.515	μm
Rq for Ring surface	0.201	μm
Combined roughness parameter (ηβσ)	0.0771	-
Combined roughness parameter (σ/β)	0.211	-
Operating temperature	25	°C
Oil density	833.8 (@15°C)	kg/m^3
Oil viscosity	50 (@40°C)	mPa.s
Pressure-viscosity coefficient	1×10^{-8}	-
Temperature-viscosity coefficient	0.04	-

This can be as the result of the Elrod method's assumption which considers a fully flooded conjunctional inlet. On the experimental side the presented results are

average of many cycles, where there are small variations (1-2%) in the measured combustion chamber pressure. Also, the position of TDC reversals can alter from cycle to cycle, this being a characteristic of inherently unbalanced single cylinders.

4.8. Inlet and Exit Boundary Flow Conditions

An important consideration is the use of realistic boundary conditions. In most hydrodynamic analyses a fully-flooded (drowned) inlet boundary is assumed, in order to keep within a generic approach. However, it is clear, through observation of wear as well as *in situ* measurements of friction using floating liner methods [135,132] that an insufficient supply of lubricant exists in parts of the piston cycle. In the upstroke motion of the piston, the inlet to the top compression ring conjunction resides within the combustion chamber. There would unlikely be a sufficient supply of lubricant in such instances to assume a fully flooded inlet. In fact, it is shown that mixed or boundary regimes of lubrication are prevalent at instances of contact reversal by many numerical predictions [23,39,46] and experimental measurements of friction [134,132]. Therefore, determination of appropriate inlet boundary conditions, leading to contact starvation is essential for realistic prediction of prevailing tribological conditions. The same is also true of contact outlet boundary conditions, where the falling pressures in a diverging gap result in lubricant film rupture in the presence of retarding friction, which also causes cavitation. The effect of cavitation was studied by Chong et al [46], who used Elrod's approximation [15] to the Jakobsson and Floberg [13] and Olsson [14] (JFO) cavitation boundary conditions. Chong et al [46] showed that cavitation reduces the lubricant availability at the TDC (Top Dead Centre) reversal, thus causing a starved contact in parts of the power stroke in the vicinity of the TDC. With the Elrod algorithm, the continuity of Couette flow is only assured, whilst the usually assumed Swift-Stieber outlet boundary condition does not embody the principle of conservation of mass flow. Therefore, in order to accurately determine the position of film rupture at the exit boundary condition, the principle of

conservation of mass flow would necessitate the solution of Navier-Stokes equations. This was the approach undertaken in this thesis [136] which provides a combined solution of Navier-Stokes and energy equations for the ring-bore contact with an assumed fully flooded inlet. No lubricant outlet boundary conditions were imposed. This approach is also taking into account the vapour transport equation and the Rayleigh-Plesset void fraction. Additionally, only pressure boundary conditions are imposed, instead of those based on lubricant availability such as a fully flooded inlet. This expounded approach, not hitherto reported in the literature, is more realistic and without artificially imposed lubricant flow conditions.

In practice observation of flow at the boundary points has shown some reverse flow, which is dependent upon surface velocities of the contiguous solids as well as thermal conditions. An analytical approach was presented by Tipei [137], based on potential flow, surface velocities and compatibility conditions to replicate the observations for the case of rolling contacts. Recently, analysis of rolling circular point contact by Mohammadpour et al [138] using Tipei's boundary conditions showed very good agreement with the experimental work initially reported by Johns-Rahnejat and Gohar [139]. Therefore, additionally this thesis extends the approach of Tipei [137] to the case of sliding contact of compression ring along the cylinder liner to establish the validity of potential flow analysis at boundary points against the full Navier-Stokes solution.

4.8.1. Analytically determined boundary conditions

Tipei [137] investigated the inlet and outlet boundaries of the domain in hydrodynamic contacts. He noted that in the inlet zone, there are swirl flows, where some reverse flow (counter flow) occurs at the inlet as is also observed in the experimental observations [140]. This means that only a fraction of the lubricant at the inlet meniscus is admitted into the contact domain. The counter flows cease at

the stagnation point, where: $\frac{\partial \vec{V}}{\partial z} = \vec{V} = 0$ (in the normal direction to the conjunction plane). This condition is known as the Prandtl-Hopkins boundary condition and defines the zero-reverse flow boundary. Considering the potential flows in the inlet region, Tipei found the compatibility condition as [137]:

$$cot^2\pi\left[\frac{1}{2}-\frac{1-k}{f(k)}\right]-cot^2\pi\sqrt{\left[\frac{1}{2}-\frac{1-k}{f(k)}\right]^2-\frac{2k}{f(k)}}=cot\pi\left\{\frac{1}{2}-\frac{1-k}{f(k)}-\sqrt{\left[\frac{1}{2}-\frac{1-k}{f(k)}\right]^2-\frac{2k}{f(k)}}\right\}\times$$

$$cot\pi\left\{\frac{1}{2}-\frac{1-k}{f(k)}+\sqrt{\left[\frac{1}{2}-\frac{1-k}{f(k)}\right]^2-\frac{2k}{f(k)}}\right\} \quad (4.13)$$

where:

$$k=\frac{U_1}{U_2} \quad (4.14)$$

and the function $f(k)$ depends on the pressure gradient at the inlet (At the inlet point *A* in figure 4.19. $\frac{dp}{d\theta_i} \propto k$). The values of $f(k)$ for the usually encountered cases of the surface velocity ratio k are listed in Table 4.5. In the case of the piston ring conjunction, $k = 0$ and $f(k) = 4$.

Table 4.5: calculated values for $\boldsymbol{f(k)}$

k	$f(k)$
0	4
0.5	7.8
1	32/3

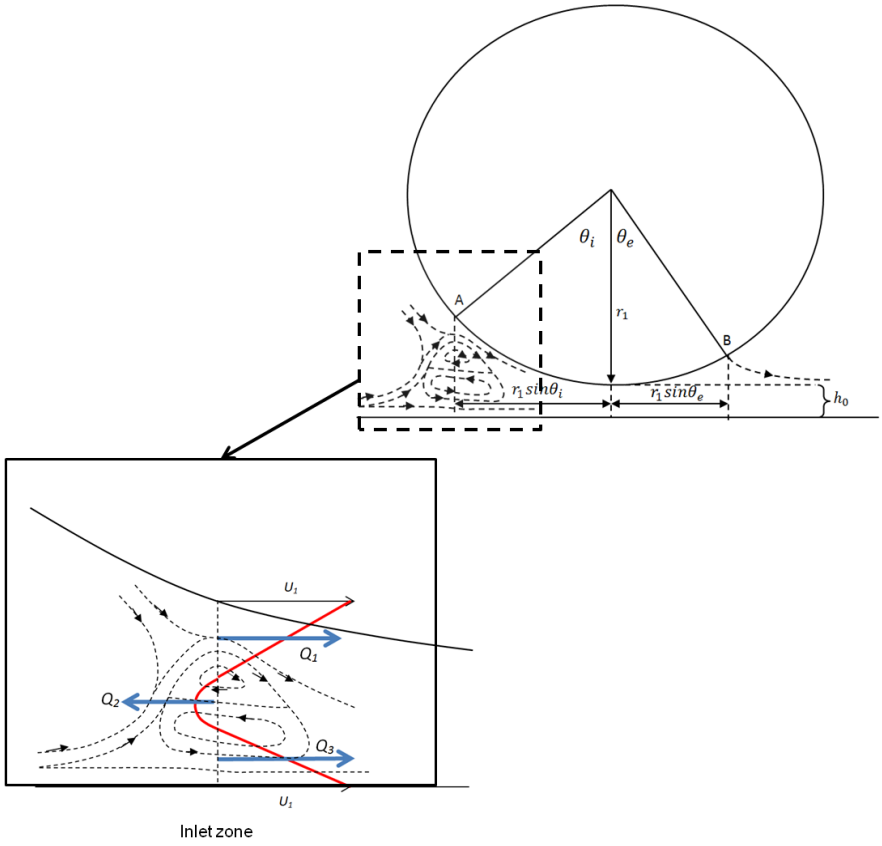

Figure 4.19: Flow through contact carried by the solid surfaces

Tipei [137] assumed a similar approach for the determination of separation boundary at the exit constriction, leading to the determination of the lubricant film rupture point, using the Prandtl-Hopkins conditions:

$$\frac{cosh\vartheta_i}{cosh\vartheta_e} = \frac{1-\frac{1}{3}\left(1+\frac{2\sqrt{k}}{1+k}\right)}{1-\frac{f(k)}{6(1+k)}} \tag{4.15}$$

$$\left[1-\frac{1}{3}\left(1+\frac{2\sqrt{k}}{1+k}\right)\right]tanh\vartheta_e - \left[1+\frac{f(k)}{6(1+k)}\right]tanh\vartheta_i - \left[1-\frac{f(k)}{6(1+k)}\right]cosh\vartheta_i[arcsin(tanh\vartheta_e) - arcsin(tanh\vartheta_i)] = 0 \tag{4.16}$$

ϑ_i and $\vartheta_e$are the ratios of film thickness at the inlet and the exit to the minimum film thickness respectively. Therefore, after calculating the parameters from Eqs. (4.15)

and (4.16) and having the minimum film thickness and the film shape (Eq. (4.1)), the distance of the inlet stagnation and outlet separation points from the centre of the ring can be found. This assumption agrees well with the experimental observations of Birkhoff and Hays [140] and Mohammadpour et al [138].

Alternatively if instead of the Prandtl-Hopkins boundary condition the Swift-Stieber conditions ($\frac{\partial p}{\partial z} = p = 0$) is used, then:

$$\frac{cosh\vartheta_e}{cosh\vartheta_i} = 1 - \frac{f(k)}{6(1+k)} \tag{4.17}$$

and:

$$tanh\vartheta_e - \left[1 + \frac{f(k)}{6(1+k)}\right] tanh\vartheta_i - \left[1 - \frac{f(k)}{6(1+k)}\right] cosh\vartheta_i [arcsin(tanh\vartheta_e) - arcsin(tanh\vartheta_i)] = 0 \tag{4.18}$$

These two boundary conditions give similar values at the inlet, but predict different values for the lubricant film rupture point at the outlet. Later, it is shown that the Prandtl-Hopkins boundary conditions conform closer to the open exit boundary determined through two- phase flow solution of Navier-Stokes equations.

4.8.2. CFD-determined boundary conditions

Initially, a comparison is made between the inlet and outlet boundaries predicted through the current CFD approach and those calculated using the analytical method (described in section 4.8.1) using the approach highlighted originally by Tipei [137]. The potential flow analysis (Eqs. (4.13) and (4.14)), together with the Prandtl-Hopkins boundary conditions yield one set of inlet and outlet conditions. Alternatively, the solution of the same potential flow with Swift-Stieber boundary conditions results in another set of inlet and outlet conditions**.**

The intention for this comparative study is twofold. Firstly, it constitutes a form of validation for the CFD approach as the analytical approach has shown very good agreement for the determination of boundary conditions with the experimental observations of Birkhoff and Hays [140] as well as with the experimental circular point contact conditions [141], both under rolling conditions. Secondly, the applicability of the analytical method for the determination of boundary conditions for sliding contacts can also be ascertained.

Table 4.6 lists three sets of predicted inlet and outlet boundaries, 2 of which are based on the analytical method for Prandtl-Hopkins and Swift-Stieber boundary conditions respectively (using the potential flow analysis) and the third set is that obtained by the current CFD approach. Close agreement between the CFD predictions and the analytical results can be observed. CFD–predicted inlet stagnation boundary agrees very well with both the Swift-Stieber and Prandtl-Hopkins boundary conditions. For the outlet boundary conditions, the CFD results conform much closer to the Swift-Stieber boundary. In fact, most reported analyses of piston ring conjunction routinely employ the Swift-Stieber boundary conditions at the exit constriction [23,39,42,44,46,142,143]. Arcoumanis et al [131] reported numerical analysis of compression ring conjunction with various outlet boundary conditions, including Swift-Stieber, limiting case of the Floberg boundary and the Coyne-Elrod cavitation boundary [144]. They found that the predicted film thickness, using the Swift-Stieber boundary conditions showed closer agreement with their experimentally measured film thickness. Their findings are in line with the current CFD predictions and the analytical potential flow analysis described here.

Table 4.6: Calculated inlet and outlet distances (stagnation point and separation point)

	CFD	Analytical method, Prandtl-Hopkins boundary condition	Analytical method, Swift-Stieber boundary condition
Inlet distance [μm]	267	265	260
Outlet distance [μm]	85	151	76

Figure 4.20 is a typical velocity flow field for the inlet-to-central conjunctional region, obtained through the current analysis. It shows the stagnation point, where the zero-reverse inlet boundary is reached ($\frac{\partial \vec{V}}{\partial z} = \vec{V} = 0$, Prandtl-Hopkins inlet boundary). This point is far from the usually assumed fully flooded inlet, which is often assumed to be at the leading edge of the ring, beyond the swirl flow region. This finding indicates that only a portion of an assumed available flow is admitted into the conjunction-proper beyond the stagnation point. Hence, under the conditions shown, and in fact throughout the engine cycle, only a partially flooded inlet is attained. The reason for this is the recirculating (swirl) flow in the inlet wedge of the conjunction as shown clearly in the zoomed-in inset to the figure.

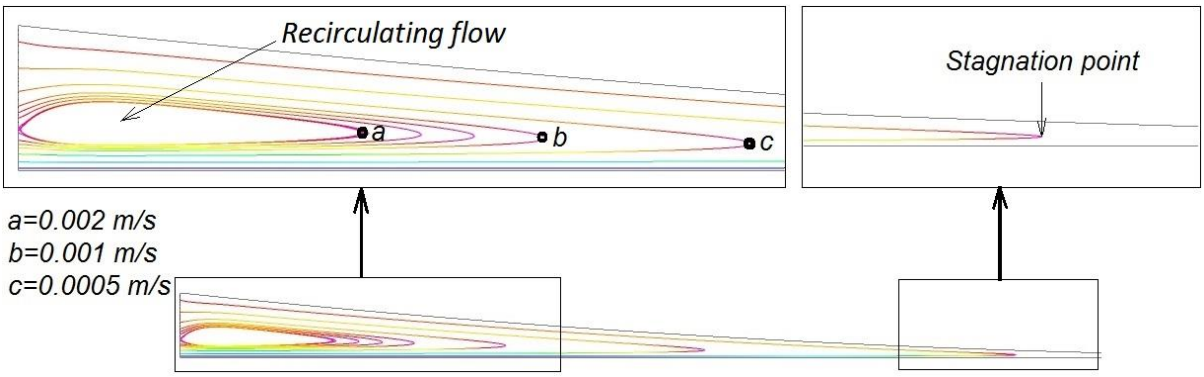

Figure 4.20: Typical velocity flow field in the inlet region of the sliding conjunction

The recirculating flow is a function of the velocity ratio of the contiguous surfaces which alters according to the piston sliding velocity. This is a function of the crank angle position. It also depends on the wedge angle as a function of the ring profile, which in turn determines the minimum film thickness. Therefore, load carrying capacity of the conjunction is affected by the ring profile and the inlet boundary (the inlet wedge velocity flow field). As the hydrodynamic load carrying capacity is critical in guarding against asperity interactions, in theory, one can optimise the ring contacting face-width to enhance the load carrying capacity.

Figure 4.21 shows the generated conjunctional pressure distributions for the actual ring face-width of b=1.15 mm (Table 4.1) and its variously assumed multiples up to 3b in the down-stroke sense of the piston. The leading edge of the ring is at the assumed atmospheric pressure (gauge pressure, p=0 in the figure). A minimum film thickness of 1μm is assumed (as a constraint) in this analysis. This enables the study of load carrying capacity of the contact as influenced by the changes arising at the inlet with differing ring face-widths.

As expected, the results show increasing load carrying capacity because of an increased conjunctional area. However, the increase is not proportional to the contact face-width as would be the case with an assumed fully flooded inlet, where:

$$W_h = \frac{2.9 b \eta \Delta U}{h_0} \tag{4.19}$$

which is based on the Swift-Stieber exit boundary condition, h_0 being the minimum film thickness (kept constant for all the cases in figure 4.21). Hence, at the same ring sliding speed, ΔU, $W_h \propto b$, Thus, doubling the ring face-width would double the load carrying capacity. With realistic boundary conditions the position of the stagnation point alters and thus the area of conjunction-proper is not a direct function of ring face-width only. Therefore, the load carrying capacity and the pressure distribution are dependent on the inlet flow field.

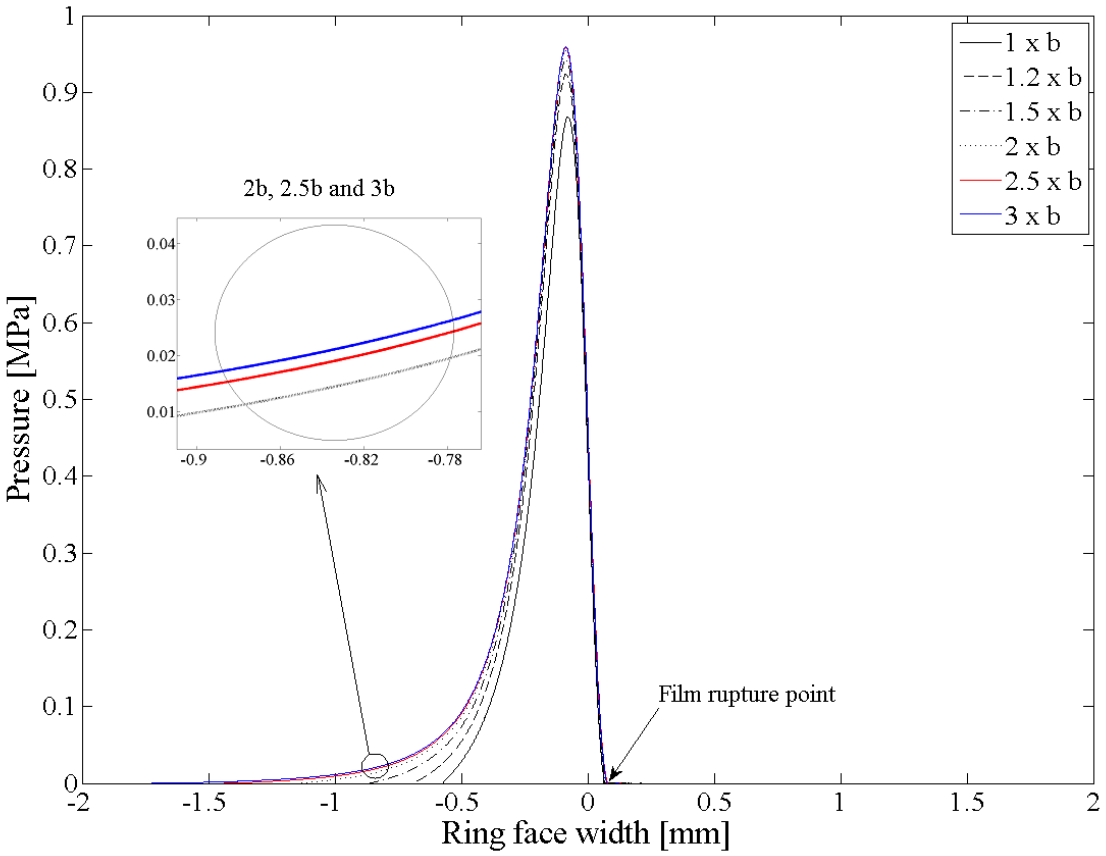

Figure 4.21: The streamlines of the flow in the ring specified 2 times wider assumed ring

The results in figure 4.21 show that the inlet trail to the position $p = 0$ on the left-hand side of the pressure traces is extended with an increasing face-width, but in none of the cases reaches anywhere near the leading edge of the ring (i.e. all contacts are only partially flooded). Furthermore, progressively increasing the ring face-width only marginally lengthens the conjunctional inlet trail as shown in the inset to the figure. Thus, a progressively reducing gain in the load carrying capacity is accrued. Figure 4.22 clearly shows this trend. The underlying reason is best observed by the inward flow into the contact conjunction. This is shown in Table 4.7. The physical inlet is assumed at the leading edge of the ring face-width. This is analogous to assuming a fully flooded inlet. Clearly, if a constant minimum film

thickness is assumed at the same sliding velocity, but with an increased contact area, then a larger flow rate (a larger volume of lubricant) is required to maintain fully flooded conditions. The difference in the flow rate at the physical inlet and that at the central contact through the minimum film thickness accounts for the backward (reverse and swirl) flow in the inlet zone. It can be seen that this difference progressively increases with an increasing ring face-width. Therefore, only a portion of the volume of the lubricant made available at the nib of the contact is actually admitted to the contact conjunction, and in none of the cases a fully flooded condition is noted. This is the reason behind partially flooded lubricated contacts in practice, which is not confined to the ring-liner conjunction only. Clearly, the outward flow from the contact at the separation boundary equates that through the minimum film thickness constriction. This is simply a restatement of the principle of conservation of mass, embodied in the Navier-Stokes equations. The flow at the outlet, beyond the lubricant film rupture boundary can contain significant vapour content, thus the reason for the inclusion of vapour transport equation in the analysis.

Table 4.7: Mass flow rates through the content

Ring face width	Physical Inlet flow (kg/s)	Central contact flow (kg/s)	Outlet flow (kg/s)
b	8.88×10^{-5}	8.751×10^{-5}	8.751×10^{-5}
1.2 *b*	9.95×10^{-5}	8.792×10^{-5}	8.792×10^{-5}
1.5 *b*	1.12×10^{-4}	8.825×10^{-5}	8.825×10^{-5}
2 *b*	1.27×10^{-4}	8.848×10^{-5}	8.848×10^{-5}
2.5 *b*	1.37×10^{-4}	8.858×10^{-5}	8.858×10^{-5}
3 *b*	1.40×10^{-4}	8.860×10^{-5}	8.860×10^{-5}

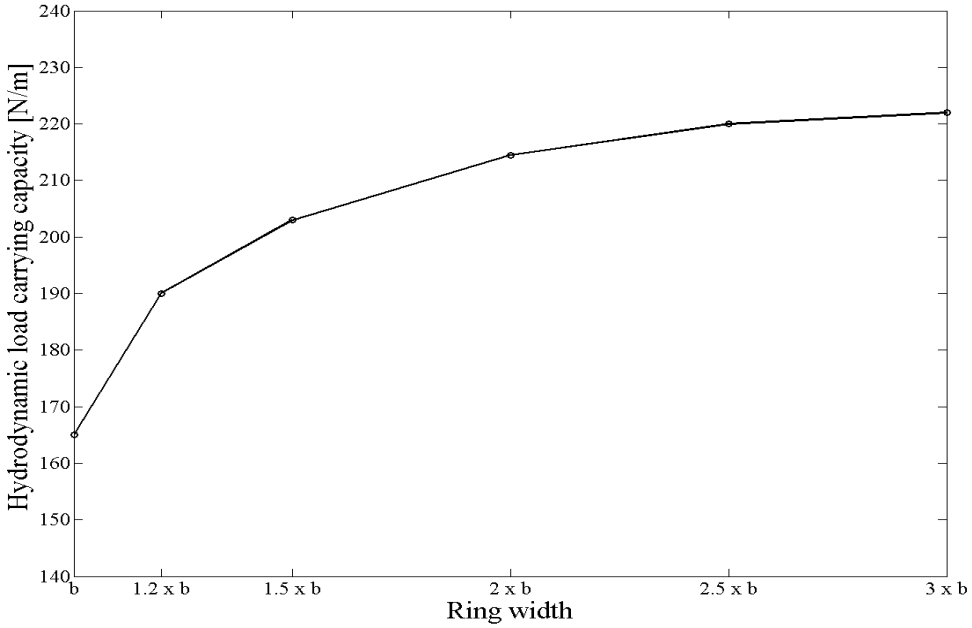

Figure 4.22: shows the integrated pressure (load carrying capacity) for different rings of figure 4.21

Often fully flooded inlet conditions are assumed during the various engine strokes. However, the measured friction [132,135] or film thickness [145] indicate mixed or boundary regimes of lubrication at or in the vicinity of the TDC. Hydrodynamic regime of lubrication is found to be dominant in other locations, such as at piston mid-span locations in the various engine strokes. Figure 4.23 shows the predicted minimum film thickness at various locations. Mid-span locations are in the compression stroke (-90° crank angle), power stroke (90° crank angle), exhaust stroke (270° crank angle) and the intake stroke (450°crank angle). The positions $\pm 5^{\circ}$ crank angle correspond to the transition from the compression to power stroke through the TDC, where mixed or boundary regimes of lubrication are prevalent [23,39,46,132,135]. Obviously, the minimum film thickness is reduced for all ring face-width cases during the reversal because of the reducing sliding velocity of the piston. The minimum film thickness is also reduced during the compression and power strokes, because of increased pressure loading behind the ring. The line

$\lambda = 3$, where $\lambda = \frac{h}{\sigma_{RMS}}$ is the Stribeck's oil film parameter, represents the boundary between lubricated hydrodynamic condition and mixed regime of lubrication. It can be seen that for the region $-5^{\circ} \leq \varphi \leq 5^{\circ}$ the lubricant film thickness is quite thin and thus a mixed regime of lubrication would be expected.

It can be seen that in all cases the film thickness gradually increases up to the ring face-width of 2*b* before no further gain is noted. The contact load, *F* (Eq. (3.47)) is known for the ring-liner conjunction at these locations. Therefore, an increasing film thickness with the broadening ring contact face-width (up to an optimum) is indicative of enhanced hydrodynamic action. To ascertain this, it would be instructive to determine the total friction (viscous and boundary contributions) for these cases.

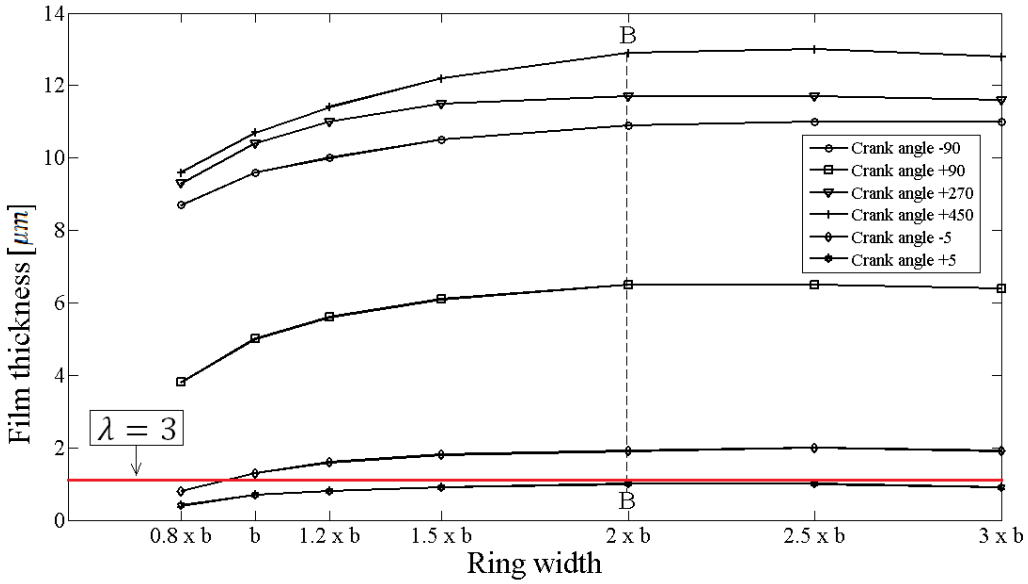

Figure 4.23: Variation of minimum film thickness for different ring widths at piston mid-span positions

Figure 4.24 shows the predicted friction for the same positions as in figure 4.23. There is no correspondence between the optimum conditions in figure 4.23 (thickest minimum conjunctional film for a ring face-width of 2*b*, indicated by the vertical line BB) and the minimum conjunctional friction for the ring width *b* (line AA in figure 4.24). In the piston mid-span locations there is insignificant contribution due to

asperity interactions as the minimum lubricant film thickness is in excess of 3 μm in all cases (figure 4.23), the least film thickness occurring during the power stroke (crank angle of 5°). Furthermore, the change in the film thickness is fairly small in the case of each particular location, thus changes in viscous shear (Eq. (3.53)) are marginal when dealing with a particular crank angle. Of course, these changes are not negligible at different crank angle positions, because of the sliding speed, effective lubricant viscosity and the film thickness (see Eq. (4.19)). The increasing friction is also as the result of increased lubricated contact area between the inlet stagnation point (the zero reverse boundary) and the lubricant film rupture point. This indicates that maximum viscous friction occurs at the mid-span position in the power-stroke, whilst the maximum boundary friction takes place at the TDC reversal for the crank angle of 5°. In fact, figure 4.25 shows the contributions from viscous and boundary frictions during the TDC reversal. Even in these locations the main contribution is due to viscous friction, with fairly thin films and increased pressure loading behind the ring; Poiseuille friction. The shear stress is given by Eq. (3.53), where the first term on the right-hand side is the contribution due to Poiseuille shear, which is a function of pressure gradient, which is higher at the TDC reversal and increases in the power stroke.

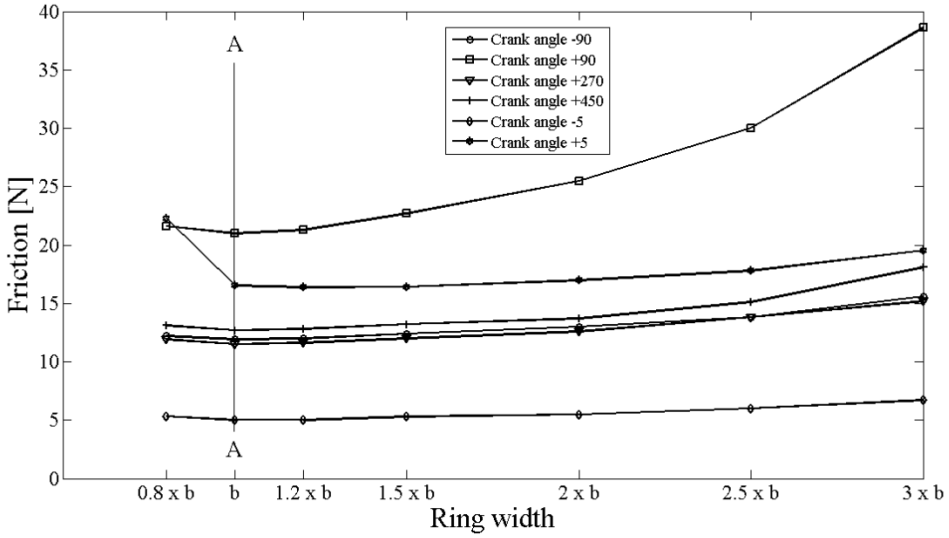

Figure 4.24: Variation of friction for different ring widths for piston at mid-span positions

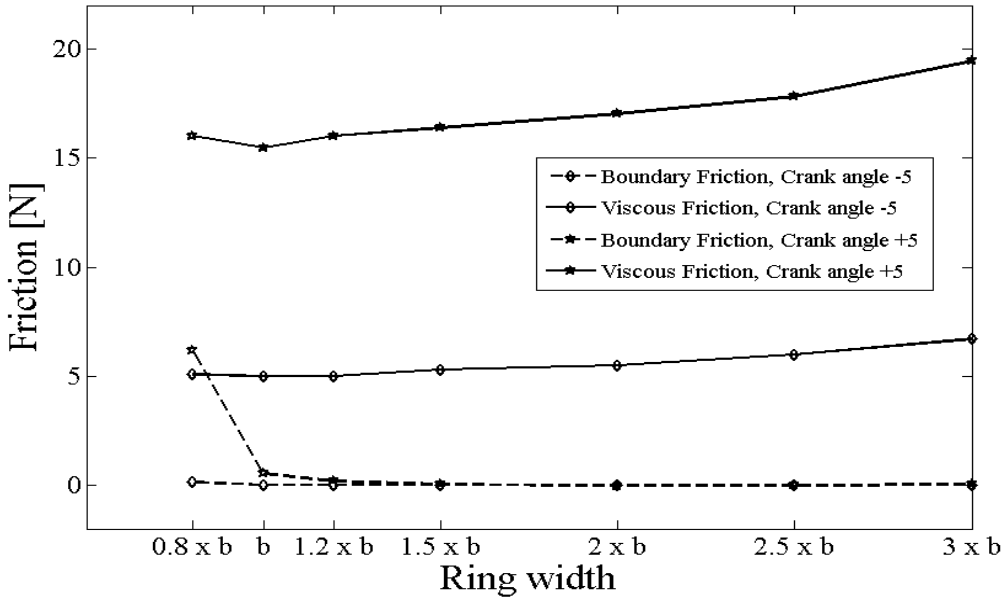

Figure 4.25: Viscous and boundary contributions to generated friction at the TDC reversal

Figure 4.26 shows the position of lubricant film rupture and the subsequent cavitation region, which is also shown by the zoomed-in inset to the figure. The contours in the figure represent different levels of void fraction (volume fraction of liberated vapour in the bulk lubricant). The figure shows significant amount of vapour content, which reduces both the load carrying capacity as well as viscous friction.

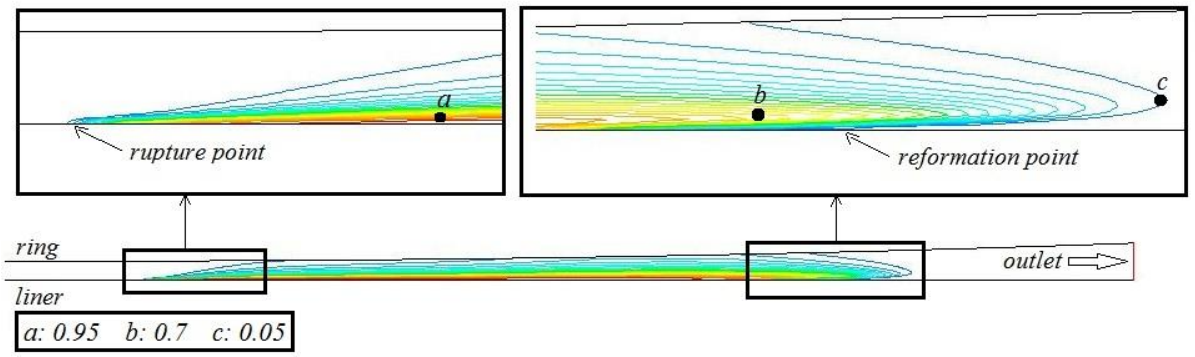

Figure 4.26: Contact exit boundary with contours of vapour content

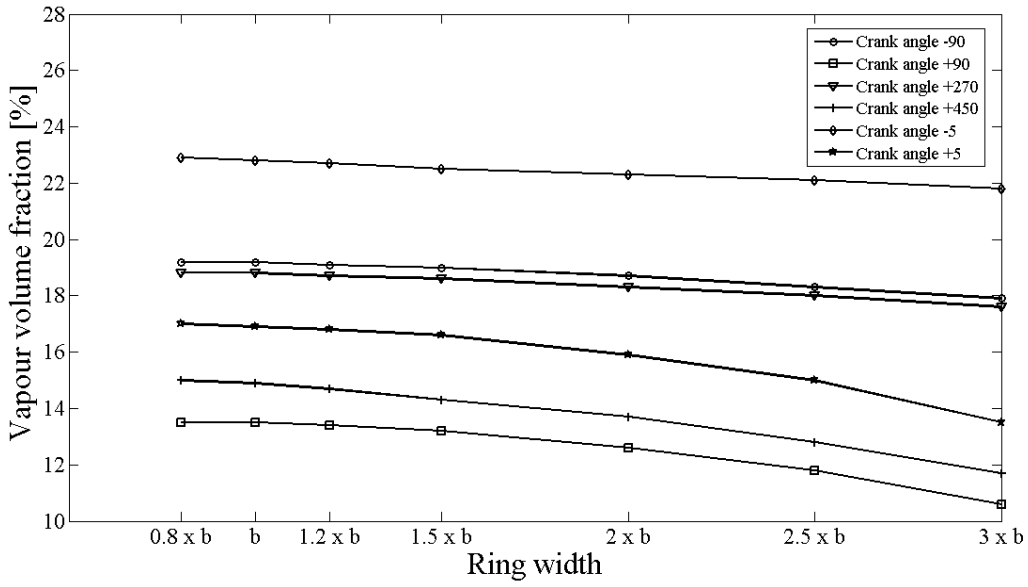

Figure 4.27: Vapour content variation in different engine strokes and ring face-width

Figure 4.27 shows the variation in vapour fraction for various crank-angle positions with different assumed ring contacting face-width. Important points to note are reduced vapour fraction in the power stroke in comparison with that in the other strokes. This is expected, because of a higher contact pressure. This is clearly shown through the TDC reversal where there is lower vapour fraction for the crank angle of 5° (power stroke) than -5° (compression stroke). With less vapour content, viscous friction is increased accordingly (figures 4.23 and 4.24).

4.9. Implement of Continuum Surface Force (CSF) model (Boundary between lubricant and vapour)

Continuum Surface Force (CSF) model is used in this study to track bubble formation and have a boundary between lubricant and vapour in the cavitation area. In this model liquid flow is considered as a continuous phase and cavitation bubbles as the dispersed phase. Bubble formation through nucleation, momentum exchange

between the void and the carrier liquid phases, bubble growth and collapse due to non-linear bubble dynamics and bubble hydrodynamic break-up are assumed to take place in cavitating flows in the model. The effect of bubble-to-bubble interaction on momentum exchange and during bubble growth would are also considered. Figure 4.28 shows images of bubble formation induced by cavitation sequence between the compression ring and the liner in the crank angle of 90° (mid-span power stroke) at the engine motored speed of 1500 rpm.

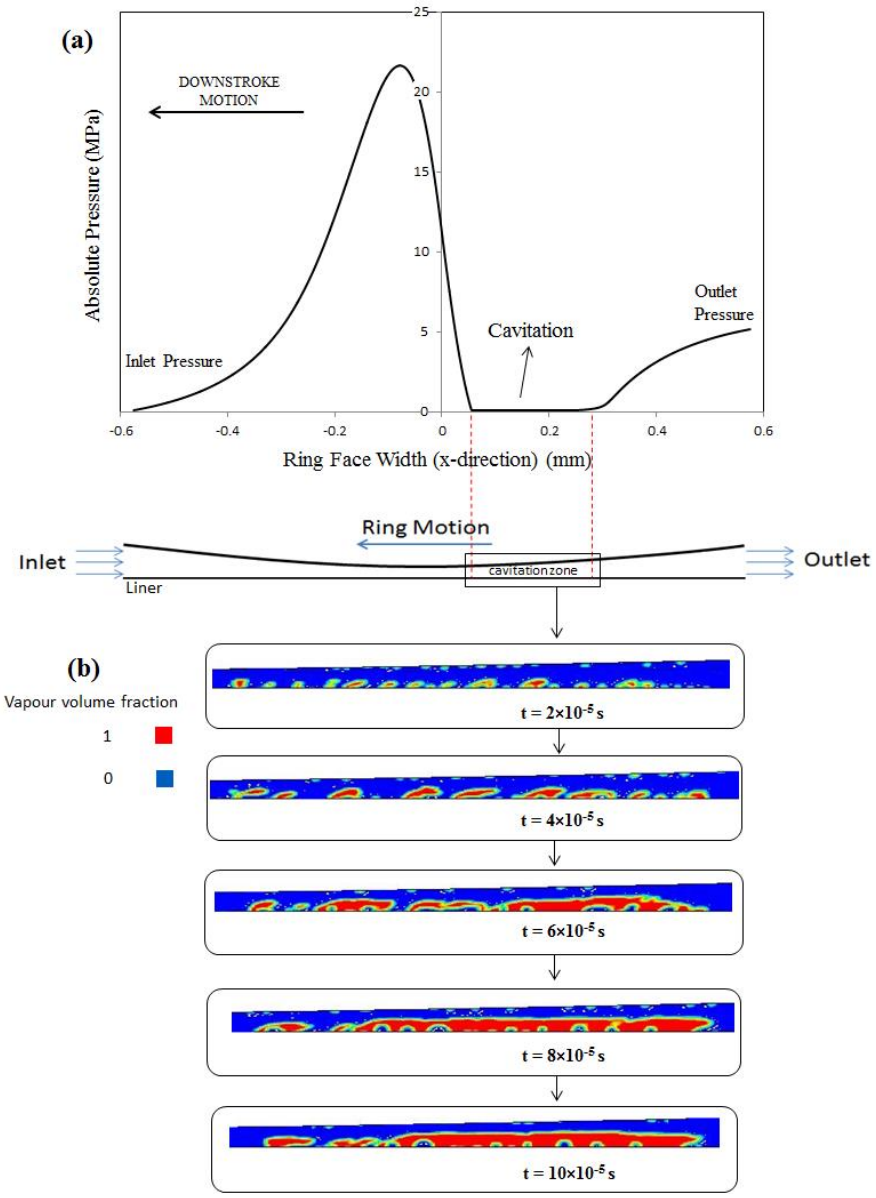

Figure 4.28: Cavitation-induced bubble formation sequence in the ring-liner conjunction at 1500 rpm

4.10. Closure

This chapter has provided results for compression ring-cylinder liner conjunction, using combined solution of Navier-Stokes, Energy, vapour transport and modified Rayleigh-Plesset equations. The results of the analysis have shown to conform well with direct *in situ* measurement of friction reported by Gore et al [134] using an instrumented floating liner. The CFD predictions have also shown to be in closer agreement with experimental results and those using Reynolds equation or Elrod cavitation algorithm.

This chapter also addresses the inlet and outlet boundary conditions which are realistic, unlike the idealistic fully flooded inlet or exit boundary conditions which do not uphold the principle of continuity of mass flow. The boundary conditions indicated by the solution methodology here conform well to the compatibility flow analysis of Tipei [137] taking into account swirl and counter flow at the conjunctional inlet as well as film rupture at the outlet separation boundary.

Chapter 5: Tribology of Journal Bearings and Effect of Cavitation

5.1. Introduction

The main considerations in modern engine development are fuel efficiency and compliance with progressively stringent emission directives. Within the pervading global competition there is also a requirement to address customer demands for maintaining adequate output power. These often contradictory attributes have led to the downsizing concept and higher output power-to-weight ratio engines. Additionally, there is a growing trend towards the use of emerging technologies such as variable valve actuation and cylinder deactivation (CDA) [148-150]. There is also progressively an interest in the concept of stop-start in congested urban environments. The adoption of these technologies is primarily based on the direct reduction of brake specific fuel consumption. However, there are also indirect repercussions such as thermal and frictional losses, as well as poor noise, vibration and harshness (NVH) refinement issues with generally light weight and poorly damped power train structures, subjected to engine power torque fluctuations [151]. With the application of CDA a greater degree of engine torque fluctuations would result [126], which is likely to lead to further deterioration in NVH refinement.

There is a dearth of analysis with respect to thermal and frictional losses, when considering CDA. A recent study by Mohammadpour et al [152] showed that CDA makes only marginal differences in parasitic frictional losses in engine bearing performance and that any significant gain would depend only on the brake specific fuel consumption. However, the analysis did not take into account some important issues such as multi-phase lubricant flow through the contact and the occurrence of cavitation. These affect the load carrying capacity of the bearing as well as the conjunction friction, viscous heat generation and heat transfer to the solid

boundaries. Brewe et al [153] have shown that Swift [31]-Stieber [32] boundary conditions can only accurately predict the film rupture point for steadily loaded bearings, which is not suitable for engine bearings, particularly with exacerbated dynamic loading under CDA. Therefore, to include the effect of cavitation, it is essential to employ realistic conjunctional outlet boundary conditions rather than the traditional Swift-Stieber [31,32] assumptions, used by Mohammadpour et al [152]. This paper strives to improve upon Mohammadpour's approach, through the combined solution of Navier-Stokes equations for fluid flow and the energy equation for heat balance.

The development of computational fluid dynamics (CFD) approach enables solution of Navier-Stokes equations for multi-phase flow to be achieved, whilst retaining the principle of conservation of mass and momenta. Some of the underlying limitations of Reynolds equation can also be removed. Tucker and Keogh [86] employed a 3D CFD approach for thermo-hydrodynamic analysis of steady-state motion of journal bearings. They used an Elrod [15] type cavitation model which allowed for the existence of the sub-ambient pressures. In this approach, the vapour fraction becomes a function of the film thickness. However, as Tucker and Keogh [86] also note for non-Couette or unsteady flows a time-dependent continuity equation should be used to determine the vapour fraction. In their analysis continuity of heat flux and compatibility of temperature was assured at the solid-fluid interface.

This chapter presents a full 3D CFD approach for thermo-hydrodynamic analysis of big-end bearings. No artificial boundary conditions are set at the exit from the conjunction. This means that the lubricant rupture and reformation boundaries are determined by the combined solution of Navier-Stokes equations, the energy equation and continuity of flow conditions (in terms of conservation of mass and momenta). In addition, the cavitation phenomenon is taken into account through solution of a vapour transport equation including the Rayleigh-Plesset source terms to take into account the growth and collapse of cavitation bubbles. The developed

method is validated against experimental results of Dowson et al [56]. The validated model is then used for analysis of a big-end engine bearing subjected to dynamic loading under normal engine operation as well as with the application of CDA; an approach not hitherto reported in the literature.

5.2. Big end bearing geometry

A schematic of the big end bearing used in IC engines is shown in Figure 5.1. In a conventional internal combustion (IC) engine, the crank-pin acts as the journal and the bearing bushing is located at the bottom end of the connecting rod. The big end bearings are usually groove-less and are pressure-lubricated using a single hole drilled through the crank pin [154]. Although in most applications a simple circular profile is used to describe the geometry of the big end bearing, in practice, an elliptic (or 'lemon shape') bore profile is used. To study the effect of CDA, the engine studied here was a high performance 4-stroke naturally aspirated engine with the specifications provided in Table 5.1.

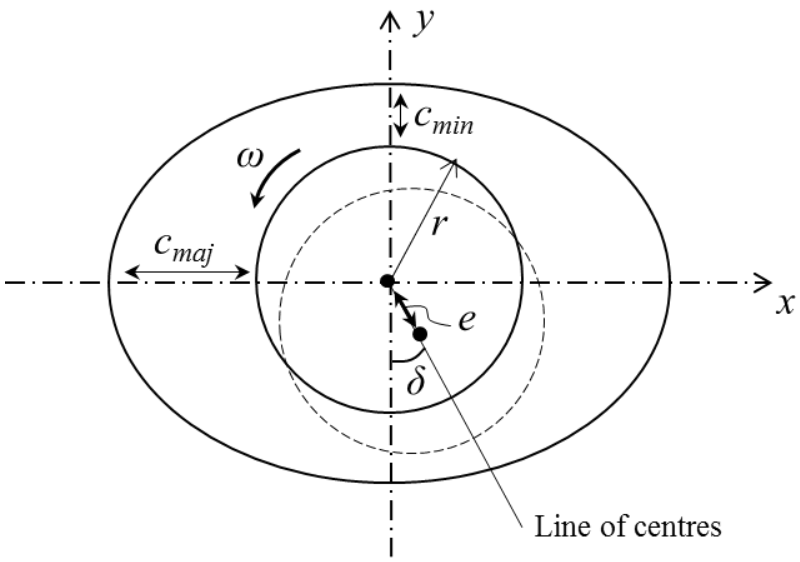

Figure 5.1: An elliptic big end bearing configuration

Table 5.1: Engine and bearing data

Parameter	Value	Unit
Crank pin radius	31	mm
Connecting rod length	107	mm
Effective translational mass	0.32	kg
Engine speed	2200	rpm
Bearing width	16.8	mm
Bearing radius	21	mm
Minor diametral clearance	20	μm
Major diametral clearance	30	μm
Composite surface roughness	1	μm
Overall overlay thickness	2	mm

The film profile for such an elliptic bore bearing is defined as (Mishra et al [155]):

$$h = c(1 + G\cos^2\theta + \varepsilon\cos\theta) + \Delta \tag{5.1}$$

where, the non-circularity is defined as: $G = \left(c_{maj} - c_{\min}\right)/c$. The parameters c, ε, θ are the average clearance, eccentricity ratio and the angular position respectively (figure 5.1). The localised deflection of the Babbitt overlay, Δ is obtained using the column method contact mechanics approach [156], where:

$$\Delta = \frac{(1-2\nu)(1+\nu)d}{E(1-\nu)}\,p\,. \tag{5.2}$$

5.3. Applied loads

Big-end bearings are designed to withstand the transmitted transient forces through the connecting rod. These are the result of combustion pressure and inertial imbalance [151].

For a typical 4-cylinder 4-stroke engine, the inertial imbalance force acting through the connecting rod along the axis of the piston is [151] (figure 5.2):

$$F_{in} \approx m_1 r_c \omega^2 \left(\cos\omega t + \frac{r_c}{l}\cos 2\omega t \right) \tag{5.3}$$

where, engine order vibrations up to the second engine order are considered here for the 4-stroke engine under consideration. The mass m_1 is the equivalent mass in translation, comprising that of the piston, the gudgeon pin and a proportion of the mass of the connecting rod in pure translation: $m_1 = m_p + m_g + m_c$ in a two degrees-of-freedom representation of piston-connecting rod-crank sub-system, where according to Thomson [157]:

$$m_c = \frac{W_c}{g}\left(1 - \frac{C}{l}\right) \tag{5.4}$$

where, W_c is the weight of the connecting rod and C denotes centre of mass of the connecting rod measured from its small end.

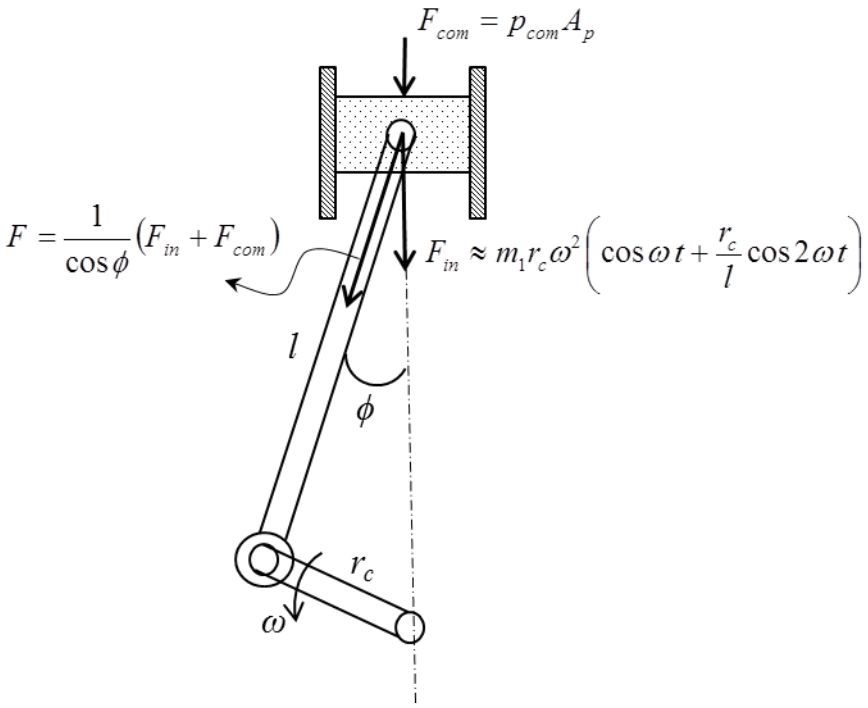

Figure 5.2: Schematic of the piston-crank system with the applied loads

The applied vertical combustion force acting upon the piston crown area is:

$$F_{com} = p_{com}A_p \tag{5.5}$$

where, p_{com} is the instantaneous in-cylinder pressure and A_p is the piston crown surface area.

Therefore, the total transient load applied on the big end bearing at any instant of time, expressed in terms of the instantaneous connecting rod obliquity angle, ϕ, is (figure 5.2) [151]:

$$F = \frac{1}{\cos\phi}(F_{in} + F_{com}) \tag{5.6}$$

where:

$$\cos\phi \approx 1 - \frac{1}{2}\left(\frac{r_c}{l}\sin\omega t\right) \tag{5.7}$$

and: $\varphi = \omega t$, φ is the crank angle.

It should be noted that smaller moment loading from adjacent cylinders also exists, which is ignored in this analysis. More information is provided in Rahnejat [158].

5.4. Boundary conditions

5.4.1. Flow boundary conditions

The flow boundary conditions are set, based on the conditions for a typical IC engine big-end bearing.

The cavitation (vaporisation) pressure is set at the atmospheric pressure of 101.3 kPa. Since the occurrence of cavitation in the current CFD analysis is treated through solution of transport equation for the vapour mass fraction alongside the general Navier-Stokes equations, there is no need to impose any particular boundary conditions for either lubricant film rupture or reformation. This is a significant fundamental improvement upon the imposed assumptions such as those of JFO or Elrod cavitation models.

In addition to the fact that the solid boundaries were considered to be impermeable, the lubricant/solid interface is also assumed to follow the no-slip condition.

The bearing shell is modelled as a stationary wall, whilst the journal is modelled as a moving body with an absolute rotational velocity.

At the inlet hole supply orifice to the bearing the lubricant is fed into the contact at a constant pressure of 0.5 MPa as already assumed by Mohammadpour et al [152].

Finally, at the bearing's axial extremities the lubricant is assumed to leak to ambient (atmospheric) pressure.

5.4.2. Conduction heat transfer in the solid bodies (journal and bearing)

In order to proceed with full thermal analysis of the journal-lubricant-bearing bushing system, one needs to take into account the conduction of the generated heat to the solid boundaries using the energy equation. The conduction of heat into the rotating journal is governed by the transient form of the heat conduction equation as:

$$\frac{1}{\alpha}\frac{\partial T}{\partial t} = \nabla^2 T \tag{5.8}$$

where, α is the thermal diffusivity for the journal's material. The convective (time dependent term) on the left hand side of the equation takes into account the rotational effect.

On the other hand, the steady-state form of the heat conduction equation is used for the stationary bushing as:

$$\nabla^2 T = 0 \tag{5.9}$$

5.4.3. Thermal boundary conditions

The thermal boundary conditions are set for a typical IC engine big-end bearing (figure 5.3). The boundary conditions used at the lubricant-solid interface ensures the continuity of heat flux and compatibility of evaluated temperatures.

After lubricant enters the contact through the oil feed hole, its temperature is increased from that in the bulk due to the heat produced in the contact as the result of shearing. The generated heat is transferred by convection through lubricant side leakage and conducted through the bounding solid surfaces. In the experiments

conducted by Dowson et al [56], the journal's extremities were exposed to the ambient air. Therefore, convection cooling would take place at these interfaces. However, for the engine conditions, it is assumed that the journal is not exposed to the ambient air and thus, any heat transfers to the journal and increases its core temperature. Finally, a portion of the heat is conducted through the bearing bushing to the surrounding ambient air [159,161]. Of course, for journal bearings, convective heat transfer by the lubricant film is most significant. Figure 5.4 demonstrates a graph of Peclet number versus crank angle for the case of the big end bearing of an active cylinder under normal engine operation, which indicates the dominance of convective heat transfer by the lubricant film relative to the heat conducted through the conjunctional surfaces.

In both the validation process and engine running conditions, it was assumed that the bearing's outer surface is exposed to the ambient temperature. Figure 5.3 illustrates thermal boundary conditions in the journal bearing. A list of the assumed ambient air temperature, lubricant and material data for the engine running conditions is provided in Table 5.2.

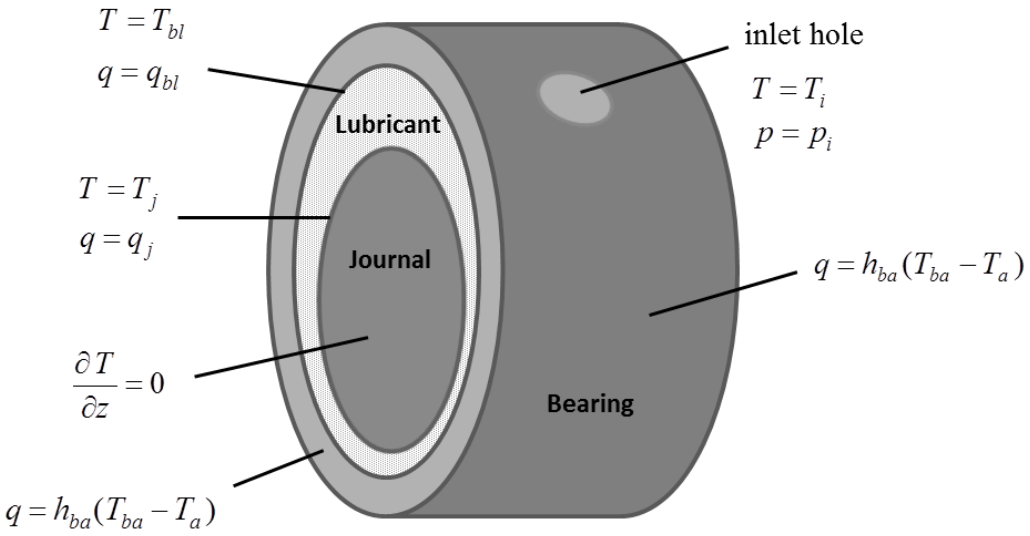

Figure 5.3: Thermal boundary conditions

Table 5.2: Lubricant and material data (this data corresponds to a Ford model vehicle big-end bearing)

Parameter	Value	Unit
Lubricant dynamic viscosity	8.0	mPa.s
Lubricant density	833.8	Kgm^{-3}
Viscosity-temperature coefficient	0.026	K^{-1}
Pressure-induced shear coefficient (γ)	0.047	-
Atmospheric limiting shear stress	2.3	MPa
Specific heat capacity of lubricant	2360	$Jkg^{-1}K^{-1}$
Thermal conductivity of lubricant	0.225	$Wm^{-1}K^{-1}$
Poison's ratio for Babbitt	0.33	-
Young's modulus for Babbitt	60	GPa
Thermal conductivity of bearing bushing k_{s1}	46	$Wm^{-1}K^{-1}$
Thermal conductivity of journal k_{s2}	25.96	$Wm^{-1}K^{-1}$
Journal material	SG cast iron	-
Bearing overlay	Babbitt	-
diffusion coefficient	10^{-8}	m^2s^{-1}
Eyring shear stress	5	MPa
Inlet pressure	0.5	MPa
Ambient temperature	50	$^{\circ}C$

In solving the coupled energy and heat conduction equations, the temperature of the entrant lubricant is computed from the initial solid component temperatures and heat fluxes at the solid interfaces. The produced heat in the lubricant is allowed to increase the journal's temperature whilst the transferred heat to the journal bushing can be convected away through ambient air. The temperature of the oil at the inlet hole was set to T_i = 42°C in the case of the validation procedure (Dowson et al [56]).

For the engine conditions this was set at 50°C. The lubricant thermal properties such as thermal conductivity and specific heat are calculated at the engine compartment temperature of 50°C under steady engine running condition and 40°C for the validation case study.

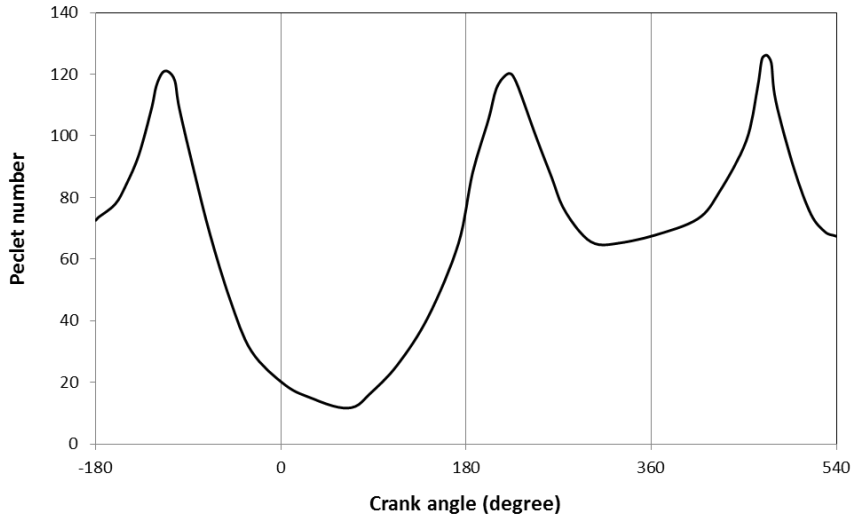

Figure 5.4: Peclet number versus crank angle for the case of the big end bearing of an active cylinder under normal engine operation

5.5. Grid (Mesh) structures and solution procedures

The governing equations described in section 3.1 were solved in the environment of ANSYS FLUENT 14.5, where a computational mesh is generated. For the conjunctional fluid domain (the lubricant) was meshed with hexahedral cells (element size 50 μm), whilst the bounding solid surfaces were discretised using tetrahedral elements with 2 mm elements. There is no need for finer solid elements as there is no local deformation of surfaces at the expected generated pressures, since $\alpha p_m \ll 1$ for the conformal contact of the contiguous surfaces as in journal bearings [110]. The interfaces between the solid surfaces and the lubricant zone were defined by face meshing method. The total number of computational control volume elements was 2,533,165.

A grid independency test for the result was performed, which showed that the number of elements used in excess of that stated did not significantly alter the results of the analyses (figure 5.5).

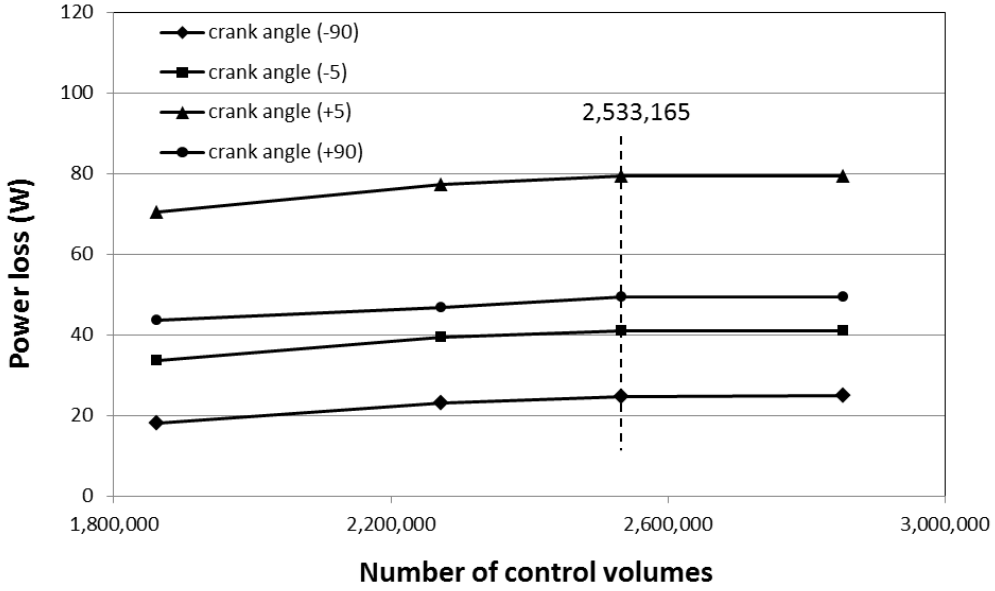

Figure 5.5: Power loss versus different numbers of control volume

Since the gap between the two solid surfaces is subject to transience with variations in applied load and speed, a dynamic mesh model was employed to calculate the lubricant film thickness at any instant of time. Boundary Layer Smoothing Method and Local Cell Remeshing are used for the dynamic mesh model.

In order to be able to include the described cavitation model (Section 3.2), a mixture model was employed to take into account the two-phase flow nature of the problem [105]. In this method, the mass continuity, momentum and energy equations are solved for the mixture while a mass/volume fraction equation (Eq. (3.36)) is solved for the secondary (gas or vapour) phase.

The velocity–pressure coupling is treated using the standard semi-implicit method for pressure-linked equations (SIMPLE algorithm) and the second-order upwind scheme is used for the momenta in order to reduce any discretisation-induced errors. A

pressure-based segregated algorithm is employed in which the equations are solved sequentially.

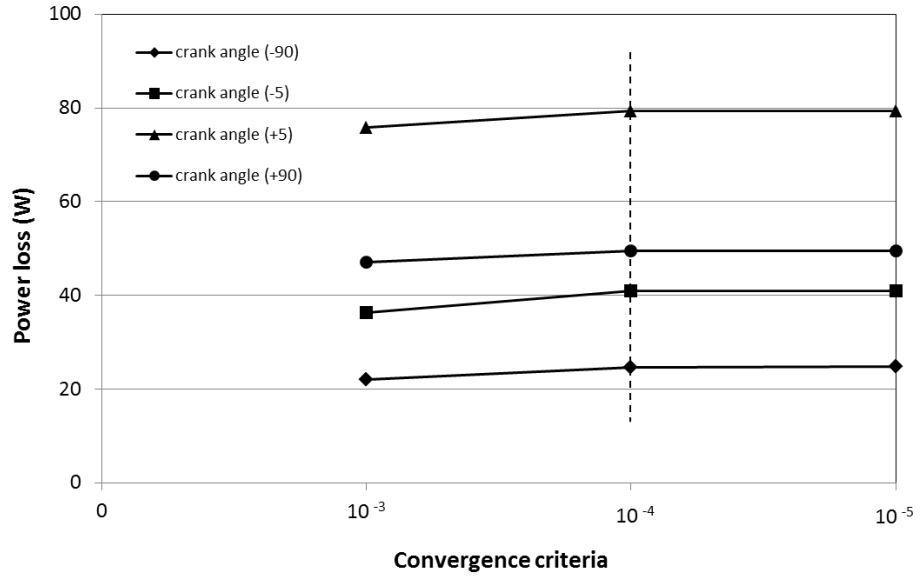

Figure 5.6: Power loss versus different convergence criteria for mass and momentum conservation and the vapour volume fraction

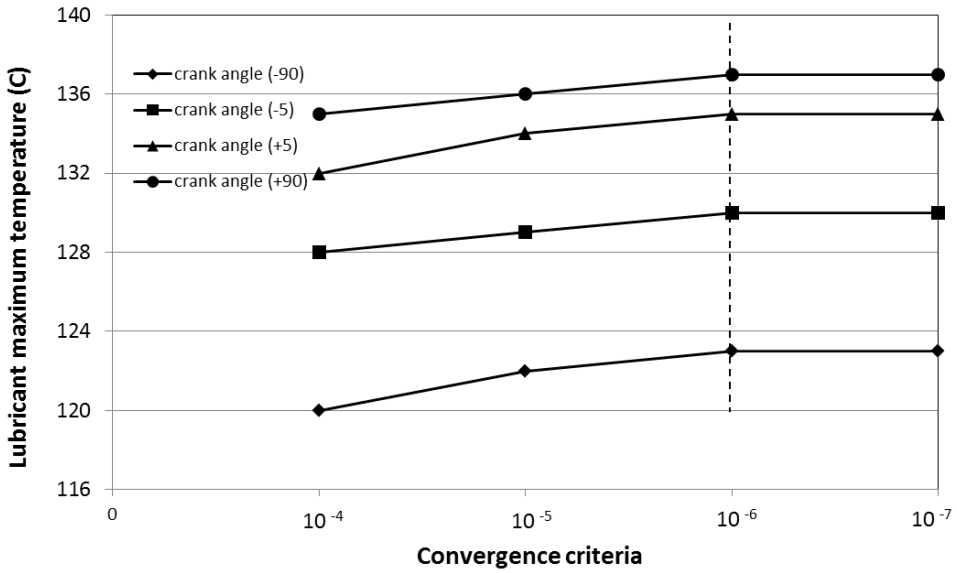

Figure 5.7: Lubricant maximum temperature versus different convergence criteria for energy conservation

For greater accuracy, an error tolerance of 10^{-4} is used for the residual terms of mass and momentum conservation and the volume fraction, whilst a tolerance value of 10^{-6} is employed for energy conservation and heat conduction equations (figures 5.6 and 5.7).

5.6. Model Validation

Prior to any analysis of engine conditions under normal operating mode or with application of CDA, it is necessary to validate the developed numerical model. A two-stage validation process is undertaken.

Firstly, the model predictions are compared with the experimental measurements reported by Dowson et al [56], which have been used for the same purpose by other research workers, including Tucker and Keogh [86], and Wang and Zhu [162]. Dowson et al [56] measured the lubricant pressure distribution in a restricted grooved journal bearing (figure 5.8). A lubricant inlet supply hole with diameter d was drilled radially through the bearing on its central plane. A distribution groove with width d was cut axially into the inner surface of the bearing with the length, L_i. The attitude angle δ is measured from the location of the axial groove to the line of centres. The journal bearing variables used in the computation are listed in Table 5.3. Dowson et al [56] noted a build-up of pressure with the passage of lubricant through the converging gap to support the applied load. In the diverging gap of the conjunctional outlet, the fall in the generated pressures resulted in the fluid film cavitating into a series of streamers below the saturation pressure of the dissolved gases.

Secondly, further numerical predictions are made using Reynolds equation and Elrod's cavitation algorithm. In the Elrod's approach the fractional film content is the proportion of the conjunctional gap which attains generated pressures in excess of

the cavitation vaporization pressure of the lubricant for a given conjunctional temperature (indicated by its bulk modulus, β), thus [144]:

$$p = \psi\beta \ln\gamma + p_{cav} \tag{5.10}$$

where, ψ is a switching function: ψ=1, γ>1, P>p_{cav} represents regions of a coherent fluid film and ψ=0, γ<1. P=p_{cav} represents the cavitation region, with clearly γ=1 defining the lubricant film rupture point.

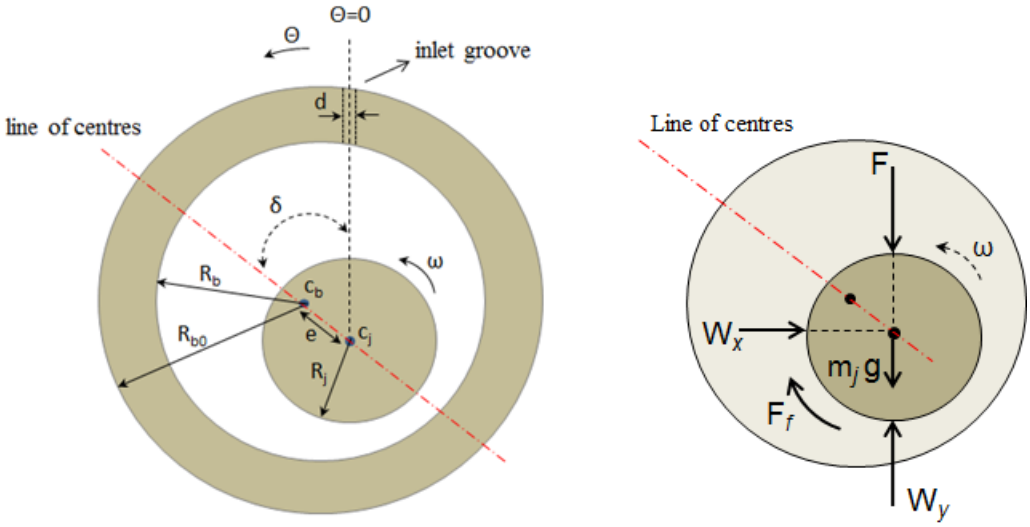

Figure 5.8: Schematic of journal bearing geometry used in Dowson et al [56] and its free-body diagram

Dowson et al [56] operated their experimental journal bearing rig at a steady speed of 1500 rpm, an applied load of 9000 N and with an attitude angle of δ=18°. This yielded a journal operating eccentricity ratio of ε=0.5. Figure 5.9 shows the numerically predicted pressure distribution in isobaric form with the current method. The position of the inlet groove is designated as θ=0° in the circumferential direction. The maximum pressure occurs at θ=206° and the lubricant film ruptures just beyond the position θ=270°.

Table 5.3: Journal bearing variables used in the validation exercise (Dowson et al [56])

Parameters	Values	Units
Bearing length, L	0.0762	m
Radial clearance, c	63.5	μm
Journal radius, R_j	0.05	m
Bearing outside diameter, R_{bo}	0.1143	m
Bearing thermal conductivity, k_b	250	W/m$^\circ$C
Journal thermal conductivity, k_j	50	W/m$^\circ$C
Heat transfer coefficient, h	50	W/m$^2{}^\circ$C
Inlet groove axial length, L_i	0.067	m
Attitude angle, δ	18	Degree
Groove width, d	0.0016	m
Ambient temperature, T_a	40	$^\circ$C

Figure 5.10 shows the cross-section through the 3D pressure distribution in the central plane of the bearing, where pressure tappings were made by Dowson et al [56]. The experimental measurements are shown, as well as the numerical predictions made by Wang and Zhu [162], which are based on Elrod's cavitation model and those from the current CFD analysis. The area under all the pressure distributions, being the lubricant reaction remains the same. Both the predictive analyses employ the same convergence tolerance limit of 10^{-6}. All the pressure distributions commence from the supplied inlet pressure of 0.5 MPa with an assumed fully flooded inlet boundary. The outlet boundary conditions differ between the numerical analyses. Those for the Elrod cavitation boundary are based on the

lubricant film rupture point, γ=1, whereas the current CFD analysis has an open exit boundary condition (not an imposed boundary condition) for the lubricant film rupture point. The different exit boundary conditions, as well as the embodied assumption of a constant pressure gradient into the depth of the lubricant film with a constant dynamic viscosity through its thickness made by Wang and Zhu [162] yield slightly different pressure profiles. This can also be attributed to the thermal gradients across the film that can alter the viscosity in that direction. Clearly, lack of artificially imposed assumptions with the CFD analysis yields results which conform closer to the experimental measurements.

Figure 5.11 shows the contours of temperature distribution for the journal and the bearing bushing surfaces obtained from the current analysis. For the journal surface the maximum temperature occurs close to the high pressure zone. The maximum temperature in the stationary bearing bushing occurs in the cavitation zone due to the high vapour volume fraction residing there with clearly poor convection cooling due to the lack of lubricant flow. Comparison of the experimental result, that from Tucker and Keogh [86] and that of the current model for journal and bearing surfaces are shown in figures 5.12 and 5.13, respectively. As it can be seen, the result of the current analysis shows closer agreement with the experimental measurements. The main difference between the Tucker and Keogh's analysis [86] and the current model is in the treatment of the flow in the cavitation region. The former uses the fraction of vapour Φ in the cavitation region, similar to the Elrod's approach:

$$\Phi = 1 - \frac{h_c}{h} \tag{5.11}$$

where h_c is the film height at the start of the cavitation region. Eq. (5.11) is based only on steady state Couette flow continuity. This ignores the mass flow continuity, which includes the vapour phase and any changes in the Poiseuille flow in a divergent gap. The current model takes these issues into account using the time-dependent continuity equation (Eq. (3.36)).

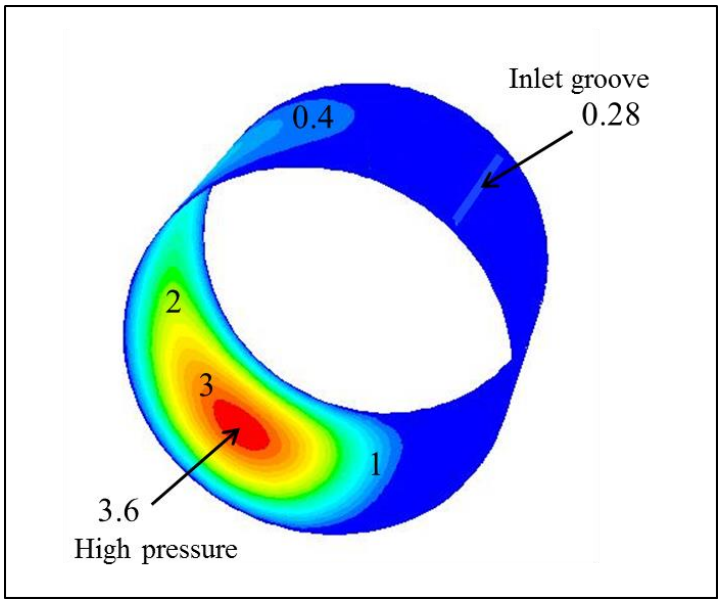

Figure 5.9: Contours of pressure (MPa) for $\varepsilon = 0.5$ at $N = 1500\,\mathrm{rpm}$

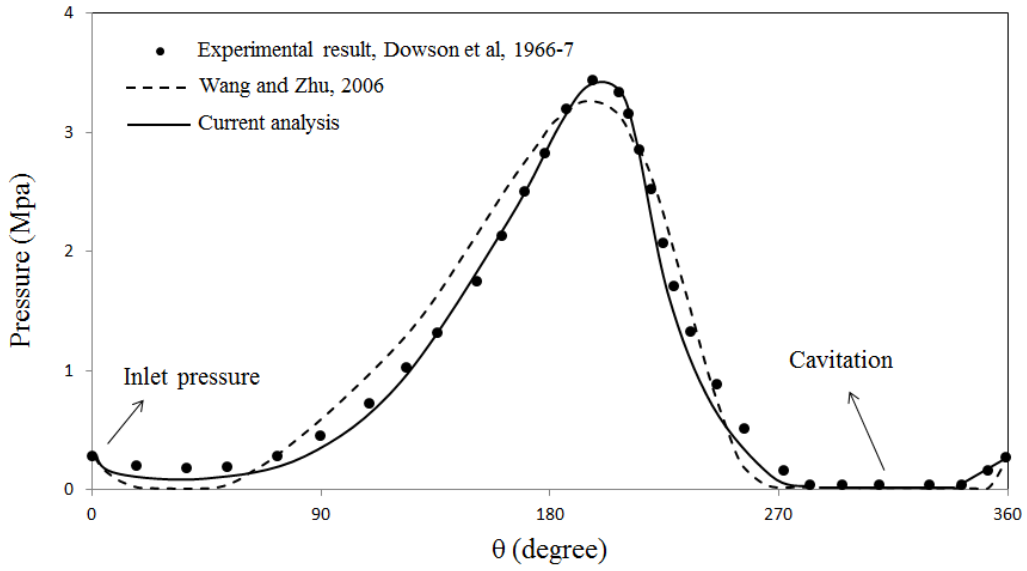

Figure 5.10: Comparison of experimental result and current analysis on pressure distribution in the centre plane for $\varepsilon = 0.5$ at $N = 1500\,\mathrm{rpm}$

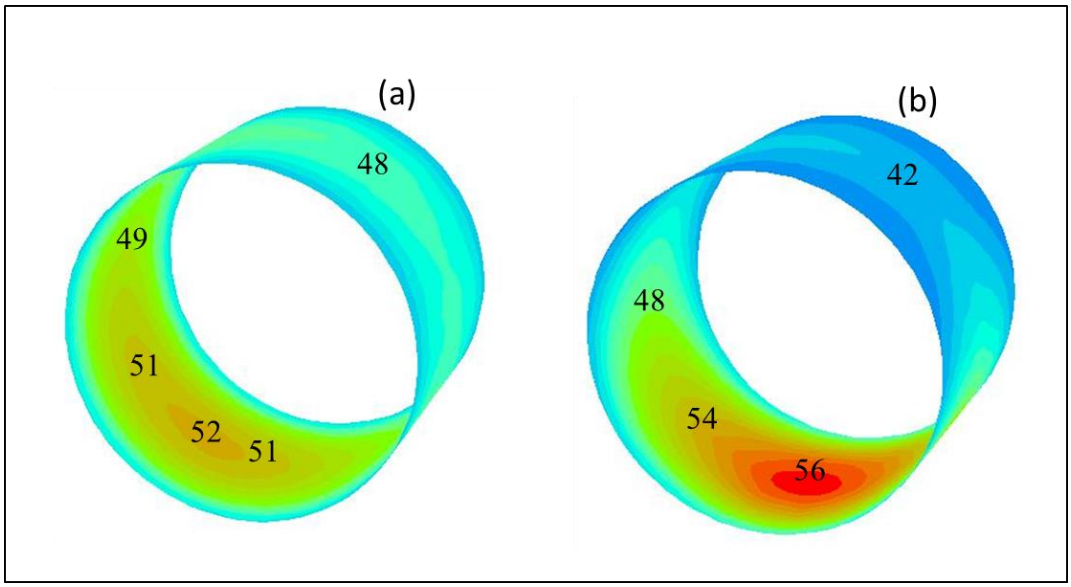

Figure 5.11: Contours of temperature (°C) for (a) circumferential journal surface (b) circumferential bearing surface for $\varepsilon = 0.5$ at $N = 1500\,\mathrm{rpm}$

Figure 5.14 shows the lubricant temperature into the depth of the lubricant at circumferential position, $\theta = 180°$. It shows that the temperature of the lubricant is higher than the temperatures of both the journal and the bearing bushing surfaces. As the temperature varies through the thickness of the lubricant film its viscosity alters locally, which indicates that the thermal flow through the contact is in the form of streamlines at different temperatures and viscosity (with different phases), thus a pressure gradient exists into the depth of the film. Hence, for an accurate prediction of flow a combined solution of Navier-Stokes equation with Rayleigh-Plesset equation is essential as is the case in the current analysis.

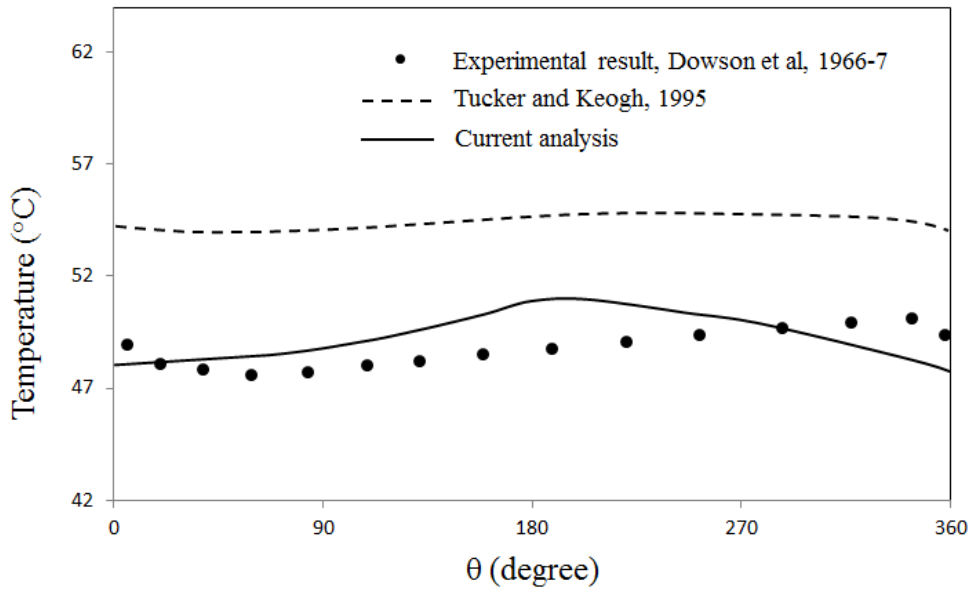

Figure 5.12: Comparison of experimental result and current analysis for the circumferential journal surface temperatures for $\varepsilon = 0.5$ at $N = 1500\,\mathrm{rpm}$

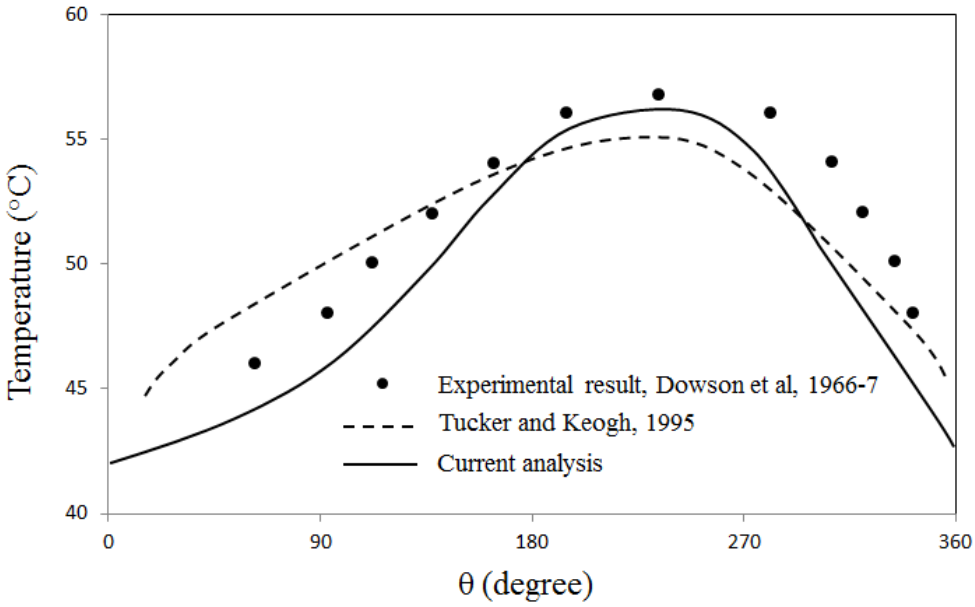

Figure 5.13: Comparison of experimental result and current analysis for circumferential bearing bushing surface temperatures for $\varepsilon = 0.5$ at $N = 1500\,\mathrm{rpm}$

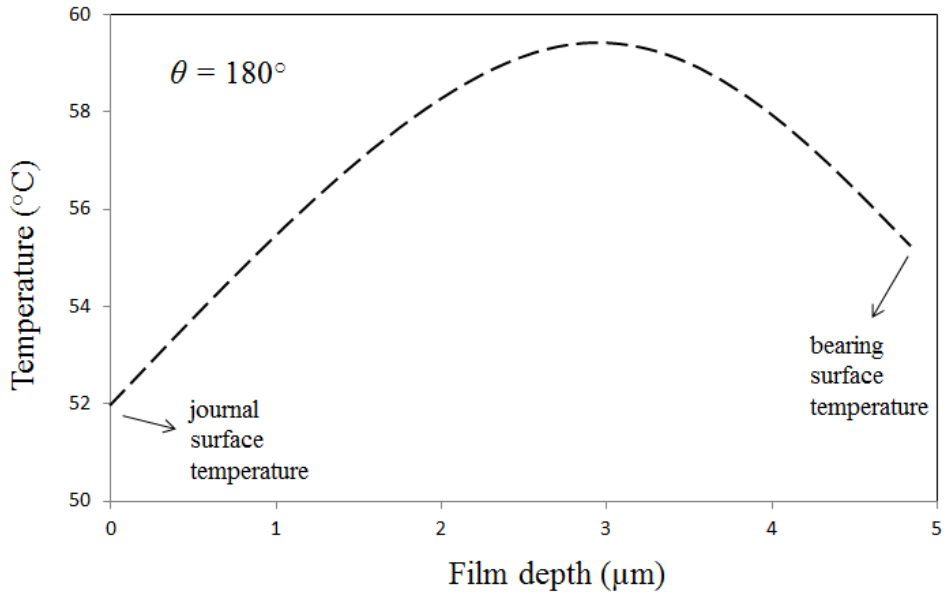

Figure 5.14: Lubricant temperature along the film depth at $\theta = 180°$

5.7. Results and discussion

It is expected that introduction of CDA would affect the thermal conditions in engine big-end bearings and influence frictional power loss. The occurrence of cavitation and its extent would also affect friction. Therefore, it is necessary to develop validated multi-phase flow methods with realistic boundary conditions such as the current method.

Now with the validated model, realistic predictions under engine operating conditions with all-active fired cylinders and alternatively with some deactivated cylinders can be carried out. The analysis reported here corresponds to a 4-cylinder 4-stroke engine under city driving condition at the speed of 25 km/h with 25% throttle action and engaged in second gear (ratio: 1:2.038). The final drive differential ratio is 1:4.07. The engine speed for this condition is 2200 rpm. All the necessary data used in the analysis are listed in Table 5.1. The results are presented for a deactivated cylinder as well as a fired cylinder. Figure 5.15 shows the combustion gas force for

an active cylinder under engine normal operation, as well as that for an active cylinder under CDA. It also shows the gas force for a deactivated cylinder, caused by the trapped air/charge with closed valves, subjected to the swept volumetric changes. Note that the gas force is increased in the active cylinders of a partially deactivated engine with the same flow rate through a common rail supply. The effect is higher temperature combustion which improves upon thermal efficiency and also enhances the operation of catalytic converter, operating at a higher temperature, thus reducing hydrocarbon emission levels. The pumping losses can also be reduced whilst higher cylinder temperature in active cylinders would reduce the lubricant viscosity, thus the frictional losses. This effect is not investigated here, but Morris et al [163] using a control volume thermal mixing model showed that the average temperature of the lubricant, thus its viscosity is primarily determined by the bore surface temperature. Therefore, there are fuel efficiency advantages in terms of reduced thermal losses as well as decreased active cylinder viscous frictional losses.

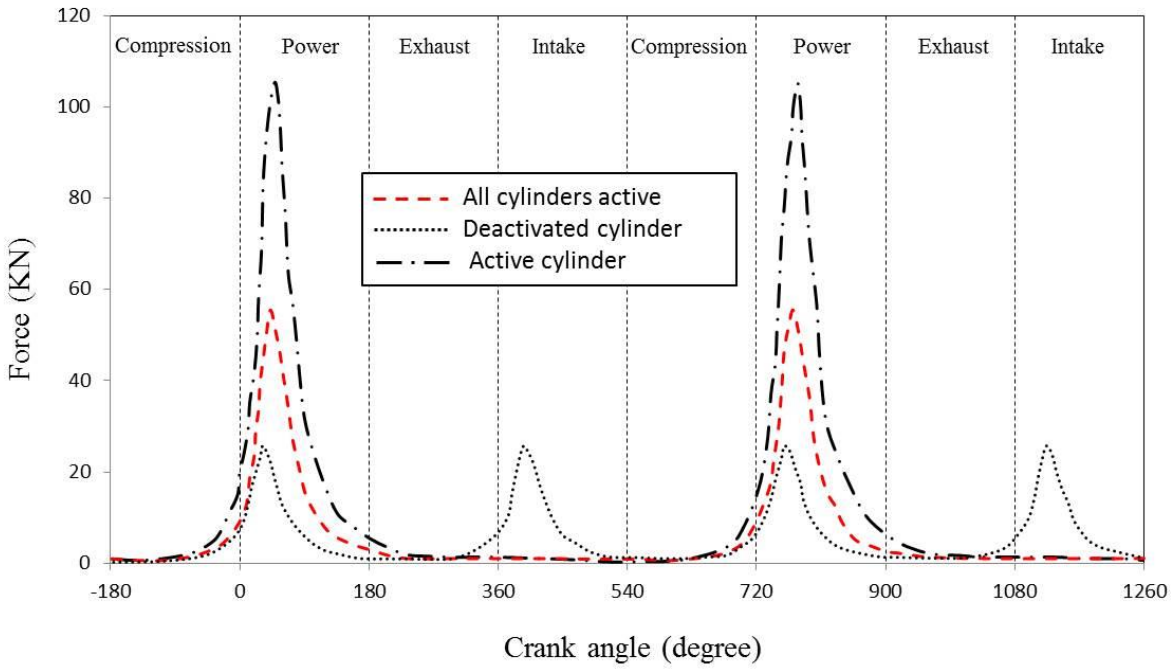

Figure 5.15: Transmitted combustion gas forces for full and partially deactivated engine operations

Cavitation occurs in the big-end bearings under low applied loads, resulting in reduced conjunctional pressures. Figures 5.16 and 5.17 show the generated pressure distribution and the corresponding volume fraction in the journal-bushing conjunction at the crank angle of $\theta = 180^{\circ}$, corresponding to the piston position at the bottom dead centre at the end of the power stroke with very low transmitted applied gas force (figure 5.15). The volume fraction of unity indicates a gap filled purely by vapour.

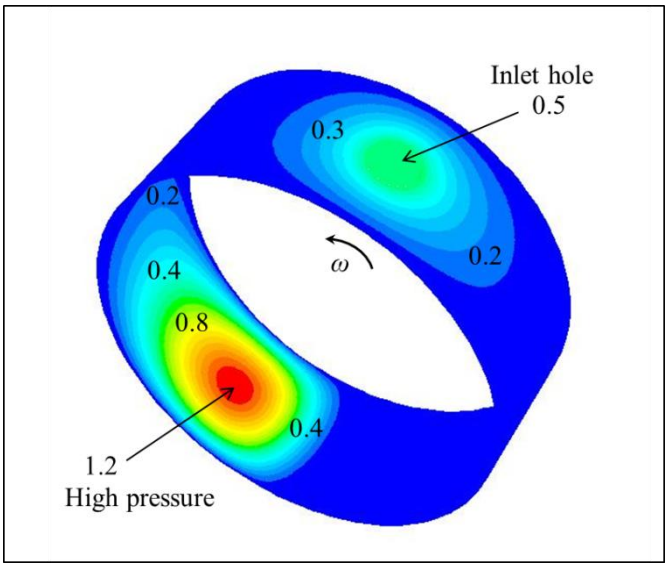

Figure 5.16: Contours of pressure (MPa) at crank angle $\boldsymbol{\theta = 180^{\circ}}$ (piston at the BDC) with all active cylinders

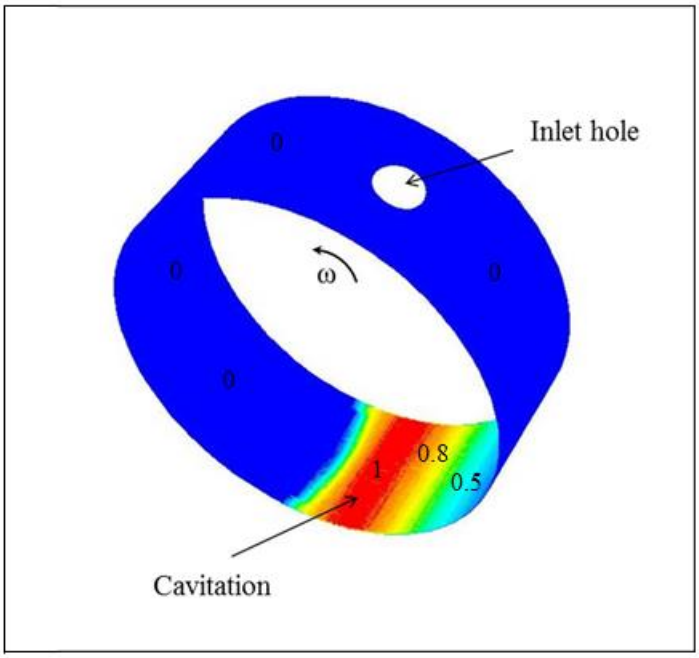

Figure 5.17: Contours of volume fraction at crank angle $\boldsymbol{\theta}$ =180° with all active cylinders

The pressure profile through the circumferential centre line of the isobaric plot of figure 5.16 is shown in figure 5.18, also including that for the big-end bearing of an active cylinder in a partially deactivated engine, as well as for a deactivated cylinder's connecting rod bearing. It can be seen that the lubricant film ruptures earlier in the case of an active cylinder in the partially deactivated engine, ahead of that for a normal engine operation which in turn ruptures ahead of the deactivated cylinder's bearing. This occurs because of progressively reduced applied bearing load at the same crankshaft speed, which is an expected outcome. The reverse trend is discernible for the lubricant film reformation boundary. Therefore, the extent of cavitation region alters in accord with the cylinder operating condition and has direct implications for bearing load carrying capacity, film thickness and frictional losses.

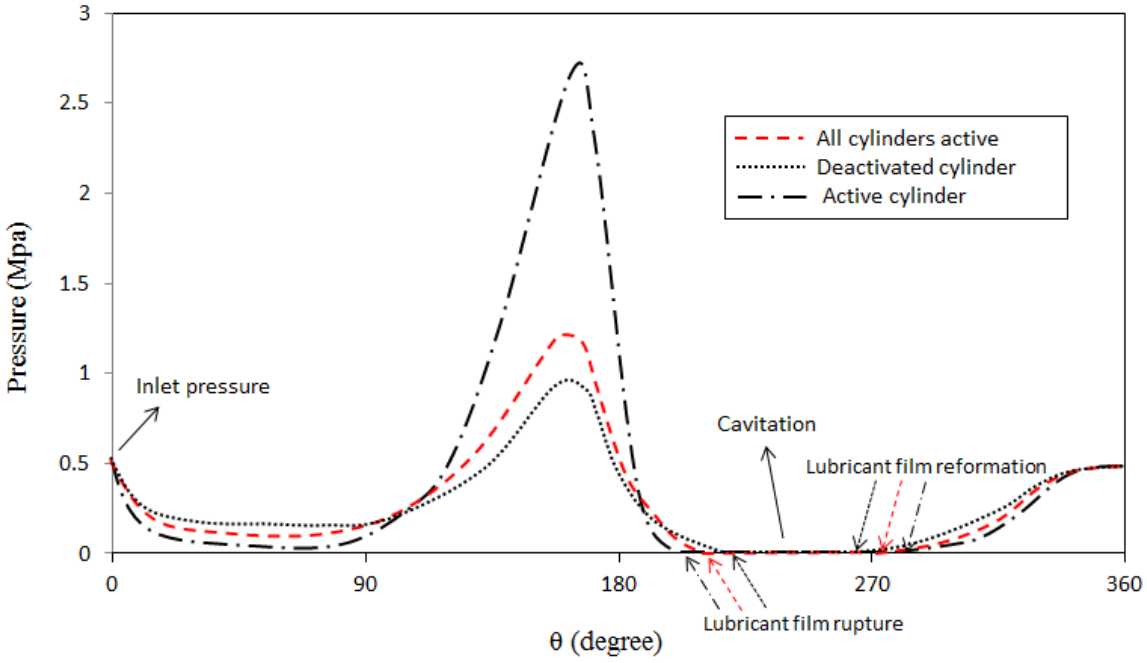

Figure 5.18: Pressure disttribution in the circumferential centre line of the bearing at crank angle of $\boldsymbol{\theta} = 180^{\circ}$ for various cylinder conditions

Figure 5.19 shows the minimum film thickness during 2 engine cycles under steady state operating condition for the big-end bearings under various cylinder conditions. In all the cases, the absolute minimum film thickness occurs a few degrees after the top dead centre position within the engine power stroke, where the maximum chamber pressures are encountered. The demarcation boundaries between the prevailing instantaneous regime of lubrication are indicated by the Stribeck's oil film parameter; $\lambda = \frac{h}{\sigma_{rms}}$, where h is the film thickness and σ_{rms} the root mean square roughness of the counterfaces (journal and the bearing bushing/shell). When, $1 < \lambda < 3$ a mixed regime of lubrication is encountered and $\lambda \leq 1$ indicates boundary regime of lubrication. Therefore, the inclusion of direct boundary interactions for determination of friction (as in Section 3.6) is essential in any analysis of engine big-end bearings. An important point to note is the incidence of boundary interactions in the in-take stroke as well as the power stroke of the engine cycle for the deactivated

cylinder because the valves remain closed and a residual bearing load is retained due to cylinder swept volume. This means that with CDA the big-end bearing contributes to boundary friction in parts of the engine cycle that is unexpected in the case of engine normal operation. This is because of the trapped air/charge volume with closed valves. This contributes to the overall frictional power loss of the engine operating under CDA as shown in figure 5.20.

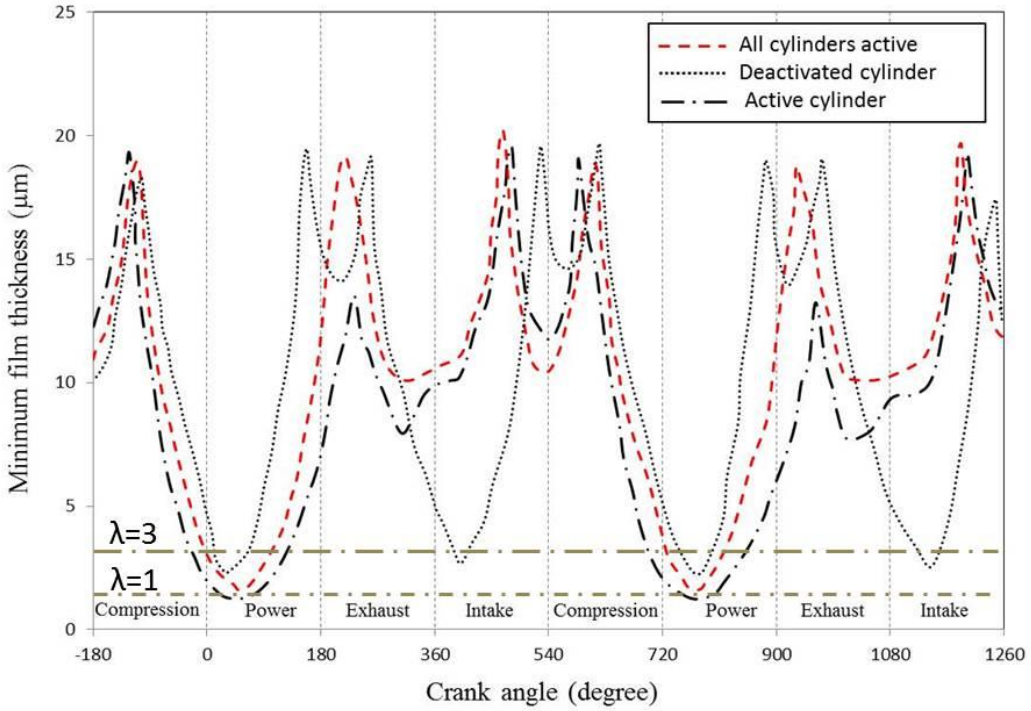

Figure 5.19: Minimum film thicknesses for various cylinder conditions

Figure 5.20 shows the frictional power loss in the deactivated cylinder's big-end bearing is in fact larger than that for an engine under normal operation mode in a typical engine cycle $0^{\circ} \leq \vartheta \leq 720^{\circ}$. The results also show that active cylinders operating at higher pressures under CDA apply higher loads, thus increasing their bearings' frictional power loss. Therefore, overall the bearing losses are increased under CDA, although this is more than offset by the efficiency gains through higher temperature combustion and reduced pumping losses accounting for 20% lower fuel consumption for the engine under consideration (a 4-cylinder 4-stroke c-segment vehicle). The

findings of the analysis agree with those of Mohammadpour et al [152] using mixed thermohydrodynamic analysis using Reynolds equation.

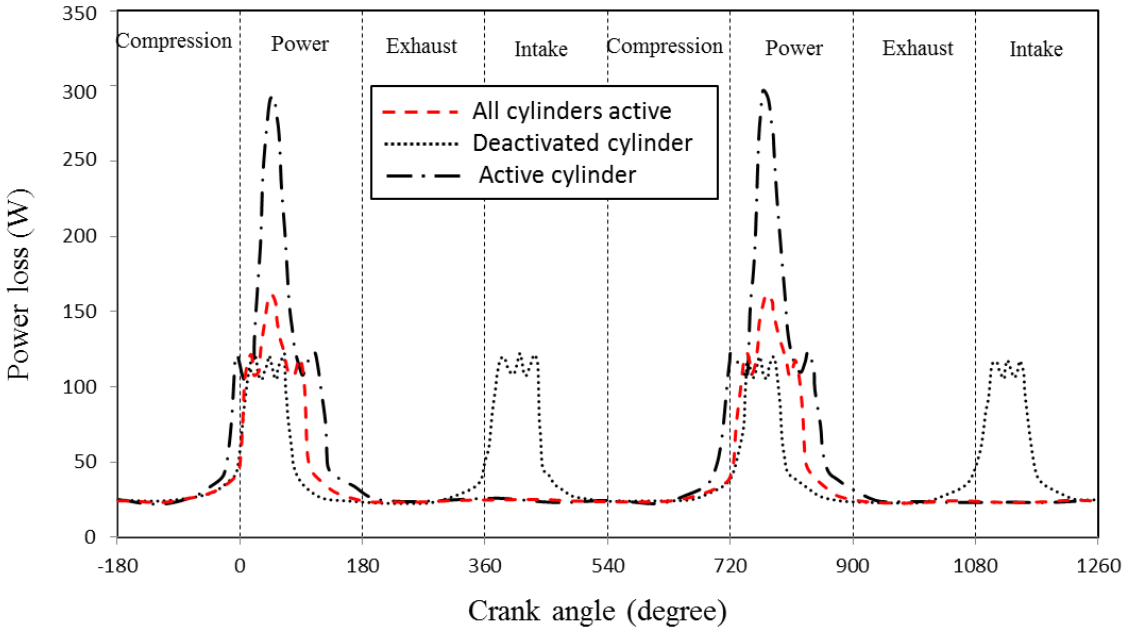

Figure 5.20: Frictional power loss for various cylinder conditions

5.8. Closure

This chapter has demonstrated the generic nature of the developed methodology in chapter 3 for the case of journal bearings, further for the demonstration of the same in chapter 4 for the case of piston compression ring-cylinder liner conjunction. Furthermore, in this case a full three dimensional contact analysis is carried out. Moreover, the resulting predictions are shown to conform well with the previously reported experimental work.

In both case studies in chapters 4 and 5, mixed regime of lubrication with instances of asperity interactions are shown to occur. These contribute disproportionately to the total generated friction. They can also lead to wear of surfaces. As the result a series of palliative measures have traditionally been applied. These include

introduction of a suitable additive package, including viscosity enhancers and friction modifying elements to the bulk base lubricant to increase load carrying capacity of thinner films and/or form thin low shear strength adsorbed layers to the contiguous surfaces to reduce friction and wear. Another additional approach has been the introduction of hard wear-resistant coatings of generally smoother surface topography or overlays in order to reduce the effect of wear.

One recent approach has been the introduction of surface textures in parts of contact which yield thin film thickness such as at the contact reversals in piston systems. Chapter 6 extends the work presented in this chapter to include the effect of surface texturing.

Chapter 6: Role of Surface Texturing Upon Tribological Performance and Cavitation

6.1. Introduction

Surface texturing is as an option to mitigate against the effect of generated boundary friction as the result of asperity interactions. Such conditions occur in the region of thin films. It has been shown that under such conditions retention of a reservoir of lubricant in surface textured features can aid lubrication and enhance the hydrodynamic load carrying capacity, thus reducing and frictional losses. Some of the features used include dimples which may reduce friction not only by acting as a lubricant reservoir [164] but also by providing hydrodynamic lift (pressure perturbations) themselves, a mechanism referred to as micro-hydrodynamics. Dimples can also be as a micro-trap for wear debris in lubricated sliding [165].

Surface texturing was successfully applied to mechanical seals resulting in an increase in seal life [166]. Partial laser surface texturing substantially increased the load carrying capacity of hydrodynamic thrust bearings [167].

The benefits of implementing laser surface texturing to piston ring surfaces were substantiated theoretically and experimentally in Ronen et al. [168] and Ryk et al. [169] works. They showed about 30% reduction of friction force by ring surface texturing in comparison to a plain ring surface.

The oil existence could improve the fretting wear resistance [170] and almost doubled the fretting fatigue life [171]; however, textured surfaces also provide traps for wear debris in the contacts subjected to fretting.

6.2. Experiment

6.2.1. Rig set up

The experimental rig shown in figure 6.1 comprises a rotating journal which is partially submerged in a reservoir of lubricant (sump). The journal is driven by an electric motor and power pack, which allows for the speed to be varied between 0 – 250 rpm. A 180° acrylic bearing pad (bushing arc) conforms closely to the journal, forming a partial pad journal bearing arrangement. Weights are hung from the bearing pad to load the conjunction. A pointer is attached to the centre of the pad arc so that the attitude angle can be directly measured.

The attitude angle is between the line of journal and the bearing pad centres and the applied vertical load. This is a direct measure of generated friction torque. The angle is read from a finely graduated scale hung behind the test rig. Therefore, the attitude angle is used to infer journal eccentricity and generated friction. The properties of the lubricant selected for the experiment are detailed in Table 6.1.

Table 6.1: Lubricant data

Density at 15 ºC kg/m3	894
Viscosity at 22 ºC mm2/s	512
Viscosity at 40 ºC mm2/s	139
Viscosity at 100 ºC mm2/s	14.3
Viscosity index	99

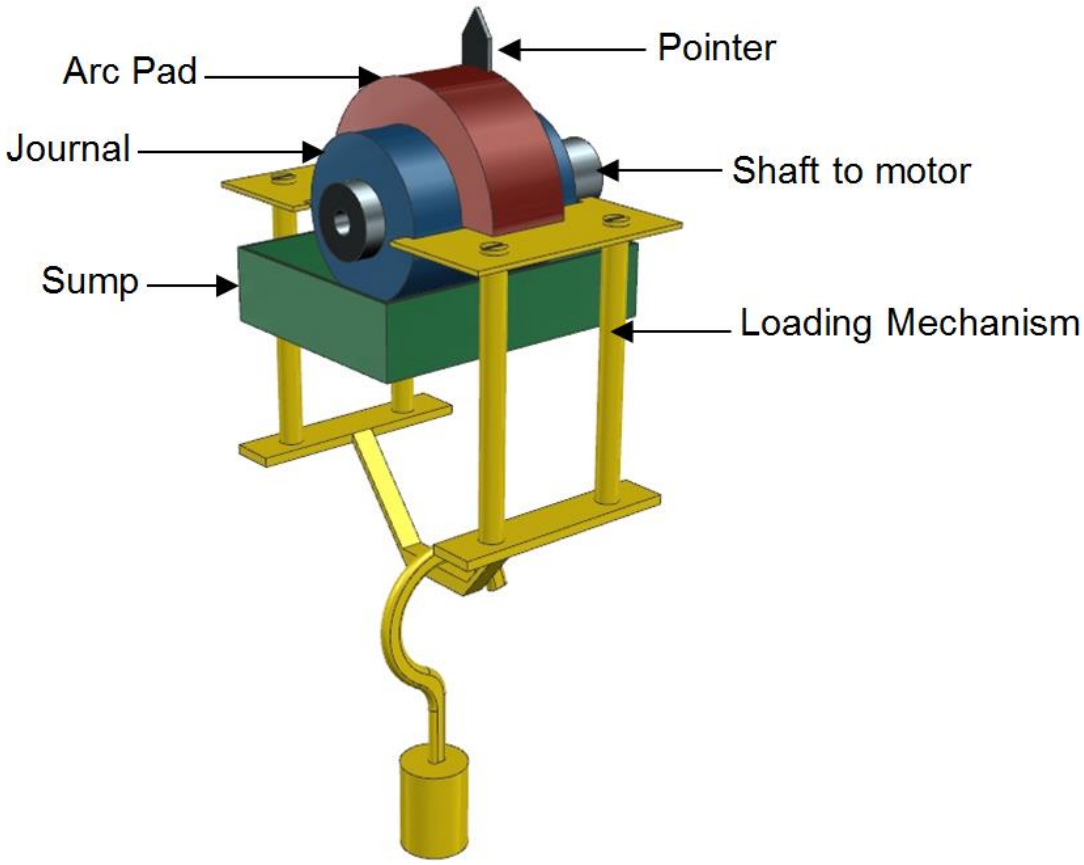

Figure 6.1: A schematic of the experimental rig (not to scale)

The topography of the journal surface was measured using an infinite focus white light interferometer. The topography of the pad had to be measured using a stylus due to its translucence. A stylus had a conical angle and a tip radius of 2 μm. The geometrical form of the journal and the pad used were measured using a Coordinate Measurement Machine (CMM) with the repeatability of 1 μm. These are shown in Figure 6.2. The dimensions, circularity and surface roughness measurements of the journal and pad are provided in Table 6.2.

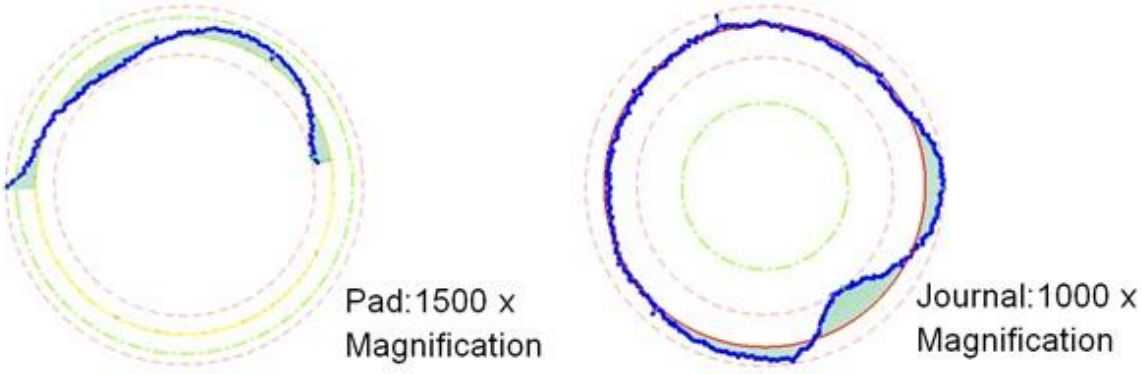

Figure 6.2: Surface form measurement with Coordinate measurement machine

Table 6.2: Test rig data

Journal Diameter	65.6961	mm
Journal Circularity	13.7	μm
Journal Roughness (Ra, Rq)	0.035,0.044	μm
Pad diameter	65.8576	mm
Pad Circularity	7.5	μm
Pad Roughness (Ra, Rq)	0.378,0.526	μm

6.2.2. Surface texturing

Two alternative journals were used. One was plain, whilst the other was textured with indented features (figure 6.3). A survey of similar previous work was undertaken to draw on the experiences reported with regard to density distribution, depth and diameter of indentations [172-174].

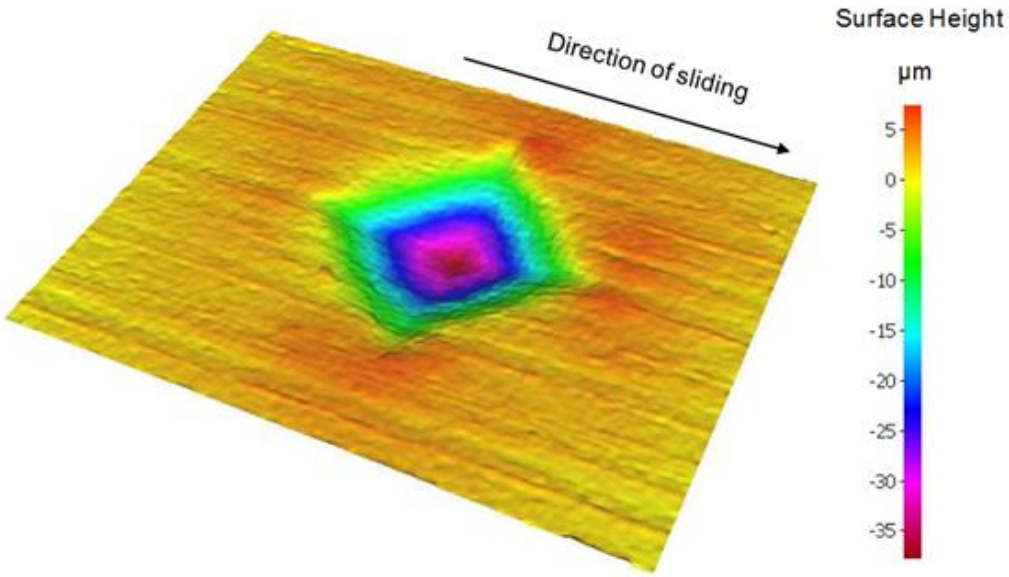

Figure 6.3: Infinite focus Microscope measurement image of an individual surface texture feature

The chosen values for the surface textures are shown in Table 6.3. The values chosen represent a compromise between the convenient production of surface texture features using readily available techniques and those suggested in open literature. A Vicker's indenter was used to produce the surface texture features to ensure good repeatability for indentation depth. A mesh of indented textures was fabricated on the journal surface (Table 6.3).

Table 6.3: Surface texture details

Centre to centre distance of textures	45	mm
Length x width	0.26×0.26	mm
Depth	40 µm	μm
Distribution pattern	Standard grid	-

6.2.3. Experimental procedure

A repeatable test procedure was carried out to determine the effect of surface texture features upon the tribological performance of the partial pad journal bearing. The test rig was run at a set load for a range of discrete speeds, between 36 – 180 rpm. The rotational speed of the journal was measured using a digital tachometer. The low speed of revolution results in an insufficient lubricant entrainment into the contact conjunction, thus promoting a mixed regime of lubrication. Under such conditions the use of a textured journal is expected to palliate generated friction.

A steady speed was maintained for a set period prior for each measurement. This was carried out in order to avoid the complications arising from an initial squeeze film effect. After four measurements were taken at each speed, the load was altered and the same range of speed tests was undertaken. A short break was made between each test and the preceding one, in order to ensure that the temperature of the lubricant sump was maintained at the recorded ambient temperature. The bath of lubricant was maintained at the constant level of 20 mm depth so that there would be a sufficient volume of lubricant to entrain into the contact for an ideal fully flooded inlet.

At the beginning of each test, the bearing pad and the journal were separated and cleaned thoroughly so that any debris produced by a previous test would be removed. After subsequent re-assembly, the rig was recalibrated and a weight was hung from the pad ensuring orthogonal loading condition.

The attitude angle was measured using the pointer and graduated scale. As the attitude angle varied slightly at a set load and speed, the average value of measured attitude angle is plotted under each test condition.

6.2.4. Experimental results

The experimental results for the plain journal for a combination of applied load and speeds are shown in figure 6.4. The results show that as the load decreases the attitude angle increases as the ratio between friction and applied load alters. Notably, with lower applied load the gradient of the line is more severe indicating increased friction. It is noteworthy that under boundary regimes of lubrication the generated friction has a weak dependence on the sliding speed, whereas viscous friction is dependent on the service parameter $\eta_0 \Delta U/h$. Therefore, the results indicate that the test rig runs under varying degrees of mixed lubrication.

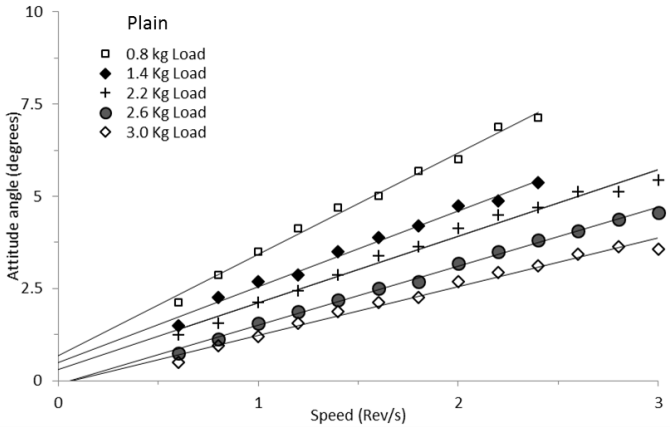

Figure 6.4: Variation of measured attitude angle with journal rotational speed for the case of plain journal surface

The results shown in figure 6.5 compare the performance with textured and plain journals at different applied loads and journal speeds. At a load of 0.8 Kg (figure 6.5a) the boundary interactions are least for all the tests carried out. Under this condition, there is little difference between the attitude angles for the two cases (textured and plain journals). As the load is increased in figures 6.5b and 6.5c, the beneficial effect of surface textures become evident on the account of a reducing attitude angle at the higher end of the speed range. At low speed conditions the

texture and plain cases have very similar attitude angles indicating that the textures have little benefit under these conditions. This is because at the very low sliding speeds the contact is particularly starved of lubricant. The results in figure 6.5d and figure 6.5e show the two clearest examples of benefits of surface texturing with significant reductions in the recorded attitude angles. It should also be noted that the changes in attitude angle observed in the results can only be due to the effect of friction. It will be later shown that (see Figure 6.8) the texturing does not alter the asymmetric distribution of the pressure in the studied journal bearing; hence the variations in the attitude angle cannot be described base don't he alteration in the pressure distribution or shift in the locus of the maximum pressure point.

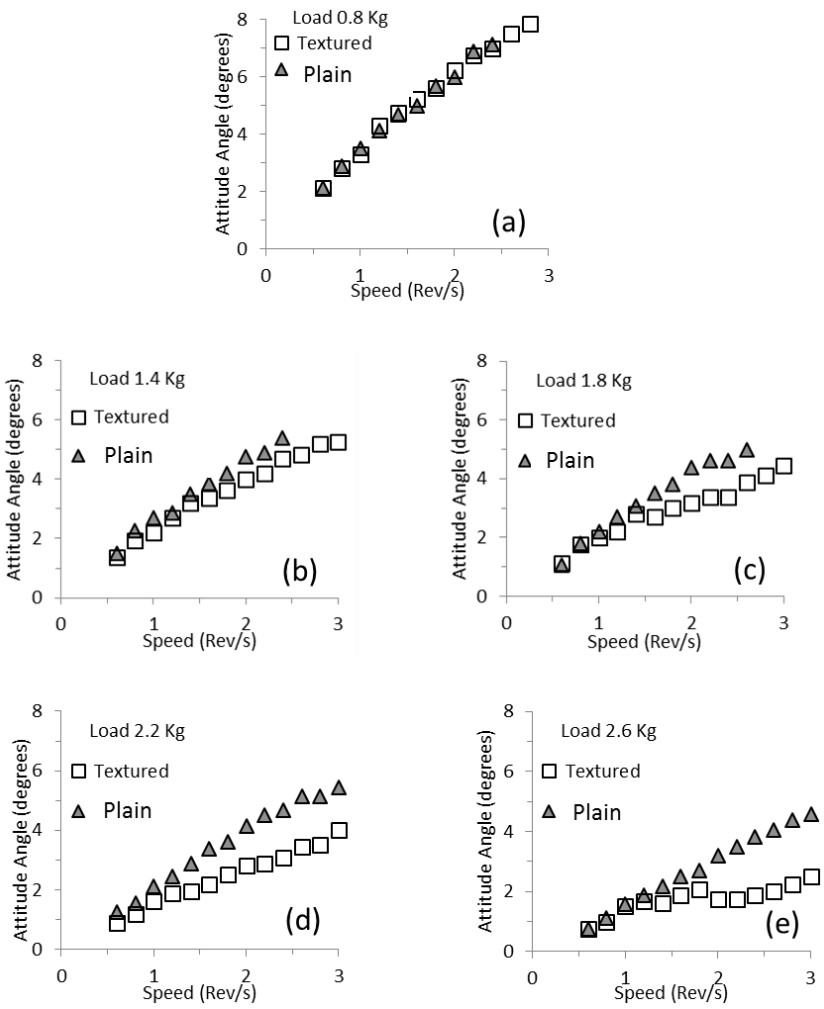

Figure 6.5: Comparison of Attitude angle with changing speed for a textured and plain journal

The experimental results indicate that the introduced surface textures are beneficial under certain conditions. When the applied load is quite low, there is little difference between the textured and plain cases. When comparatively moderate loads are applied, the surface textures produce a beneficial effect. At higher loads and medium to low speeds however little advantage is accrued by the textured bearing.

The benefit produced by the surface textures appears to be closely linked to the prevalent regime of lubrication. All the experiments run in the mixed regime of lubrication. However, the extent of asperity interactions changes with different conditions. Therefore, a numerical analysis of the experimental case is required to understand the salient phenomena underlying the role of surface textures.

6.3. Boundary Conditions and Numerical Solution Procedure

The system of Eqs. (3.1), (3.2) and (3.24) is solved through finite volume method. For this purpose a model geometry was constructed using ANSYS design modeller which was subsequently spatially discretised (meshed) by taking advantage of ANSYS meshing application. Tetrahedral size-controlled elements were used. The entire flow domain was then meshed using approximately one million tetrahedral cells. The isothermal and pressure-based mixture model [105] is chosen for the present analysis. The velocity–pressure coupling is treated using the Semi-Implicit Method for Pressure Linked Equations (SIMPLE) algorithm and the second-order upwind scheme is used for the momentum to reduce the discretisation-induced errors in the calculations. As the load is assumed to be constant, the eccentricity ratio depends on the pressure equilibrium over the journal surface. To compute eccentricity, the dynamic mesh method was used [175], but it may be simpler and faster to compute the friction map over the journal surface for various eccentricities.

Atmospheric pressure of 101.3 kPa is assumed for the cavitation (vaporisation) pressure. Since the occurrence of cavitation in the current analysis is treated through

solution of transport equation for the vapour mass fraction alongside the general Navier-Stokes equations, there is no need to impose any particular boundary conditions for either lubricant film rupture or reformation. This is a significant fundamental improvement upon the imposed assumptions such as those of JFO [13, 14] or the Elrod's cavitation algorithm [15].

The solid boundaries were considered to be impermeable and the lubricant/solid interface is assumed to follow no-slip condition. The bearing pad is modelled as a stationary wall, whilst the journal is modelled as a moving body with an absolute rotational velocity. At the inlet and outlet, the pressure is set to ambient pressure. Finally, at the bearing's axial extremities the lubricant is assumed to leak to the ambient (atmospheric) pressure.

6.4. Results and Discussion

6.4.1. Model Validation

Figures 6.6 and 6.7 show the predicted attitude angle for textured and plain journal surface as well as those measured under the same conditions and for 2 different applied loads. Note that an attitude angle of zero denotes static journal condition subjected to a normal vertical applied load. In all cases the attitude angle is quite small, indicating high eccentricity ratio, usually corresponding to mixed or boundary regimes of lubrication. This is due to the intentional low journal speed to promote such conditions, where surface texturing is likely to improve lubricant retention and mitigate undue boundary interactions. Good agreement is noted between the predictions and the measured conditions. The numerical results show consistently lower attitude angle for the textured journal, indicating lower contributions due to asperity interactions. The experimental results show the same trend with an increased applied load.

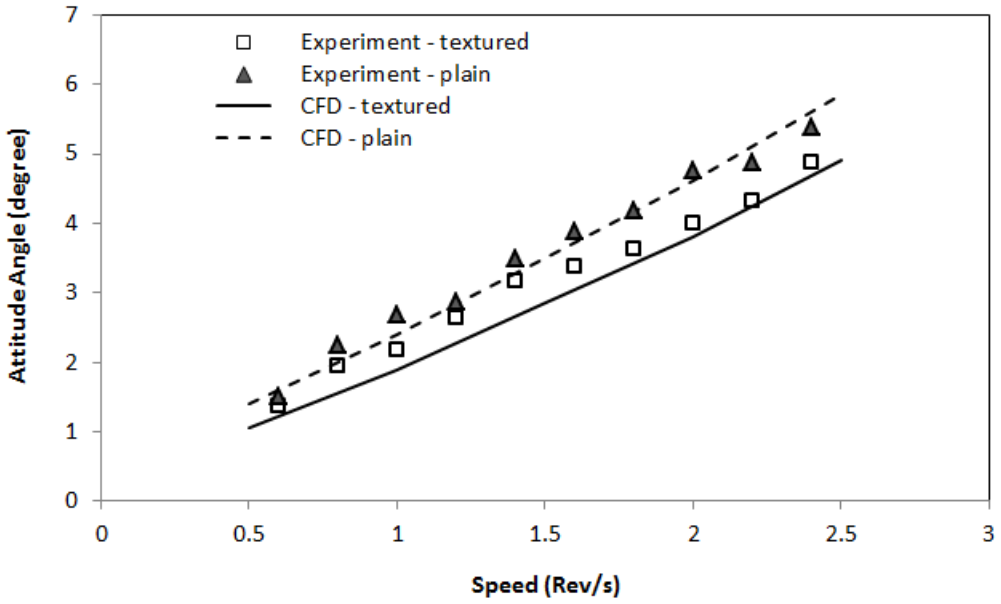

Figure 6.6: Changes of attitude angle over a range of speeds Contours of pressure distribution for 1.4 kg load condition (CFD and experimental results)

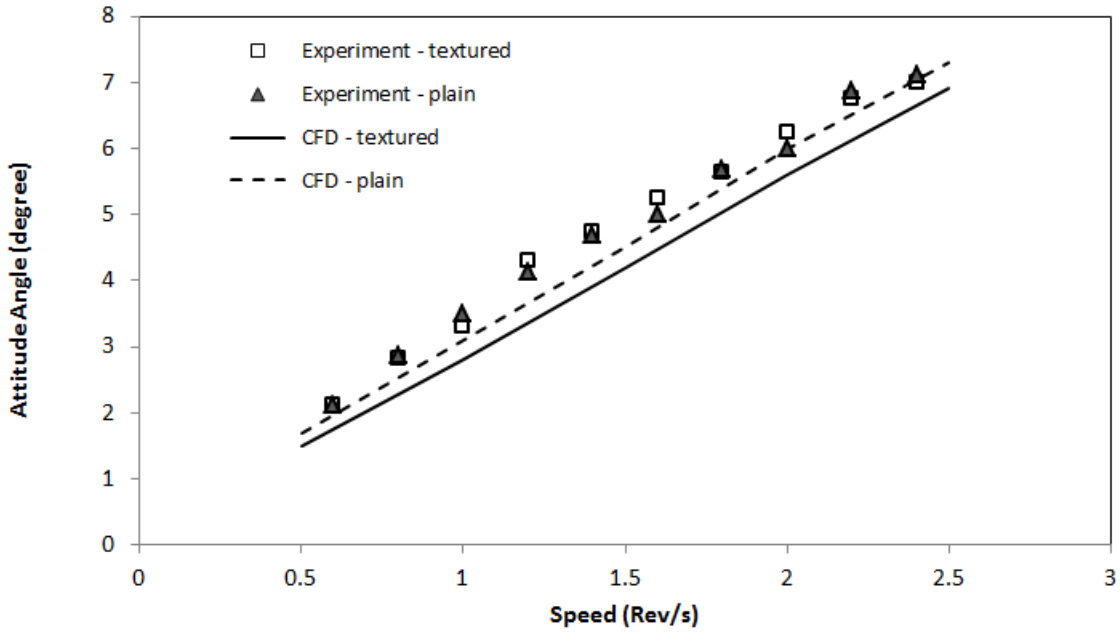

Figure 6.7: Changes of attitude angle over a range of speeds Contours of pressure distribution for 0.8 kg load condition (CFD and experimental results)

6.4.2. Pressure distribution

With the validated numerical predictions, it is instructive to seek the underlying mechanism for the improved performance of the textured relative to the plain case. Figure 6.8 shows the central line of the generated hydrodynamic contact pressure distributions for the textured and plain cases. These are coincident as would be expected; with pressures generated in the first part of the arc of contact ($0 < \theta \leq \theta_c$, where θ_c is the lubricant film rupture point), followed by cavitation thereafter. There are pressure perturbations at the positions of the indented surface textures as indicated on the figure. Morris et al [176] noted the same for the case of a thin strip with a contacting face of a typical piston compression ring traversing a series of laser textured chevrons on a flat plate. They showed that the textured features retained a volume of lubricant which caused pressure perturbation due to the micro-hydrodynamic effect, enhancing the load carrying capacity of the contact, thus reducing the measured friction. The results here indicate that the same phenomenon may be responsible for improved conditions in the case of the textured journal.

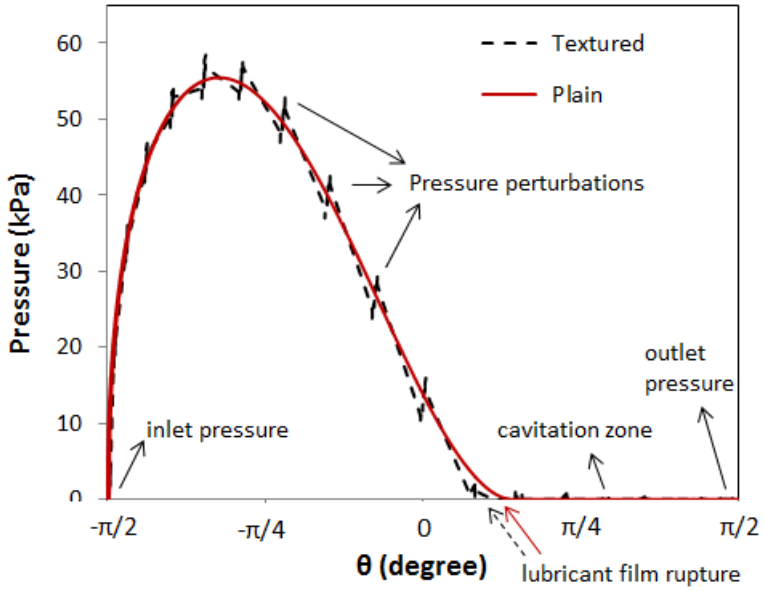

Figure 6.8: Pressure distribution in the centre plane for 1.4 kg load condition

6.4.3. Vapour volume fraction

Figures 6.9 (A) and (B) show contours of predicted vapour volume fraction for the cases of the textured and plain journals respectively. It can be observed that the lubricant film rupture boundary is shifted further towards the contact outlet. Therefore, a larger area of full film results in the case of the textured journal. Furthermore, a smaller overall cavitation region emerges. Also, in the case of the textured journal, the cavitation region enjoys a higher lubricant film content, thus contributing to the load carrying capacity of the contact.

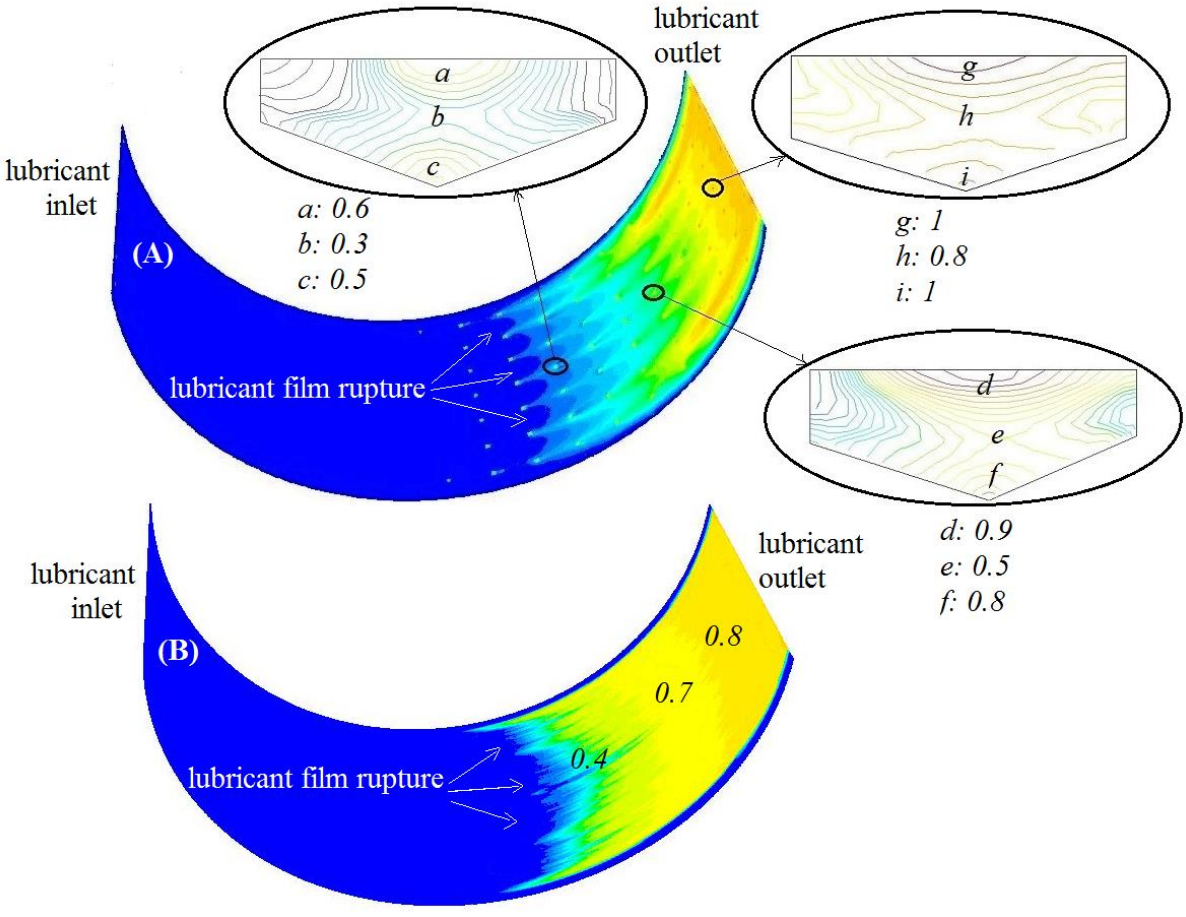

Figure 6.9: Contours of vapour volume fraction for (A) textured and (B) plain journal bearing

The insets to the figure 6.9(A) provide more instructive information about the role of introduced indentation upon multi-phase flow through the cavitation region. It is clear that within each texture feature multi-phase flow occurs. At the lubricant film rupture boundary the liberated vapour from the lubricant resides on top of the lubricant-vapour mix filling the indented feature. With increasing overall cavitation in the diverging contact wedge, only a small proportion of liquid lubricant fills the textured features. Clearly, in the region between the fully flooded inlet and the lubricant rupture boundary the indented features are filled with the single phase lubricant flow, with pressure perturbations shown in figure 6.8.

It is clear that texture form and distribution would affect the flow dynamics through the contact conjunction. In the case studied here the conditions investigated correspond to low speed of entraining motion of the lubricant into the contact to promote mixed regime of lubrication. It is clear that for fully hydrodynamic regime of lubrication the texture features would contribute marginally. Indeed the complex flow dynamics in the textured features demonstrate some swirl flow as well as onset of reverse flow conditions, which may contribute to increased viscous friction. Furthermore, very little side leakage occurs under test conditions investigated. With higher journal speeds the enhanced lubrication due to texturing may lead to increased oil loss.

Chapter 7: Conclusions and Suggestions for Future Work

7.1. Conclusions

The following represent the major conclusions and findings of the research presented in this thesis:

1. For realistic predictions, it is necessary to include salient features of physical phenomena in tribological conjunctions. These should include the underlying assumptions of the governing equations. One such case is the use of appropriate flow equation. Reynolds equation is based on single phase flow through the conjunction. Furthermore, it is assumed that there is no pressure gradient through the lubricant film due to its thinness. With full Navier-Stokes equations such an assumption is not made. Also, multi-phase flow dynamics can be considered. This is the approach used in this thesis, which shows that in fact, lubricant flows like a series of streamers with different viscosity due to pressure variation across the lubricant film, as well as temperature. For the latter, the energy equation is solved simultaneously with the Navier-Stokes equations.

2. Another issue is the treatment of cavitation within the conjunction. Although various exit boundary conditions have been reported in literature, such as Elrod's cavitation algorithm [15], and JFO boundary conditions [13, 14], these do not completely satisfy the continuity of mass flow within the cavitation zone. For example, with Elrod modification of Reynolds equation, the flow in the cavitation zone assumes a balance between Couette flow and squeeze film motion. In reality, liberated vapour should also be taken into account in this zone, or indeed elsewhere where voids/bubbles may be formed.

Therefore, it is essential to include Rayleigh-Plesset model [11] to predict onset of vaporisation as well as including vapour transport equation. For the case of the former, it is important to modify the conditions to restrict the growth of cavities within a conjunction of finite dimensions. The overall approach is in fact one of the main contributions of this thesis to knowledge. It is shown that regions of cavities emerge within the contact domain, particularly after film rupture.

3. The use of realistic boundary conditions is essential for numerical predictions of phenomena. In particular, assumption of fully flooded or drowned inlet is very idealised and in fact hardly noted in practice. With the CFD approach flow dynamics at the converging wedge is studied in this thesis and compared with potential flow analysis carried out by Tipei [137] and observed in the case of rolling contacts by Birkhoff and Hays [140]. Swirl and reversing flows give way to a stagnation boundary which agrees well with these published works. The cases studied here agree with the assertions of Tipei that such recirculating and backward flows require the use of Swift-Stieber inlet boundary, which is not often appreciated. The same issue is also important in the case of lubricant film rupture and separation boundary. This boundary is as the result of viscous shear of the lubricant, generated heat, pressure variation in a diverging wedge and retarding friction. The combined solution of Navier-Stokes, energy, vapour transport and modified Rayleigh-Plesset equations show that the exit boundary actually conforms to the Prandtl-Hopkins zero reverse flow conditions for the cases studied in this thesis.

7.2. Achievement of Research Objectives

The specific objectives of the current study, as stated in Chapter 1, have all been achieved.

- Developing a CFD model to predict mixed hydrodynamics of the compression ring as well as journal bearings

Chapter 3 provided the methodology developed in this thesis. The methodology comprises finite volume solution of Navier-Stokes equations, together with the energy equation, the modified Rayleigh-Plesset equation and vapour transport equation. The methodology is applied to the top compression ring of IC engine as well as the big-end bearings, thus meeting the following set of objectives as well:

- Predict film thickness, generated pressures and friction
- Determine the global cavitation flow of the compression ring and journal bearing
- Verification of all numerical and analytical methods with reported experimental tests, including with IC engine data.

Validation of the compression ring-liner model is carried out against direct the measured results of Furuhama and sasaki [132] as well as Gore et al [134]. Very good agreement was found in both cases.

Having applied the developed generic formulation and applied the same to piston compression ring-liner contact and the big-end bearing, it was essential to ascertain the applicability of the approach to the stated problems. This was carried out with a set of well-defined experimental verifications. Some comparative work was carried out against previously reported experimentation by Dowson et al [56] (Chapter 5). Further verification was also carried out against a specially developed partial tilting pad journal bearing rig with various surface topographies as described in chapter 6, including the effect of texturing on the journal surface. Furthermore, application of methodology was made to assess real engine conditions, particularly with the current interest in cylinder deactivation, as set out in the following research objective:

- Applying the developed methods to real engine applications with modern emerging technologies such as cylinder deactivation as well as use of surface engineered textures to encourage micro-hydrodynamics through pressure perturbation.

Therefore, all the initial research objectives have been met.

7.3. Contributions to Knowledge

This thesis has presented some key contributions to knowledge. These are:

1. A combined solution of Navier-Stokes, energy, modified Rayleigh-Plesset and vapour transport equations is made with no artificially imposed cavitation boundary conditions. In addition, a control volume analytical thermal mixing model is used to determine flash temperature of the boundary solids as boundary conditions. This approach has not hitherto been reported in literature.

2. The methodology has been validated with experimental work using floating liners for direct in situ measurement of friction, an approach which is rarely reported in the case of ring-bore contact. Extensive validation is carried out in the case of journal bearing analysis, including for textured journals.

3. The validated methodology has been applied to ring geometry for improved efficiency. Therefore, already useful outcomes from the predictive methods have emerged.

7.4. Critical Assessment of Approach and Suggestions for Future Work

In this study the vaporisation pressure is assumed to be constant. However, in reality the vaporisation pressure is a function of temperature [177]. Therefore, at various operating conditions, the assumed vaporisation temperature at ambient conditions needs to be altered. This constitutes a change which can be implemented in future work.

According to Jakobsson [178] the experiments by Floberg have shown that the tensile strength in the liquids can have an important effect on the growth and collapse of cavitation bubbles. However, in this thesis the effect of the tensile strength on the variation in the bubble size is not explored. It is assumed that the pressure inside the bubble remains at the vaporisation pressure of the lubricant at the ambient temperature.

The appearance of finger-shaped bubbles has also been speculated to be related to the various forms of fluid flow instability similar to those observed in the case of Rayleigh-Taylor type instabilities [179]. Whilst Rayleigh-Taylor type instabilities occur at the interfaces of two fluids due their density differential, it is also known that the shear differences in a continuous fluid or the velocity difference across an interface of two fluids can also introduce instabilities in a flow. These are known as Kelvin-Helmholtz type instabilities. Since there are at least two phases in the cases studied in the current work, it is highly likely that the instabilities caused by the velocity or shear difference between the two phases can induce instabilities which would produce finger-shaped cavity patterns. To observe such a phenomenon one needs to perform a complete 3D simulation of the contact with a very fine mesh. This necessitates inclusion of side leakage flow direction in the analysis. As the result of relatively large number of mesh points that would be required the computational effort would be significant. This approach was deemed not essential and beyond the

scope of this thesis. It is, therefore, suggested that flow instability issues as well as sub-ambient pressures and tensile strength of formed bubble boundaries should be included in future research.

In addition to the understanding of fundamentals of cavitation and its tribological effects such as on load carrying capacity and friction, some of the consequences the phenomenon are of practical importance. Most importantly, is the collapse of cavitation bubbles and the ensuing erosion of adjacent boundary solid surfaces. This issue is particularly important in the case of journal bearings. Although some volume of research work already exists in this regard [91, 180], further investigation of this phenomenon would be of practical use.

Finally, the collapse of cavities can also result in vibration and noise due to localised pressure perturbations. This would also be an important field of investigation for future research.

References

[1] Richardson, D.E., Review of power cylinder friction for diesel engines, Journal of Engineering for Gas Turbines and Power, Transactions of the ASME, 122, 2000, pp. 506-519.

[2] Reynolds, O., On the theory of lubrication and its application to Beauchamp Tower's experiments, including an experimental determination of the viscosity of olive oil, Phi. Trans. R. Soc. London Ser. A 177, 1886, pp. 157-233.

[3] Elrod, H. G. and Adams, M. L., "A Computer Program for Cavitation and Starvation Problems," Cavitation and Related Phenomena in Lubrication, Mechanical Engineering Publications, New York, pp 37-41, 1967.

[4] Andrés, L. S., LIQUID CAVITATION IN FLUID FILM BEARINGS, *Note 6, 2009*

[5] Knapp R T, Daily J W, Hammitt F G. Cavitation. McGraw-Hill, New York, 1970.

[6] Delannoy Y, Kueny J L. Two Phase Flow Approach in Unsteady Cavitation Modelling. Cavitation and Multiphase Flow Forum, ASME-FED 98, 1990, pp. 153–158.

[7] Chen Y, Heister S D. A Numerical Treatment for Attached Cavitation. J. Fluid Eng-T.ASME, 116, 1994, pp. 613-618.

[8] Kubota A, Kato H, Yamaguchi H. A new modeling of cavitating flows: a numerical study of unsteady cavitation on a hydrofoil section. J. Fluid Mech., 240, 1992, pp. 59–96.

[9] Merkle C L, Feng J Z, Buelow P E O. Computational modeling of the dynamics of sheet cavitation. Proc. Third International. Symposium. on Cavitation, Grenoble, France, 1998.

[10] Kunz R F, Boger D A, Stinebring D R, et al. A preconditioned Navier-Stokes method for two-phase flows with application to cavitation prediction. Computer and Fluids, ,29, 2000, pp. 849.

[11] Singhal A K, Li N H, Athavale M, et al. Mathematical basis and validation of the full cavitation model. ASME Fluids Engineering Division Summer Meeting, ASME Paper FEDSM2001-18015, 2001.

[12] Senocak I, Shyy W. Numerical Simulation of Turbulent Flows with Sheet Cavitation. CAV2001 4th International Symposium on Cavitation, Paper No. CAV2001A7.002, 2001.

[13] Jacobson, B. and Floberg, L., "The Finite Journal Bearing Considering Vaporization," Trans. of Chalmers University of Tech., Gothenburg. Sweden, 1957.

[14] Olsson. K. O., "Cavitation in Dynamically Loaded Bearings," Trans. Trans. of Chalmers University of Tech., Gothenburg. Sweden, 1965.

[15] Elrod, H. G., "A Cavitation Algorithm", ASME J. of Lub. Tech., 103, 1981, pp. 350-354.

[16] Hill, S.B. and Newman, B.A., Piston Ring Design for Reduced Friction, SAE Paper 841222, 1984

[17] Jeng, Y., "Friction and Lubrication Analysis of a Piston Ring Pack", SAE Paper 920492, 1992

[18] Nakada, M., Piston and Piston Ring Tribology and Fuel Economy, Proceedings of International Tribology Conference, Yokohama, 1995

[19] Cullen, J. A. and Frodsham, G. M., Reduced Cross Section Compression Rings for Diesel Engines, SAE Paper 971146, 1997

[20] Richardson, D. E. Comparison of measured and theoretical inter-ring gas pressure on a diesel engine. Society of Automotive Engineers, Inc., SAE Technical Papers Series 961909. Pp. 7–20, 1996.

[21] Tomanik, E., Nigro, E., Zabeu, C.B. and Peixoto, V.J.M., Reduced Friction Power Cell Components, SAE Paper 2000-01-3321, 2000

[22] Ma, M. T., Smith, E. H., and Sherrington, I., "A Three-dimensional Analysis of Piston Ring Lubrication, Part I: Modelling," in Proc. of the Inst. of Mech. Eng., Purr J, 209, 1995, pp 1-14.

[23] Ma, M. T., Sherrington, I. and Smith, E. H., "Implementation of an Algorithm to Model the Starved Lubrication of a Piston Ring a Distorted Bores: Prediction of Oil Row and Onset of Gas Blow-by," in Proc. of the Inst. of Mech. Eng., Part J, 210, 1996, pp. 29-44.

[24] Ma, M. T., Sherrington, I. and Smith, E. H., "Analysis of Lubrication and Friction for a Complete Piston-Ring Pack with an Improved Oil Availability Model, Pan I: Circumferentially Uniform Film," in Proc. of the Inst. of Mech. Eng., Part J, 211, 997, pp. 1-15.

[25] Castleman, R. A., "A Hydrodynamic Theory of Piston Ring Lubrication," Physics, 7.9, 1936, pp 364-367.

[26] Eilon, S. and Saunders, 0. A., "A Study of Piston Ring Lubrication." in Proc. of the Inst. of Mech. Eng., 171, 1957, pp 427-433.

[27] Ting. L. L., "Piston Ring Lubrication and Cylinder Bore Wear Analysis, Part I - Theory", ASME Jour. of Lub. Tech., 96, 1974, pp. 305-314.

[28] Rohde, S.M., "A Mixed Friction Model for Dynamically Loaded Contacts with Application to Piston Ring Lubrication", Friction and Traction: Proc. of 7th 1eeds-Lyon Symp. Trib., Butterworth, Guilford, England, p 262, 1980.

[29] Miltsios. C. K . , Patterson, D. J. and Paranastasiou, T. C., "Solution of the Lubrication Problem and Calculation of the Friction Force on the Piston Ring, "ASME Jour: of Trib., 111, 1989, pp 635-642.

[30] Dowson, D., Economou, P. N.. Ruddy, B. L., Strachan, P. J., and Baker. A. J. S., "Piston Ring Lubrication-Part II, Theoretical Analysis of a Single Ring and a Complete Ring Pack," Energy Conservation Through Fluid. Film Lubrication Technology: Frontiers in Research and Design, ASME Press, New York, pp 23-52, 1978.

[31] Swift, H. W., "The stability of lubritationg films in journal bearings", Proc. Inst. Civil Eng., 233, 1932, 267-288

[32] Stieber, W., "Das schwimmlager: Hydrodynamische Theorie", des Gleitlagres, no. V.D.I., Berlin, p. 106, 1933

[33] Jeng, Y., "Theoretical Analysis of Piston Ring Lubrication-Part I: Fully Flooded Lubrication", Trib. Trans., 35, 1992a, pp. 696-706.

[34] Jeng, Y., "Theoretical Analysis of Piston Ring Lubrication-Part II: Starved Lubrication and Its Application to a Complete Ring Pack," Trib. Trans., 35, 1992b, pp. 707-714.

[35] Yalng. Q., and Keith. T. G., "An Elastohydrodynamic Cavitation Algorithm for Piston King Lubrication", Trib. Trans., 38, 1995, pp. 97-107.

[36] Yang, Q. and Keith. T. G., "Two-Dimensional Piston Ring Lubrication-Part I: Rigid Ring and Liner Solution". Trib. Trans., 39, 1996, pp. 757-768.

[37] Radakovic. D. J., and Khonsari. M. M., "Heat Transfer in a Thin-Film Flow in the Presence of Squeeze and Shear Thinning: Application to Piston Rings", ASME Jour. of Heat Transfer. 119, 1997, pp. 249-257.

[38] Gulwadi, S. D., "A Mixed Lubrication and Oil Transport Model for Piston Rings Using a Mass-Conserving Algorithm," ASME J. of Eng. for Gas Turbines and Power, 120, 1998, pp. 199-208.

[39] Morris, N., Rahmani, R., Rahnejat, H., King, P.D. and Fitzsimons, B., "The influence of piston ring geometry and topography on friction", Proc. IMechE, Part J: J. Engng. trib., 2012, DOI: 10.1177/1350650112463534

[40] Rahmani R., Theodossiades S., Rahnejat, H. and Fitzsimons B., "Transient elastohydrodynamic lubrication of rough new or worn piston compression ring conjunction with an out-of-round cylinder bore", Proc. IMechE, Part J: J. Engng. trib., 226(4), 2012, pp. 284-305.

[41] Akalin O. and Newaz G.M., "Piston ring-cylinder bore friction modeling in mixed lubrication regime: Part II-Correlation with bench test data", Trans. ASME, J. Trib., 123(1), 2001, pp. 219-223.

[42] Mishra P.C., Balakrishnan S. and Rahnejat H., "Tribology of compression ring-to-cylinder contact at reversal", Proc. IMechE, Part J: J. Engng. Trib, 222(7), 2008, pp. 815-826.

[43] Mishra P.C., Rahnejat H. and King P.D., "Tribology of the ring-bore conjunction subject to a mixed regime of lubrication", Proc. IMechE, Part C: J. Mech. Engng. Sci., 223(4), 2009, pp. 987-998.

[44] Bolander N.W. Steenwyk, B.D., Sadeghi F. and Gerber G.R., “Lubrication regime transitions at the piston ring-cylinder liner interface”, Proc. IMechE. Part J: J. Engng. Trib., 219, 2005, pp. 19–31.

[45] Baker C.E., Theodossiades S., Rahnejat H. and Fitzsimons B., "Influence of in-plane dynamics of thin compression rings on friction in internal combustion engines", Trans. ASME, J. of Eng. for Gas Turbines & Power, 134, 2012, 092801.

[46] Chong W.W.F., Teodorescu M. and Vaughan N.D., "Cavitation induced starvation for piston-ring/liner tribological conjunction", Trib. Int., 44(4), 2011, pp. 483-497.

[47] Tung, S.C., McMillan, M.L., Automotive tribology overview of current advances and challenges for the future, Tribology International, 37, 2004, pp. 517–536

[48] Becker, E.P., Trends in tribological materials and engine technology, Tribology International, 37, 2004, pp. 569-575.

[49] Taylor, C.M., Fluid-film lubrication in the internal combustion engine: an invited review, J. Phys. D: Appl. Phys., 25, 1992, pp. A91-A100.

[50] Taylor, C.M., Automobile engine tribology—design considerations for efficiency and durability, Wear, Vol. 221, pp.1-8.

[51] Adam, A., Prefot, M., Wilhelm, W., 2010, Crankshaft bearings for engines with start-stop systems, MTZ worldwide, 71, 1992, pp. 22-25.

[52] Gudin, D., Mian, O., Sanders, S., Experimental measurement and modelling of plain bearing wear in start–stop applications, Proc. IMechE Part J: J. Engineering Tribology, 227, 2013, pp. 433-446.

[53] Beaurepaire, O., Uehara, S., George, J., Engine bearings with a durable polymer coating for hybrids and start-stop applications, International congress on the Spark Ignition Engine of the Future, November 30 – December 1, Strasbourg – INSA, France, 2011.

[54] George, J.W., Brock, R., Polymeric engine bearings for hybrid and start stop applications, SAE paper No. 2012-01-1966, 2012.

[55] Woolacott, R.G., Cooke, W.L., Thermal aspects of hydrodynamic journal bearing performance at high speeds, Proc. Instn. Mech. Engrs., 181, 1966-7, pp. 127-135.

[56] Dowson, D., Hudson, J.D., Hunter, B., March, C.N., An experimental investigation of the thermal equilibrium of steadily loaded journal bearings, Proc. Instn. Mech. Engrs., 181, 1966-7, pp. 70-80.

[57] Dowson, D., March, C.N., A thermohydrodynamic analysis of journal bearings, Proc. Instn. Mech. Engrs., Vol. 181, 1966-7, pp. 117-126.

[58] Suganami, T. and Szeri, A.Z., A thermohydrodynamic analysis of journal bearings, Journal of Tribology, 101, 1979, pp. 21-27.

[59] Medwell, J. O., Gethin, D. T., Taylor, C., A Finite Element Analysis of the Navier-Stokes Equations Applied to High Speed Thin Film Lubrication, Journal of Tribology 109(1), pp. 71-76

[60] Jang, JY., Khonsari, MM., Design of bearings on the basis of thermohydrodynamic analysis, Proceedings of the Institution of Mechanical Engineers, Part J: Journal of Engineering Tribology, 218, 2004, pp. 355-363.

[61] Ferron, J., Frene, J., Boncompain, R.A., Study of the thermohydrodynamic performance of a plane journal bearing; comparison between theory and experiments, Journal of Lubrication Technology, Transactions of the ASME, 105, 1983, pp. 422-438

[62] Mitsui, J., Hori, Y., Tanaka, M., Thermohydrodynamic analysis of cooling effect of supply oil in circular journal bearing, Journal of Lubrication Technology, Transactions of the ASME, 105, 1983, pp. 414-420.

[63] Mitsui, J., Hori, Y. and Tanaka, M., An experimental investigation on the temperature distribution in circular journal bearings, Journal of Tribology, Transactions of the ASME, 108, 1986,pp. 621-627.

[64] Mitsui, J., A study of thermohydrodynamic lubrication in a circular journal bearing, Tribology international, 20, 1987, pp. 331-341.

[65] Lund, J.W., Hansen, P.K., An approximate analysis of the temperature conditions in a journal bearing. Part I: Theory, Journal of Tribology, Transactions of the ASME, 106, 1984, pp. 228-236.

[66] Chauhan, A., Sehgal, R., Sharma, R.K., Thermohydrodynamic analysis of elliptical journal bearing with different grade oils, Tribology International, 43, pp. 2010, pp. 1970–1977.

[67] Lund, J.W., Hansen, P.K., An approximate analysis of the temperature conditions in a journal bearing. Part II: Application, Journal of Tribology, Transactions of the ASME, 106, 1984, pp. 237-244.

[68] Boncompain, R.A., Fillon, M., Ferne, J., Analysis of Thermal Effects in Hydrodynamic Bearings, Journal of Lubrication Technology, Transactions of the ASME, Vol. 108, 1986, pp. 219-224.

[69] Knight, J.D., Niewiarowski, A.J., Effects of two film rupture models on the thermal analysis of a journal bearing, Journal of Tribology, Transactions of the ASME, 112, 1990, pp. 183-188.

[70] Ma, M.-T., Taylor, C.M., Prediction of temperature fade in the cavitation region of two-lobe journal bearings, Proceedings of the Institution of Mechanical Engineers, Part J: Journal of Engineering Tribology, 208, 1994, pp. 133-139.

[71] Syverud, T., Experimental investigation of the temperature fade in the cavitation zone of full journal bearings, Tribology International, 34, 2001, pp. 859-870.

[72] Heshmat, H., Experimental studies in cavitation, In: Current research in cavitating fluid films, NASA Technical Memorandum 103184, 1990.

[73] Gethin, D.T., El-Deihi, M.K.I., Thermal behaviour of a twin axial groove bearing under varying loading direction, Proc. Instn. Mech. Engrs., Part C: Journal of Mechanical Engineering Science, 204, 1990, pp. 77-90.

[74] Kuznetsov, E., Glavatskih, S., Fillon, M., THD analysis of compliant journal bearings considering liner deformation, Tribology International, 44, 2011, pp. 1629-1641.

[75] Han, T., Paranjpe, R.S., A finite volume analysis of the thermohydrodynamic performance of finite journal bearings, Journal of Tribology, Transactions of the ASME, 112, 1990, pp. 557-565.

[76] Dowson, D., A generalized Reynolds equation for fluid-film lubrication, Int. J. Mech. Sci., 4, 1962, pp. 159-170

[77] Hussian, A., Mistry, K., Biswas, S., Athre, K., Thermal analysis of noncircular bearings, Journal of Tribology, Transactions of the ASME, 188, 1996, pp. 246-254.

[78] Khonsari, M.M., Jang, J.Y., Fillon, M., On the generalization of thermohydrodynamic analyses for journal bearings, Journal of Tribology, Transactions of the ASME, 118, 1996, pp. 571-579.

[79] Shi, F., Wang, Q.J., A mixed-TEHD model for journal-bearing conformal contacts – Part I: Model formulation and approximation of heat transfer considering asperity contact, Journal of Tribology, Transactions of the ASME, 120, 1998, pp. 198-205

[80] Wang, Y., Zhang, C., Wang, Q.J., Lin, C., A mixed-TEHD analysis and experiment of journal bearings under severe operating conditions, Tribology International, 35, 2002, pp. 395–407.

[81] Patir, N., Cheng, H.S., An average flow model for determine effects of three dimensional roughness on partial hydrodynamic lubrication, ASME Journal of Lubrication Technology, 100, 1978, pp. 12-17.

[82] Brewe, D.E., “Theoretical Modeling of the Vapor Cavitation in Dynamically Loaded Journal Bearings,” ASME Journal of Tribology, 108, 1986, pp. 628-638.

[83] Dowson, D., and Taylor, C.M., “Fundamental Aspects of Cavitation in Bearings,” Cavitation and Related Phenomena in Lubrication, ImechE, England, 1974, pp. 15-26.

[84] Floberg, L., “Experimental Investigation of Cavitation Regions in Journal Bearings,” Transactions of Chalmers University of Technology, No. 238, 1961.

[85] Mistry, K., Biswas, S., and Athre, K., “A New Theoretical Model for Analysis of the Fluid Film in the Cavitation Zone of a Journal Bearing,” ASME Journal of Tribology, 1997, pp. 741-746.

[86] Tucker, P.G., Keogh, P.S., A generalized computational fluid dynamics approach for journal bearing performance prediction, Proceedings of the Institution of Mechanical Engineers, Part J: Journal of Engineering Tribology, 209, 1995, pp. 99-108.

[87] Sawicki, J.T., Yu, B., Analytical solution of piston ring lubrication using mass conserving cavitation algorithm, Tribology Transactions, 43, 2000, pp. 587-594.

[88] Nassab, S.A.G., Moayeri, M.S., Three-dimensional thermohydrodynamic analysis of axially grooved journal bearings, Proceedings of the Institution of Mechanical Engineers, Part J: Journal of Engineering Tribology, 216, 2002, pp. 35-47.

[89] Nassab, S.A.G., Inertia effect on the thermohydrodynamic characteristics of journal bearings, Proceedings of the Institution of Mechanical Engineers, Part J: Journal of Engineering Tribology, 219, 2005, pp. 459-467.

[90] Skinner, S., On the occurrence of cavitation in lubrication, Proceedings of the Physical Society, XIX, 1903, pp. 73-81.

[91] Dowson, D., Taylor, C.M., Cavitation in Bearings Annual Review of Fluid Mechanics, 11, 1979, pp. 35-66.

[92] Heshmat, H., Experimental studies in cavitation, In: Current research in cavitating fluid films, NASA Technical Memorandum 103184, 1990.

[93] Jacobson, B., Good lubricant cleanliness - as important as good finish for the life of bearing, 4th nordic symposium on tribology lubrication, friction and wear, Hirtshals, Denmark, 1990.

[94] Dowson, D., Taylor, C.M., Miranda, A.A.S., The prediction of liquid film journal bearing performance with a consideration of lubricant film reformation Part 2: theoretical results, Proceedings of Institution of Mechanical Engineers, 199, 1985a, pp. 95-102.

[95] Dowson, D., Taylor, C.M., Miranda, A.A.S., The prediction of liquid film journal bearing performance with a consideration of lubricant film reformation Part 2: experimental results, Proceedings of Institution of Mechanical Engineers, 199, 1985b, pp. 103-111.

[96] Vijayaraghavan, D., Keith, T.G., Development and evaluation of a cavitation algorithm, Tribology Transactions, 32, 1989, pp. 225-233.

[97] Paydas, A., Smith, E.H., A flow-continuity approach to the analysis of hydrodynamic journal bearings, Proceedings of the Institution of Mechanical Engineers, Part C: Journal of Mechanical Engineering Science, 206, 1992, pp. 57-69.

[98] Hirani, H., Athre, K., Biswas, S., A simplified mass conserving algorithm for journal bearing under large dynamic loads, International Journal of Rotating Machinery, 7, 2001, pp. 41-51.

[99] Giacopini, M., Fowell, M.T., Dini, D., Strozzi, A., A mass-conserving complementarity formulation to study lubricant films in the presence of cavitation, Journal of Tribology, Transactions of the ASME, 132, 2010, pp. 1-12.

[100] Etsion, I., Ludwig, L.P., Observation of Pressure Variation in the Cavitation Region of Submerged Journal Bearings, ASME Journal of Lubrication Technology, 104, 1982, pp. 157-167.

[101] Groper, M., Etsion, I., The effect of shear flow and dissolved gas diffusion on the cavitation in a submerged journal bearing, Journal of Tribology, Transactions of the ASME, 123, 2001, pp. 494-500.

[102] Groper, M., Etsion, I., Reverse flow as a possible mechanism for cavitation pressure build-up in a submerged journal bearing, Journal of Tribology, Transactions of the ASME, 214, 2002, pp. 320-326.

[103] Nassab, S.A.G, Maneshian, B., Thermohydrodynamic analysis of cavitating journal bearings using three different cavitation models, Proceedings of the Institution of Mechanical Engineers, Part J: Journal of Engineering Tribology, 221, 2007, pp. 501-513.

[104] White F. M., 1996, "Viscous Fluid Flow", McGraw-Hill, 2nd Edition, 1991.

[105] Manninen M., Taivassalo V. and Kallio S., "On the mixture model for multiphase flow", VTT Publications 288 Technical Research Centre of Finland.

[106] Schiller L. and Naumann, Z., "Z. Ver. Deutsch. Ing.. 77. 318. 1935.

[107] Brackbill, J. U., Kothe, D. B. and Zemach, C., "A Continuum Method for Modeling Surface Tension". J. Comput. Phys., 100, 1992, pp. 335–354.

[108] Brennen C. E., Cavitation and Bubble Dynamics. Oxford University Press. 1995.

[109] Markatos, N. C., and Singhal, A. K., ‘‘Numerical Analysis of One-Dimensional, Two-Phase Flow a Vertical Cylindrical Pump,’’ Adv. Eng. Software, 43, 1982,pp. 99–106.

[110] Gohar R. and Rahnejat H., Fundamentals of Tribology, Imperial College Press, 2008.

[111] Roelands, C.J.A., Correlational aspects of the viscosity-temperature-pressure relationship of lubricating oils. Ph.D thesis, Technical University Delft, Delft, The Netherlands, 1966.

[112] Houpert, L., New results of traction force calculations in elastohydrodynamic contacts. J. Tribol. Trans. ASME, 107, 1985, pp. 241–248.

[113] Lee, P.M., Stark, M.S., Wilkinson, J.J., Priest, M., Lindsay Smith, J.R., Taylor, R.I., Chung, S., The degradation of lubricants in gasoline engines: development of a test procedure to evaluate engine oil degradation and its consequences for rheology. Tribol. Int. Eng. Ser. 48, 2005, pp. 593–602.

[114] Greenwood, J.A., Tripp, J.H., The contact of two nominally flat rough surfaces, Proc. Instn. Mech. Engrs., 185, 1970-1, pp. 625-633.

[115] Teodorescu, M., Balakrishnan, S., Rahnejat, H., Integrated tribological analysis within a multi-physics approach to system dynamics, Tribology and Interface Engineering Series, 48, 2005, pp. 725-737.

[116] Guangteng, G. and Spikes, H.A., “An Experimental Study of Film Thickness in the Mixed Lubrication Regime”, Tribology Series, 32, 1997, pp. 159-166.

[117] Greenwood, J.A. and Williamson, B.P., “Contact of Nominally Flat Surfaces”, Proc. R. Soc. Lond., Series A, 295, 1966, pp. 300-319.

[118] Buenviaje, C.K., Ge, S.-R., Rafaillovich, M.H. and Overney, R.M., “Atomic force microscopy calibration methods for lateral force, elasticity, and viscosity”, Mat. Res. Soc. Symp. Proc. 522, 1998, pp. 187-192

[119] Styles, G., Rahmani, R., Rahnejat, H. and Fitzsimons, B., “In-cycle and life-time friction transience in piston ring–liner conjunction under mixed regime of lubrication”, Int. J. of Engine Research, 15, 2014, pp. 862-876

[120] Eyring, H., “Viscosity, plasticity and diffusion as examples of reaction rates”, J. Chem. Phys., 4, 1926, pp. 283–291.

[121] Briscoe, B.J. and Evans, D.C.B., ‘’The shear properties of Langmuir-Blodgett llayers’’, Proc. Roy. Soc. Series A: Mathematical and Physical Sciences, 380, 1982, pp. 389-407.

[122] Langmuir, I., ‘’The constitution and fundamental properties of solids and liquids II, liquids 1’’, J. American Chemical Society, 39, 1917, pp.1847-1906.

[123] Bowden, F.P. and Tabor, D., ‘’The friction and lubrication of solids’’, Clarendon Press, Oxford, 1950

[124] Andersson B.S. "Company's Perspective in Vehicle Tribology- Volvo", Tribology Series (Elsevier), Vehicle Tribology, 18, 1991, pp. 503-506.

[125] Haddad S. D. and Tian K.-T. "An analytical study of offset piston and crankshaft designs and the effect of oil film on piston slap excitation in a diesel engine", Mechanism and Machine Theory, 30, 1995, pp. 271–284.

[126] Rahnejat H. Multi-body dynamics: vehicles, machines and mechanisms. Professional Engineering Publishing, Bury St Edmunds, UK: IMechE and Warrandale, PA, USA: SAE, joint publishers, 1998.

[127] Bin Chik, A., and Fessler H., "Radial pressure exerted by piston rings", J. Strain Anal Eng. Des. I, 2, 1966, pp. 165–171.

[128] Felter C. L., "Numerical simulation of piston ring lubrication", Trib. Int., 41, 2008, pp. 914-919.

[129] Snyder D. O., Koutsavdis E. K. and Anttonen J. S. R., "Transonic store separation using unstructured CFD with dynamic meshing". Technical Report AIAA-2003-3913, 33th AIAA Fluid Dynamics Conference and Exhibition, American Institute of Aeronautics and Astronautics, 2003.

[130] Ghosh MK., Gupta K., “Thermal effect in hydrodynamic lubrication of line contacts-piezoviscous effect neglected”, Int. J. Mech. Sci., 40, 1998, pp. 603–616.

[131] Arcoumanis, C., Duszynski, M., Flora, H., and Ostovar, P., "Development of a Piston-Ring Lubrication Test-Rig and Investigation of Boundary Conditions for Modelling Lubricant film Properties", Society of Automotive Engineers, Inc., SAE paper 952468,1995, pp 1-19.

[132] Furuhama S. and Sasaki S., “New device for the measurement of piston frictional forces in small engines”, Society of Automotive Engineers, Pap. No. 831284. 1983.

[133] Chong, WWF, Teodorescu, M and Rahnejat, H, “Mixed thermo-elastohydrodynamic cam–tappet power loss in low-speed emission cycles”, Int. J. Engine Res., 2012, doi: 10.1177/1468087412461631.

[134] Gore, M., Theaker, M., Howell-Smith, S., Rahnejat, H. and King, P.D., “Direct measurement of piston friction of internal combustion engines using the floating liner principle”, Proc. IMechE, Part D: J. Automobile Engng., 228, 2014, pp. 344-354.

[135] Gore, M., Howell-Smith, S., King, P.D. and Rahnejat, H., “Measurement of in-cylinder friction using the floating liner principle”, Proc. ASME 2012 Internal Combustion Engine Div. Spring Tech. Conf., Turin, Italy, May 2012, ICES2012-81028.

[136] Shahmohamadi, H., Rahmani, R., Rahnejat, H., Garner, C. P. and King, P. D., “Thermo-Mixed Hydrodynamics of Piston Compression Ring Conjunction”, Tribology Letters, 51, 2013, pp. 323-340.

[137] Tipei, N., “Boundary Conditions of a Viscous Flow Between Surfaces With Rolling and Sliding Motion”, Trans. ASME, J. Lubn. Tech. 90, 1968, pp. 8-16

[138] Mohammadpour, M., Johns-Rahnejat, P. M., Rahnejat, H. and Gohar, R., "Boundary Conditions for Elastohydrodynamics of Circular Point Contacts", Tribology Letters, 53, 2014, pp. 51-70

[139]- Johns-Rahnejat, P. M. and Gohar, R., “Measuring contact pressure distributions under elastohydrodynamic point contacts”, Tribotest, 1, 1994, pp. 33-53

[140] Birkhoff, G. and Hays, D., “Free Boundaries in Partial Lubrication”, J. Math. and Phys., 42, 1963, pp. 126-138

[141] Mohammadpour, M., Johns-Rahnejat, P. M., Rahnejat, H. and Gohar, R., "Boundary Conditions for Elastohydrodynamics of Circular Point Contacts", Tribology Letters, 53, 2014, pp. 51-70

[142] Tian, T., “Dynamic behaviours of piston rings and their practical impact; Part 1: ring flutter and ring collapse and their effects on gas flow and oil transport”, Proc. Instn. Mech. Engrs., Part J: J. Engng. Tribology, 216, 2002, 209-227

[143] Sherrington, I. "Measurement techniques for piston-ring tribology." Tribology and Dynamics of Engine and Powertrain: Fundamentals, Applications and Future Trends (2010): 387.

[144] Coyne, J. C. and Elrod, H. G., "Conditions for the rupture of a lubricating film—Part II: New boundary conditions for Reynolds equation" , Trans. ASME, J. Tribology, 93, 1971, pp. 156-167.

[145] Furuhama, S., Hiruma, M. and Tsuzita, M., “Piston ring motion and its influence on engine tribology”, SAE Technical Paper790860, 1979.

[146] Blake, W.K., Mechanics of Flow Induced Sound and Vibration, Academic Press, 1986.

[147] Brennen, C.E., Bubble Dynamics, Damage and Noise, Chapter 6, Hydrodynamics of Pumps,Oxford University Press and Concepts ETI, Internet (HTML) edition, ©2000 Concepts NREC.

[148] Falkowski, A., McElwee, M. and Bonne, M., “Design and Development of the DaimlerChrysler 5.7L HEMI® Engine Multi-Displacement Cylinder Deactivation System,” SAE Technical Paper 2004 01-2106, 2004, doi: 10.4271/2004-01-2106.

[149] Roberts, C., “Variable Valve Timing,” SwRI Project No. 03.03271, Clean Diesel III Program, March 2004.

[150] Wilcutts, M., Switkes, J., Shost, M. and Tripathi, A., "Design and Benefits of Dynamic Skip Fire Strategies for Cylinder Deactivated Engines," SAE Int., J. Engines 6(1), 2013, pp. 278-288.

[151] Vafaei, S., Menday, M. and Rahnejat, H., “Transient high-frequency elasto-acoustic response of a vehicular drivetrain to sudden throttle demand”, Proc. IMechE, J. Multi-body Dynamics, 216(1), 2001, pp. 35-52.

[152] Mohammadpour, M., Rahmani, R. and Rahnejat, H., “Effect of cylinder deactivation on the tribo-dynamics and acoustic emission of overlay big end bearings”, Proc. IMechE, J. Multi-body Dynamics, 228(2), 2014, pp.138-151.

[153] Brewe, D.E., Ball, J.H. and Khonsari, M.M., “Current research in cavitating fluid films”, NASA Technical Memorandum 103184, 1990.

[154] Boedo, S. "Practical Tribological Issues in Big End Bearings", Tribology and Dynamics of Engine and Powertrain, Woodhead Publishing, Cambridge, 2010, pp. 615-635.

[155] Mishra, P.C. and Rahnejat, H., “Tribology of big-end-bearings”, IN: Rahnejat, H. (ed). Tribology and Dynamics of Engine and Powertrain: Fundamentals, Applications and Future Trends. Woodhead Publishing Ltd, 2010, pp. 635 - 659.

[156] Rahnejat, H., ‘’Multi-body dynamics: historical evolution and application’’, Proc. IMechE., J. Mech. Eng. Sci., 214(1), 2000, pp. 149-173.

[157] Thomson, W. T., “Vibration Theory and Applications”, 5th Impression, Prentice Hall Inc., Guildford, Surrey, UK, 1976.

[158] Rahnejat, H., ed. “Tribology and dynamics of engine and powertrain: Fundamentals, applications and future trends”, Elsevier, 2010, ISBN 978-84569-361-9.

[159] Ferron, J., Frene, J., and Boncompain, R.A., ‘’Study of the Thermohydrodynamic Performance of a Plain Journal Bearing Comparison Between Theory and Experiments’’, J. Tribol. 105, 1983, pp. 422-428

[160] Shi, F., and Wang, Q., ‘’A Mixed-TEHD Model for Journal-Bearing Conformal Contacts—Part I: Model Formulation and Approximation of Heat Transfer Considering Asperity Contact’’.

[161] Khonsari, M. M., and Beaman, J. J., ‘’Thermohydrodynamic Analysis of Laminar Incompressible Journal Bearings’’, Tribo. Trans., 29, 1986, pp. 141-150.

[162] Wang, X.L. and Zhu, K.Q., “Numerical analysis of journal bearings lubricated with micropolar fluids including thermal and cavitating effects”, Tribology Int., 33, 2006, pp. 227–237.

[163] Morris, N., Rahmani, R., Rahnejat, H., King, P.D. and Fitzsimons, B., “Tribology of piston compression ring conjunction under transient thermal mixed regime of lubrication”, Tribology Int., 59, 2013, pp. 248-258.

[164] Nilsson B, Rosen B-G, Thomas TR, Wiklund D, Xiao L. Oil pockets and surface topography: mechanism of friction reduction. In: Proceedings of the XI international colloquium on surfaces, Chemnitz, Germany, 2004.

[165] Etsion I. State of the art in laser surface texturing. ASME Journal of Tribology, 125, 2005, pp. 248–253.

[166] Surface Technologies Ltd. URL /http://surface-tech.comS.

[167] Brizmer V, Kligerman Y, Etsion I. A laser surface textured parallel thrust bearing. Tribology Transaction, 46, 2003, pp. 397–403.

[168] Ronen A, Etsion I, Kligernman Y. Friction-reducing surface texturing in reciprocating automotive components. Tribology Transactions, 44, 2001, pp. 359–366.

[169] Ryk G, Kligernman Y, Etsion I. Experimental investigation of laser surface texturing for reciprocating automotive components. Tribology Transactions, 45, 2002, pp. 444–449.

[170] Varenberg M, Halperim G, Etsion I. Different aspects of the role of wear debris in fretting wear. Wear, 252, 2002, pp. 902–910.

[171] Volchok A, Halperin G, Etsion I. The effect of surface regular topography on fretting fatigue life. Wear, 253, 2002, pp. 509–515.

[172] Galda L., Pawlus P. and Sep J., Dimples shape and distribution effect on characteristics of Stribeck curve, Tribology International, 42, 2009, pp. 1505–1512.

[173] Koszela W., Pawlus P. and Galda L., The effect of oil pockets size and distribution on wear in lubricated sliding, Wear, 263, 2007, pp. 1585-1592.

[174] Tala-Ighil N., Fillon M. and Maspeyrot P., Effect of textured area on the performances of a hydrodynamic journal bearing, Tribology International 44, 2011, pp. 211-219.

[175] Shahmohamadi H., Rahmani R., Rahnejat H., Garner C.P. and Dowson D., Big End Bearing Losses with Thermal Cavitation Flow under Cylinder Deactivation, Tribology Letters, 57, 2015, pp. 1-17.

[176] Morris, NJ., Rahnejat, H. and Rahmani, R.: Tribology of partial pad journal bearings with textured surfaces, Österreichische Tribologische Gesellschaft (The Austrian Tribology Society), 2011.

[177] Parker, J.C. and Lenhard, R.J.: A model for hysteretic constitutive relations governing multiphase flow: 1. Saturation-pressure relations." Water Resources Research 23, 1987, pp. 2187-2196.

[178] Jacobsson, B.: A survey of Swedish lubrication research 1957-69 at Chalmers and Lund technical universities, Proceedings of the Institution of Mechanical Engineers, Conference Proceedings, 183, 1968, pp.164-171.

[179] Prosperetti, A.: Personal communication in Annual meetings of ICR, City University London, (2012, 2013 and 2014).

[180] Garner, D.R., James, R.D. and Warriner, J.F.: Cavitation erosion damage in engine bearings: theory and practice." Journal of Engineering for Gas Turbines and Power 102, 1980, pp. 847-857.

Appendix: Published Papers

Tribol Lett (2013) 51:323–340
DOI 10.1007/s11249-013-0163-5

ORIGINAL PAPER

Thermo-Mixed Hydrodynamics of Piston Compression Ring Conjunction

H. Shahmohamadi · R. Rahmani · H. Rahnejat · C. P. Garner · P. D. King

Received: 10 April 2013 / Accepted: 17 May 2013 / Published online: 4 June 2013

Abstract A new method, comprising Navier–Stokes equations, Rayleigh–Plesset volume fraction equation, an analytical control-volume thermal-mixed approach and asperity interactions, is reported. The method is employed for prediction of lubricant flow and assessment of friction in the compression ring–cylinder liner conjunction. The results are compared with Reynolds-based laminar flow with Elrod cavitation algorithm. Good conformance is observed for medium load intensity part of the engine cycle. At lighter loads and higher sliding velocity, the new method shows more complex fluid flow, possessing layered flow characteristics on the account of pressure and temperature gradient into the depth of the lubricant film, which leads to a cavitation region with vapour content at varied volume fractions. Predictions also conform well to experimental measurements reported by other authors.

Keywords Piston ring conjunction · Mixed-mode friction · Navier–Stokes equations · Raleigh–Plesset volume fraction

List of Symbols

A	Apparent contact area
A_a	Asperity contact area
b	Ring axial face width
C_p	Lubricant specific heat
d	Ring thickness
E_1	Young's modulus of elasticity of the ring
E_2	Young's modulus of elasticity of the liner
E'	Equivalent (reduced) modulus of elasticity
f_b	Boundary friction
f_t	Total friction
f_v	Viscous friction
F_T	Ring tension force
F_G	Combustion gas force
F_2, $F_{5/2}$	Statistical functions
g	Ring end gap
g_s	Switch function
H	Enthalpy
h	Elastic film shape
h_m	Minimum film thickness
h_s	Ring axial profile
h_t	Heat transfer coefficient of boundary layer
I	Ring cross-sectional second area moment of inertia
k	Lubricant thermal conductivity
k_{s1}	Thermal conductivity of the bore/liner
k_{s2}	Thermal conductivity of the ring
l	Connecting rod length
L	Ring peripheral length
p_{atm}	Atmospheric pressure
p_c	Cavitation/lubricant vaporisation pressure
p_h	Hydrodynamic pressure
p_{gb}	Gas pressure acting behind the ring
$\dot{Q}_1$	Conductive heat flow rate through the liner
$\dot{Q}_2$	Conductive heat flow rate through the ring
$\dot{Q}_{cv}$	Convective heat flow rate
r	Crank-pin radius
r_0	Nominal bore radius
R_l	Conductive thermal resistance for the lubricant layer

H. Shahmohamadi · R. Rahmani (✉) · H. Rahnejat · C. P. Garner · P. D. King
Wolfson School of Mechanical and Manufacturing Engineering, Loughborough University, Loughborough LE11 3TU, Leicestershire, UK
e-mail: r.rahmani@lboro.ac.uk

R_v	Convective thermal resistance of the boundary layer (between film and surface)
Re	Reynolds number
t	Time
U	Ring sliding velocity
U_1, U_2	Surface velocities of contacting bodies
$\vec{V}$	Velocity vector
W	Contact load
W_a	Load share of asperities
W_h	Load carried by the lubricant film
x_c	Oil film rupture point
Z	Pressure–viscosity index

Greek Symbols

α_0	Pressure/temperature–viscosity coefficient
β	Lubricant bulk modulus
φ	Crank angle
ζ	Number of asperity peaks per unit contact area
η	Lubricant dynamic viscosity
η_0	Lubricant dynamic viscosity at atmospheric pressure
κ	Average asperity tip radius
λ	Stribeck's oil film parameter
μ	Pressure coefficient for boundary shear strength of asperities
ν_1	Poisson's ratio of the ring material
ν_2	Poisson's ratio of the liner material
ρ	Lubricant density
ρ_0	Lubricant density at atmospheric pressure
σ_r	Liner surface roughness
σ_l	Ring surface roughness
τ	Shear stress
τ_0	Eyring shear stress
Γ	Diffusion coefficient
θ	Temperature
θ_e	Average (effective) lubricant temperature

1 Introduction

The primary function of the piston compression ring is to seal the combustion chamber. This prevents the escape of high-pressure gases from the combustion chamber and conversely lubricant leakage into the chamber. However, effective sealing function of the compression ring can result in increased friction and thus parasitic losses [1].The piston assembly accounts for approximately 35–45 % of engine frictional losses [2, 3]. Therefore, in order to improve engine performance as well as reducing emission levels, it is important to have a deeper understanding of frictional behaviour of piston–cylinder system as a pre-requisite. The current work addresses these issues with regard to the piston compression ring.

There have been many numerical predictions of compression ring–cylinder liner conjunction, where the analyses have included a host of parameters which interact with each other, making the tribology of ring–liner conjunction particularly complex. These parameters include the effect of the ring's axial profile along its contacting face width with the cylinder liner and its surface topography [4], and the effect of evolving wear process upon friction and sealing effectiveness of the ring in an out-of-round bore [5, 6]. These and similar analyses [7–13] have included mixed regime of lubrication, where direct interaction of surfaces can occur at piston dead centre reversals with momentary cessation of lubricant entraining motion into the contact under assumed fully flooded or starved inlet conditions. Although ring fitment analysis is taken into account in the works reported in [5, 6, 11, 12], including in some cases with bore out of roundness, the ring–bore conformability should also take into account the modal behaviour of the ring as described, for example, by Baker et al. [14]. They showed that ring elastodynamics in fact conforms it to the bore in the high-pressure region with a low sliding velocity (i.e. at the reversals). This ensures good ring sealing at the expense of increased friction. However, in some parts of the engine cycle, ring elastodynamics as well as its axial profile can exacerbate the convergent–divergent conjunctional passage and clearance, which suggests lubricant film rupture and the emergence of a cavitation region. This can also affect the compression ring sealing function. The effect of cavitation is studied by Chong et al. [15], who used Elrod's approximation [16] to the Jakobsson and Floberg [17] and Olsson [18] (JFO) cavitation boundary condition. Chong et al. [15] showed that cavitation formed at the lubricant film contact exit in the compression stroke reduces the lubricant availability at the top dead centre (TDC) reversal, thus causing a starved contact in parts of the power stroke in the vicinity of the TDC.

Therefore, the multivariate nature of the problem is quite apparent. The current analysis combines the use of an open (free) exit boundary condition instead of an imposed cavitation boundary condition. This is achieved by solving the Navier–Stokes equations for multi-phase flow dynamics instead of the usual Reynolds equation. Additionally, this approach readily enables simultaneous solution with the energy equation. Thus, the effect of rise in surface temperatures, caused by viscous shear of the lubricant in the conjunction, upon lubricant film formation as well as viscosity variation into the depth of the film are included in the solution. Unlike Reynolds or Elrod flow equations, with the Navier–Stokes equations, the pressure gradient across the film is retained. This enables more accurate prediction of viscous friction due to Poiseuille flow as well as in Couette shear. This approach together with the inclusion of lubricant rheological state and asperity interactions, to

represent boundary friction, has not hitherto been reported in the literature.

2 Problem Description

Figure 1 is a schematic representation of ring–liner conjunction along the ring axial face width. The ring profile $h_s(x)$ is assumed to be parabolic with a maximum crown height of c and a face width of b:

$$h_s(x) = \frac{cx^2}{(b/2)^2} \tag{1}$$

The current analysis assumes good conformance of the ring to the liner surface in the circumferential direction of the bore. This simplifies the problem to a one-dimensional contact, which is valid for ring–bore contact of bore diameter-to-ring face width ratio: $2\pi r_0/b \geq 30$ as shown by Haddad and Tian [19], which is applicable to the engine studied here. The engine studied here is a high-performance V12 4-stroke naturally aspirated engine with specifications as detailed in Table 1.

It is assumed that the ring does not undergo any relative motion with respect to the piston sliding at the velocity U. In practice, the ring may be subject to axial motion within its retaining groove, a motion termed as ring flutter. Thus, according to Rahnejat [20]:

$$U(\varphi) = -r\omega \sin\varphi \left\{ 1 + \cos\varphi \left[\left(\frac{l}{r}\right)^2 - \sin^2\varphi \right]^{-\frac{1}{2}} \right\} \tag{2}$$

where ϕ is the crank angle, l is the connecting rod length, r the crank-pin radius and ω is the engine rotational speed. Figure 2 shows the piston sliding speed variation for the engine speeds of 1,500 and 6,000 rpm, respectively.

Forces acting on the ring are considered as radial in-plane forces. In its radial plane, the ring is subjected to two outward forces: ring elastic tension force F_T and the gas force F_G, acting on the inner rim of the ring. These forces strive to conform the ring to the bore surface. Thus, the total outward force (towards the liner interface), acting on the ring, is: $F = F_T + F_G$. The ring tension force, F_T, is obtained as [21]:

Table 1 Engine data

Parameters	Values	Units
Crank-pin radius, r	39.75	Mm
Connecting rod length, l	138.1	Mm
Bore nominal radius, r_0	44.52	Mm
Ring crown height, c	10	μm
Ring axial face width, b	1.15	Mm
Ring radial width, d	3.5	Mm
Ring free end gap, g	10.5	Mm

$$F_T = p_e\, b\, r_0 \quad \left(\text{where } p_e = \frac{gEI}{3\pi b r_0^4}\right) \tag{3}$$

where p_e is the elastic pressure, r_0 is the bore nominal radius and g is the ring end gap in its free (unfitted) state. The gas force acting on the back of the ring varies according to the chamber pressure in an engine cycle; thus:

$$F_G(\varphi) = 2\pi b r_0 p_g(\varphi) \tag{4}$$

A gas blow-by analysis is required to obtain the exact value of gas pressure acting behind the ring. In the current analysis, it is assumed that the gas pressure behind the ring is equal to the in-cylinder gas pressure.

These outward forces (ring elastic tension and the gas force) are opposed by the contact force generated as the result of combined actions of generated conjunctional hydrodynamic pressures and the load share carried by the direct contact of surfaces themselves. The latter is often the load shared by a small portion of asperities on the opposing surfaces. Thus, the instantaneous contact load is determined as $W(\varphi) = W_a(\varphi) + W_h(\varphi)$, where the load carried

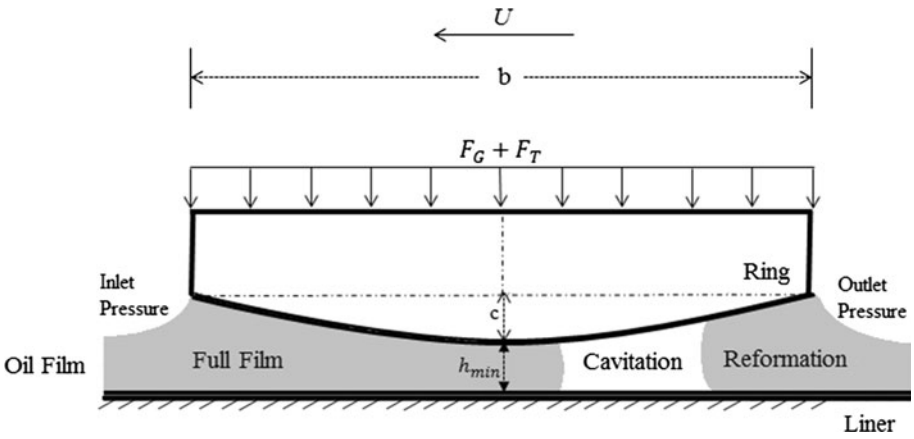

Fig. 1 2D diagram of piston ring–liner conjunction

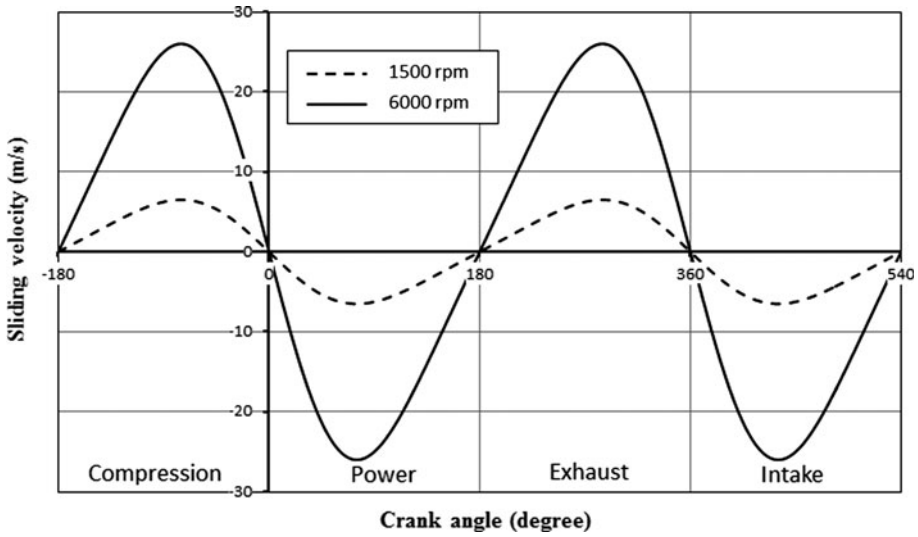

Fig. 2 Piston sliding speed for engine speeds of 1,500 and 6,000 rpm

by any film of lubricant is the integrated pressure distribution as:

$$W_h(\phi) = 2\pi r_0 \int_0^b p_h(\phi) dxdy \tag{5}$$

As shown in Fig. 1, in general, the contact region may be considered as comprising of three distinct regions: (1) full film (a coherent lubricant film region), (2) film rupture and cavitation, and (3) lubricant film reformation. The Elrod cavitation model is the usual basis for the tribological analysis, taking into account these various conjunctional regions. To describe the physics of fluid flow in the cavitated region, in which at least these various states of lubricant film coexist, a suitable two-phase flow model needs to be employed alongside the use of the Navier–Stokes equations. This would be an elegant approach which for moderately and heavily loaded conditions represents a reasonable compromise between computational speed and predictive accuracy [22]. However, it can be fairly complex to implement.

3 Numerical Model

3.1 General Navier–Stokes and Energy Equations

The general continuity and Navier–Stokes momentum equations for compressible viscous fluid flow can be described as [23]:

$$\frac{D\rho}{Dt} + \rho \nabla \vec{V} = 0 \tag{6}$$

$$\rho \frac{D\vec{V}}{Dt} = -\nabla p + \nabla(\bar{\tau}_{ij}) + \vec{F} \tag{7}$$

where $\frac{D}{Dt}$ is the covariant derivative operator, ρ is the lubricant density, p is the pressure, $\bar{\tau}_{ij}$ is the viscous stress tensor and $\vec{F}$ is the body force field vector. In addition, $\vec{V} = U\hat{i} + V\hat{j} + W\hat{k}$ is the velocity vector in which U is the component of velocity in the direction of axial lubricant flow entrainment; V is that in the side-leakage direction, along the y-axis (which may reasonably be discarded as there is negligible side leakage in the thin film ring–bore conjunction); and W is the squeeze film velocity, $\frac{\partial h}{\partial t}$. The viscous stress tensor is:

$$\bar{\tau}_{ij} = \eta\left(\frac{\partial U_i}{\partial x_j} + \frac{\partial U_j}{\partial x_i} - \delta_{ij}\frac{2}{3}\nabla\vec{V}\right) \tag{8}$$

where η is the effective lubricant dynamic viscosity, δ_{ij} is the Kronecker delta and it is defined as:

$$\delta_{ij} = \begin{cases} 0 & \text{if } i \neq j \\ 1 & \text{if } i = j \end{cases} \tag{9}$$

One possibility in a CFD model is to evaluate fluid viscosity as a function of pressure and temperature along the liner and into the depth of the lubricant film. The latter is neglected in the conventional hydrodynamic lubrication approaches, which are based on Reynolds equation. Finally, the energy equation can be stated as [23]:

$$\rho \frac{DH}{Dt} = \frac{Dp}{Dt} + \nabla(k\nabla\theta) + \bar{\tau}_{ij}\frac{\partial U_i}{\partial x_j} \tag{10}$$

where H is the fluid enthalpy, θ is the temperature and k is the lubricant thermal conductivity.

3.2 Cavitation Model: Vapour Mass Fraction and Vapour Transport Equations

With cavitation, the liquid–vapour mass transfer (evaporation and condensation) is governed by the vapour transport equation as [24]:

$$\frac{\partial}{\partial t}(\alpha_v \rho_v) + \nabla(\alpha_v \rho_v \vec{V}_v) = R_e - R_c \tag{11}$$

where ρ_v is the vapour density, $\vec{V}_v$ is the velocity vector of the vapour phase, R_e and $R_c$are mass transfer source terms related to the growth and collapse of the vapour bubbles, respectively. The growth and collapse of a bubble cluster are modelled based on the Rayleigh–Plesset equation, describing the growth of a single vapour bubble in a liquid, which provides the rate equation, controlling vapour generation and condensation. Singhal et al. [25] assumed that a working fluid is a mixture of liquid and vapour and introduced a modified form of the above equation, based upon the vapour mass fraction, f_{mass} as:

$$\frac{\partial}{\partial t}(\rho_m f_{\text{mass}}) + \nabla(\rho_m \vec{V}_v f_{\text{mass}}) = \nabla(\Gamma \nabla f_{\text{mass}}) + R_e - R_c \tag{12}$$

where ρ_m is the mixture density and Γ is the diffusion coefficient. The mass transfer rate expressions are derived from the Rayleigh–Plesset equations, based upon limiting bubble size considerations (interface surface area per unit volume of vapour). These rates are functions of the instantaneous, local pressure and are given by:

$$R_e = C_e \frac{V_{\text{ch}}}{\sigma_s} \rho_l \rho_v \sqrt{\frac{2(p_{\text{sat}} - p)}{3\rho_l}} (1 - f_{\text{mass}}), \quad \text{for} \quad p < p_{\text{sat}} \tag{13}$$

$$R_c = C_c \frac{V_{\text{ch}}}{\sigma_s} \rho_l \rho_v \sqrt{\frac{2(p - p_{\text{sat}})}{3\rho_l}} f_{\text{mass}}, \quad \text{for} \quad p > p_{\text{sat}} \tag{14}$$

where the suffices l and v denote the liquid and vapour phases, respectively, V_{ch} is a characteristic velocity, σ_s is the surface tension coefficient of the liquid, p_{sat} is the liquid saturation vaporisation pressure at a given temperature and C_e and C_c are empirical constants and are considered to be 50 and 0.01, respectively, according to Kubota et al. [26].

3.3 Conventional Hydrodynamic Cavitation Model (Elrod's Method)

For the engine under investigation, the ring perimeter-to-width ratio is over 100. Therefore, as a first approximation, the piston ring/liner conjunction can be viewed as an infinitely long slider bearing [7] (envisaged as unwrapped). Although this assumes uniform radial loading and neglects piston secondary motion as well as ring dynamics, the final results can provide some valuable predictions. If the flow is considered as laminar, the behaviour of most lubricated conjunctions can be predicted using Reynolds equation:

$$\frac{\partial}{\partial x}\left(\frac{\rho h^3}{6\eta}\frac{\partial p}{\partial x}\right) = U\frac{\partial}{\partial x}(\rho h) + 2\frac{d}{dt}(\rho h) \tag{15}$$

Elrod's modification [16] provides an acceptable solution if cavitation is present: In the full film region of the contact, both Couette and Poiseuille terms are considered, whilst in the cavitation region, only Couette flow is taken into account and lubricant squeeze film motion [27]. To account for this, a switching term, g_s, is defined as:

$$g_s = \begin{cases} 1 & \text{if} \quad \xi \geq 1 \quad \text{(full film region)} \\ 0 & \text{if} \quad 0 < \xi < 1 \quad \text{(cavitation region)} \end{cases} \tag{16}$$

in which ξ is defined as the fractional film content. This allows defining the contact pressure distribution as a function of film ratio ξ as:

$$p = g_s \beta \ln \xi + p_c \tag{17}$$

where p_c is the lubricant's cavitation vaporisation pressure and β is the lubricant's bulk modulus. Reynolds equation is now modified using Eqs. (15) and (17) as:

$$\frac{\partial}{\partial x}\left(\frac{\rho h^3}{6\eta} g_s \beta \frac{\partial \xi}{\partial x}\right) = U\frac{\partial}{\partial x}(\xi \rho h) + 2\frac{d}{dt}(\xi \rho h) \tag{18}$$

Lubricant viscosity and density vary with contact pressures and temperatures as described in Sect. 3.5 below.

3.4 Boundary Conditions

In both the Navier–Stokes and Elrod's models, the following boundary conditions are used along the axial x-direction of the contact (i.e. along the ring face width)

$$\begin{cases} p_h(-b/2) = p_L \\ p_h(+b/2) = p_U \\ p_h(x_c) = p_c \end{cases} \tag{19}$$

However, the Elrod model satisfies another pressure gradient boundary condition $\left.\frac{dp(x)}{dx}\right|_{x=x_c} = 0$ at the film rupture point (x_c is the location of rupture point), whereas no artificial exit boundary condition needs to be stated with the Navier–Stokes approach.

3.5 Lubricant Rheology

The lubricant bulk rheological properties including density and viscosity are affected by pressure and temperature [5]. The density–pressure relationship is [28]:

$$\rho = \rho_0 \left(1 + \frac{6.0 \times 10^{-10}(p_{\text{h}} - p_{\text{atm}})}{1 + 1.7 \times 10^{-9}(p_{\text{h}} - p_{\text{atm}})}\right) \times \left[1 - 0.65 \times 10^{-3}(\Theta - \Theta_0)\right] \tag{20}$$

in which p_{atm} is the atmospheric pressure and Θ_0 is temperature in K (i.e. $\Theta_0 = \theta_0 + 273$). Lubricant density at atmospheric pressure, ρ_0, is given in Table 2.

Variations of lubricant dynamic viscosity with pressure and temperature can be expressed based on Roelands' equation [29] and further developed by Houpert [30], as follows:

$$\eta = \eta_0 \exp\left\{(\ln(\eta_0) + 9.67)\left[\left(\frac{\Theta - 138}{\Theta_0 - 138}\right)^{-S_0} \times \left(1 + \frac{p_h - p_{atm}}{1.98 \times 10^8}\right)^{Z} - 1\right]\right\} \quad (21)$$

in which, η_0 is the lubricant dynamic viscosity at atmospheric pressure and temperature, and Z and S_0 are constants:

$$Z = \frac{\alpha_0}{5.1 \times 10^{-9}[\ln(\eta_0) + 9.67]} \quad \text{and} \quad S_0 = \frac{\beta_0(\Theta_0 - 138)}{\ln(\eta_0) + 9.67} \quad (22)$$

where α_0 and β_0 are constants at atmospheric temperature and pressure. Details of lubricant rheological parameters are given in Table 2. It should be noted that the rheological parameters are for fresh lubricant. In practice, the lubricant is subject to shear thinning, oxidation and contamination [31].

3.6 Heat Generation and Thermal Boundary Conditions

Lubricant temperature rises due to internal friction. In the Navier–Stokes approach, solving the energy Eq. (10) with the appropriate boundary conditions provides a prediction of heat generated in the contact conjunction due to viscous shear. However, temperatures of contacting surfaces also increase with the rising contact temperature of the lubricant. Therefore, temperature boundary conditions are themselves a function of internal heat. For the liner, the measured temperature, using a thermocouple very close to the sliding surface, is used as shown in Fig. 3. Therefore, instantaneous temperature boundary condition for the liner is that measured. The compression ring temperature is obtained through internal heat partitioning, thus is not adiabatic. To obtain the temperature rise of the bounding surfaces, a thermal heat transfer partitioning model needs to be used which takes into account the transferred heat to the contacting surfaces (boundaries) as well as the heat which is carried away by the lubricant flow though the contact. Morris et al. [4] have described an analytical model, based on a control-volume approach which takes into account the local temperature rise on the contacting surfaces due to conduction from the lubricant and also direct asperity contacts. The method described by Morris et al. [4] is also adopted here in conjunction with the Navier–Stokes analysis.

Table 2 Lubricant properties in atmospheric pressure and 40 °C

Parameters	Values	Units
Lubricant viscosity, η_0	0.05	kg/m s
Lubricant density, ρ_0	833	kg/m^3
Lubricant specific heat, C_p	1,968	J/kg K
Lubricant thermal conductivity, k	0.145	w/m K
α_0	1×10^{-8}	m^2/N
β_0	4×10^{-2}	–

In the thermal heat transfer model, at any instant of time, corresponding to a crank angle position, the equality of inlet and outlet flows is maintained. This is an outcome of the instantaneous quasi-static equilibrium at any given crank angle. However, the flow rate is subject to change between subsequent crank angle positions, as the variations of the film thickness with time $\left(\frac{\partial h}{\partial t}\right)$ are taken into account. In addition, there is a convection thermal flux at the inlet nib to the conjunction from the solid boundaries to the entrant lubricant supply at a lower temperature θ_{in}. This raises the inlet lubricant to θ_0 from its assumed bulk flow temperature (inlet heating):

$$\theta_0 = \frac{\theta_{s1}U_1 + \theta_{s2}U_2}{U_1 + U_2} \quad (23)$$

where θ_{s1} and θ_{s2} are the initial surface temperatures of the bore/liner and ring surface. Since one of the surfaces is stationary, therefore from Eq. (23), $\theta_0 = \theta_{s1}$ at the inlet due to the convective thermal flux. The liner temperature is measured from the engine liner surface and, therefore, is known a priori at any given crank angle location (see Fig. 3).

The oil temperature distribution obtained through solution of energy Eq. (10) is based upon an initially assumed temperature for the ring surface. Therefore, the heat partitioning method described by Morris et al. [4] can predict the quantity of heat transfer from the ring, contributing to the rise in its temperature when considering the heat removal through convection cooling by the lubricant, flowing through the contact exit (see Fig. 4).

Since the thermal model is a control-volume-based approach, the effective temperature of the lubricant, obtained from solving Eq. (10), is averaged throughout the contact as:

$$\theta_e = \frac{\int_0^b \int_0^{h(x)} \theta(x,z)dzdx}{\int_0^b \int_0^{h(x)} dzdx} \quad (24)$$

The rise in the ring surface temperature is obtained from the following relationship (Morris et al. [4]):

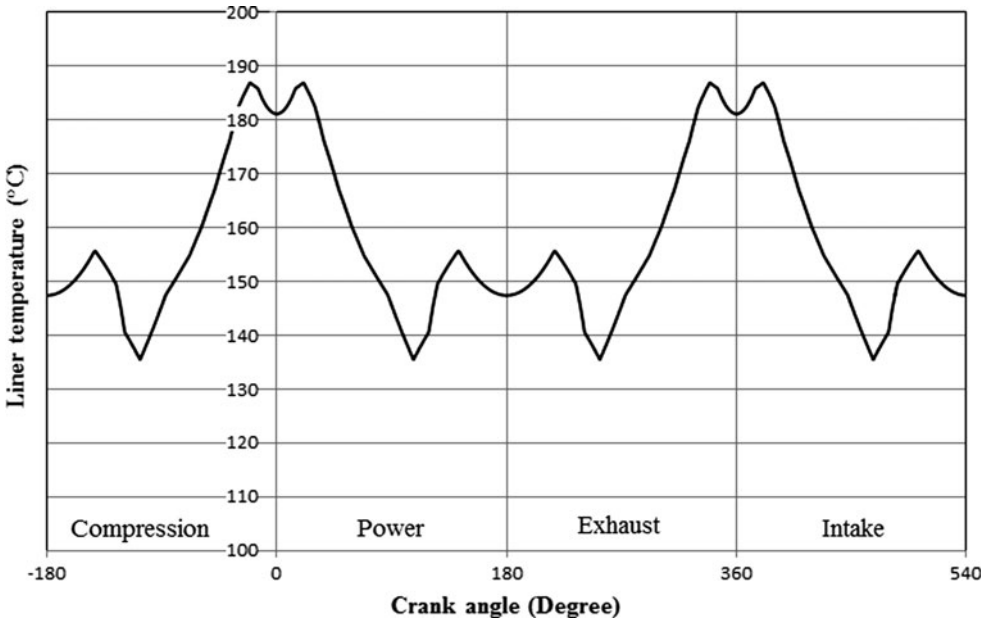

Fig. 3 The temperature of the liner at the ring contact location throughout the engine strokes

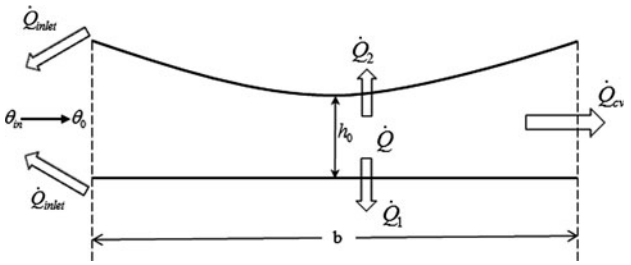

Fig. 4 Thermal flow within the contact (Morris et al. [4])

$$\Delta\theta_{s2} = \frac{R_f}{R_l + R_v + R_f}(\theta_e - \theta_{s2}) \tag{25}$$

in which, θ_{s2} is the initial ring surface temperature and R_l, R_v and R_f are the thermal resistances associated with conduction through the lubricating film, convective heat transfer through the boundary layer and the rise in the solid surface flash temperature, respectively (Olver and Spikes [32]). These parameters were calculated according to the given relationships in Morris et al. [4]. In addition, ring and liner mechanical/thermal properties are provided in Table 3, Sect. 3.7.

Table 3 Material properties and surface topographical parameters

Parameters	Values	Units
Liner material	Grey cast iron	–
Modulus elasticity of liner material	92.3	GPa
Poisson ratio for liner material	0.211	–
Density for liner material	7,200	kg/m^3
Thermal conductivity for liner material	55	W/m K
Specific heat capacity for liner material	460	J/kg K
Ring material	Steel SAE 9254	–
Modulus elasticity of ring material	203	GPa
Poisson ratio for ring material	0.3	–
Roughness parameter ($\zeta\kappa\sigma$)	0.04	–
Measure of asperity gradient (σ/κ)	0.001	–
Density for ring material	7,700	kg/m^3
Thermal conductivity for ring material	25	W/m K
Specific heat capacity for ring material	460	J/kg K

3.7 Asperity Interaction

The share of load carried by the interacting asperities in the contiguous is obtained as [5]:

$$W_a = \frac{16\sqrt{2}}{15}\pi(\zeta\kappa\sigma)^2\sqrt{\frac{\sigma}{\kappa}}E^*AF_{5/2}(\lambda) \tag{26}$$

The dimensionless group $\zeta\kappa\sigma$ is known as the roughness parameter, whilst σ/κ is a measure of a typical asperity slope. These can be obtained through topographical measurements. E^* is the composite elasticity modulus and it is obtained as:

$$\frac{1}{E^*} = \frac{1-v_1^2}{E_1} + \frac{1-v_2^2}{E_2} \tag{27}$$

where v_1 and v_2 are the Poisson's ratios, and E_1 and E_2 the moduli of elasticity for the materials of bounding solid surfaces. The statistical function $F_{5/2}(\lambda)$ is introduced to match the assumed Gaussian distribution of asperities as a function of the Stribeck oil film parameter, $\lambda = h/\sigma$.

Using a fifth-order polynomial curve fit, this statistical function can be described as [5]:

$$F_{5/2}(\lambda) = -0.0046\lambda^5 + 0.0574\lambda^4 - 0.2958\lambda^3 + 0.7844\lambda^2 - 1.0776\lambda + 0.6167 \quad (28)$$

Table 3 lists the material properties as well as the surface topographical parameters for both the compression ring and the liner samples used in this analysis.

3.8 Conjunctional Friction

At any instant of time, viscous shear of a film of lubricant, h, is obtained as [1]

$$\vec{\tau} = \left| \pm \frac{h}{2} \nabla p - \Delta \vec{V} \frac{\eta}{h} \right| \quad (29)$$

If this shear stress is below the limiting Eyring [33] shear stress of the lubricant used, $\tau_0 = 2\,\text{MPa}$ (in this case), then the lubricant follows a Newtonian shear behaviour and friction is obtained as $f_v = \tau A$, where $A = 2\pi r_0 b$ is the apparent contact area.

Under the mixed elastohydrodynamic analysis and at high shear, the lubricant film is usually quite thin and subject to non-Newtonian traction $(\tau > \tau_0)$ at the tip of asperities [1]. The total friction is, therefore, a summation of viscous shear of the lubricant and boundary contribution due to asperity interactions on the contiguous surfaces:

$$f_\text{t} = f_\text{v} + f_\text{b} \quad (30)$$

The boundary friction is obtained as [34]

$$f_\text{b} = \tau_0 A_\text{a} + \mu W_a \quad (31)$$

where μ is the pressure coefficient for boundary shear strength of asperities on the softer counterface. A value of $\mu = 0.17$ for ferrous-based surfaces was chosen. In addition, the cumulative area of asperity tips, A_a, is found as [34]

$$A_a = \pi^2 (\zeta \kappa \sigma)^2 \sqrt{\frac{\sigma}{\kappa}} A F_2(\lambda) \quad (32)$$

where $F_2(\lambda)$ is a function representative of the Gaussian distribution of asperities in terms of λ (the Stribeck oil film parameter) [5]:

$$F_2(\lambda) = -0.0018\lambda^5 + 0.0281\lambda^4 - 0.1728\lambda^3 + 0.5258\lambda^2 - 0.8043\lambda + 0.5003 \quad (33)$$

The viscous friction force, f_v, is obtained as:

$$f_\text{v} = \tau (A - A_\text{a}) \quad (34)$$

The total power loss from ring–bore conjunction is because of both viscous and boundary contributions to the overall friction. The power loss due to boundary friction is:

$$P_{fb} = f_\text{b} U \quad (35)$$

Therefore, the total friction loss is $P_f = P_{fb} + P_{fv}$.

4 Solution Procedure

A 2D simulation model is developed using the CFD package FLUENT 14.0. The pre-processor ANSYS Design Modeller and Meshing is used for the grid generation. The geometrical nature of the problem examined here (the film thickness is very small compared with bore radius) imposes the use of only quadrilateral cells. After conducting a grid sensitivity test on the accuracy of predictions, forty divisions were employed across the film thickness and 1,500 divisions along the ring face width, thus a mesh of 60,000 cells. Calculation of Reynolds number for the studied conditions showed that the flow is well within the laminar region. The operating pressure and vaporisation (cavitation) pressure are set to the atmospheric pressure of 101.3 kPa.

Pressure inlet and outlet boundary conditions are used for the leading and trailing edges of the ring/liner contact. Therefore, when the piston undergoes upstroke motion, the inlet pressure is that of the combustion chamber as given in Fig. 5, whilst at the exit, the crank-case pressure is assumed, which also is assumed to be the atmospheric pressure. On the other hand, for the down-stroke sense of the piston, the inlet pressure is set to that of the crank-case (atmospheric) pressure, whilst the outlet pressure is that of the combustion chamber. The chamber (combustion) pressure varies with engine stroke, speed and throttle demand. Figure 5 shows the in-cylinder pressure for the engine speeds of 1,500 and 6,000 rpm with 63 % throttle.

The pressure-based mixture model [35] is chosen for the present CFD analysis. The velocity–pressure coupling is treated using the SIMPLE algorithm, and the second-order upwind scheme is used for the momentum to reduce the discretisation-induced errors in the calculations. For greater accuracy, a value of 10^{-6} is used for all residual terms.

For solution of Elrod's cavitation model an analytical method, originally described by Sawicki and Yu [36] is employed. However, the method is modified to include the variations of viscosity and density/bulk modulus with pressure and temperature, using the equations given in Sect. 3.5. Once the pressure distribution is obtained either from CFD analysis or the Elrod's method, it is integrated over the contact area to obtain the hydrodynamic reaction (see Eq. (5)).

The solution procedure is as follows:

Step 1: At a given crank angle, calculate the total force exerted on the ring due to combustion gas pressure and ring elastic force [Eqs. (3) and (4)].

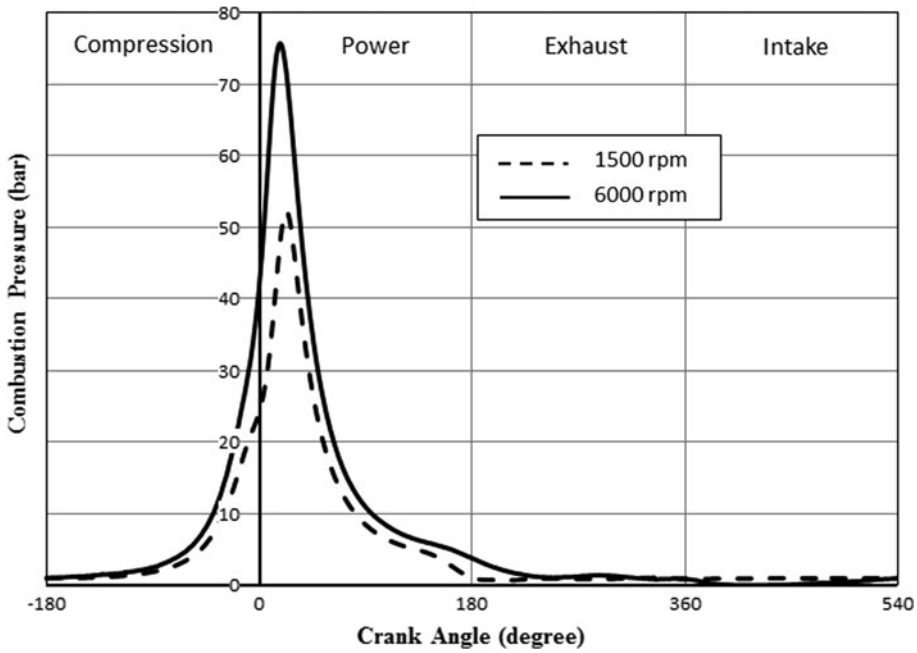

Fig. 5 Variation of chamber pressure with crank angle for engine speeds of 1,500 and 6,000 rpm

Step 2: Assuming an initial value for the minimum film thickness, lubricant film temperature and pressure distribution, and the lubricant bulk rheological properties are calculated. In addition, an initial value for the ring surface temperature is assumed.

Step 3: The contact pressure distribution is obtained using two-phase flow CFD analysis described in Sects. 3.1 and 3.2, or the Elrod's cavitation model described in Sect. 3.3.

Step 4: The predicted pressures are used to update the rheological properties, and Step 3 is repeated until the pressure in the Elrod's method in two successive iteration steps remains within the stated convergence criterion. It is noted that in the CFD approach, the lubricant rheological properties are updated internally for the generated pressure and temperature distributions as the solution proceeds. In addition, using the heat partitioning model described in Sect. 3.6, the rise in the ring surface temperature is also calculated.

Step 5: The load carried by asperities is calculated using Eq. (26).

Step 6: The pressure distribution is used to obtain the hydrodynamic reaction. Since the method of solution is quasi-static, this conjunctional reaction together with the load carried by asperities should support the total applied load exerted by the gas and ring elastic forces at each crank angle. The quasi-static balance of applied forces on the ring is sought through:

$$\mathrm{Err}_{\mathrm{load}} = \frac{|F(\varphi) - W(\varphi)|}{F(\varphi)} \leq 1.0 \times 10^{-3} \tag{36}$$

where $\mathrm{Err}_{\mathrm{load}}$ is the error in the load balance condition. If this criterion is not met, then the minimum film thickness is updated using the following equation:

$$h_m^n = (1 + \delta \mathrm{X}) h_m^o \tag{37}$$

where X is an adjusting parameter, $\mathrm{X} = F(\varphi) - W(\varphi)/\max\{F(\varphi), W(\varphi)\}$. Superscripts n and o denote new and old steps in the iteration process. A damping coefficient $\delta = 0.05$ is used to achieve faster load convergence, whilst maintaining numerical stability. It is noted that the 'dynamic mesh' concept [37] is employed for variations in the minimum film thickness in the CFD analysis. In this method, the corresponding user-defined function (UDF) determines the desired position of the ring using the dynamic mesh technique. To achieve this, a smoothing mesh method is used with a convergence tolerance of 10^{-5}

With a new value for the minimum film thickness, the Steps 2–6 are repeated until the convergence criterion in Step 6 is met.

Step 7: Calculate the corresponding viscous and boundary friction contributions, and hence the total friction, using Eqs. (34), (31) and (30). Then, proceed to the next crank angle, repeating all the above steps.

5 Results and Discussion

5.1 Pressure Distributions in Isothermal Condition

As the first step, it would be interesting to note the validity of the CFD approach developed here. A good comparison can be made with the Elrod's approach, which is traditionally used

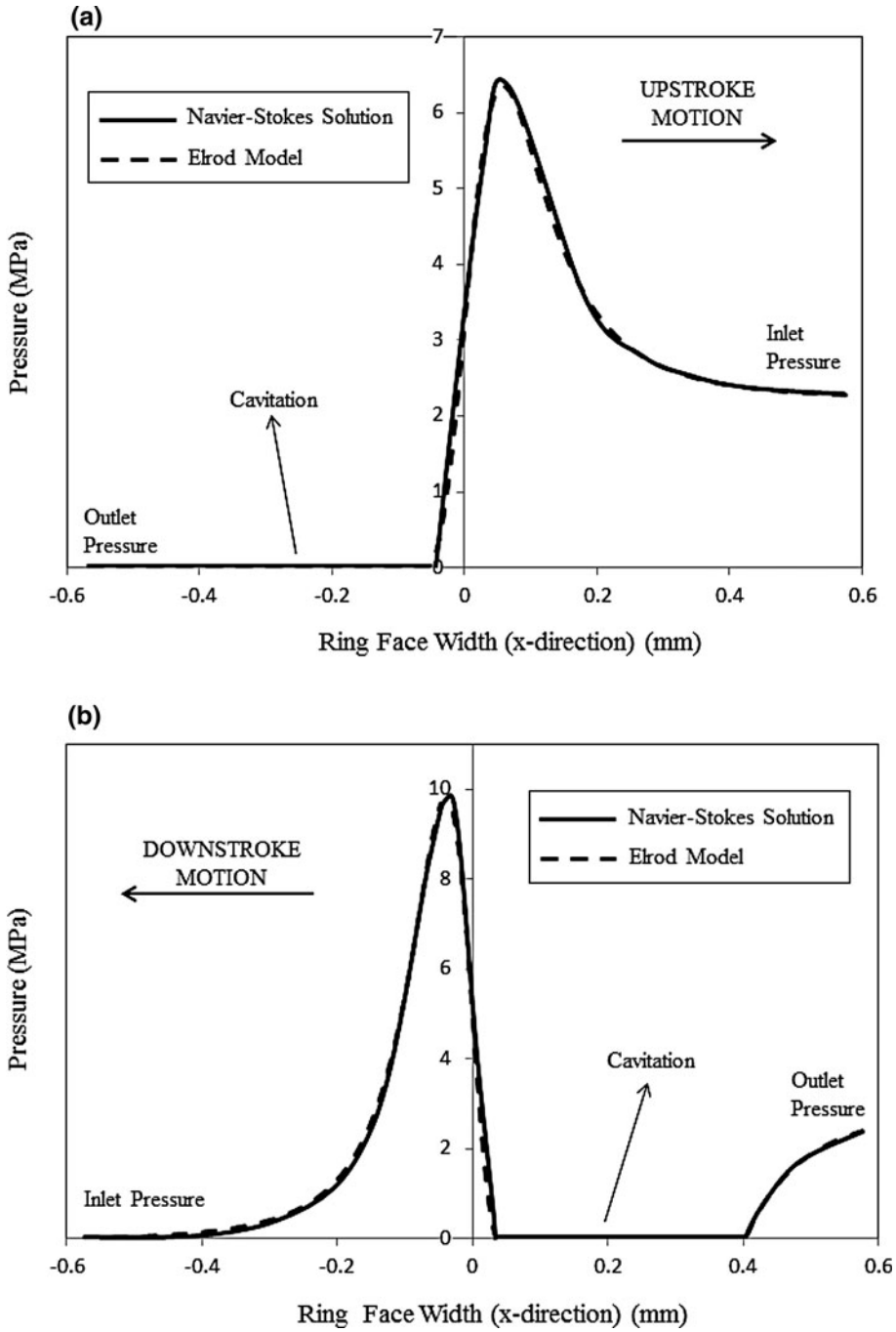

Fig. 6 Pressure distribution along the ring face width (x-direction) for **a** $\varphi = -1°$and **b** $\varphi = +1°$, at engine speed of 1,500 rpm

for such tribological contacts. Furthermore, an isothermal analysis somewhat simplifies the problem.

Figures 6, 7 and 8 present the results for axial pressure profiles along the ring face width at crank angles: $\pm 1°$, $\pm 21°$ and $\pm 90°$ under assumed isothermal conditions. The predictions are made by two different methods: (I) two-phase flow Navier–Stokes equations and (II) the Elrod's modified approach to Reynolds equation. Good agreement is observed in all cases. Note that the crank angle of 0° corresponds to the position of TDC in transition from the compression to the power stroke. The region bounded by the crank angles $\pm 1°$ corresponds to quite low speeds of entraining motion of the lubricant. Inlet reversals can be noted as the piston sense of motion alters (Fig. 6a, b). Figure 7b corresponds to the detonation point, where the maximum combustion pressure occurs. The differences between the two methods of analysis emerge in Figs. 7a, and 8a, b. These correspond to relatively lightly loaded contact conditions with higher speeds of entraining motion of the lubricant into the conjunction. These differences are

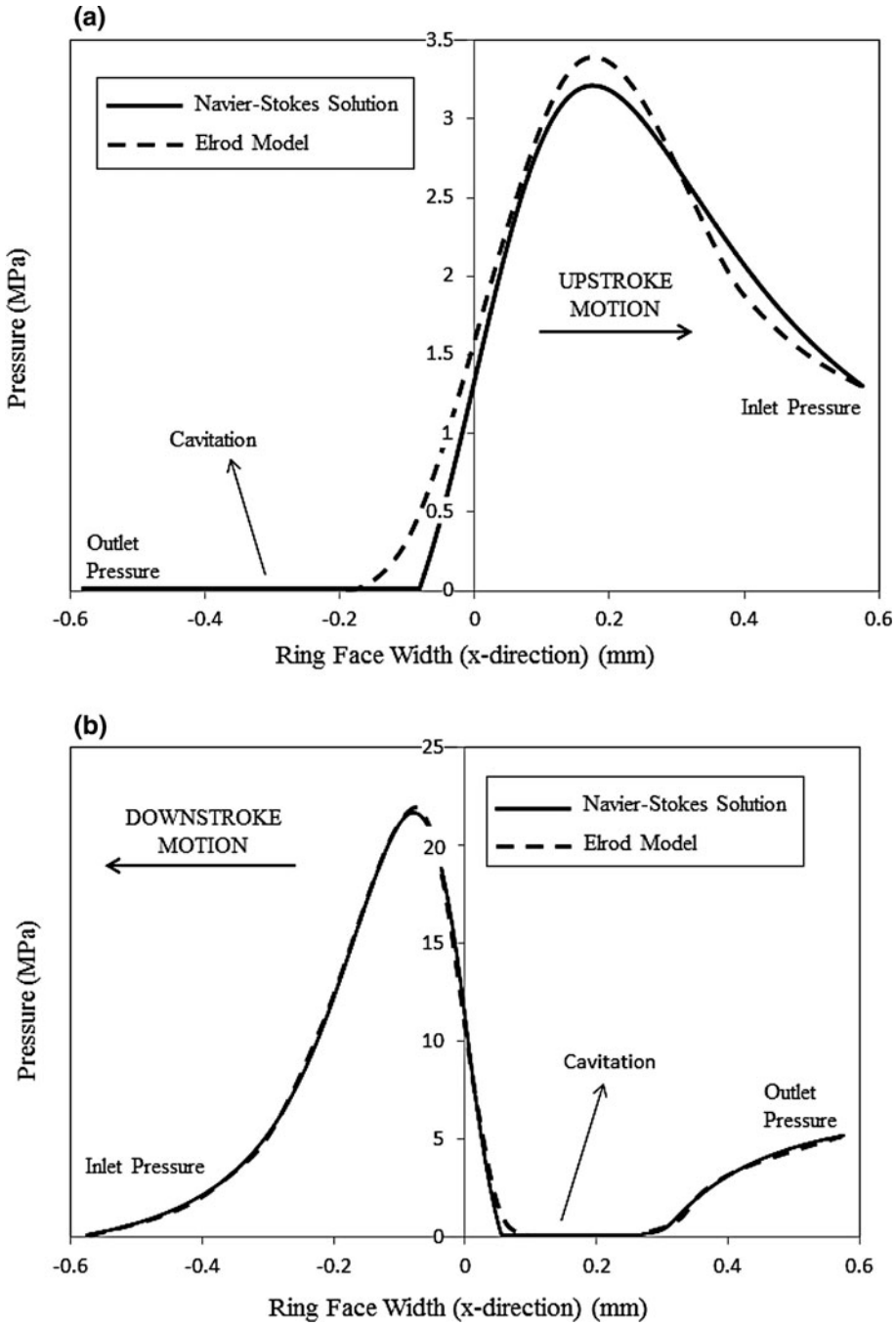

Fig. 7 Pressure distribution along the ring face width (*x*-direction) for **a** $\varphi = -21^\circ$ (*compression stroke prior to TDC*) and **b** $\varphi = +21^\circ$ (*detonation in power stroke*), at engine speed of 1,500 rpm

as the result of outlet boundary conditions, which are clearly based on the film rupture point, beyond which cavitation region occurs. With the Elrod's approach, there are prescribed contact outlet boundary conditions, which are based on the value of film ratio $\xi < 1$. The CFD approach is based on open boundary condition (i.e. there is no prescriptive outlet boundary condition for the lubricant film rupture location). Since lightly loaded conditions with higher lubricant entraining velocity (in cases of $\varphi = \pm 90^\circ$, mid-span piston position) lead to film rupture and cavitation, any prescriptive outlet conditions may be regarded as somewhat artificial. The difference is more significant in terms of friction than pressure distribution (see later).

5.2 Minimum Lubricant Film Thickness

The key parameter predicted by the lubrication model is the cyclic variation in minimum film thickness. There is clearly a direct correlation between film thickness and friction. Therefore, it is particularly important to investigate parts of engine cycle where the film thickness is insufficient to guard against direct surface interactions.

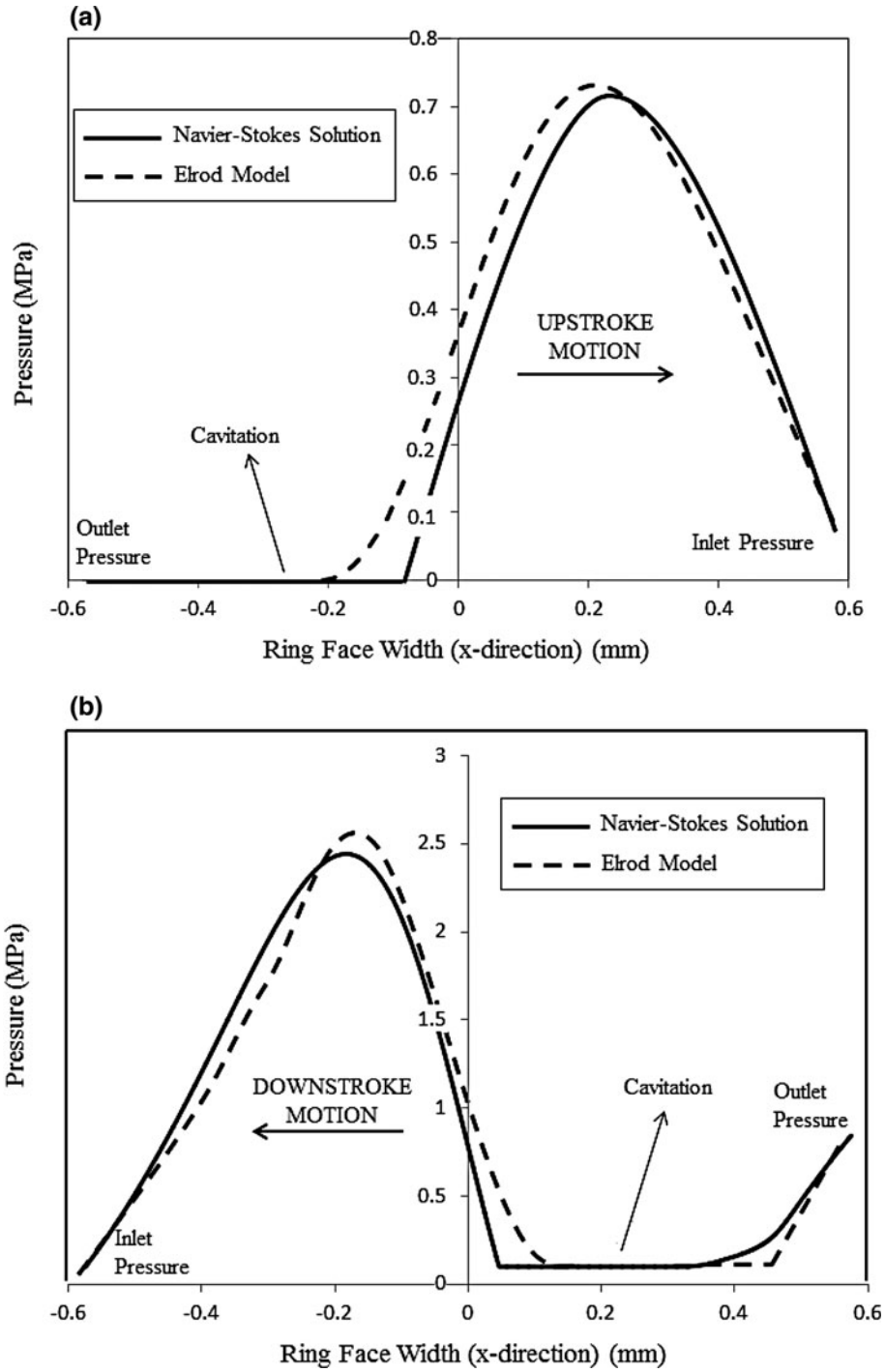

Fig. 8 Pressure distribution along the ring face width (*x*-direction) for **a** $\varphi = -90^\circ$ (*mid-compression stroke*) and **b** $\varphi = +90^\circ$ (*mid-power stroke*), at engine speed of 1,500 rpm

Figure 9 shows the CFD-predicted minimum film thickness variation for the parabolic ring profile at the engine speed of 1,500 rpm in comparison with that predicted by the Elrod's model, both under assumed isothermal conditions. The results of these analyses are quite close. Both solutions exhibit the expected characteristic shape of the curve with instances of thin films occurring around the dead centre reversals, where the lubricant entrainment velocity is negligible. Sufficient film thickness exists at the mid-stroke positions, where there is adequate entrainment velocity. The thickness of lubricant film is generally thinner during the power stroke owing to the higher gas loading of the ring. The figure also includes the CFD-predicted minimum film thickness variations for thermal condition at the same engine speed. With thermal effects taken into account, the film thickness is considerably reduced and the ring–bore conjunction resides in mixed or boundary regimes of lubrication for a significant proportion of the engine cycle.

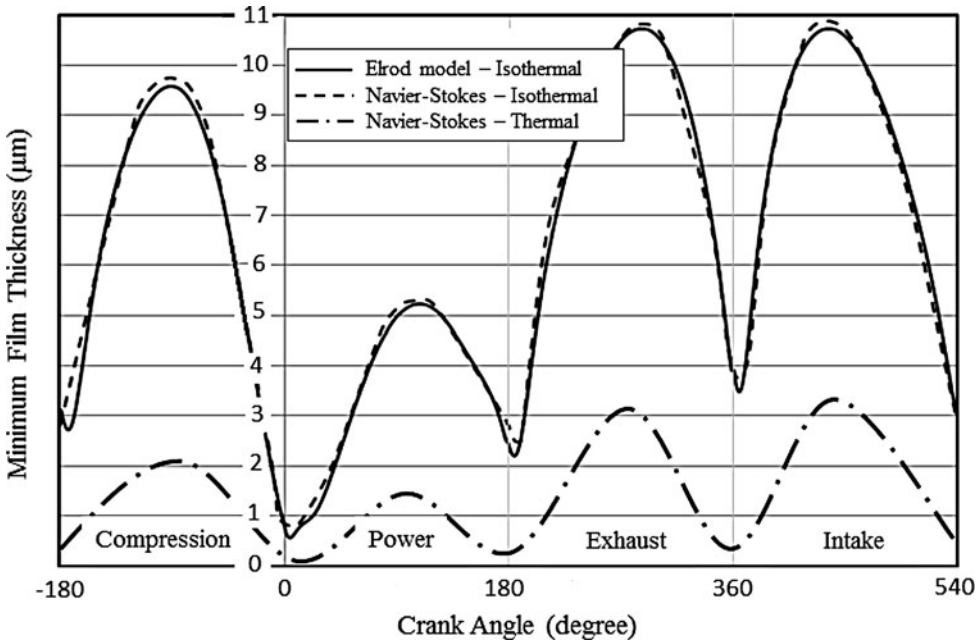

Fig. 9 Minimum film thickness at engine speeds of 1,500 rpm

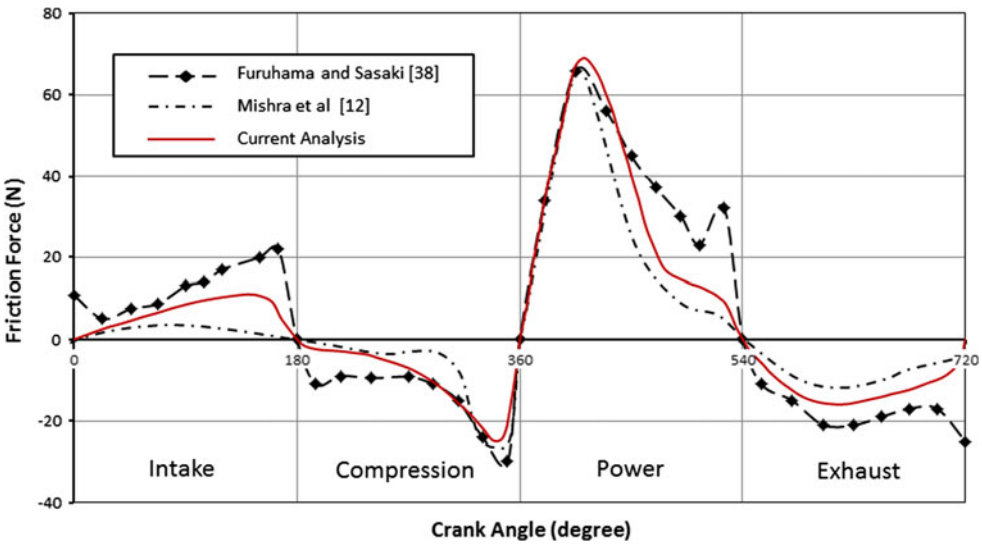

Fig. 10 Comparison of current work with experimental measurements for friction force

This is a more realistic result with regard to observed and measured friction, for instance by Furuhama and Sasaki [38] and Gore et al. [39]. Therefore, the significant differences between isothermal and thermal analyses shown by Gosh and Gupta [40] is justified, but not often noted in much of the reported studies.

5.3 Prediction of Friction

Piston-cylinder friction is a dominant source of parasitic mechanical losses in IC engines, accounting for nearly 9 % of the input fuel energy expended [41]. Therefore, one of the overriding industrial objectives is to predict frictional losses from all the conjunctions of the piston-cylinder system. Figure 10 shows the CFD-predicted friction compared with the experimental measurements by Furuhama and Sasaki [38] from a 2-cylinder rig made from an 8-cylinder Chevrolet engine running at the engine speed of 1,200 rpm. The other predictions in the figure are those by Mishra et al. [12]. The CFD predictions conform well to the experimental results and are an improvement upon those of Mishra et al. [12] which are isothermal and use Reynolds equation with Swift–Stieber exit boundary condition for the hydrodynamic contribution. The agreement is particularly striking for the power stroke and for the later stages of the compression stroke. There are some differences at mid-span in the power stroke. There seems to be more boundary interactions in the experimental results.

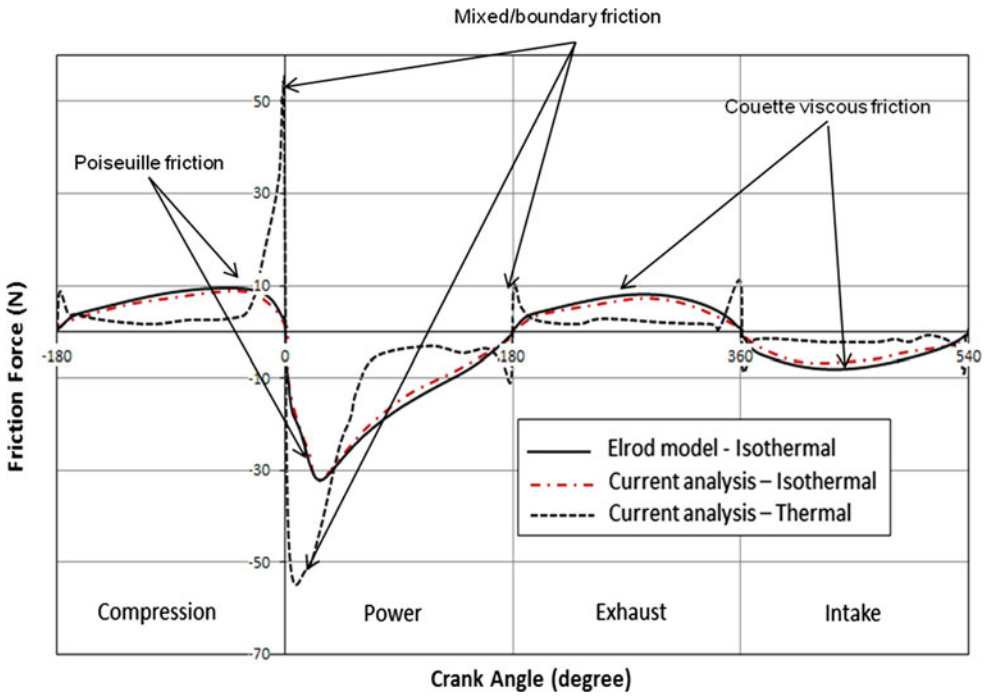

Fig. 11 Predicted friction under isothermal and thermal conditions with CFD and Elrod-type analyses

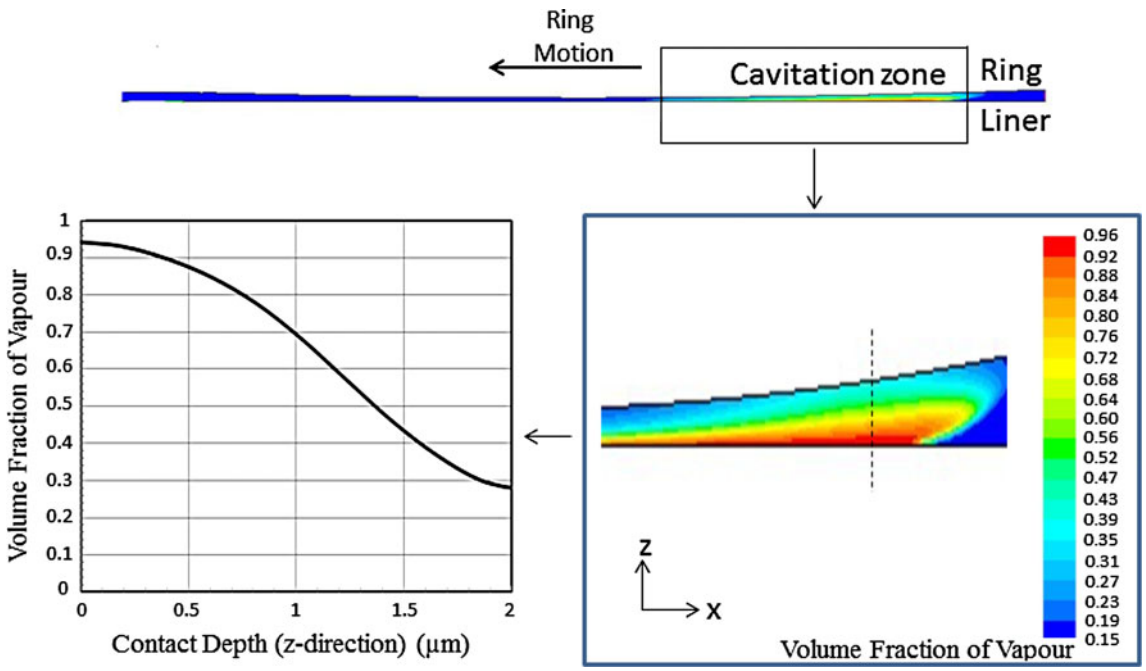

Fig. 12 Changes of vapour volume fraction into the depth of the lubricant film at the crank angle position 90° at the engine speed 6,000 rpm (cavitation zone, $x = 0.2$ mm)

This may well be because of bore out of roundness, thus some reduced clearance, which would be expected of all cylinder bores in practice. However, such data are not provided in [38]. The current analysis assumes a right circular cylindrical bore with circumferentially conforming ring–bore contact.

Comparison of friction forces for isothermal and thermal cases is demonstrated in Fig. 11. Note that the isothermal analysis would be representative of cold steady-state condition, for example, similar to those at low engine speed emission tests defined by the NEDC (New European Drive Cycle) [42], where the lubricant viscosity used in the analysis

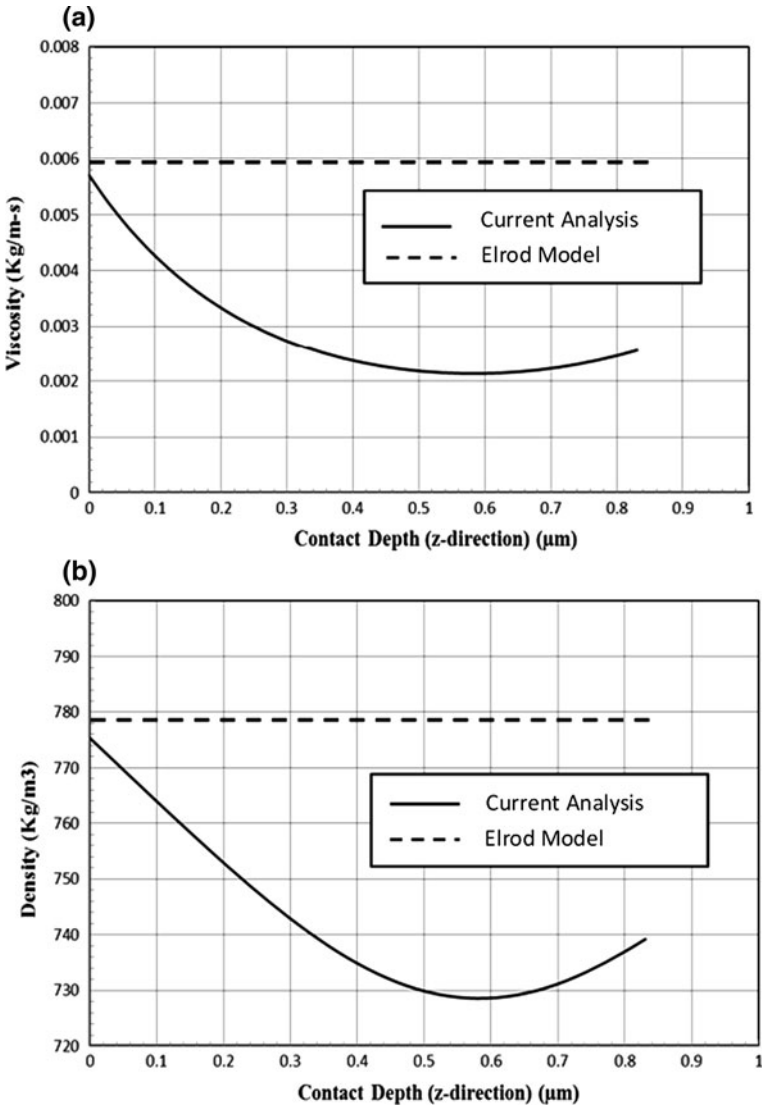

Fig. 13 The changes in lubricant viscosity (**a**) and density (**b**) into the depth of the lubricant film at the crank angle of 90° and engine speed of 6,000 rpm (full film region, $x = -0.1$ mm)

corresponds to the temperature of 40 °C. Various regions of predicted engine cycle frictional characteristics are marked on the figure. Under isothermal (cold engine condition) viscous, friction is generally higher because of a higher lubricant viscosity. Furthermore, the dominant source of viscous shear is Couette flow, which follows the piston sliding speed [second term in Eq. (29)]. The exception is the region in transition from compression to the power stroke and extending past the detonation point. Under cold engine condition, it can be seen that the pure proportionality $\tau_v \propto U$is lost in this region, because there is significant pressure loading of the ring conjunction (combustion curves in Fig. 5). In this region, lubricant action is dominated by Poiseuille shear [the first term in Eq. (29)].

The important point to note is that viscous friction, in general, is lower in the thermal case due to reduced lubricant viscosity. However, at the dead centre reversals, because of low entraining velocity, the film thickness is significantly reduced (Fig. 9), which leads to boundary interactions in the case of thermal case. This can be representative of hot steady-state portion of the NEDC emission cycle [42]. The sharp rise rate in friction characteristics at dead centre reversals, due to mixed or boundary regime of lubrication, is also marked on Fig. 11. In particular, the results show that friction at TDC reversal in transition from compression to the power stroke corresponds to a significant proportional of all cyclic frictional losses.

5.4 Fluid Properties and Flow Parameters Changes Along Depth of Film

Predictive methods based on Reynolds equation with appropriate boundary conditions, for example that of Elrod [16] or Sawicki and Yu [36], determine lubricant film rupture and reformation boundaries (Fig. 1). The cavitation

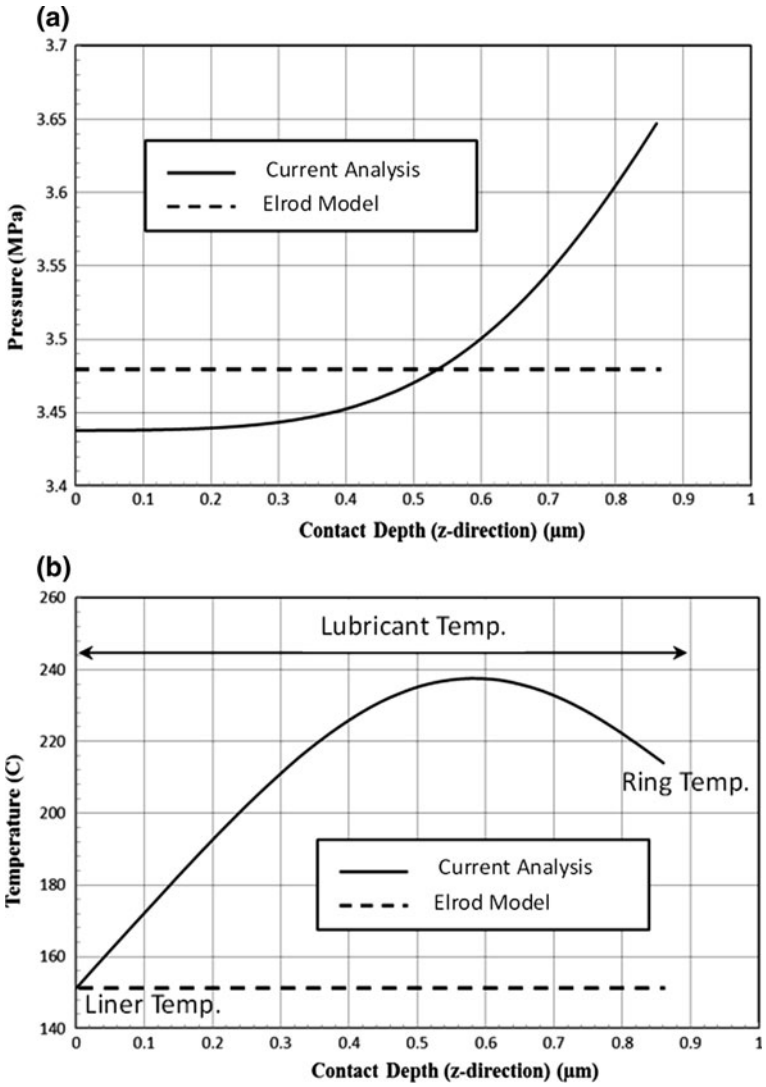

Fig. 14 Changes in lubricant pressure (**a**) and temperature (**b**) into the depth of the lubricant film at the crank angle of 90° and engine speed of 6,000 rpm (full film region, $x = -0.1$ mm)

region is regarded to be contained within the contact zone, where $\xi < 1$. However, as Reynolds equation assumes no pressure gradient through the thickness of the lubricant film due to its thinness (i.e. $dp/dz = 0$), there is no prediction of disposition of the fluid phases. The use of Navier–Stokes equations with Rayleigh–Plesset equation and analytical control-volume thermal model, described here, enables the presence of fluid phases to be surmised according to void fraction as shown in Fig. 12, in this case at the engine speed of 6,000 rpm and at crank angle of 90°. The choice of these conditions is because at higher piston sliding velocity and relatively lighter contact load, a larger variation in fluid volume fraction results in the cavitation region as shown in Fig. 12. With the Reynolds-based approaches, there is no significant contribution to friction nor to the contact load carrying capacity as the cavitation region is assumed to remain under atmospheric conditions. In the Navier–Stokes equations, there exists some contribution due to the presence of a volume of liquid lubricant.

Unlike other models, in the current CFD approach, all operating and lubricant rheological parameters alter with the depth of the lubricant film. The changes of lubricant properties and flow parameters in the z direction (film depth) for crank angle 90° at engine speed 6,000 rpm, in high-pressure zone (region of full film, $x = -0.1$ mm), are plotted in Figs. 13 and 14. The parametric variations show that the flow of lubricant through the contact may be viewed as layered streamlines at different rheological states. This means that in practice, there would be internal friction and load carrying capacity contained within the streamlined flow, which would be more realistic than the idealised conditions belying Reynolds equation.

6 Conclusions

A new thermo-mixed hydrodynamic analysis method to study transient conditions in piston compression ring–

cylinder liner conjunction is presented. The method makes use of Navier–Stokes equations, combined with Rayleigh–Plesset equation and analytical control-volume thermal model. It also incorporates the Greenwood and Tripp method to take into account the effect of asperity interactions in the region of thin films. This approach has not hitherto been reported in the literature and highlights some important findings, when compared with the traditional approaches, such as Elrod's modification to Reynolds equation, based on the JFO boundary conditions.

Firstly, the lubricant flow may be envisaged as streamlined flow with variable layered potential energy contributing to load carrying capacity and internal friction. The layered characteristic flow leads to regions with varied volume fraction of vapour in the cavitation region of the contact. The exact disposition of vapour cavities in the form of bubbles and their flow dynamics would constitute the use of Lagrange–Euler method for discrete phases in the future extension of the current research.

Secondly, the results show that except at dead centre piston reversals, the underlying mechanism for friction is through viscous shear of the lubricant. This implies that reduced viscosity of the lubricant would be beneficial in reducing friction, if an alternative palliative measure can be identified to reduce the effect of boundary friction at piston TDC reversal particularly in transition from compression to power stroke. However, reducing lubricant viscosity cannot be accommodated because the same engine oil flows through the higher load intensity contacts such as the cam–follower pair, where high loads necessitate use of lubricants which have sufficient load carrying capacity, that is, high viscosity. Palliative action at the TDC may be achieved through fabrication of surface textured reservoirs as shown by Rahnejat et al. [43] and Ryk and Etsion [44]. However, this action may lead to oil loss and lubricant degradation in fully flooded parts of the engine cycle. The current analysis indicates that in the lightly loaded parts of the engine cycle at high sliding speeds, regions of cavitation may occupy these intended textured reservoirs and reduce the load carrying capacity of the contact. Further investigation of these effective micro-bearing would be required with the approach expounded in the current analysis.

Acknowledgments The authors would like to express their gratitude to the Lloyd's Register Educational Foundation (LREF) for the financial support extended to this research. Thanks are also due to the Engineering and Physical Sciences Research Council (EPSRC) for the Encyclopaedic Program Grant, some of research findings of which are used in this paper.

References

1. Gohar, R., Rahnejat, H.: Fundamentals of Tribology. Imperial College Press, London (2008)
2. Andersson, B.S.: Company's perspective in vehicle tribology-volvo. In: Tribology Series, Vehicle Tribology, vol 18, pp. 503–506. Elsevier (1991)
3. Richardson, D.E.: Review of power cylinder friction for diesel engines. Trans. ASME J. Eng. Gas Turbine Power **122**, 506–519 (2000)
4. Morris, N., Rahmani, R., Rahnejat, H., King P.D., Fitzsimons, B.: The influence of piston ring geometry and topography on friction. Proc. Inst. Mech. Eng. Part J J. Eng. Tribol. (2012). doi: 10.1177/1350650112463534
5. Rahmani, R., Theodossiades, S., Rahnejat, H., Fitzsimons, B.: Transient elastohydrodynamic lubrication of rough new or worn piston compression ring conjunction with an out-of-round cylinder bore. Proc. Inst. Mech. Eng. Part J J. Eng. Tribol. **226**, 284–305 (2012)
6. Ma, M.T., Sherrington, I., Smith, E.H.: Implementation of an algorithm to model the starved lubrication of a piston ring a distorted bores: prediction of oil flow and onset of gas blow-by. Proc. Inst. Mech. Eng. Part J J. Eng. Tribol. **210**, 29–44 (1996)
7. Jeng, Y.: Theoretical analysis of piston ring lubrication-part I: fully flooded lubrication. Tribol. Trans. **35**, 696–706 (1992)
8. Jeng, Y.: Theoretical analysis of piston ring lubrication-pan 11: starved lubrication and its application to a complete ring pack. Tribol. Trans. **35**, 707–714 (1992)
9. Ma, M.T., Sherrington, I., Smith, E.H.: Analysis of lubrication and friction for a complete piston-ring pack with an improved oil availability model, Part I: circumferentially uniform film. Proc. Inst. Mech. Eng. Part J J. Eng. Tribol. **211**, 1–15 (1997)
10. Akalin, O., Newaz, G.M.: Piston ring-cylinder bore friction modelling in mixed lubrication regime: Part II-Correlation with bench test data. Trans. ASME J. Tribol. **123**, 219–223 (2001)
11. Mishra, P.C., Balakrishnan, S., Rahnejat, H.: Tribology of compression ring-to-cylinder contact at reversal. Proc. Inst. Mech. Eng. Part J J. Eng. Tribol. **222**, 815–826 (2008)
12. Mishra, P.C., Rahnejat, H., King, P.D.: Tribology of the ring-bore conjunction subject to a mixed regime of lubrication. Proc. Inst. Mech. Eng. Part J J. Eng. Tribol. **223**, 987–998 (2009)
13. Bolander, N.W., Steenwyk, B.D., Sadeghi, F., Gerber, G.R.: Lubrication regime transitions at the piston ring-cylinder liner interface. Proc. Inst. Mech. Eng. Part J J. Eng. Tribol. **219**, 19–31 (2005)
14. Baker, C.E., Theodossiades, S., Rahnejat, H., Fitzsimons, B.: Influence of in-plane dynamics of thin compression rings on friction in internal combustion engines. Trans. ASME J. Eng. Gas. Turbines Power **134**, 092801 (2012)
15. Chong, W.W.F., Teodorescu, M., Vaughan, N.D.: Cavitation induced starvation for piston-ring/liner tribological conjunction. Tribol. Int. **44**, 483–497 (2011)
16. Elrod, H.G.: A cavitation algorithm. Trans. ASME J. Lubr. Technol. **103**, 350–354 (1981)
17. Jakobsson, B., Floberg, L.: The Finite Journal Bearing Considering Vaporization. Trans. of Chalmers University of Tech, Gothenburg (1957)
18. Olsson, K.O.: Cavitation in Dynamically Loaded Bearings. Trans. of Chalmers University of Technology, Gothenburg (1965)
19. Haddad, S.D., Tian, K.T.: An analytical study of offset piston and crankshaft designs and the effect of oil film on piston slap excitation in a diesel engine. Mech. Mach. Theory **30**, 271–284 (1995)
20. Rahnejat, H.: Multi-Body Dynamics: Vehicles, Machines and Mechanisms. Professional Engineering Publishing, Bury St Edmunds. (IMechE and Warrandale, PA, USA: SAE, joint publishers) (1998)
21. Bin Chik, A., Fessler, H.: Radial pressure exerted by piston rings. J. Strain Anal. Eng. Des. **I**(2), 165–171 (1966)
22. Felter, C.L.: Numerical simulation of piston ring lubrication. Tribol. Int. **41**, 914–919 (2008)

23. White, F.M.: Viscous Fluid Flow, 2nd edn. McGraw-Hill, New York (1991)
24. Senocak, I., Shyy, W.: Interfacial dynamics-based modelling of turbulent cavitating flows, Part-1: model development and steady-state computations. Int. J. Numer. Methods Fluids **44**, 975–995 (2004)
25. Singhal, A.K., Li, H.Y., Athavale M.M., Jiang Y.: Mathematical Basis and Validation of the Full Cavitation Model. ASME FEDSM'01, New Orleans, Louisiana, (2001)
26. Kubota, A., Kato, H., Yamaguchi, H.: A new modelling of cavitating flows: a numerical study of unsteady cavitation on a hydrofoil section. J. Fluid Mech. **240**, 59–96 (1992)
27. De la Cruz, M., Chong, W.W.F., Teodorescu, M., Theodossiades, S., Rahnejat, H.: Transient mixed thermo-elastohydrodynamic lubrication in multi-speed transmissions. Tribol. Int. **49**, 17–29 (2012)
28. Dowson, D., Higginson, G.R.: A numerical solution to the elastohydrodynamic problem. J. Mech. Eng. Sci. **1**, 6–15 (1959)
29. Roelands, C.J.A.: Correlational aspects of the viscosity-temperature-pressure relationship of lubricating oils. Ph.D thesis, Technical University Delft, Delft, The Netherlands (1966)
30. Houpert, L.: New results of traction force calculations in elastohydrodynamic contacts. J. Tribol. Trans. ASME **107**, 241–248 (1985)
31. Lee, P.M., Stark, M.S., Wilkinson, J.J., Priest, M., Lindsay Smith, J.R., Taylor, R.I., Chung, S.: The degradation of lubricants in gasoline engines: development of a test procedure to evaluate engine oil degradation and its consequences for rheology. Tribol. Int. Eng. Ser. **48**, 593–602 (2005)
32. Olver, A.V., Spikes, H.A.: Prediction of traction in elastohydrodynamic lubrication. Proc. Inst. Mech. Eng. Part J J. Eng. Tribol. **212**, 321–332 (1998)
33. Eyring, H.: Viscosity, plasticity and diffusion as examples of reaction rates. J. Chem. Phys. **4**, 283–291 (1936)
34. Greenwood, J.A., Tripp, J.H.: The contact of two nominally flat rough surfaces. Proc. Inst. Mech. Eng. **185**, 625–634 (1970–1971)
35. Manninen, M., Taivassalo, V., Kallio, S.: On the mixture model for multiphase flow. VTT Publications 288 Technical Research Centre of Finland (1996)
36. Sawicki, J.T., Yu, B.: Analytical solution of piston ring lubrication using mass conserving cavitation algorithm. Tribol. Trans. **43**, 587–594 (2000)
37. Snyder, D.O., Koutsavdis, E.K., Anttonen, J.S.R.: Transonic store separation using unstructured CFD with dynamic meshing. In: Technical Report AIAA-2003-3913, 33th AIAA Fluid Dynamics Conference and Exhibition, American Institute of Aeronautics and Astronautics (2003)
38. Furuhama, S., Sasaki, S.: New Device for the Measurement of Piston Frictional Forces in Small Engines. Society of Automotive Engineers, Paper No. 831284 (1983)
39. Gore, M., Howell-Smith, S.J., King, P.D., Rahnejat, H.: Measurement of in-cylinder friction using the floating liner principle. In: ASME 2012 International Engine Division Spring Technical Conference, May 6–9, 2012, Torino, Italy, Paper No. ICES2012-81028, 6 pp
40. Ghosh, M.K., Gupta, K.: Thermal effect in hydrodynamic lubrication of line contacts-piezoviscous effect neglected. Int. J. Mech. Sci. **40**, 603–616 (1998)
41. Andersson, B.S., Company's perspective in vehicle tribology. In: Leeds-Lyon Symposium on Tribology, pp. 503–506 (1991)
42. Chong, W.W.F., Teodorescu, M., Rahnejat, H.: Mixed thermo-elastohydrodynamic cam—tappet power loss in low-speed emission cycles. Int. J. Engine Res. (2012). doi:10.1177/1468087412461631
43. Rahnejat, H., Balakrishnan, S., King, P.D., Howell-Smith, S.: In-cylinder friction reduction using a surface finish optimization technique. Proc. Inst. Mech. Eng. Part D J. Automob. Eng. **220**, 1309–1318 (2003)
44. Ryk, G., Etsion, I.: Testing piston rings with partial laser surface texturing for friction reduction. Wear **261**, 792–796 (2006)

Tribology International 90 (2015) 164–174

Contents lists available at ScienceDirect

Tribology International

journal homepage: www.elsevier.com/locate/triboint

On the boundary conditions in multi-phase flow through the piston ring-cylinder liner conjunction

H. Shahmohamadi [a], M. Mohammadpour [a], R. Rahmani [a], H. Rahnejat [a,*], C.P. Garner [a], S. Howell-Smith [b]

[a] Wolfson School of Mechanical and Manufacturing Engineering, Loughborough University, Loughborough, LE11 3TU Leicestershire, UK
[b] Capricorn Automotive Ltd., Basingstoke, Hampshire, UK

ARTICLE INFO

Article history:
Received 6 November 2014
Received in revised form
25 March 2015
Accepted 16 April 2015
Available online 24 April 2015

Keywords:
Mixed multi-phase regime of lubrication
Zero reverse inlet boundary
Cavitation
Friction

ABSTRACT

Prediction of load capacity and friction depends on the assumed boundary conditions. The inlet comprises swirl and counter flows, admitting only a portion of the inward flow into the conjunctional gap. At the contact exit, the lubricant film ruptures with multi-phase flow through a cavitation region. Therefore, the boundary conditions affect the load carrying capacity and friction. A Navier–Stokes solution of multi-phase flow, including vapour transport is presented, with determined realistic boundary conditions.

The evaluated boundaries agree with potential flow analysis satisfying compatibility conditions, not hitherto reported in literature. The investigation is extended to the determination of optimum compression ring contacting geometry.

1. Introduction

The main function of the compression ring in the piston-ring pack is to seal the combustion chamber. This reduces low-by, lubricant degradation and power loss. Effective sealing prevents the high-pressure gases escaping from the combustion chamber as well as lubricant leakage into it. Therefore, sealing is critical for improved efficiency and reduced emissions. However, ideal sealing yields a diminished ring-cylinder liner conjunctional gap, which worsens friction [1]. Piston assembly accounts for approximately 35–45% of all the internal combustion engine frictional losses [2]. The top compression ring's contribution is nearly 30% of these losses, which translates to 2–3% of the fuel energy consumption. Therefore, it is essential to strike a balance between good sealing function and low friction. To gain a good insight into the interplay between sealing, load carrying capacity and frictional characteristics of the piston ring conjunctional gap, a plethora of issues need to be addressed, making for very complex and time intensive numerical analysis. These issues include physical non-conformity of an elastic ring (subject to modal elastodynamic behaviour: in its radial plane [3] as well as axially out-of-plane such as ring flutter [4]) with the cylinder bore, which in reality is not an idealised right circular cylinder, either radially or in its axial profile [5]. The non-conformity leads to loss of sealing and blow-by as well as oil loss and cavitation in diverging gaps. Most analyses disregard circumferential non-conformity of ring-bore conjunctional gap as this would depend on the engine cylinder configuration. This approach, although idealistic, yields a generic-type solution. It also leads to a one dimensional solution for ring-bore conjunctional gap in the axial direction of the ring (*i.e.* along the ring's contacting face-width profile).

An important consideration is the use of realistic boundary conditions. In most hydrodynamic analyses a fully-flooded (drowned) inlet boundary is assumed, again to keep within a generic approach. However, it is clear, through observation of wear as well as *in situ* measurements of friction using floating liner methods [6–8] that an insufficient supply of lubricant exists in parts of the piston cycle. In the upstroke motion of the piston, the inlet to the top compression ring conjunctional gap resides within the combustion chamber. There would unlikely be a sufficient supply of lubricant in such instances to assume a fully flooded inlet. In fact, it is shown that mixed or boundary regime of lubrication is prevalent at instances of contact reversal by many numerical predictions [9–10] and experimental measurements of friction [6–8]. Therefore, determination of appropriate inlet boundary conditions, leading to contact starvation is essential for realistic prediction of prevailing tribological conditions. The same is also true of contact outlet boundary conditions, where the falling pressures in a diverging gap result in lubricant film rupture in the presence of retarding

* Corresponding author.
E-mail address: h.rahnejat@lboro.ac.uk (H. Rahnejat).

http://dx.doi.org/10.1016/j.triboint.2015.04.025

Nomenclature

A	apparent contact area
A_a	asperity contact area
b	ring axial face-width
c	maximum crown height of ring
d	ring thickness
E_1	Young's modulus of elasticity of the ring
E_2	Young's modulus of elasticity of the liner
E'	equivalent (reduced) modulus of elasticity
f_b	boundary friction
f_{mass}	vapour mass function
f_t	total friction
f_v	viscous friction
F_T	ring tension force
F_G	combustion gas force
F_2, $F_{5/2}$	statistical functions
g	ring end gap
h	elastic film shape
h_s	ring axial profile
I	ring cross-sectional second area moment of inertia
k	speed ratio
l	connecting rod length
L	ring peripheral length
P_f	frictional power loss
p	absolute pressure
p_{atm}	atmospheric pressure
p_{sat}	liquid saturation vaporisation pressure
p_L	ring lower edge pressure
p_U	ring upper edge pressure
p_e	elastic pressure
p_g	gas pressure
p_h	hydrodynamic pressure
r	crank-pin radius
r_0	nominal bore radius
R_c,R_e	transfer source terms related to the growth and collapse of the vapour bubbles
t	time
ΔU	ring sliding velocity
U_1, U_2	surface velocities of contacting bodies
$\vec{V}$	velocity vector
$\vec{V}_v$	velocity vector of the vapour phase
W	contact load
W_a	load share of asperities
W_h	load carried by the lubricant film
x	axial position along ring face width
x_c	oil film rupture point
Z	pressure–viscosity index

Greek symbols

α_0	pressure–viscosity coefficient
β_0	temperature–viscosity coefficient
φ	crank angle
λ	Stribeck's oil film parameter
ζ	number of asperity peaks per unit contact area
η	lubricant dynamic viscosity
η_0	lubricant dynamic viscosity at atmospheric pressure
κ	average asperity tip radius
$\lambda_,$	Stribeck's oil film parameter
λ'	pressure-induced shear coefficient
ϑ_i	ratio of the film thickness at the stagnation point to the central film thickness
ϑ_e	ratio of the film thickness at the rupture point to the central film thickness
ν_1	Poisson's ratio of the ring material
ν_2	Poisson's ratio of the liner material
ρ	lubricant density
ρ_0	lubricant density at atmospheric pressure
ρ_m	mixture density
ρ_v	vapour density
σ_r	liner surface roughness
σ_l	ring surface roughness
σ_{RMS}	root mean square roughness of the counterface: $\sigma_{RMS}=\sigma_r+\sigma_l$
τ	shear stress
τ_L	limiting shear stress
τ_{L0}	limiting shear stress at atmospheric pressure
Γ	diffusion coefficient
ω	engine rotational speed

friction, which also causes cavitation. The effect of cavitation was studied by Chong et al. [11], who used Elrod's approximation [12] to the Jakobsson and Floberg [13] and Olsson [14] (JFO) cavitation boundary conditions. Other general cavitation algorithms, taking into account the effect of lubricant compressibility, arising from conjunctional geometry or surface topography, whilst upholding the conservation of mass flow have also been reported [15]. Chong et al. [11] showed that cavitation reduces the lubricant availability at the Top Dead Centre (TDC) reversal, thus causing a starved contact in parts of the power stroke in the vicinity of the TDC. With the Elrod algorithm, the continuity of Couette flow is only assured, whilst the usually assumed Swift–Stieber outlet boundary condition does not embody the principle of conservation of mass flow. Therefore, in order to accurately determine the position of film rupture at the exit boundary condition, the principle of conservation of mass flow would necessitate the solution of Navier–Stokes equations. This was the approach undertaken by Shahmohamadi et al. [16] who provided a combined solution of Navier–Stokes and energy equations for the ring-bore contact with an assumed fully flooded inlet. No lubricant outlet boundary conditions were imposed. This is the approach also undertaken in the current paper, also taking into account the vapour transport equation and the Rayleigh–Plesset void fraction. Additionally, only pressure boundary conditions are imposed, instead of those based on lubricant availability such as a fully flooded inlet. This expounded approach, not hitherto reported in literature, is more realistic and without artificially imposed lubricant flow conditions. In practice observation of flow at the boundary points has shown some reverse flow, which is dependent upon surface velocities of the contiguous solids as well as thermal conditions. An analytical approach was presented by Tipei [17], based on potential flow, surface velocities and compatability conditions to replicate the observations for the case of rolling contacts. Recently, analysis of rolling circular point contact by Mohammadpour et al. [18] using Tipei's boundary conditions showed very good agreement with the experimental work initially reported by Johns-Rahnejat and Gohar [19]. Therefore, additionally this paper extends the approach of Tipei [17] to the case of sliding contact of compression ring along the cylinder liner to establish the validity of potential flow analysis at boundary points against the full Navier–Stokes solution.

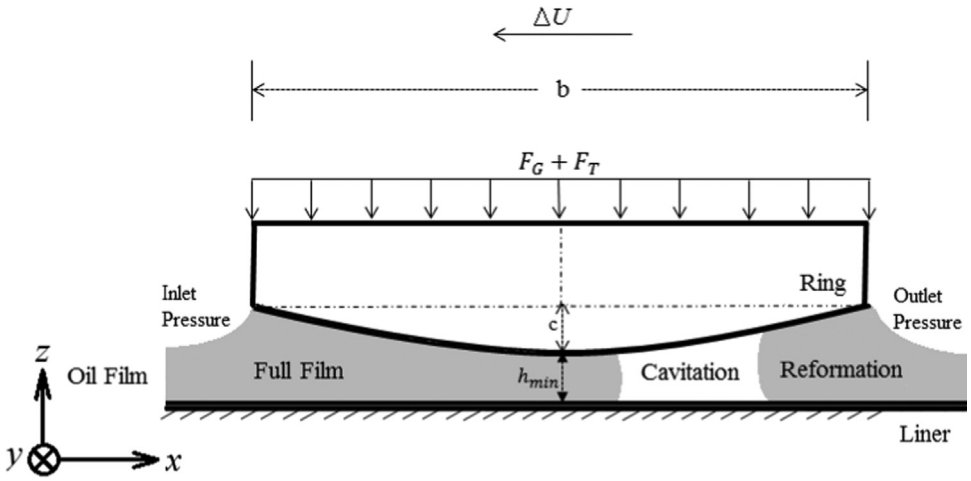

Fig. 1. Schematics of piston ring-liner conjunctional gap.

2. Physics of the problem

Fig. 1 shows the schematics of ring-liner conjunctional gap along the axial face-width of the ring. The ring subject to this analysis is a steel barrel faced rectangular ring[1], where the profile of the ring, $h_s(x)$ is assumed to be parabolic:

$$h_s(x) = \frac{cx^2}{(b/2)^2} \tag{1}$$

where, c is the crown height of the ring and b is its face-width.

In this paper good conformance of the ring to the liner surface is assumed in the circumferential direction of the bore. Therefore, the problem is simplified to a one dimensional contact, which is valid for ring-bore contact of bore diameter-to-ring face-width ratio: $2\pi r_0/b \geq 30$ as shown by Haddad and Tian [20], which is applicable to the engine studied here. The studied engine is a high performance V12 4-stroke naturally aspirated engine. The general data for the studied engine is provided in Table 1.

It is assumed that the ring does not undergo any relative motion with respect to the retaining groove. In practice, the ring may be subject to axial motion termed as ring flutter [5]. The piston sliding velocity is [21]:

$$\Delta U(\varphi) = -r\omega \sin\phi\left\{1 + \cos\varphi\left[\left(\frac{l}{r}\right)^2 - \sin^2\varphi\right]^{-\frac{1}{2}}\right\} \tag{2}$$

where φ is the crank-angle, l is the connecting rod length, r the crank pin radius and ω is the engine rotational speed. $\Delta U = U_2 - U_1 = U_2$ is the sliding velocity of the ring relative to the stationary liner: $U_1 = 0$.

The forces acting on the ring are considered as those in its radial plane. The ring is subjected to two outward forces: ring elastic tension force F_T and the gas forceF_G, acting on the inner rim of the ring. These forces conform the ring to the bore surface. Therefore, total outward force (towards the liner interface), acting on the ring is:

$$F = F_T + F_G \tag{3}$$

The ring tension force, F_T, is obtained as [22]:

$$F_T = p_e b r_0 \quad \left(\text{where } p_e = \frac{gEI}{3\pi b r_0^4}\right) \tag{4}$$

where, p_e is the elastic pressure, r_0 is the bore nominal radius and g is the ring end gap in its free (unfitted) state. The gas force acting on the back of the ring varies according to the chamber pressure in an engine cycle, thus:

$$F_G(\varphi) = 2\pi b r_0 p_g(\varphi) \tag{5}$$

The value of the gas pressure can be obtained through an appropriate blow-by analysis. In the current analysis the gas pressure is assumed to be equal to the in-cylinder pressure.

The outward radial forces (*i.e.* ring elastic tension and the gas force) are supported by the hydrodynamic reaction and the share of load carried by any interacting asperities. This is often the load shared by a small portion of asperities on the opposing surfaces. Thus, the instantaneous contact load is determined as $W(\varphi) = W_a(\varphi) + W_h(\varphi)$, where the hydrodynamic reaction is the integrated lubricant pressure distribution as follows:

$$W_h(\phi) = 2\pi r_0 \int_0^b p_h(\phi) dx\, dy \tag{6}$$

As shown in Fig. 1, in general, there are three conjunctions regions: (i) full film, (ii) film rupture and cavitation, and (iii) lubricant film reformation. A suitable two-phase flow model needs to be employed alongside the Navier–Stokes equations. This should take the form of vapour transport equation.

The share of load carried by the interacting asperities on the contiguous solid surfaces is obtained as [23]:

$$W_a = \frac{16\sqrt{2}}{15}\pi(\zeta\kappa\sigma)^2\sqrt{\frac{\sigma}{\kappa}}E^* A F_{5/2}(\lambda) \tag{7}$$

The dimensionless group $\zeta\kappa\sigma$ is known as the Tabor's roughness parameter, whilst σ/κ is a measure of a typical asperity slope [1]. These can be obtained through topographical measurements. E^* is the composite effective modulus of elasticity:

$$\frac{1}{E^*} = \frac{1-\nu_1^2}{E_1} + \frac{1-\nu_2^2}{E_2} \tag{8}$$

where ν_1 and ν_2 are the Poisson's ratios, and E_1 and E_2 the moduli of elasticity for the materials of bounding solid surfaces. The statistical function $F_{5/2}(\lambda)$ is introduced to match the assumed Gaussian distribution of asperities as a function of the Stribeck oil film parameter, $\lambda = h/\sigma$. Using a fifth-order polynomial curve fit this statistical function can be described as follows:

$$F_{5/2}(\lambda) = -0.0046\lambda^5 + 0.0574\lambda^4 - 0.2958\lambda^3 + 0.7844\lambda^2 - 1.0776\lambda + 0.6167 \tag{9}$$

[1] Internal combustion engines – Piston rings – Part 2: Rectangular rings made of steel should comply withISO 6622-2:2003

Table 1
Engine data.

Parameters	Values	Units
Crank-pin radius, r	39.75	mm
Connecting rod length, l	138.1	mm
Bore radius, r_0	44.5	mm
Ring crown height, c	10	μm
Ring axial face-width, b	1.15	mm
Ring radial width, d	3.5	mm
Ring free gap, g	10.5	mm

Table 2
Material properties and surface topographical parameters.

Parameters	Values	Units
Liner material	Grey cast iron[a]	–
Modulus elasticity of liner material	92.3	GPa
Poisson ratio for liner material	0.211	–
Density for liner material	7200	kg/m^3
Ring material	Steel SAE 9254[b]	–
Modulus elasticity of ring material	203	GPa
Poisson ratio for ring material	0.3	–
Roughness parameter ($\zeta\kappa\sigma$)	0.04	–
Measure of asperity gradient (σ/κ)	0.001	–
Density for ring material	7700	kg/m^3

[a] Centrifugal cast iron to ASTM-A 48, Class 30/DIN 1691 GG 30 standard.
[b] The ring has face coating of Chromium. The coating and slight back chamfer have known effects on ring tension and force correction factors, not taken into account in the current analysis. Back chamfers have a subtle, but important effect on the gas sealing of the ring against the groove.

Table 2 lists the materials' properties as well as the surface topographical parameters for both the compression ring and the cylinder liner.

3. Numerical model

3.1. General Navier–Stokes equation

The continuity and Navier–Stokes momentum equations for compressible viscous fluid flow are [24] as follows:

$$\frac{D\rho}{Dt}+\rho\nabla.\vec{V}=0 \tag{10}$$

$$\rho\frac{D\vec{V}}{Dt}=-\nabla p+\nabla.(\bar{\tau}_{ij})+\vec{F} \tag{11}$$

where D/Dt is the covariant derivative operator, ρ is the lubricant density, p is pressure, $\bar{\tau}_{ij}$ is the viscous stress tensor and $\vec{F}$ is the body force field vector. $\vec{V}=U\hat{i}+V\hat{j}+W\hat{k}$ is the velocity vector in which U is the component of velocity in the direction of axial lubricant entrainment, V is that in the side-leakage direction; along the y-axis (which may reasonably be discarded as there is negligible side-leakage in the thin film ring-bore conjunctional gap), and W is that in the direction of lubricant thickness. The viscous stress tensor is as follows:

$$\bar{\tau}_{ij}=\eta\left(\frac{\partial U_i}{\partial x_j}+\frac{\partial U_j}{\partial x_i}-\delta_{ij}\frac{2}{3}\nabla.\vec{V}\right) \tag{12}$$

where η is the local lubricant dynamic viscosity and δ_{ij} is the Kronecher delta. One possibility in a CFD model is to evaluate fluid viscosity as a function of pressure along the liner and into the depth of the lubricant film. The latter is neglected in the conventional hydrodynamic lubrication approach using Reynolds equation, where: $p/z=0$.

3.2. Cavitation model – vapour mass fraction and vapour transport equations

With cavitation, the liquid–vapour mass transfer (evaporation and condensation) is governed by the vapour transport equation as [25]:

$$\frac{\partial}{\partial t}(\alpha_v\rho_v)+\nabla.(\alpha_v\rho_v\vec{V}_v)=R_e-R_c \tag{13}$$

where ρ_v is the vapour density, $\vec{V}_v$ is the velocity vector of the vapour phase, R_e and R_c are mass transfer source terms related to the growth and collapse of vapour bubbles. The growth and collapse of a bubble cluster is modelled based on the Rayleigh–Plesset equation, describing the growth of a single vapour bubble in a liquid. This provides the rate equation, controlling vapour generation and condensation. Singhal et al. [26] assumed that a working fluid is a mixture of liquid and vapour and introduced a modified form of the above equation, based upon the vapour mass fraction, f_{mass} as follows:

$$\frac{\partial}{\partial t}(\rho_m f_{mass})+\nabla.(\rho_m\vec{V}_v f_{mass})=\nabla.(\Gamma\nabla f_{mass})+R_e-R_c \tag{14}$$

where ρ_m is the mixture density and Γ is the diffusion coefficient. The mass transfer rate expressions are derived from the Rayleigh–Plesset equations. The cavitation bubble size should be confined for the diminutive tribological conjunctions. This is based upon the limiting bubble size considerations (*i.e.* interfacial surface area per unit volume of vapour). The rates for formation/growth and collapse of cavitation bubbles are functions of the instantaneous local pressure and are given by:

$$R_e=C_e\frac{V_{ch}}{\sigma_s}\rho_l\rho_v\sqrt{\frac{2(p_{sat}-p)}{3\rho_l}}(1-f_{mass}),\quad \text{for}\quad p<p_{sat} \tag{15}$$

$$R_c=C_c\frac{V_{ch}}{\sigma_s}\rho_l\rho_v\sqrt{\frac{2(p-p_{sat})}{3\rho_l}}f_{mass},\quad \text{for}\quad p>p_{sat} \tag{16}$$

where the suffices l and v denote the liquid and vapour phases respectively, V_{ch} is the characteristic velocity, σ_s is the surface tension coefficient of the lubricant, p_{sat} is the liquid saturation vaporisation pressure at a given temperature and C_e and C_c are empirical constants, considered to be 0.02 and 0.01 respectively [26].

3.3. Lubricant rheology

The lubricant bulk rheological properties including density and viscosity are affected by pressure. The density–pressure relationship is [27]

$$\rho=\rho_0\left[1+\frac{0.6\times10^{-9}(p-p_{atm})}{1+1.7\times10^{-9}(p-p_{atm})}\right]\left[1-0.65\times10^{-3}(T-T_0)\right] \tag{17}$$

Using an analytical control volume thermal mixing model Morris et al. [28] showed that the lubricant temperature in the compression ring-liner conjunctional gap closely follows that of the

Table 3
Lubricant properties in atmospheric pressure and 40 °C.

Parameters	Values	Units
Lubricant viscosity, η_0	0.05	Pa s
Lubricant density, ρ_0	833	kg/m^3
α_0	1×10^{-8}	Pa^{-1}
β_0	0.004	K^{-1}
Atmospheric limiting shear stress (τ_{L0})	2.3	MPa
Pressure-induced shear coefficient (λ')	0.047	-
Average liner temperature for fired engine condition, T	160	°C

cylinder liner, with generated heat due to viscous shear heating of the lubricant in passage through the contact only accounting for less than 2%. Therefore, in the current analysis the average temperature of the liner, T is used (see Table 3). This temperature was measured directly from a fired engine. T_0 is considered to be the bulk oil sump temperature. Hence, no solution of energy equation was deemed necessary.

In the current analysis the measured average temperature of the lubricant (grade 5W30) is used for the vaporisation pressure. In practice the vaporisation pressure alters with lubricant temperature which in turn varies with the liner temperature as noted above.

The lubricant viscosity–pressure and temperature dependence is given as follows [29]:

$$\eta = \eta_0 \exp\{(\ln \eta_0 + 9.67) \times \left[-1 + \left(1 + 5.1 \times 10^{-9}(p - p_{atm})\right)^{z_0} \left(\frac{T - 138}{T_0 - 138}\right)^{-s_0}\right]\} \quad (18)$$

where

$$z_0 = \frac{\alpha_0}{5.1 \times 10^{-9}(\ln \eta_0 + 9.67)} \text{ and } s_0 = \frac{\beta_0 (T_0 - 138)}{(\ln \eta_0 + 9.67)} \quad (19)$$

where α_0 is the viscosity–pressure coefficient and β_0 is the viscosity–temperature coefficient. Details of lubricant rheological parameters are given in Table 3.

3.4. Boundary conditions

Fig. 2 shows the computation domain with the boundary surfaces being that of the ring and the liner. The boundary conditions are also indicated in the figure. The ring surface is subject to the sliding velocity U_2, whilst that of the liner is stationary. Furthermore, it is assumed that the lubricant adheres to the boundary solid surfaces (*i.e.* no slip boundary condition).

As it can be seen the pressure inlet and outlet boundary conditions are used for the lower and upper edges of the ring/liner contact as follows:

$$\begin{cases} p_h(-b/2) = p_L \\ p_h(+b/2) = p_U \\ p_h(x_c) = p_{sat} \end{cases} \quad (20)$$

Therefore, when the piston undergoes its upstroke motion, the inlet pressure is that of the combustion chamber shown in Fig. 3, whilst at the exit the crank-case pressure is assumed to be the atmospheric pressure. On the other hand, for the down-stroke sense of the piston, the inlet pressure is set to that of the crank-case (atmospheric) pressure, whilst the outlet pressure is that of the combustion chamber. The chamber pressure varies with the engine stroke, speed and throttle demand. Fig. 3 shows the measured in-cylinder pressure by a plug-type Kistler pressure transducer for the engine speed of 1500 rpm at 63% throttle input.

The cylinder liner has been assumed as the stationary wall with no-slip boundary condition. On the other hand, the ring is assumed as the moving wall with no-slip boundary condition. The engine sump (operation pressure) and cavitation vaporisation pressure are assumed to be at atmospheric pressure (101.3 kPa) at all times. No exit boundary condition such as the Swift–Steiber or Prandtl–Hopkins boundary conditions need to be stated with the Navier–Stokes approach.

3.5. Solution procedure

A 2D CFD model is developed. A computational mesh is generated using the ANSYS Design Modeller. The geometrical nature of the problem examined here imposes the use of only quadrilateral cells. After conducting a grid sensitivity analysis, 40 divisions were employed across the lubricant film (z-direction) and 1500 divisions along the ring face-width (x-direction), thus a mesh of 60,000 computational cells is used. Calculation of Reynolds number for the studied conditions showed that the flow is well within the laminar region.

A pressure-based mixture multi-phase model [30] is chosen for the present CFD analysis. No discrete regional control volume(s) of vapour are defined in such a model, which would require specifically defined boundary conditions. Instead, the mixture model provides the void fraction in various regions of the contact. The velocity–pressure coupling is treated using the SIMPLE algorithm and the second-order upwind scheme is employed for conservation of momentum to reduce the discretisation-induced errors in the calculation process. To achieve better accuracy, an error tolerance value of 10^{-6} is used for all the parametric residual terms.

Once the pressure distribution is obtained from the solution of Navier–Stokes equations, it is integrated over the contact area to obtain the hydrodynamic reaction (Eq. (6)).

The following solution procedure is followed:

Step 1: At a given crank angle, φ the total contact load F, exerted on the ring due to combustion gas pressure and ring elastic force is calculated (Eq. (3)).

Step 2: Assuming an initial value for the minimum film thickness (gap size), the lubricant pressure distribution and its rheological properties are calculated. The contact pressure

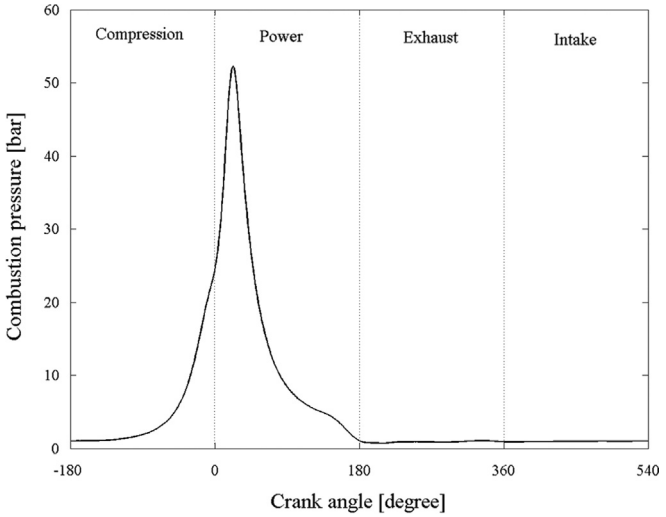

Fig. 3. Variation of chamber pressure with crank angle for engine speeds of 1500 rpm.

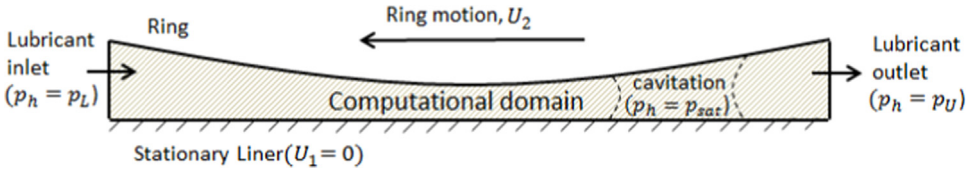

Fig. 2. Schematics of the computational domain and boundary conditions.

distribution is obtained using two-phase flow CFD analysis. It is noted that in the CFD approach the lubricant rheological properties are updated internally for the generated pressure and the assumed average contact temperature as the solution proceeds.

Step 3: The load carried by the asperities is calculated using Eq. (7). The pressure distribution is used to obtain the hydrodynamic reaction (Eq. (6)). Since the method of solution is quasi-static, this conjunctional reaction together with the asperity- carried load are assumed to support the total applied load exerted by the gas pressure and ring elastic force at each crank angle. The quasi-static balance of applied forces on the ring is sought through:

$$Err_{load}=\frac{|F(\varphi)-W(\varphi)|}{F(\varphi)}\leq 10^{-3} \tag{21}$$

If this criterion is not met, then the minimum film thickness is updated using the following equation:

$$h_m^n=(1+\delta X)h_m^o \tag{22}$$

where X is an adjusting parameter, $X=F(\varphi)-W(\varphi)/\max\{F(\varphi), W(\varphi)\}$. Superscripts n and o denote new and old steps in the iteration process. A damping coefficient $\delta=0.05$ is used to achieve faster load convergence, whilst maintaining numerical stability. It is noted that the 'dynamic mesh' concept [31] is employed for variations in the minimum film thickness in the CFD analysis. A smoothing mesh method is used with a convergence tolerance of 10^{-5}.

With a new value for the minimum film thickness, the Steps 2 to 3 are repeated until the convergence criterion in Step 3 is met.

4. Analytically determined boundary conditions

Tipei [17] investigated the inlet and outlet boundaries of the domain in hydrodynamic contacts. He noted that in the inlet zone, there are swirl flows, where some reverse flow (counter flow) occurs at the inlet as is also observed in the experimental observations [32]. This means that only a fraction of the lubricant at the inlet meniscus is admitted into the contact domain. The counter flows cease at the stagnation point, where: $\partial\vec{V}/\partial z=0$ and $\vec{V}=0$ (is the normal direction to the conjunction plane). This condition os known as the Prandtl–Hopkins boundary condition and defines the zero-reverse flow boundary. Considering the potential flows in the inlet region, Tipei found the compatibility condition as follows [17]:

$$\begin{aligned}&\cot^2\pi\left[\tfrac{1}{2}-\tfrac{1-k}{f(k)}\right]-\cot^2\pi\sqrt{\left[\tfrac{1}{2}-\tfrac{1-k}{f(k)}\right]^2-\tfrac{2k}{f(k)}}\\&=\cot\pi\left\{\frac{1}{2}-\frac{1-k}{f(k)}-\sqrt{\left[\frac{1}{2}-\frac{1-k}{f(k)}\right]^2-\frac{2k}{f(k)}}\right\}\\&\times\cot\pi\left\{\frac{1}{2}-\frac{1-k}{f(k)}+\sqrt{\left[\frac{1}{2}-\frac{1-k}{f(k)}\right]^2-\frac{2k}{f(k)}}\right\}\end{aligned} \tag{23}$$

where

$$k=\frac{U_1}{U_2} \tag{24}$$

where U_1 and U_2 are surface velocities of contacting bodies (cylinder liner and the piston ring respectively). The function $f(k)$ depends on the pressure gradient at the inlet. The values of $f(k)$ for the usually encountered cases of the surface velocity ratio k are listed in Table 4. In the case of the piston ring conjunctional gap, $k=0$ and $f(k)=4$.

Table 4
Calculated values for $f(k)$.

k	$f(k)$
0	4
0.5	7.8
1	32/3

Tipei [17] assumed a similar approach for the determination of separation boundary at the exit constriction, leading to the determination of the lubricant film rupture point, using the Prandtl–Hopkins conditions:

$$\frac{\cosh\vartheta_i}{\cosh\vartheta_e}=\frac{1-\frac{1}{3}(1+\frac{2\sqrt{k}}{1+k})}{1-\frac{f(k)}{6(1+k)}} \tag{25}$$

$$\begin{aligned}&\left[1-\tfrac{1}{3}\left(1+\tfrac{2\sqrt{k}}{1+k}\right)\right]\tanh\vartheta_e-\left[1+\tfrac{f(k)}{6(1+k)}\right]\tanh\vartheta_i-\left[1-\tfrac{f(k)}{6(1+k)}\right]\\&\cosh\vartheta_i\left[\arcsin(\tanh\vartheta_e)-\arcsin(\tanh\vartheta_i)\right]=0\end{aligned} \tag{26}$$

ϑ_i and ϑ_e are the ratios of film thickness at the inlet and the exit to the minimum film thickness respectively. Therefore, after calculating the parameters from Eqs. (25) and (26) and having the minimum film thickness and the film shape (Eq. (1)), the distance of the inlet stagnation and outlet separation points from the centre of the ring can be found. This assumption agrees well with the experimental observations of Birkhoff and Hays [32] and Mohammadpour et al. [16].

Alternatively if instead of the Prandtl–Hopkins boundary condition the Swift–Stieber conditions ($\partial p/\partial z=0$ and $p=0$) is used, then:

$$\frac{\cosh\vartheta_e}{\cosh\vartheta_i}=1-\frac{f(k)}{6(1+k)} \tag{27}$$

and

$$\begin{aligned}&\tanh\vartheta_e-\left[1+\tfrac{f(k)}{6(1+k)}\right]\tanh\vartheta_i-\left[1-\tfrac{f(k)}{6(1+k)}\right]\cosh\vartheta_i\\&\times\left[\arcsin(\tanh\vartheta_e)-\arcsin(\tanh\vartheta_i)\right]=0\end{aligned} \tag{28}$$

These two boundary conditions give similar values at the inlet, but predict different values for the lubricant film rupture points at the outlet. Later, it is shown that the Prandtl–Hopkins boundary conditions conform closer to the open exit boundary determined through two-phase flow solution of Navier–Stokes equations.

5. Determination of generated friction

A friction model is required in order to calculate the parasitic losses in the conjunction. The total friction comprises two components; boundary friction and viscous friction:

$$f_t=f_v+f_b \tag{29}$$

At any instant of time, viscous shear of the lubricant film is obtained as [1]:

$$\vec{\tau}=\left|\pm\frac{h}{2}\nabla p-\Delta\vec{V}\frac{\eta}{h}\right| \tag{30}$$

If the shear stress remains below the limiting shear stress of the lubricant [33,34], then the calculated value from Eq. (30) is used. For shear values exceeding the limiting value, which is a property of lubricant and dependent on pressure, the limiting shear stress becomes [34]:

$$\tau_L=\tau_{L0}+\lambda' p \tag{31}$$

The values of the coefficients in the above equation are presented in Table 3. Then, the viscous friction force is obtained as:

$$f_v = \tau A, \tag{32}$$

where $A = 2\pi r_0 b$ is the apparent contact area.

When the Stribeck oil film parameter, $\lambda = h/\sigma \leq 3$, a mixed regime of lubrication is encountered. In this case a non-Newtonian high shear thin film is assumed to form at the summit of the asperities or trapped in-between them. Under this condition, the shear stress can exceed its limiting value, and it is assumed to equate to the limiting value given by Eq. (31). The asperity pressure is as follows:

$$p_a = \frac{W_a}{A_a} \tag{33}$$

The share of load carried by the asperities, W_a is calculated using Eq. (7). A small portion of asperities carry this load, the total summit area of which is obtained through statistical analysis. For an assumed Gaussian distribution of asperities, this area is obtained as follows [23]:

$$A_a = \pi^2(\zeta\kappa\sigma)^2\sqrt{\frac{\sigma}{\kappa}}AF_2(\lambda) \tag{34}$$

where $F_2(\lambda)$ is a function, representative of the Gaussian distribution of asperities in terms of λ (the Stribeck oil film parameter):

$$F_2(\lambda) = -0.0018\lambda^5 + 0.0281\lambda^4 - 0.1728\lambda^3 + 0.5258\lambda^2 - 0.8043\lambda + 0.5003 \tag{35}$$

Now having the limiting shear stress at the asperity tips and the asperity surface area, the boundary friction can be calculated as follows:

$$f_b = \tau_L A_a \tag{36}$$

Therefore, the combination of Eqs. (29)–(36) and Eq. (7) gives the total friction generated in the conjunctional gap. The total power loss from the ring-bore conjunctional gap is due to this friction:

$$P_f = f\Delta U \tag{37}$$

6. Results and discussion

Initially, a comparison is made between the inlet and outlet boundaries predicted through the current CFD approach and those calculated using the analytical method (described in Section 4) using the approach highlighted originally by Tipei [17]. The potential flow analysis (Eqs. (23) and (24)), together with the Prandtl–Hopkins boundary conditions yield one set of inlet and outlet conditions. Alternatively, the solution of the same potential flow with Swift–Stieber boundary conditions results in another set of inlet and outlet conditions. The intention for this comparative study is twofold. Firstly, it constitutes a form of validation for the CFD approach as the analytical approach has shown very good agreement for the determination of boundary conditions with the experimental observations of Birkhoff and Hays [32] as well as with the experimental circular point contact conditions [18], both under rolling conditions. Secondly, the applicability of the analytical method for the determination of boundary conditions for sliding contacts can also be ascertained.

Table 5 lists 3 sets of predicted inlet and outlet boundaries, 2 of which are based on the analytical method for Prandtl–Hopkins and Swift–Stieber boundary conditions respectively (using the potential flow analysis) and the third set is that obtained by the current CFD approach. Close agreement between the CFD predictions and the analytical results can be observed. CFD – predicted inlet stagnation boundary agrees very well with both the Swift–Stieber and Prandtl–Hopkins boundary conditions. For the outlet boundary conditions, the CFD results conform much closer to the Swift–Stieber boundary.

Table 5
Calculated inlet and outlet distances (stagnation point and separation point).

	CFD	Analytical method, Prandtl–Hopkins boundary condition	Analytical method, Swift–Stieber boundary condition
Inlet distance [μm]	267	265	260
Outlet distance [μm]	85	151	76

In fact, most reported analyses of piston ring conjunctional gap routinely employ the Swift–Stieber boundary conditions at the exit constriction [9–11,35,36]. Arcoumanis et al. [37] reported numerical analysis of compression ring conjunctional gap with various outlet boundary conditions, including Swift–Stieber, limiting case of the Floberg boundary and the Coyne–Elrod cavitation boundary [38]. They found that the predicted film thickness, using the Swift–Stieber boundary conditions showed closer agreement with their experimentally measured film thickness. Their findings are in line with the current CFD predictions and the analytical potential flow analysis described here.

Fig. 4 is a typical velocity flow field for the inlet-to-central conjunctional region, obtained through the current analysis. It shows the stagnation point, where the zero-reverse inlet boundary is reached ($\partial\vec{V}/\partial z = 0$ and $\vec{V} = 0$), Prandtl–Hopkins inlet boundary. This point is far from the usually assumed fully flooded inlet, which is often assumed to be at the leading edge of the ring, beyond the swirl flow region. This finding indicates that only a portion of an assumed available flow is admitted into the conjunction-proper beyond the stagnation point. Hence, under the conditions shown, and in fact throughout the engine cycle, only a partially flooded inlet is attained. The reason for this is the recirculating (swirl) flow in the inlet wedge of the conjunction as shown clearly in the zoomed-in inset to the figure.

The recirculating flow is a function of the velocity ratio of the contiguous surfaces which alters according to the piston sliding velocity. This is a function of the crank angle position. It also depends on the wedge angle as a function of the ring profile, which in turn determines the minimum film thickness. Therefore, load carrying capacity of the conjunctional gap is affected by the ring profile and the inlet boundary (the inlet wedge velocity flow field). As the hydrodynamic load carrying capacity is critical in guarding against asperity interactions, in theory, one can optimise the ring contacting face-width to enhance the load carrying capacity.

Fig. 5 shows the generated conjunctional pressure distributions for the actual ring face-width of $b = 1.15$ mm (Table 1) and its variously assumed multiples up to $3b$ in the down-stroke sense of the piston. The leading edge of the ring is at the assumed atmospheric pressure (gauge pressure, $p = 0$ in the figure). A minimum film thickness of 1μm is assumed (as a constraint) in this analysis. This enables the study of load carrying capacity of the contact as influenced by the changes arising at the inlet with differing ring face-widths.

As expected, the results show increasing load carrying capacity because of an increased conjunctional area. However, the increase is not proportional to the contact face-width as would be the case with an assumed fully flooded inlet, where:

$$W_h = \frac{2.9b\eta\Delta U}{h_0} \tag{38}$$

which is based on the Swift–Stieber exit boundary condition [1], h_0 being the minimum film thickness (kept constant for all the cases in Fig. 5). Hence, at the same ring sliding speed, ΔU, $W_h \propto b$, Thus, doubling the ring face-width would double the load carrying

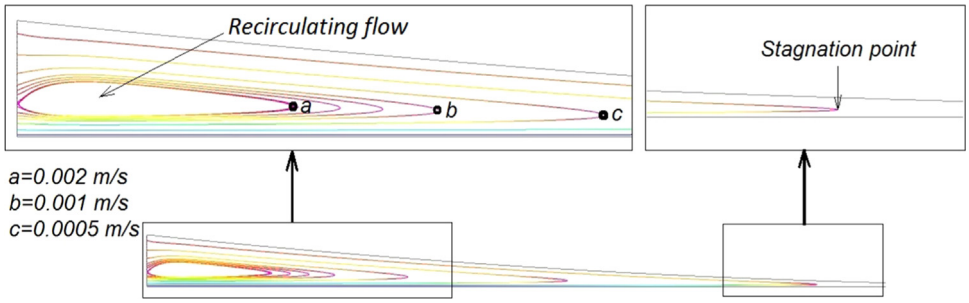

Fig. 4. Typical velocity flow field in the inlet region of the sliding conjunction.

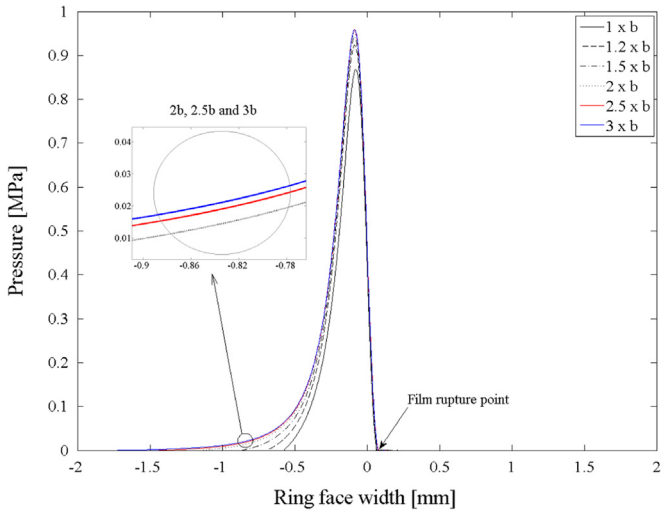

Fig. 5. The streamlines of the flow in the ring specified in Table 2 compared with those of various scaled widths.

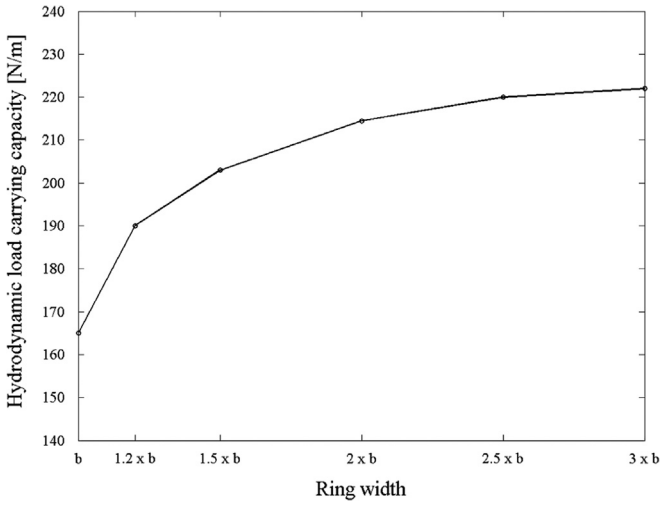

Fig. 6. Shows the load carrying capacity per unit length for different rings of Fig. 5.

capacity. With realistic boundary conditions the position of the stagnation point alters and thus the area of conjunction-proper is not a direct function of ring face-width only. Therefore, the load carrying capacity and the pressure distribution are dependent on the inlet flow field. The results in Fig. 5 show that the inlet trail to the position $p=0$ on the left-hand side of the pressure traces is extended with an increasing face-width, but in none of the cases reaches anywhere near the leading edge of the ring (*i.e.* all contacts are only partially flooded). Furthermore, progressively increasing the ring face-width only marginally lengthens the conjunctional inlet trail as shown in the inset to the figure. Thus, progressively a reduced load carrying capacity would result. Fig. 6 clearly shows this trend. The underlying reason is best observed by the inward flow into the contact conjunction. This is shown in Table 6. The physical inlet is assumed at the leading edge of the ring face-width. This is analogous to assuming a fully flooded inlet. Clearly, if a constant minimum film thickness is assumed at the same sliding velocity, but with an increased contact area, then a larger volumetric lubricant flow rate is required to maintain fully flooded conditions. The difference in the flow rate at the physical inlet and that at the central contact through the minimum film thickness accounts for the backward (reverse and swirl) flow in the inlet zone. It can be seen that this difference progressively increases with an increasing ring face-width. Therefore, only a portion of the volume of the lubricant made available at the nib of the contact is actually admitted to the contact conjunction, and in none of the cases a fully flooded condition is noted. This is the reason behind partially flooded lubricated contacts in practice, which is not confined to the ring-liner conjunctional gap only. Clearly, the outward flow from the contact at the separation boundary equates that through the minimum film thickness constriction. This is simply a

Table 6
Mass flow rates through the content.

	Physical inlet flow (kg/s)	Central contact flow (kg/s)	Outlet flow(kg/s)
B	8.88×10^{-5}	8.751×10^{-5}	8.751×10^{-5}
1.2*b*	9.95×10^{-5}	8.792×10^{-5}	8.792×10^{-5}
1.5*b*	1.12×10^{-4}	8.825×10^{-5}	8.825×10^{-5}
2*b*	1.27×10^{-4}	8.848×10^{-5}	8.848×10^{-5}
2.5*b*	1.37×10^{-4}	8.858×10^{-5}	8.858×10^{-5}
3 *b*	1.40×10^{-4}	8.860×10^{-5}	8.860×10^{-5}

restatement of the principle of conservation of mass, embodied in continuity equation together with the Navier–Stokes equations. The flow at the outlet, beyond the lubricant film rupture boundary can contain significant vapour content, thus the reason for the inclusion of vapour transport equation in the analysis.

Often fully flooded inlet conditions are assumed during the various engine strokes. However, the measured friction [6–8] or film thickness [39] indicate mixed or boundary regimes of lubrication at or in the vicinity of the TDC. Hydrodynamic regime of lubrication is found to be dominant in other locations, such as at piston mid-span locations in the various engine strokes. Fig. 7 shows the predicted minimum film thickness at various locations. Mid-span locations are in the compression stroke (-90° crank angle), power stroke (90° crank angle), exhaust stroke (270° crank angle) and the intake stroke (450°crank angle). The positions $\pm5^\circ$ crank angle correspond to the transition from the compression to power stroke through the TDC, where mixed or boundary regimes of lubrication are prevalent [7–11]. Obviously, the minimum film thickness is reduced for all ring face-width cases during the reversal because of the reducing sliding velocity of the piston. The minimum

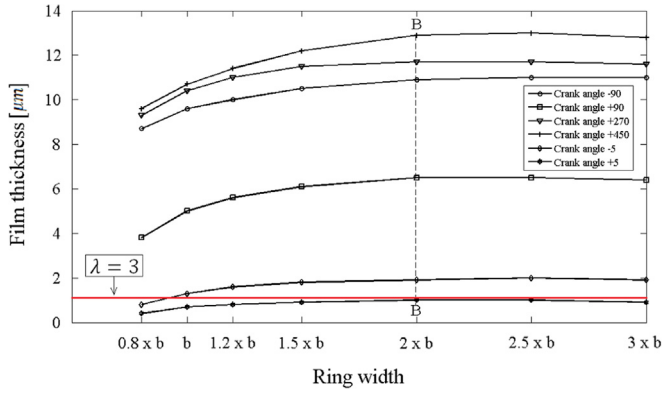

Fig. 7. Variation of minimum film thickness for different ring widths at piston mid-span positions and 5° crank angle either side of the TDC (combustion).

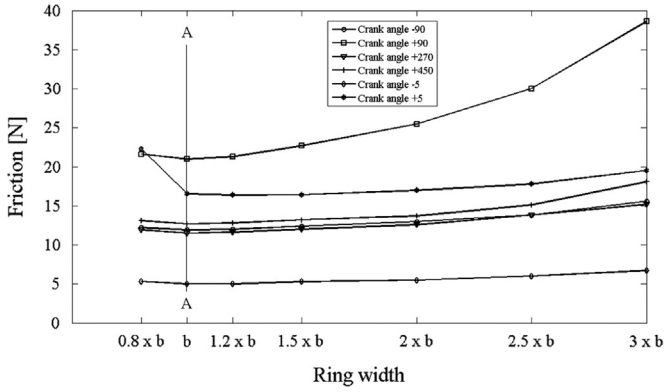

Fig. 8. Variation of friction for different ring widths for piston at mid-span positions.

film thickness is also reduced during the compression and power strokes, because of increased pressure loading behind the ring. The line = 3, where $=h/\sigma_{RMS}$ is the Stribeck's oil film parameter, represents the boundary between lubricated hydrodynamic condition and mixed regime of lubrication. It can be seen that for the region $-5^\circ \le \varphi \le 5^\circ$ the lubricant film thickness is quite thin and thus a mixed regime of lubrication would be expected.

It can be seen that in all cases the film thickness gradually increases up to the ring face-width of 2*b* before no further gain is noted. The contact load, *F* (Eq. (3)) is known for the ring-liner conjunction at these locations. Therefore, an increasing film thickness with the broadening ring contact face-width (up to an optimum) is indicative of enhanced hydrodynamic action. To ascertain this, it would be instructive to determine the total friction (viscous and boundary contributions) for these cases.

Fig. 8 shows the predicted friction for the same positions as in Fig. 7. There is no correspondence between the optimum conditions in Fig. 7 (thickest minimum conjunctional film for a ring face-width of 2*b*, indicated by the vertical line BB) and the minimum conjunctional friction for the ring width *b* (line AA in Fig. 8). In the piston mid-span locations there is insignificant contribution due to asperity interactions as the minimum lubricant film thickness is in excess of 3 μm in all cases (Fig. 7), the least film thickness of the investigated crank angles occurring during the power stroke (crank angle of 5°). Furthermore, the change in the film thickness is fairly small in the case of each particular location, thus changes in viscous shear (Eq. (30)) are marginal when dealing with a particular crank angle. Of course, these changes are not negligible at different crank angle positions, because of the sliding speed, effective lubricant viscosity and the

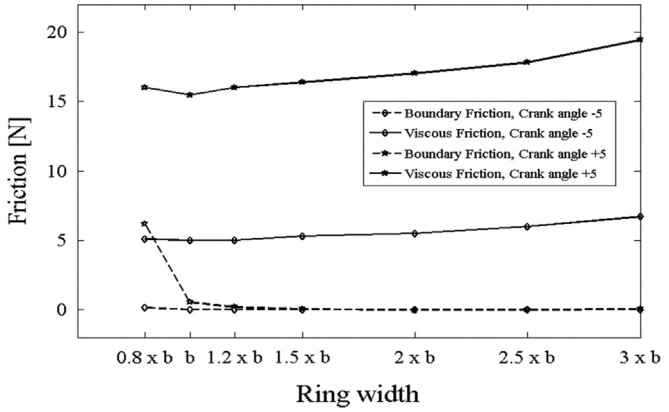

Fig. 9. Viscous and boundary contributions to generated friction immediately prior to, and just after the TDC reversal (combustion).

film thickness (see Eq. (38)). The increasing friction is also as the result of increased lubricated contact area between the inlet stagnation point (the zero reverse boundary) and the lubricant film rupture point. This indicates that maximum viscous friction occurs at the mid-span position in the power-stroke, whilst the maximum boundary friction takes place at the TDC reversal for the crank angle of 5°. In fact, Fig. 9 shows the contributions from viscous and boundary frictions during the TDC reversal. Even in these locations the main contribution is due to viscous friction, with fairly thin films and increased pressure loading behind the ring; Poiseuille friction. The shear stress is given by Eq. (30), where the first term on the right-hand side is the contribution due to Poiseuille shear, which is a function of pressure gradient, which is higher at the TDC reversal and increases in the power stroke.

Fig. 10 shows the position of lubricant film rupture and the subsequent cavitation region, which is also shown by the zoomed-in inset to the figure. The contours in the figure represent different levels of void fraction (volume fraction of liberated vapour in the bulk lubricant). The figure shows significant amount of vapour content, which reduces both the load carrying capacity as well as viscous friction.

Fig. 11 shows the variation in vapour fraction for various crank-angle positions with different assumed ring contacting face-width. Important points to note are reduced vapour fraction in the power stroke in comparison with that in the other strokes. This is expected, because of a higher contact pressure. This is clearly shown through the TDC reversal where there is lower vapour fraction for the crank angle of 5° (start of the power stroke) than −5° (end of the compression stroke). With less vapour content, viscous friction is increased accordingly (Figs. 7 and 8).

7. Conclusions

The paper shows that the compression ring-liner conjunctional gap is only partially flooded, irrespective of a sufficient volume of lubricant assumed at a physical inlet set at the leading edge of the ring. The inlet and outlet boundary conditions, determined through combined solution of Navier–Stokes and vapour transport equations, conform closely to the potential flow analysis of Tipei [17]. This puts the realistic inlet boundary at the stagnation point, where no reverse flow takes place. This is in line with the use of Prandtl–Hopkins boundary conditions. At the contact outlet, the current analysis agrees with Swift–Stieber boundary conditions to determine the position of lubricant film rupture. Furthermore, the use of Rayleigh–Plesset equation within the analysis determines the cavitation zone.

The key finding of the analysis is the determination of the effect of ring contact face to optimise tribological conditions. This shows that a unique optimal ring face-width cannot be found, which

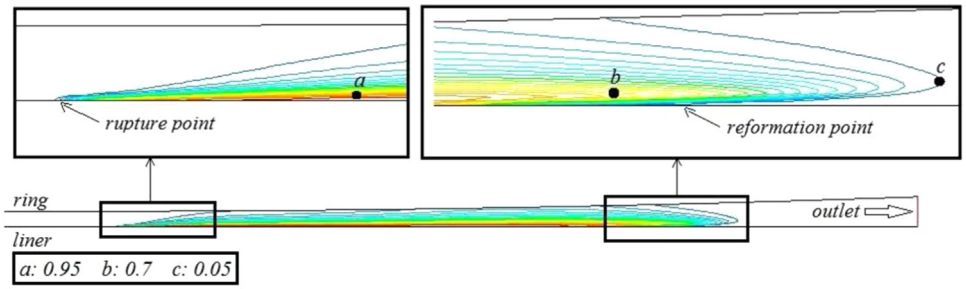

Fig. 10. Contact exit boundary with contours of vapour content.

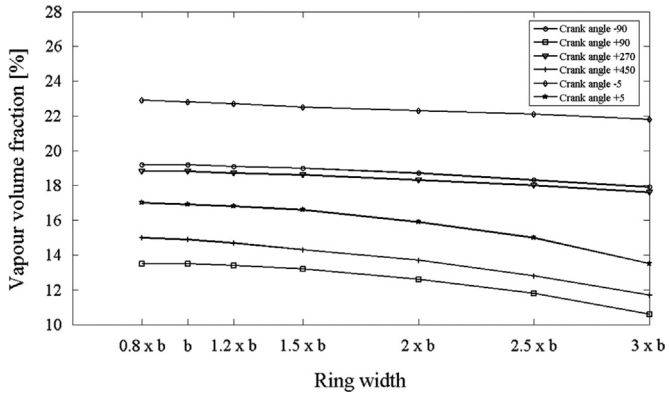

Fig. 11. Vapour content variation in different engine strokes and ring face-width.

would optimise film thickness (thus, the load carrying capacity) as well as friction (comprising viscous and boundary contributions). This is because of the transient nature of the conjunction, which is also affected by contact temperature, generation of vapour and changes in contact kinematics as well as gas pressure loading.

Ideally, a near-optimal solution can be sought through multivariate optimisation techniques. However, there are also practical engineering considerations which may inhibit use of certain ring geometries. At high speeds the ring is subject to high inertial forces, which would potentially, at critical points, unseat the more heavier compression rings (*e.g.* $>3b$) from their lower sealing face, thereby degrading operational performance [39]. Indeed, ISO 6622-2 suggests that ring widths should be limited to an upper limit of 2.5 mm (or 2.17*b* in the case of the current analysis). On the other hand, a thin ring (e.g. 0.8*b*) can be subject to considerable modal response (radial in-plane vibration and axial out-of-plane twist [3,4]), which can result in loss of sealing, blow-by and reverse blow-by.

Together with material and manufacturing limitations, the above considerations effectively narrows the available choice of ring axial face-width to a far narrower band than that implied by the results of parametric optimisation studies highlighted here.

Acknowledgements

The authors wish to express their gratitude to the Lloyd's Register Foundation (LRF) for the financial support extended to the International Institute for Cavitation Research. Thanks are also due to the Engineering and Physical Sciences Research Council (EPSRC) for the Encyclopaedic Programme Grant (EP/G012334/1); some of research findings of which are used in this paper. The technical and financial support of Capricorn Automotive is also acknowledged.

References

[1] Gohar R, Rahnejat H. Fundamentals of tribology. London, UK: Imperial College Press; 2008 ISBN: 10-1-84816-184-0.
[2] Richardson DE. Review of power cylinder friction for diesel engines. Trans ASME, J Tribol 2000;122(4):506–19.
[3] Baker CE, Theodossiades S, Rahnejat H, Fitzsimons B. Influence of in-plane dynamics of thin compression rings on friction in internal combustion engines. J Eng Gas Turbines Power 2012;134(9):092801.
[4] Tian T. Dynamic behaviours of piston rings and their practical impact; Part 1: ring flutter and ring collapse and their effects on gas flow and oil transport. Proc Inst Mech Eng, Part J: J Eng Tribol 2002;216:209–27.
[5] Rahmani R, Theodossiades S, Rahnejat H, Fitzsimons B. Transient elastohydrodynamic lubrication of rough new or worn piston compression ring conjunction with an out-of-round cylinder bore. Proc IMechE, Part J: J Eng Tribol 2012;226(4):284–305.
[6] Sherrington I. Measurement techniques for piston-ring tribology. Tribol Dyn Engine Powertrain: Fundam, Appl Future Trends 2010:387.
[7] Furuhama S, Sasaki S. New device for the measurement of piston frictional forces in small engines, SAE, Paper no. 831284; 1983.
[8] Gore M, Theaker M, Howell-Smith S, Rahnejat H, King PD. Direct measurement of piston friction of internal-combustion engines using the floating-liner principle. Proc IMechE, Part D: J Automob Eng 2014;228(3):344–54.
[9] Ma MT, Sherrington I, Smith EH. Implementation of an algorithm to model the starved lubrication of a piston ring a distorted bores: prediction of oil flow and onset of gas blow-by. Proc IMechE, Part J: J Eng Tribol 1996;210:29–44.
[10] Morris N, Rahmani R, Rahnejat H, King PD, Fitzsimons B. The influence of piston ring geometry and topography on friction. Proc IMechE, Part J: J Eng Tribol 2012;227(2):141–53.
[11] Chong WWF, Teodorescu M, Vaughan ND. Cavitation induced starvation for piston-ring/liner tribological conjunction. Tribol Int 2011;44(4):483–97.
[12] Elrod SHG. A cavitation algorithm. Trans ASME, J Lubr Technol 1981; 103(3):350–4.
[13] Jakobsson B, Floberg L. The finite journal bearing considering vaporisation. Gothenburg, Sweden: Trans. of Chalmers University of Tech; 1957.
[14] Olsson KO. "Cavitation in dynamically loaded bearings". Trans. of Chalmers University of Technology; 1965.
[15] Sahlin F, Almqvist A, Larsson R, Glavatskih S. A cavitation algorithm for arbitrary lubricant compressibility. Tribol Int 2007;40(8):1294–300.
[16] Shahmohamadi H, Rahmani R, Rahnejat H, Garner CP, King PD. Thermo-mixed hydrodynamics of piston compression ring conjunction. Tribol Lett 2013; 51(3):323–40.
[17] Tipei N. Boundary conditions of a viscous flow between surfaces with rolling and sliding motion. Trans ASME, J Lubr Technol 1968;90(1):8–16.
[18] Mohammadpour M, Johns-Rahnejat PM, Rahnejat H, Gohar R. Boundary conditions for elastohydrodynamics of circular point contacts. Tribol Lett 2014;53(1):51–70.
[19] Johns-Rahnejat PM, Gohar R. Measuring contact pressure distributions under elastohydrodynamic point contacts. Tribotest 1994;1(1):33–53.
[20] Haddad SD, Tian K-T. Analytical study of offset piston and crankshaft designs and the effect of oil film on piston slap excitation in a diesel engine. Mech Mach Theory 1995;30(2):271–84.
[21] Rahnejat H. Multi-body dynamics: vehicles, machines and mechanisms. Bury St Edmunds: Professional Engineering Publishing; 0768002699.
[22] Bin Chik A, Fessler H. Radial pressure exerted by piston rings. J Strain Anal Eng Des I 1966;2:165–71.
[23] Greenwood JA, Tripp JH. The contact of two nominally flat rough surfaces. Proc IMechE 1970–1971;185:625–34.
[24] White FM. Viscous fluid flow. 2nd EditionMcGraw-Hill; 1991.
[25] Senocak I, Shyy W. Interfacial dynamics-based modelling of turbulent cavitating Flows, Part-1: Model development and steady-state computations. Int J Numer Methods Fluids 2004;44:975–95.
[26] Singhal AK, Li HY, Athavale MM, Jiang Y. Mathematical basis and validation of the full cavitation model ASME FEDSM'01, New Orleans, Louisiana; 2001.
[27] Dowson D, Higginson GR. A numerical solution to elastohydrodynamic problem. J Mech Eng Sci 1959;1(1):6–15.
[28] Morris N, Rahmani R, Rahnejat H, King PD, Fitzsimons B. Tribology of piston compression ring conjunction under transient thermal mixed regime of lubrication. Tribol Int 2013;59:248–58.
[29] Houpert L. New results of traction force calculations in elastohydrodynamic contacts. Trans ASME, J Tribol, 107; 1985. p. 241–8.
[30] Manninen M, Taivassalo V, Kallio S. On the mixture model for multiphase flow/VTT publications 288 technical research centre of Finland; 1996.

[31] Snyder DO, Koutsavdis EK, Anttonen JSR. Transonic store separation using unstructured CFD with dynamic meshing. Technical Report AIAA-2003-3913, 33th AIAA Fluid Dynamics Conference and Exhibition, American Institute of Aeronautics and Astronautics; 2003.
[32] Birkhoff G, Hays D. Free boundaries in partial lubrication. J Math Phys 1963; 42(2):126–38.
[33] Briscoe BJ, Evans DCB. The shear properties of Langmuir–Blodgett layers. Proc RSoc, Ser A.: Math Phys Sci 1982;380(1779):389–407.
[34] Mohammadpour M, Theodossiades S, Rahnejat H, Saunders T. Non-Newtonian mixed elastohydrodynamics of differential hypoid gears at High Loads. Meccanica 2014;49(5):1115–38.
[35] Bolander NW, Steenwyk BD, Sadeghi F, Gerber GR. Lubrication regime transitions at the piston ring-cylinder liner interface. Proc IMechE. Part J: J EngTribol 2005;219:19–31.
[36] Mishra PC, Balakrishnan S, Rahnejat H. Tribology of compression ring-to-cylinder contact at reversal. Proc IMechE, Part J: J Eng Tribol 2008; 222(7):815–26.
[37] Arcoumanis, C, Duszynski, M, Flora, H, Ostovar, P, Development of a piston-ring lubrication test-rig and investigation of boundary conditions for modelling lubricant film properties. SAE Technical Paper 952468; 1995.
[38] Coyne JC, Elrod HG. “Conditions for the rupture of a lubricating fil—Part II: new boundary conditions for Reynolds equation. Trans ASME, J Tribol 1971;93 (1):156–67.
[39] Furuhama, S, Hiruma, M, Tsuzita, M. Piston ring motion and its influence on engine tribology. SAE Technical Paper790860, 1979.

Tribol Lett (2015) 57:2
DOI 10.1007/s11249-014-0444-7

ORIGINAL PAPER

Big End Bearing Losses with Thermal Cavitation Flow Under Cylinder Deactivation

H. Shahmohamadi · R. Rahmani · H. Rahnejat · C. P. Garner · D. Dowson

Received: 15 August 2014 / Accepted: 13 October 2014 / Published online: 10 January 2015

Abstract The paper presents a mixed thermo-hydrodynamic analysis of elliptic bore bearings using combined solution of Navier–Stokes, continuity and energy equations for multi-phase flow conditions. A vapour transport equation is also included to ensure continuity of flow in the cavitation region for the multiple phases as well as Rayleigh–Plesset to take into account the growth and collapse of cavitation bubbles. This approach removes the need to impose artificial outlet boundary conditions in the form of various cavitation algorithms which are often employed to deal with lubricant film rupture and reformation. The predictions show closer conformance to experimental measurements than have hitherto been reported in the literature. The validated model is then used for the prediction of frictional power losses in big end bearings of modern engines under realistic urban driving conditions. In particular, the effect of cylinder deactivation (CDA) upon engine bearing efficiency is studied. It is shown that big-end bearings losses contribute to an increase in the brake specific fuel consumption with application of CDA contrary to the gains made in fuel pumping losses to the cylinders. The study concludes that implications arising from application of new technologies such as CDA should also include their effect on tribological performance.

Keywords Internal combustion engines · Journal bearings · Mixed thermohydrodynamics · Navier–Stokes · Cavitation · Cylinder deactivation

H. Shahmohamadi · R. Rahmani (✉) · H. Rahnejat · C. P. Garner · D. Dowson
Wolfson School of Mechanical and Manufacturing Engineering, Loughborough University,
Loughborough, Leicestershire LE11 3TU, UK
e-mail: R.Rahmani@lboro.ac.uk

List of symbols

A	Apparent contact area
A_a	Asperity contact area
A_p	Piston cross-sectional area
A_v	Area subject to viscous friction
a, b	Measures along the semi-major and semi-minor directions of elliptic bore
C	Centre of mass of the connecting rod
c_{maj}	Contact clearance along the semi-major axis
c_{min}	Contact clearance along the semi-minor axis
c	$c = \frac{c_{maj}+c_{min}}{2}$
c_p	Specific heat capacity
E	Young's modulus of elasticity
E'	Composite Young's modulus of elasticity of contacting solids $\left(\frac{1}{E'} = \frac{1-v_1^2}{E_1} + \frac{1-v_2^2}{E_2}\right)$
e	Eccentricity
F_2, $F_{5/2}$	Statistical functions
F_{com}	Combustion gas force
F_{in}	Inertial force
f	Total friction
f_b	Boundary friction
f_{vis}	Viscous friction
f_v	Vapour mass fraction
g	Gravitational acceleration
h	Film thickness
h_0	Minimum film thickness
h_t	Coefficient of heat transfer
i	Contacting surface identifier ($i = 1$ for bearing and $i = 1$ for journal)
k	Lubricant thermal conductivity
k_j	Thermal conductivity of the journal
k_b	Thermal conductivity of the bearing
L	Bearing width
l	Connecting rod length

m_1 Effective mass in translational motion
m_{con} Equivalent translational mass of the connecting rod
m_g Gudgeon pin mass
m_p Piston mass
p Hydrodynamic pressure
p_{atm} Atmospheric pressure
P_c Combustion gas pressure
p_{cav} Cavitation/lubricant vaporisation pressure
p_{in} Inlet lubricant supply pressure
Q Frictional heat
r Journal radius
r_c Crank pin radius
T Temperature
T_a Ambient temperature
T_{ba} Bearing outside surface temperature
T_{bl} Bearing and lubricant interface temperature
T_j Journal and lubricant interface temperature
T_i Inlet temperature of the lubricant
t Time
U Speed of lubricant entraining motion
V Velocity of side-leakage flow along the bearing width
$\vec{V}$ Velocity vector
W Contact reaction
W_{con} Total weight of the connecting rod
W_a Load carried by asperities
W_h Hydrodynamic load carrying capacity
x, y Lateral radial co-ordinates
z Axial direction along the bearing width

Greek symbols

α Thermal diffusivity
α_0 Pressure/temperature–viscosity coefficient
β Lubricant bulk modulus
β_0 Viscosity–temperature coefficient
ΔT Lubricant temperature rise
ε Eccentricity ratio
ϕ Connecting rod obliquity angle
γ Fraction lubricant film ratio
δ Journal's attitude angle
Δ Local deflection of the Babbitt overlay
Δ_{ij} Kronecker delta
θ Circumferential direction in bearing
ζ Number of asperity peaks per unit contact area
η Lubricant dynamic viscosity
η_0 Lubricant dynamic viscosity at atmospheric pressure
κ Average asperity tip radius
λ Stribeck's oil film parameter
μ Pressure coefficient for boundary shear strength of asperities
ν Poisson's ratio
ρ Lubricant density
ρ_0 Lubricant density at atmospheric pressure
τ Shear stress
τ_0 Eyring shear stress
Γ Diffusion coefficient
ω Angular speed of the crankshaft (engine speed)

1 Introduction

The main considerations in modern engine development are fuel efficiency and compliance with progressively stringent emission directives. Within the pervading global competition there is also a requirement to address customer demands for maintaining adequate output power. These often contradictory attributes have led to the downsizing concept and higher output power-to-weight ratio engines. Additionally, there is a growing trend towards the use of emerging technologies such as variable valve actuation and cylinder deactivation (CDA) [1–3]. There is also progressively an interest in the concept of stop-start in congested urban environments. The adoption of these technologies is primarily based on the direct reduction of brake specific fuel consumption. However, there are also indirect repercussions such as thermal and frictional losses, as well as poor noise, vibration and harshness (NVH) refinement issues with generally light weight and poorly damped power train structures, subjected to engine power torque fluctuations [4]. With the application of CDA a greater degree of engine torque fluctuations would result [5], which is likely to lead to further deterioration in NVH refinement.

There is a dearth of analysis with respect to thermal and frictional losses, when considering CDA. A recent study by Mohammadpour et al. [6] showed that CDA makes only marginal differences in parasitic frictional losses in engine bearing performance and that any significant gain would depend only on the brake specific fuel consumption. However, the analysis did not take into account some important issues such as multi-phase lubricant flow through the contact and the occurrence of cavitation. These affect the load carrying capacity of the bearing as well as the conjunction friction, viscous heat generation and heat transfer to the solid boundaries. Brewe et al. [7] have shown that Swift [8], Stieber [9] boundary conditions can only predict accurately the film rupture point for steadily loaded bearings, which is not suitable for engine bearings, particularly with exacerbated dynamic loading under CDA. Therefore, to include the effect of cavitation, it is essential to employ realistic conjunctional outlet boundary conditions rather than the traditional Swift–Stieber [8, 9] assumptions, used by Mohammadpour et al. [6]. This paper

strives to improve upon Mohammadpour's approach, through the combined solution of Navier–Stokes equations for fluid flow and the energy equation for heat balance.

The occurrence and complex nature of lubricant cavitation in journal bearings has received much attention since the pioneering works of Skinner [10] through a series of experiments. Later, Dowson and Taylor [11] reported the earlier predictive analyses of the cavitation phenomenon in bearings. They discussed three main modelling approaches, based on contact outlet boundary conditions. One is the traditional lubricant film rupture boundary conditions, proposed by Reynolds/Swift–Stieber [8, 9], the others being the JFO (Jakobsson–Floberg [12], Olsson [13]) boundary conditions and Coyne and Elrod's separation condition [14, 15]. The JFO boundary conditions are based upon the principle of conservation of mass flow beyond the point of lubricant film rupture point into a cavitation region in the form of striations. It is a significant improvement upon the traditional Swift–Stieber [8, 9] boundary conditions (which do not adhere to the principle of mass flow continuity beyond the lubricant film rupture). However, the JFO [12, 13] boundary conditions require consideration of any reverse flow, viscous dissipation and heat transfer within the contact in order to determine the temperature distribution within the conjunction. Therefore, proper implementation of the JFO [12, 13] boundary conditions is quite difficult in a numerical solution using Reynolds equation. Elrod's separation boundary conditions are a simplification of the JFO approach, which are based on the definition of a fractional film content and the continuity of Couette flow beyond the lubricant rupture point. Dowson and Taylor [11] pointed out that although for different working conditions, one or more of the above mentioned boundary conditions may determine the location of the lubricant film rupture with reasonable accuracy, the physics underlying the cavitation phenomenon remains mostly unknown. At the same time they also emphasised the importance of accurately predicting lubricant film reformation, especially in the case of journal bearings because of its influence, not only on the load carrying capacity, but also on the mechanism of heat transfer from the bearing.

Dowson and Taylor [11] concluded that for lightly loaded lubricated contacts, represented by a cylinder-on-plane conjunction, flow separation is the major mechanism determining the cavity location. For lightly loaded journal bearings, operating at low eccentricity ratios, the use of Coyne and Elrod [14, 15] separation boundary condition appears to lead to better predictions. At lower eccentricity ratios, there is considerable lubricant flow between cavities and hence Floberg's rupture conditions show better agreement with experimental observations.

Dowson et al. [16] used the Elrod [17] cavitation algorithm in a numerical study in order to predict the location of lubricant film rupture and reformation boundaries in a plain journal bearing. They also conducted an experimental study [18] in order to investigate the validity of their numerical analysis. Their tests included investigation of the effect of varying eccentricity ratio, supply pressure and shaft rotational speed on the film rupture and reformation points. They obtained good correlation between their numerical predictions and their experimental results for the side leakage flow. They noted that the inclusion of film reformation through use of the Elrod [17] cavitation algorithm is crucial for accurate prediction of the side leakage flow. On the other hand, the use of Swift–Stieber [8, 9] boundary conditions resulted in some errors. However, at lower eccentricity ratios (<0.6) and supply pressures a significant difference between the experimental results and the numerical predictions was observed with the Elrod boundary conditions. In addition, there was poor correlation between the numerical predictions and the experimental results for the location of the film reformation point. Dowson and Taylor [11] attributed this to the inadequacy in the utilised rupture process model which does not allow for negative gauge pressures to be generated in the lubricant film.

The Elrod [17] cavitation model was later modified to improve its computational stability by Vijayaraghavan and Keith [19], Paydas and Smith [20], Hirani et al. [21], Payvar and Salant [22], and Xiong and Wang [23]. Alternative models, including the mass-conserving flow through the cavitation region have also been developed, such as that of Giacopini et al. [24].

The development of computational fluid dynamics (CFD) approach enabled solution of Navier–Stokes equations for multi-phase flow to be achieved, whilst retaining the principle of conservation of mass and momenta. Some of the underlying limitations of Reynolds equation could also be removed. Tucker and Keogh [25] employed a 3D CFD approach for thermo-hydrodynamic analysis of steady-state motion of journal bearings. They used an Elrod [17] type cavitation model which allowed for the existence of the sub-ambient pressures. In this approach, the vapour fraction becomes a function of the film thickness. However, as Tucker and Keogh [25] also note for non-Couette or unsteady flows a time-dependent continuity equation should be used to determine the vapour fraction. In their analysis continuity of heat flux and compatibility of temperature was assured at the solid–fluid interface.

This paper presents a full 3D CFD approach for thermo-hydrodynamic analysis of big-end bearings. No artificial boundary conditions are set at the exit from the conjunction. This means that the lubricant rupture and reformation boundaries are determined by the combined solution of

Navier–Stokes equations, the energy equation and continuity of flow conditions (in terms of conservation of mass and momenta). In addition, the cavitation phenomenon is taken into account through solution of a vapour transport equation including the Rayleigh–Plesset source terms to take into account the growth and collapse of cavitation bubbles. The developed method is validated against experimental results of Dowson et al. [26]. The validated model is then used for analysis of a big-end engine bearing subjected to dynamic loading under normal engine operation as well as with the application of CDA; an approach not hitherto reported in the literature.

2 Big End Bearing Model

2.1 Big End Bearing Geometry

A schematic of the big end bearing used in IC engines is shown in Fig. 1. In a conventional internal combustion (IC) engine, the crank-pin acts as the journal and the bearing bushing is located at the bottom end of the connecting rod. The big end bearings are usually groove-less and are pressure-lubricated using a single hole drilled through the crank pin [27]. Although in most applications a simple circular profile is used to describe the geometry of the big end bearing, in practice, an elliptic (or 'lemon shape') bore profile is used. To study the effect of CDA, the engine studied here was a high performance four-stroke naturally aspirated engine with the specifications provided in Table 1.

The film profile for such an elliptic bore bearing is defined as (Mishra et al. [28]):

$$h = c\,(1 + G\cos^2\theta + \varepsilon\cos\theta) + \Delta \tag{1}$$

Table 1 Engine and bearing data

Parameter	Value	Unit
Crank pin radius	31	mm
Connecting rod length	107	mm
Effective translational mass	0.32	kg
Engine speed	2,200	rpm
Bearing width	16.8	mm
Bearing radius	21	mm
Minor diametral clearance	20	μm
Major diametral clearance	30	μm
Composite surface roughness	1	μm
Overall overlay thickness	2	mm

where, the non-circularity is defined as: $G = (c_{\mathrm{maj}} - c_{\mathrm{min}})/c$. The parameters c, ε, θ are the average clearance, eccentricity ratio and the angular position respectively (Fig. 1). The localised deflection of the Babbitt overlay, Δ is obtained using the column method contact mechanics approach [29], where: $\Delta = \frac{(1-2\nu)(1+\nu)d}{E(1-\nu)}p$.

2.2 Applied Loads

Big-end bearings are designed to withstand the transmitted transient forces through the connecting rod. These are the result of combustion pressure and inertial imbalance [4].

For a typical four-cylinder four-stroke engine, the inertial imbalance force acting through the connecting rod along the axis of the piston is [4] (Fig. 2):

$$F_{\mathrm{in}} \approx m_1 r_{\mathrm{c}}\omega^2\left(\cos\omega t + \frac{r_{\mathrm{c}}}{l}\cos 2\omega t\right) \tag{2}$$

where, engine order vibrations up to the second engine

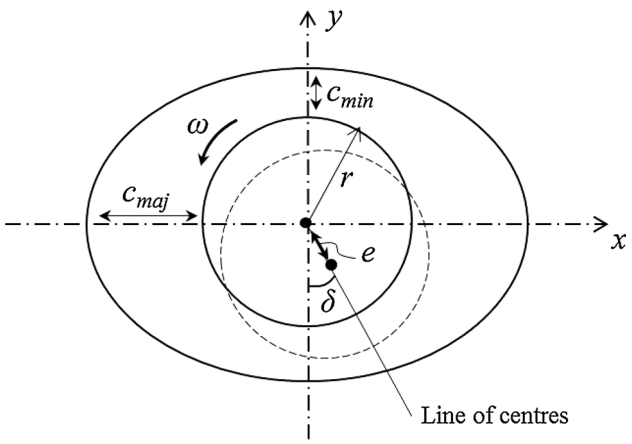

Fig. 1 An elliptic big end bearing configuration

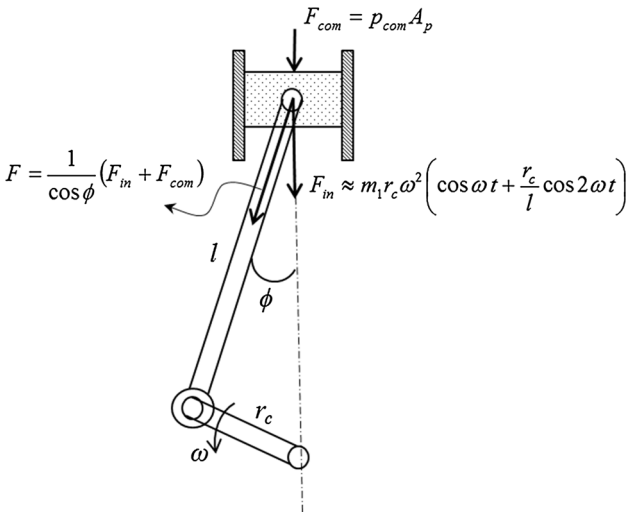

Fig. 2 Schematic of the piston–crank system with the applied loads

order are considered here for the four-stroke engine under consideration. The mass m_1 is the equivalent mass in translation, comprising that of the piston, the gudgeon pin and a proportion of the mass of the connecting rod in pure translation: $m_1 = m_p + m_g + m_c$ in a two degrees-of-freedom representation of piston-connecting rod-crank subsystem, where according to Thomson [30]:

$$m_c = \frac{W_c}{g}\left(1 - \frac{C}{l}\right) \tag{3}$$

where, W_c is the weight of the connecting rod and C denotes centre of mass of the connecting rod measured from its small end.

The applied vertical combustion force acting upon the piston crown area is:

$$F_{com} = p_{com} A_p \tag{4}$$

where, p_{com} is the instantaneous in-cylinder pressure and A_p is the piston crown surface area.

Therefore, the total transient load applied on the big end bearing at any instant of time, expressed in terms of the instantaneous connecting rod obliquity angle, φ is (Fig. 2) [4]:

$$F = \frac{1}{\cos\varphi}(F_{in} + F_{com}) \tag{5}$$

where:

$$\cos\varphi \approx 1 - \frac{1}{2}\left(\frac{r_c}{l}\sin\omega t\right) \tag{6}$$

and $\vartheta = \omega t$, ϑ is the crank angle.

It should be noted that smaller moment loading from adjacent cylinders also exists, which is ignored in this analysis. More information is provided in Rahnejat [31].

3 Theory

3.1 General Navier–Stokes and Energy Equations

The general form of mass and momentum continuity (Navier–Stokes) equations for the flow of a compressible viscous fluid can be described as (White [31]):

$$\frac{D\rho}{Dt} + \rho\vec{\nabla}\cdot\vec{V} = 0 \tag{7}$$

$$\rho\frac{D\vec{V}}{Dt} = -\vec{\nabla}p + \vec{\nabla}\cdot(\bar{\tau}_{ij}) + \vec{F} \tag{8}$$

where D/Dt is the material covariant derivative operator. The parameters ρ and p are scalar quantities and represent the density and pressure of the fluid. $\vec{F}$ and $\vec{V}$ are the body force field and velocity vectors, and $\bar{\tau}_{ij}$ is the second order viscous shear stress tensor.

The only body force in the current analysis is the gravitational force due to the weight of the fluid. Although this has a negligible effect in comparison with the shear and pressure induced forces in lubrication studies, it has been taken into account in the current analysis for the sake of completeness.

In addition, $\vec{V} = u\hat{i} + v\hat{j} + w\hat{k}$ is the velocity vector expressed in the Cartesian frame of reference in which u is the component of velocity in the direction of axial lubricant flow entrainment (along the x-axis), v is that in the transverse or side-leakage direction along the y-axis and w is the velocity component in the direction perpendicular to the contacting surfaces (squeeze film action) along the z-axis.

Furthermore, the viscous shear stress tensor, $\bar{\tau}_{ij}$, can be expressed as spatial derivatives of the velocity field vector components for an isotropic fluid. In Einstein's notation this becomes:

$$\bar{\tau}_{ij} = \eta\left(\frac{\partial u_i}{\partial x_j} + \frac{\partial u_j}{\partial x_i} - \Delta_{ij}\frac{2}{3}\frac{\partial u_k}{\partial x_k}\right) \tag{9}$$

where, u is the general representation of (scalar) velocity components, η is the effective dynamic viscosity of the lubricant and Δ_{ij} is the Kronecker delta, defined as:

$$\Delta_{ij} = \begin{cases} 0 & \text{if } i \neq j \\ 1 & \text{if } i = j \end{cases} \tag{10}$$

Finally, the energy conservation equation in the most general form can be stated as (White [32]):

$$\rho\frac{DH}{Dt} = \frac{Dp}{Dt} + \vec{\nabla}\cdot(k\vec{\nabla}T) + \bar{\tau}_{ij}\frac{\partial u_i}{\partial x_j} \tag{11}$$

where H is the fluid enthalpy, T is the fluid temperature and k is its thermal conductivity. It is noted that the last term on the right hand side of the equation is the sources term which takes into account the heat produced due to viscous shear of the fluid.

3.2 Cavitation Model

The full cavitation model proposed by Singhal et al. [33] is used here, where the transport equation for the vapour mass fraction is expressed as:

$$\frac{\partial}{\partial t}(\rho f_v) + \vec{\nabla}\cdot(\rho f_v \vec{V}_v) = \vec{\nabla}\cdot(\Gamma\vec{\nabla}f_v) + R_e - R_c \tag{12}$$

where, Γ is the diffusion coefficient, $\vec{V}_v$ is the velocity vector of the vapour phase and f_v is the vapour mass fraction defined as:

$$f_v = \frac{\rho - \rho_l}{1 - (\rho_l/\rho_v)} \tag{13}$$

where, the subscripts l and v denote the liquid and vapour phases respectively.

In addition, R_e and R_c are the source terms which account for vapour generation and condensation rates, respectively. Singhal et al. [33] defined these phase change rates, based on the generalised Rayleigh–Plesset equation, thus:

$$R_e = C_e \frac{V_{ch}}{\sigma_s} \rho_l \rho_v \sqrt{\frac{2(p_{sat} - p)}{3\rho_l}} (1 - f_v), \quad \text{for} \quad p \leq p_{sat} \tag{14}$$

$$R_c = C_c \frac{V_{ch}}{\sigma_s} \rho_l \rho_v \sqrt{\frac{2(p - p_{sat})}{3\rho_l}} f_v, \quad \text{for} \quad p > p_{sat} \tag{15}$$

where, σ_s denotes the surface tension of lubricant and V_{ch} is a characteristic velocity associated with the local relative velocity between the liquid and vapour phases. In these models it is assumed that the bubble pressure, p equates to the saturation (vapour) pressure, p_{sat}, at a given temperature which is the case if one assumes that no dissolved gases are present. In addition, C_e and C_c are empirical constants which are considered to be 0.02 and 0.01 respectively according to Singhal et al. [33].

3.3 Boundary Conditions for the Fluid Flow

The flow boundary conditions are set, based on the conditions for a typical IC engine big-end bearing.

The cavitation (vaporisation) pressure is set at the atmospheric pressure of 101 kPa. Since the occurrence of cavitation in the current CFD analysis is treated through solution of transport equation for the vapour mass fraction alongside the general Navier–Stokes equations, there is no need to impose any particular boundary conditions for either lubricant film rupture or reformation. This is a significant fundamental improvement upon the imposed assumptions such as those of JFO [12, 13] or Elrod [17] cavitation models.

In addition to the fact that the solid boundaries were considered to be impermeable, the lubricant/solid interface is also assumed to follow the no-slip condition.

The bearing shell is modelled as a stationary wall, whilst the journal is modelled as a moving body with an absolute rotational velocity.

At the inlet hole supply orifice to the bearing the lubricant is fed into the contact at a constant pressure of 0.5 MPa as already assumed by Mohammadpour et al. [6].

Finally, at the bearing's axial extremities the lubricant is assumed to leak to ambient (atmospheric) pressure.

3.4 Conduction Heat Transfer in the Solid Bodies (Journal and Bearing)

In order to proceed with full thermal analysis of the journal–lubricant–bearing bushing system, one needs to take into account the conduction of the generated heat to the solid boundaries using the energy equation. The conduction of heat into the rotating journal is governed by the transient form of the heat conduction equation as:

$$\frac{1}{\alpha} \frac{\partial T}{\partial t} = \nabla^2 T \tag{16}$$

where, α is the thermal diffusivity for the journal's material. The convective (time dependent term) on the left hand side of the equation takes into account the rotational effect.

On the other hand, the steady-state form of the heat conduction equation is used for the stationary bushing as:

$$\nabla^2 T = 0 \tag{17}$$

3.5 Thermal Boundary Conditions

The thermal boundary conditions are set for a typical IC engine big- end bearing (Fig. 3). At the lubricant–solid interface these conditions ensure the continuity of heat flux and compatibility of evaluated temperatures.

After lubricant enters the contact through the oil feed hole, its temperature is increased from that in the bulk due to the heat produced in the contact as the result of shearing. The generated heat is transferred by convection through lubricant side leakage and conducted through the bounding solid surfaces. In the experiments conducted by Dowson et al. [26], the journal's extremities were exposed to the ambient air. Therefore, convection cooling would take place at these interfaces. However, for the engine conditions, it is assumed that the journal is not exposed to the ambient air and thus, any heat transfers to the journal increases its core temperature. Finally, a portion of the heat is conducted through the bearing bushing to the surrounding ambient air. Of course, for journal bearings, convective heat transfer by the lubricant film is most significant [34–36]. In both the validation process and engine running conditions, it was assumed that the bearing's outer surface is exposed to the ambient temperature. Thus, the temperature of the outer surface of the bearing bushing (for the case of engine simulations) is set at 50 °C. The

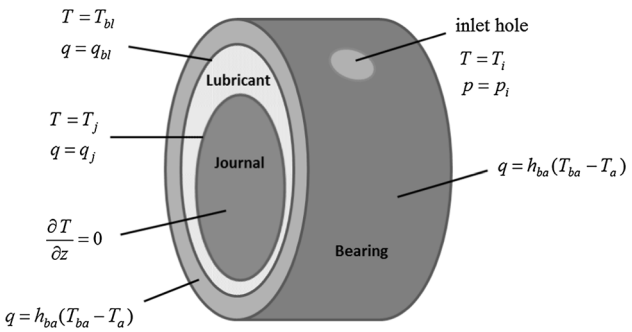

Fig. 3 Thermal boundary conditions

temperature of the inner surface of the bushing, T_{bl} is assumed to be that of the lubricant obtained through solution of energy equation. In reality, the temperature of lubricant would be slightly higher than the interface temperature of the solids. Figure 3 illustrates thermal boundary conditions in the journal bearing. A list of the assumed engine compartment temperature, lubricant and material data for the engine running conditions is provided in Table 2.

In solving the coupled energy and heat conduction equations, the temperature of the entrant lubricant is computed from the initial solid component temperatures and heat fluxes at the solid interfaces. The heat produced in the lubricant is allowed to increase the journal's temperature whilst the transferred heat to the journal bushing can be convected away through ambient air. To include the effect of journal temperature a detailed thermal model for the entire crankshaft system would be required, which is outside the scope of the paper. This would necessitate a full engine model including the effect of all the adjacent cylinders. This is the reason for assuming no axial temperature gradient for the journal in the current analysis. The temperature of the oil at the inlet hole was set to $T_i = 42$ °C in the case of the validation procedure (Dowson et al. [26]). For the engine conditions this was set at 50 °C. The lubricant thermal properties such as thermal conductivity and specific heat are calculated at the engine compartment temperature of 50 °C under steady engine running condition and 40 °C for the validation case study.

Table 2 Lubricant and material data

Parameter	Value	Unit
Lubricant dynamic viscosity	8.0	mPa s
Lubricant density	833.8	kg m^{-3}
Viscosity–temperature coefficient	0.026	K^{-1}
Pressure-induced shear coefficient (γ)	0.047	–
Atmospheric limiting shear stress	2.3	MPa
Specific heat capacity of lubricant	2,360	Jkg^{-1} K^{-1}
Thermal conductivity of lubricant	0.225	Wm^{-1} K^{-1}
Surface tension of lubricant	0.03	N m^{-1}
Poison's ratio for Babbitt	0.33	–
Young's modulus for Babbitt	60	GPa
Thermal conductivity of bearing bushing (k_{s1})	46	Wm^{-1} K^{-1}
Thermal conductivity of journal (k_{s2})	25.96	Wm^{-1} K^{-1}
Journal material	SG cast iron	–
Bearing overlay	Babbitt	–
Diffusion coefficient	10^{-8}	m^2 s^{-1}
Eyring shear stress	5	MPa
Inlet pressure	0.5	MPa
Engine compartment temperature	50	°C

3.6 Lubricant Rheology

Density and viscosity of the lubricant are the two most important rheological properties that need to be defined for the operating pressures and temperatures.

A density model proposed by Dowson and Higginson [37], modified for temperature variation by Yang et al. [38] provides:

$$\rho = \rho_0\left(1 + \frac{6.0 \times 10^{-10}(p - p_{atm})}{1 + 1.7 \times 10^{-9}\,(p - p_{atm})}\right)\left[1 - 0.65 \times 10^{-3}(T - T_0)\right] \tag{18}$$

in which p_{atm} is the atmospheric pressure and T_0 is the reference temperature with density ρ_0. Table 2 provides the data associated with the lubricant properties.

Variation of lubricant dynamic viscosity with pressure and temperature is given by Houpert [39] as:

$$\eta = \eta_0 \exp\left\{(\ln(\eta_0) + 9.67)\left[\left(\frac{T + 135}{T_0 + 135}\right)^{-S_0}\left(1 + \frac{p - p_{atm}}{1.98 \times 10^8}\right)^{Z} - 1\right]\right\} \tag{19}$$

where, η_0 is the lubricant dynamic viscosity at atmospheric pressure and reference temperature T_0, and Z and S_0 are constants (Gohar and Rahnejat [40]):

$$Z = \frac{1.96 \times 10^8 \alpha_0}{\ln(\eta_0) + 9.67} \quad \text{and} \quad S_0 = \frac{\beta_0(T_0 + 135)}{\ln(\eta_0) + 9.67} \tag{20}$$

where, α_0 and β_0 are constants at ambient conditions (Table 2). It should be noted that the rheological parameters used are for a fresh lubricant. In practice, the lubricant is subject to shear thinning, oxidation and contamination (Lee et al. [41]).

3.7 Asperity Contact Model for Mixed/Boundary Regime of Lubrication

Journal bearings are designed to ideally operate in the hydrodynamic regime of lubrication. Therefore, ordinarily, it is expected that a coherent film of lubricant is maintained, guarding against direct contact of ubiquitous asperities on the contiguous surfaces. However, this may not be the case in applications such as those encountered in the big-end bearings of IC engines due to the transient nature of engine operations. The large variations in the applied load, as well as stop-start running conditions, contact of asperities on the contiguous surfaces is unavoidable. Consequently, some of the applied load can

be carried by the direct contact of surfaces at asperity level. Therefore, the applied load is carried by a combination of hydrodynamic reaction and direct asperity contact as:

$$F = W_{\mathrm{h}} + W_{\mathrm{a}} \tag{21}$$

where, the hydrodynamic reaction is obtained by integration of the hydrodynamic contact pressure obtained through solution of Navier–Stokes equations:

$$W_{\mathrm{h}} = \iint p(\theta, z)\, r\mathrm{d}\theta\mathrm{d}z \tag{22}$$

The asperity load is a function of surface roughness and material properties. For an assumed Gaussian distribution of asperities the load supported by the asperity tips can be expressed as (Greenwood and Tripp [42]):

$$W_{\mathrm{a}} = \frac{16\sqrt{2}}{15}\pi(\xi\beta\sigma)^2\sqrt{\frac{\sigma}{\beta}}E'AF_{5/2}(\lambda) \tag{23}$$

where, A is the apparent area of contact and E' is the composite modulus of elasticity. The statistical function $F_{5/2}(\lambda)$ is a function of the Stribeck oil film parameter $\lambda = \frac{h}{\sigma}$, where σ is the composite root mean square roughness of the contiguous surfaces. This statistical function can be represented by a polynomial-fit function as (Teodorescu et al. [43]):

$$F_{5/2}(\lambda) = \begin{cases} -0.004\lambda^5 + 0.057\lambda^4 - 0.296\lambda^3 + 0.784\lambda^2 - 1.078\lambda + 0.617; & \text{for } \lambda \le \lambda_{\mathrm{cr}} \\ 0; & \text{for } \lambda > \lambda_{\mathrm{cr}} \end{cases} \tag{24}$$

where, for the current analysis a critical film ratio of $\lambda_{\mathrm{cr}} \approx 3$ is assumed, below which mixed regime of lubrication (including asperity interactions) is deemed to occur. This value of critical Stribeck oil film parameter depends on the surface topographical asperity distribution and the chosen statistical parameter. Some researchers have used lower or slightly higher values for the transition boundary between mixed and full fluid film regimes of lubrication. In particular, Guanteng and Spikes [44] used thin film interferometry and showed that full film lubrication is only realised when $\lambda > 2$. They noted that there is no clear-cut demarcation boundary between mixed and boundary regimes of lubrication, based on the Stribeck's oil film parameter. As already noted above, $\lambda_{\mathrm{cr}} > 3$ is assumed for fluid film lubrication in the current analysis.

According to Greenwood and Williamson [45] and Greenwood and Tripp [42], the roughness parameter $\xi\beta\sigma$ is reasonably constant with a value in the range of 0.03–0.07 for steel surfaces. The ratio σ/β which is a representation of the average asperity slope (Gohar and Rahnejat [40]) is in the range 10^{-4}–10^{-2} according to Teodorescu et al. [43]. In the current study it is assumed that $\sigma_1 = \sigma_2$, $\xi\beta\sigma = 0.055$ and $\sigma/\beta = 0.001$. Since a thin smooth hard layer of bismuth is applied as the outer layer of the shell overlay with a thickness of 3 μm, the boundary friction is assumed to largely depend on the rougher surface of the steel crank pin.

3.8 Friction Force and Power Loss

The total friction force in mixed regime of lubrication is obtained as:

$$f_{\mathrm{t}} = f_{\mathrm{vis}} + f_{\mathrm{b}} \tag{25}$$

where, the viscous friction, f_{vis}, is obtained by integrating the generated shear stress over the lubricant-surface interface as:

$$f_{\mathrm{vis}} = \iint \tau\mathrm{d}A \tag{26}$$

The boundary component of friction takes into account the direct dry asperity contact as well as the non-Newtonian shear of pockets of lubricant entrapped between the asperity tips, as (Teodorescu et al. [43]):

$$f_{\mathrm{b}} = \tau_0 A_{\mathrm{a}} + \varsigma W_{\mathrm{a}} \tag{27}$$

where, the parameter ς is the pressure coefficient for boundary shear strength of asperities on the softer counterface. In the case of the big-end bearing this is the steel surface of the journal. A value of $\varsigma = 0.17$ is obtained using an atomic force microscope. The procedure followed is the same as that described by Buenviaje et al. [46] and Styles et al. [47]. In addition, limiting Eyring shear stress [48] for the engine oil is $\tau_0 = 2$ MPa.

The underlying hypothesis in the use of Eq. (27) is that the asperities are wetted by adsorption of an ultra-thin film of boundary active molecules within the lubricant. Briscoe and Evans [49] assume that a thin Langmuir–Blodgett [50] layer of adsorbed of boundary active lubricant species are formed at the tip of asperities and entrapped in their interspatial valleys. This layer is subject to non-Newtonian Eyring shear [48]. An alternative hypothesis would be that the opposing asperities form adhesive junctures which are submerged in the menisci formed between them.

Therefore, boundary friction may be considered as the effort required to break such meniscus bridges (Bowden and Tabor [51]) in addition to overcoming the adhesion of cold welded asperity junctures themselves. Such an approach is reported by Teodorescu et al. [43]. A shortcoming of the approach reported in [50] is the need to specify the proportion of contact in dry contact of asperities. On the other hand the approach in [43] makes use of asperity contact area A_a, based on the assumption of asperity distribution, which is considered to follow a Gaussian distribution as in [42].

The cumulative area of asperity tips, A_a, is found as (Greenwood and Tripp [42]):

$$A_a = \pi^2(\zeta\kappa\sigma)^2\sqrt{\frac{\sigma}{\kappa}}AF_2(\lambda) \tag{28}$$

where $F_2(\lambda)$ is a function representative of the Gaussian distribution of asperities in terms of λ as:

$$F_2(\lambda) = \begin{cases} -0.0018\lambda^5 + 0.0281\lambda^4 - 0.1728\lambda^3 + 0.5258\lambda^2 - 0.8043\lambda + 0.5003; & \text{for } \lambda \le \lambda_{cr} \\ 0; & \text{for } \lambda > \lambda_{cr} \end{cases} \tag{29}$$

The total frictional power loss from the bearing, due to both viscous and boundary contributions to the overall friction, is calculated as follows:

$$P_f = f_t r\omega \tag{30}$$

4 Method of Solution

The governing equations described in Sect. 3.1 were solved in the environment of ANSYS FLUENT 14.5, where a computational mesh is generated. For the conjunctional fluid domain (the lubricant) was meshed with hexahedral cells (element size 50 μm and 20 division for film thickness direction), whilst the bounding solid surfaces were discretised using tetrahedral elements with 2 mm elements. There is no need for finer solid elements as there is no local deformation of surfaces at the expected generated pressures, since $\alpha p_m \ll 1$ for the conformal contact of the contiguous surfaces as in journal bearings [40]. The interfaces between the solid surfaces and the lubricant zone were defined by face meshing method. The total number of computational control volume elements was 2,533,165. A grid independency test for the result was performed, which showed that the number of elements used in excess of that stated did not significantly alter the results of the analyses (see "Appendix"). Since the gap between the two solid surfaces is subject to transience with variations in applied load and speed, a dynamic mesh model was employed to calculate the lubricant film thickness at any instant of time. Boundary Layer Smoothing Method and Local Cell Remeshing are used for the dynamic mesh model.

In order to be able to include the described cavitation model (Sect. 3.2), a mixture model was employed to take into account the two-phase flow nature of the problem [52]. In this method, the mass continuity, momentum and energy equations are solved for the mixture while a mass/volume fraction equation (Eq. 12) is solved for the secondary (gas or vapour) phase.

The velocity–pressure coupling is treated using the standard semi-implicit method for pressure-linked equations (SIMPLE algorithm) and the second-order upwind scheme is used for the momenta in order to reduce any discretisation-induced errors. A pressure-based segregated algorithm is employed in which the equations are solved sequentially.

For greater accuracy, an error tolerance of 10^{-4} is used for the residual terms of mass and momentum conservation and the volume fraction, whilst a tolerance value of 10^{-6} is employed for energy conservation and heat conduction equations (see "Appendix").

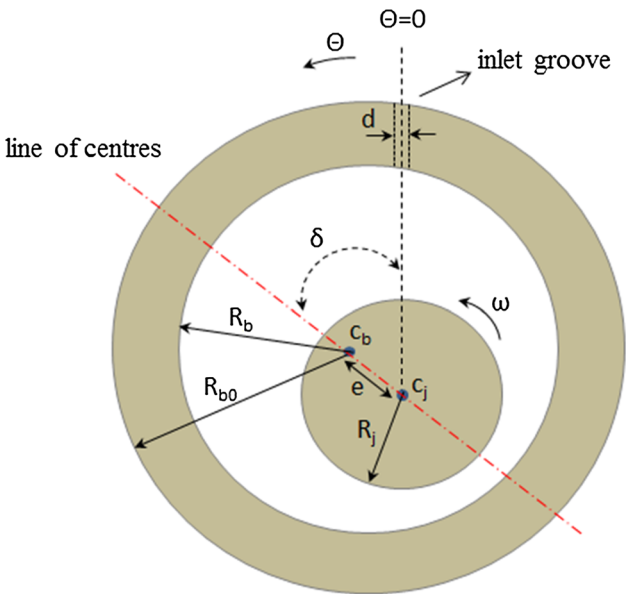

Fig. 4 Schematic of journal bearing geometry used in Dowson et al. [26]

5 Model Validation

Prior to any analysis of engine conditions under normal operating mode or with application of CDA, it is necessary to validate the developed numerical model. A two-stage validation process is undertaken.

Firstly, the model predictions are compared with the experimental measurements reported by Dowson et al. [26], which have been used for the same purpose by other research workers, including Tucker and Keogh [25], and Wang and Zhu [53]. Dowson et al. [26] measured the lubricant pressure distribution in a restricted grooved journal bearing (Fig. 4). A lubricant inlet supply hole with diameter d was drilled radially through the bearing on its central plane. A distribution groove with width d was cut axially into the inner surface of the bearing with the length, L_i. The attitude angle δ is measured from the location of the axial groove to the line of centres. The journal bearing variables used in the computation are listed in Table 3. Dowson et al. [26] noted a build-up of pressure with the passage of lubricant through the converging gap to support the applied load. In the diverging gap of the conjunctional outlet, the fall in the generated pressures resulted in the fluid film cavitating into a series of streamers below the saturation pressure of the dissolved gases.

Secondly, further numerical predictions were made using Reynolds equation and Elrod's cavitation algorithm [17]. In the Elrod's approach the fractional film content is the proportion of the conjunctional gap which attains generated pressures in excess of the cavitation vaporization pressure of the lubricant for a given conjunctional temperature (indicated by its bulk modulus, β), thus [17]:

$$p = \psi\beta \ln \gamma + p_{\text{cav}} \tag{31}$$

where, ψ is a switching function: $\psi = 1$, $\gamma > 1$, $P > p_{\text{cav}}$ represents regions of a coherent fluid film and $\psi = 0$, $\gamma < 1$. $P = p_{\text{cav}}$ represents the cavitation region, with clearly $\gamma = 1$ defining the lubricant film rupture point.

Table 3 Journal bearing variables used in the validation exercise (Dowson et al. [26])

Parameters	Values	Units
Bearing length (L)	0.0762	m
Radial clearance (c)	63.5	μm
Journal radius (R_j)	0.05	m
Bearing outside diameter (R_{bo})	0.1143	m
Bearing thermal conductivity (k_b)	250	W m^{-1} °C
Journal thermal conductivity (k_j)	50	W m^{-1} °C
Heat transfer coefficient (h)	50	W m^{-2} °C
Inlet groove axial length (L_i)	0.067	m
Attitude angle (δ)	18	°
Groove width (d)	0.0016	m
Ambient temperature (T_a)	40	°C

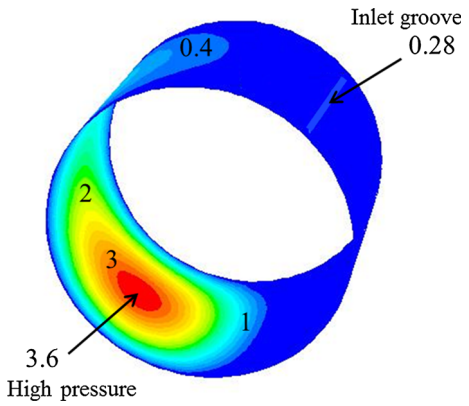

Fig. 5 Contours of pressure (MPa) for $\varepsilon = 0.5$ at $N = 1{,}500$ rpm

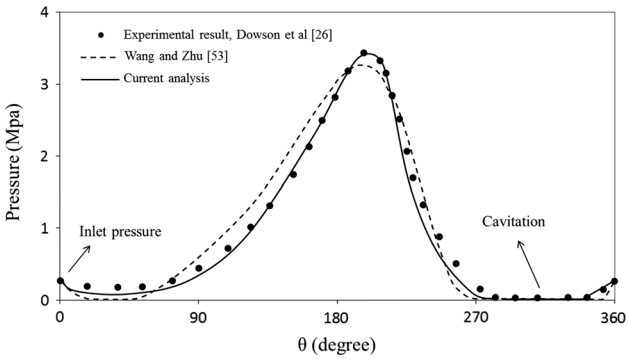

Fig. 6 Comparison of experimental result and current analysis on pressure distribution in the centre plane for $\varepsilon = 0.5$ at $N = 1{,}500$ rpm

Dowson et al. [26] operated their experimental journal bearing rig at a steady speed of 1,500 rpm, an applied load of 9,000 N and with an attitude angle of $\delta = 18°$. This yielded a journal operating eccentricity ratio of $\varepsilon = 0.5$. Figure 5 shows the numerically predicted pressure distribution in isobaric form using the current method. The position of the inlet groove is designated as $\theta = 0°$ in the circumferential direction. The maximum pressure occurs at $\theta = 206°$ and the lubricant film ruptures just beyond the position $\theta = 270°$.

Figure 6 shows the cross-section through the 3D pressure distribution in the central plane of the bearing, where pressure tappings were made by Dowson et al. [26]. The experimental measurements are shown, as well as the numerical predictions made by Wang and Zhu [53], which are based on Elrod's cavitation model [17] and those from the current CFD analysis. The area under all the pressure distributions, being the lubricant reaction remains the same. Both the predictive analyses employed the same convergence tolerance limit of 10^{-6}. All the pressure distributions commence from the supplied inlet pressure of

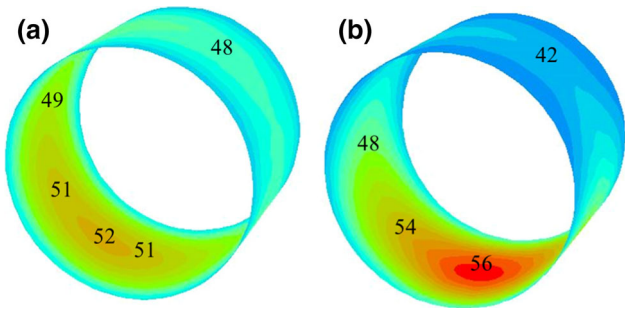

Fig. 7 Contours of temperature (°C) for **a** circumferential journal surface, **b** circumferential bearing surface for $\varepsilon = 0.5$ at $N = 1{,}500$ rpm

0.5 MPa with an assumed fully flooded inlet boundary. The outlet boundary conditions differ between the numerical analyses. Those for the Elrod cavitation boundary are based on the lubricant film rupture point, $\gamma = 1$, whereas the current CFD analysis has an open exit boundary condition (not an imposed boundary condition) for the lubricant film rupture point. The different exit boundary conditions, as well as the embodied assumption of a constant pressure gradient into the depth of the lubricant film with a constant dynamic viscosity through its thickness made by Wang and Zhu [53] yield slightly different pressure profiles. Clearly, lack of artificially imposed assumptions with the CFD analysis yields results which conform more closely to the experimental measurements.

Figure 7 shows the contours of temperature distribution for the journal and the bearing bushing surfaces obtained from the current analysis. For the journal surface the maximum temperature occurs close to the high pressure zone. The maximum temperature in the stationary bearing bushing occurs in the cavitation zone due to the high vapour volume fraction residing there with clearly poor convection cooling due to the lack of lubricant flow. Comparison of the experimental result, that from Tucker and Keogh [25] and that of the current model for journal

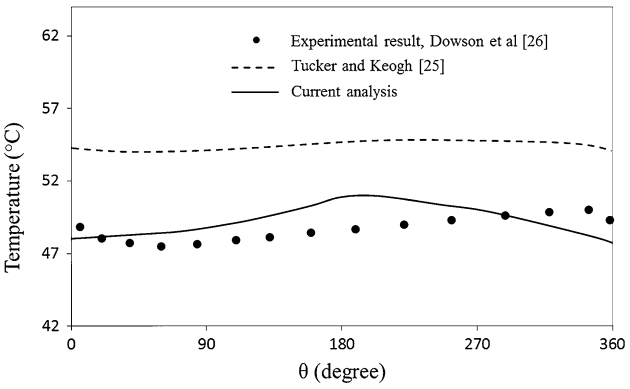

Fig. 8 Comparison of experimental result and current analysis for the circumferential journal surface temperatures for $\varepsilon = 0.5$ at $N = 1{,}500$ rpm

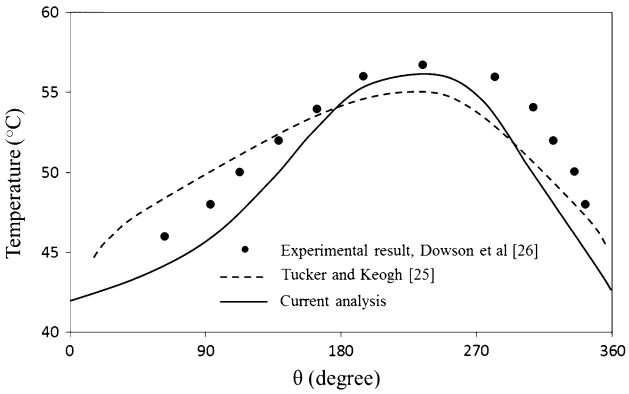

Fig. 9 Comparison of experimental result and current analysis for circumferential bearing bushing surface temperatures for $\varepsilon = 0.5$ at $N = 1{,}500$ rpm

and bearing surfaces are shown in Figs. 8 and 9, respectively. As it can be seen, the result of the current analysis shows closer agreement with the experimental measurements. The main difference between the Tucker and Keogh's analysis [25] and the current model is in the treatment of the flow in the cavitation region. The former uses the fraction of vapour Φ in the cavitation region, similar to the Elrod's approach [17]:

$$\Phi = 1 - \frac{h_c}{h} \tag{32}$$

where h_c is the film height at the start of the cavitation region. Equation (32) is based only on steady state Couette flow continuity. This ignores the mass flow continuity, which includes the vapour phase and any changes in the Poiseuille flow in a divergent gap. The current model takes these issues into account using the time-dependent continuity equation (Eq. 12).

Figure 10 shows the lubricant temperature into the depth of the lubricant at circumferential position, $\theta = 180°$. It shows that the temperature of the lubricant is higher than the temperatures of both the journal and the bearing

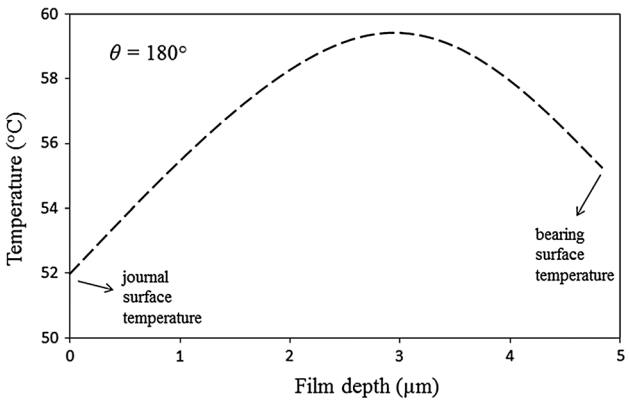

Fig. 10 Lubricant temperature along the film depth at $\theta = 180°$

bushing surfaces. As the temperature varies through the thickness of the lubricant film its viscosity alters locally, which indicates that the thermal flow through the contact is in the form of streamlines at different temperatures and viscosity (with different phases), thus a pressure gradient exists into the depth of the film. Hence, for an accurate prediction of flow a combined solution of Navier–Stokes equation with Rayleigh–Plesset equation is essential as is the case in the current analysis.

6 Engine Big End Bearing Analysis with CDA

It is expected that introduction of CDA would affect the thermal conditions in engine big-end bearings and influence frictional power loss. The occurrence of cavitation and its extent would also affect friction. Therefore, it is necessary to develop the validated multi-phase flow methods with realistic boundary conditions such as that adopted in the current method.

Now with the validated model, realistic predictions under engine operating conditions with all-active fired cylinders and alternatively with some deactivated cylinders can be carried out. The analysis reported here corresponds to a four-cylinder four-stroke engine under city driving condition at the speed of 25 km/h with 25 % throttle action and engaged in second gear (ratio 1:2.038). The final drive differential ratio is 1:4.07. The engine speed for this condition is 2,200 rpm. All the necessary data used in the analysis are listed in Table 1. The results are presented for a deactivated cylinder as well as a fired cylinder. Figure 11 shows the combustion gas force for an active cylinder under engine normal operation, as well as that for an active cylinder under CDA. It also shows the gas force for a deactivated cylinder, caused by the trapped air/charge with closed valves, subjected to swept volumetric changes. Note that the gas force is increased in the active cylinders of a partially deactivated engine with the same flow rate through a common rail supply. The effect is higher temperature combustion which improves upon thermal efficiency and also enhances the operation of the catalytic converter, operating at a higher temperature, thus reducing hydrocarbon emission levels. The pumping losses can also be reduced whilst higher cylinder temperatures in active cylinders would reduce the lubricant viscosity, thus the frictional losses. This effect is not investigated here, but Morris et al. [54] using a control volume thermal mixing model showed that the average temperature of the lubricant, thus its viscosity, is primarily determined by the bore surface temperature. Therefore, there are fuel efficiency advantages in terms of reduced thermal losses as well as decreased active cylinder viscous frictional losses.

When periodic steady state conditions are reached the interfacial temperature T_{bl} (defined in Fig. 3) reaches a maximum value of 145 °C when the engine is operating under normal conditions (no CDA). For an engine under CDA operating mode, the maximum interfacial temperature reached in the bearing of an active cylinder is 160 °C and for the big end bearing of the deactivated it reaches 135 °C. Although the deflection of the 100 μm thick Babbitt overlay is included in the analysis, the maximum conjunctional pressure reached (maximum of 20 MPa), under the investigated conditions yields an inappreciable value (<0.02 μm). However, under more severe operating conditions (higher engine speed and a greater throttle input), this may not be the case.

Cavitation occurs in the big-end bearings under low applied loads, resulting in reduced conjunctional pressures. Figures 12 and 13 show the generated pressure distribution and the corresponding volume fraction in the journal-bushing conjunction at the crank angle of $\vartheta = 180°$, corresponding to the piston position at the bottom dead centre

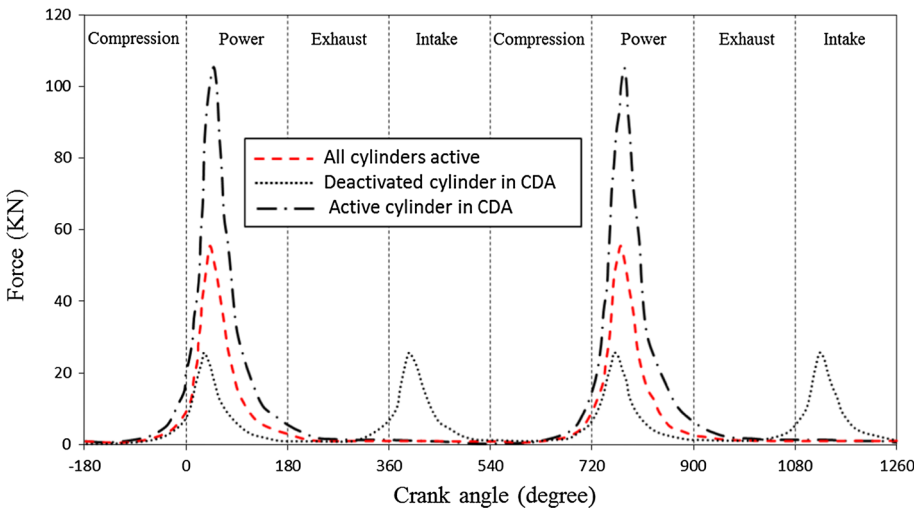

Fig. 11 Transmitted combustion gas forces for full and partially deactivated engine operations

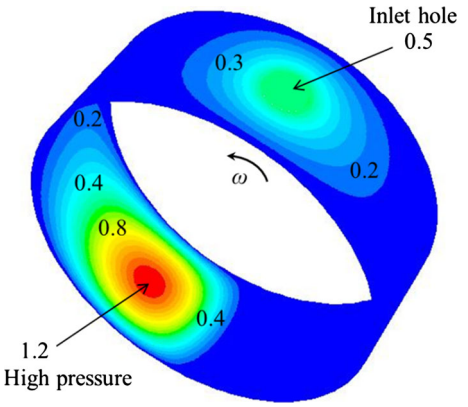

Fig. 12 Contours of pressure (MPa) at crank angle $\vartheta = 180°$ (piston at BDC) with all active cylinders

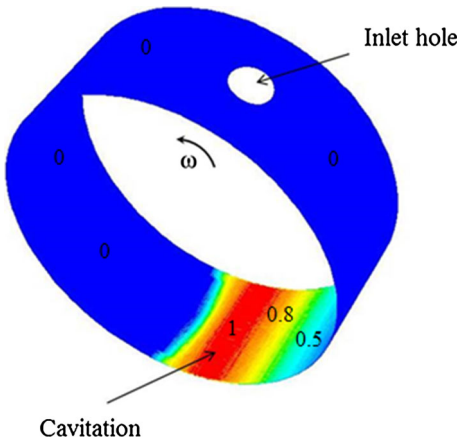

Fig. 13 Contours of volume fraction at crank angle $\vartheta = 180°$ with all active cylinders

at the end of the power stroke with very low transmitted applied gas force (Fig. 11). The volume fraction of unity indicates a gap filled purely by vapour.

The pressure profile through the circumferential centre line of the isobaric plot of Fig. 12 is shown in Fig. 14, also including that for the big-end bearing of an active cylinder in a partially deactivated engine, as well as for a deactivated cylinder's connecting rod bearing. It can be seen that the lubricant film ruptures earlier in the case of an active cylinder in the partially deactivated engine, ahead of that for a normal engine operation, which in turn ruptures ahead of the deactivated cylinder's bearing. This occurs because of progressively reduced applied bearing load at the same crankshaft speed, which is an expected outcome. The reverse trend is discernible for the lubricant film reformation boundary. Therefore, the extent of the cavitation region alters in accord with the cylinder operating condition and has direct implications for bearing load carrying capacity, film thickness and frictional losses.

Figure 15 shows the minimum film thickness during two engine cycles under steady state operating condition for the big-end bearings under various cylinder conditions. In all the cases, the absolute minimum film thickness occurs a few degrees after the top dead centre position within the engine power stroke, where the maximum chamber pressures are encountered. The demarcation boundaries between the prevailing instantaneous regime of lubrication are indicated by the Stribeck's oil film parameter; $\lambda = \frac{h}{\sigma_{\text{rms}}}$, where h is the film thickness and σ_{rms} the root mean square roughness of the counterfaces (journal and the bearing bushing/shell). When, $1 < \lambda < 3$ a mixed regime of lubrication is encountered and $\lambda \leq 1$ indicates a boundary regime of lubrication. Therefore, the inclusion of direct boundary interactions for determination of friction (as in Sect. 3.8) is essential in any analysis of engine big-end bearings. An important point to note is the incidence of boundary interactions in the in-take stroke as well as the power stroke of the engine cycle for the deactivated

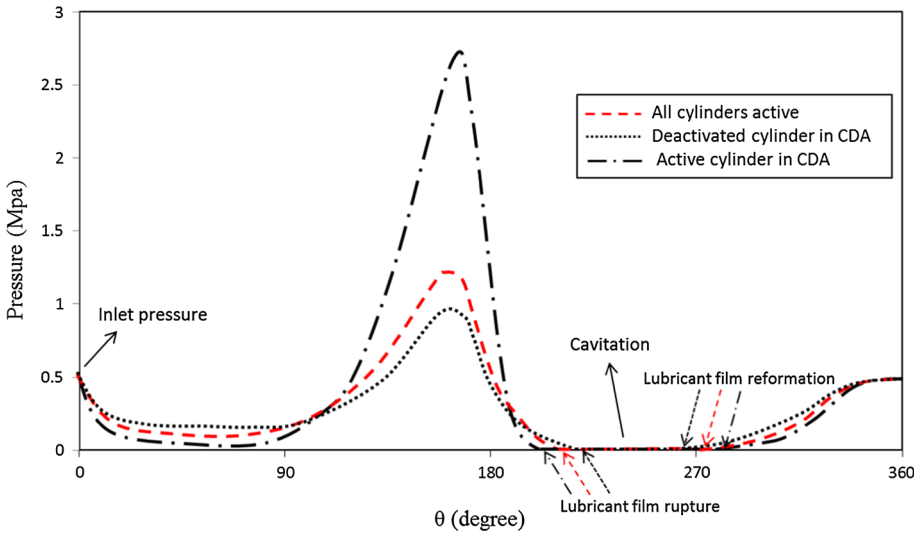

Fig. 14 Pressure distribution in the circumferential centre line of the bearing at crank angle of $\vartheta = 180°$ for various cylinder conditions

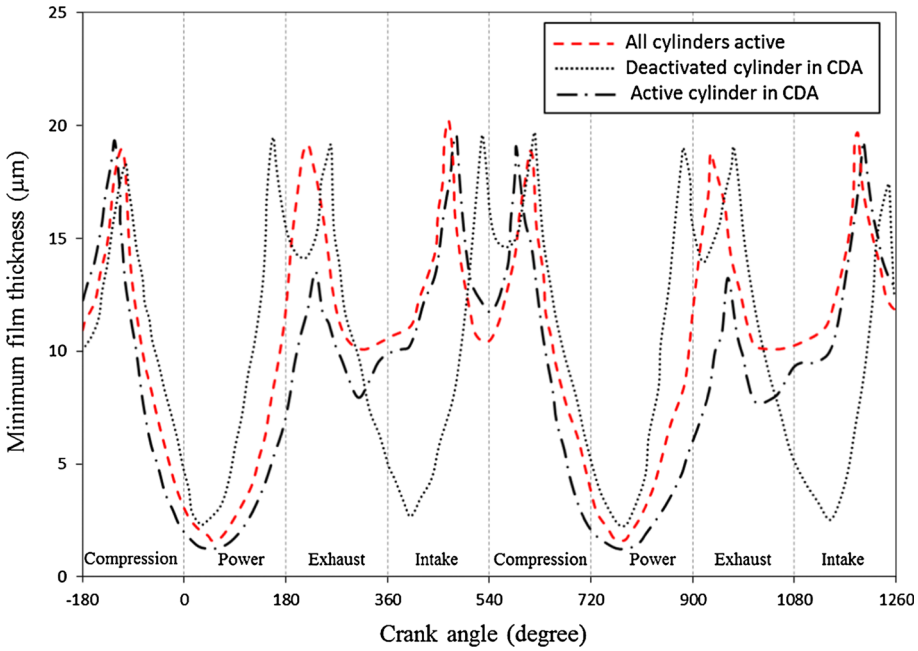

Fig. 15 Minimum film thicknesses for various cylinder conditions

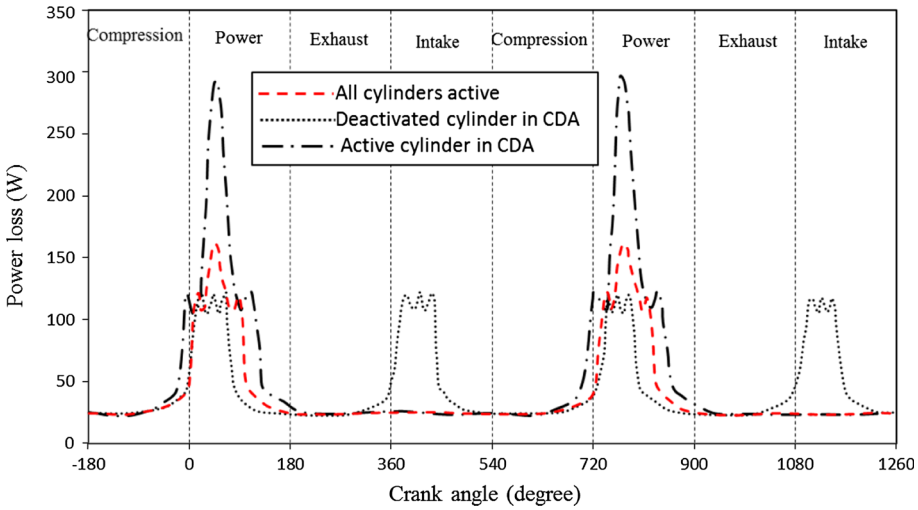

Fig. 16 Frictional power loss for various cylinder conditions

cylinder because the valves remain closed and a residual bearing load is retained due to cylinder swept volume. This means that with CDA the big-end bearing contributes to boundary friction in parts of the engine cycle that is unexpected in the case of normal engine operation. This is because of the trapped air/charge volume with closed valves. This contributes to the overall frictional power loss of the engine operating under CDA as shown in Fig. 16.

Figure 16 shows the frictional power loss in the deactivated cylinder's big-end bearing is in fact larger than that for an engine under normal operation mode in a typical engine cycle $0° \leq \vartheta \leq 720°$. The results also show that active cylinders operating at higher pressures under CDA apply higher loads, thus increasing their bearings' frictional power loss. Therefore, overall the bearing losses are increased under CDA, although this is more than offset by the efficiency gains through higher temperature combustion and reduced pumping losses accounting for 20 % lower fuel consumption for the engine under consideration (a four-cylinder four-stroke c-segment vehicle). The findings of the analysis agree with those of Mohammadpour et al. [6] using mixed thermohydrodynamic analysis, using Reynolds equation.

7 Conclusions

One of the main conclusions of the current study is the importance of determining the correct boundary conditions in the study of journal bearing lubrication. In particular, it is important to include mass conserving flow dynamics through the conjunction. This requires the solution of Navier–Stokes equation, also including vapour transport and

energy equations. In this manner the effects of shear heating, multi-phase and any reverse flow conditions are automatically included for the determination of lubricant film rupture point and its subsequent reformation. The results obtained show closer conformance to the experimental measurements than other methods reported in literature, which impose cavitation algorithms such as the Elrod's algorithm [17].

With respect to the application of CDA as one of the rapidly emerging engine technologies, the analysis shows that unlike the gains made through application of CDA in reduced pumping losses and fuel consumption, the big-end bearing frictional losses are actually increased. This is particularly concerning as the results of analysis corresponds to low speed city driving conditions where application of CDA is seen to be most effective. Of course gains made through reduced pumping losses and fuel consumption outweigh the increased frictional losses shown here. Nevertheless, the findings here indicate that tribological conditions should also be considered in more detail, whilst adopting new technologies.

The area under the power loss curve for a typical cycle $0° \leq \vartheta \leq 720°$ corresponds to the enregy consumed within a bearing at the stated operating conditions. With the four-cylinder engine studied, under CDA condition, two cylinders are deemed to be deactivated simultaneously with the other two operating as active cylinders. The reason for this operating configuration is to reduce the engine crankshaft torsional oscillations which can be exacerbated through increased imbalances induced by applied combustion torque fluctuations [5] with CDA. Taking these points into account, the area under the power loss curve for the various big-end bearing conditions and the calorific value of fuel, the equivalent fuel consumed by the big-end bearings under normal engine operation at the city driving speed of 25 km/h for 100 km is 65.8 g, whilst that under CDA condition amounts to 87.5 g. This represents an increase in brake specific fuel consumption of nearly 25 % by the big-end bearings under CDA, which stands in contrast to the gains made in pumping losses to the cylinders. A main conclusion of the study is that tribology of engine conjunctions should be taken into account with application of new technologies such as CDA. Hitherto, the approach most commonly used disregards any detailed analysis, opting to evaluate more direct gains in fuel efficiency through control of combustion and determination of fuel injection rates.

Acknowledgments The authors would like to express their gratitude to the Lloyd's Register Foundation (LRF) for the financial support extended to this research.

Appendix

The number of control volumes was varied in order to determine the optimum for convergence and numerical accuracy. Figures 17, 18 and 19 show the effect of an increasing number of control volumes as well as numerical convergence error tolerance upon for some key computed parameters and at different crank-angle locations.

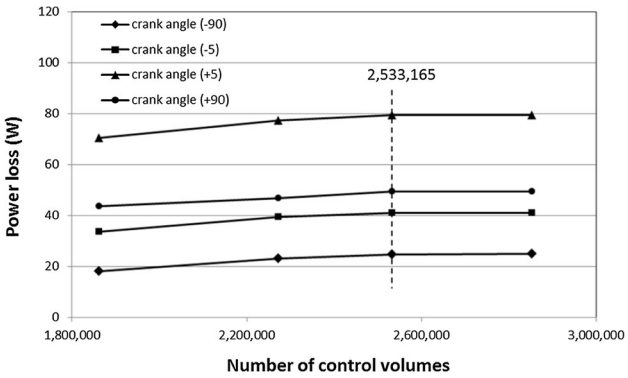

Fig. 17 Power loss versus different numbers of control volume

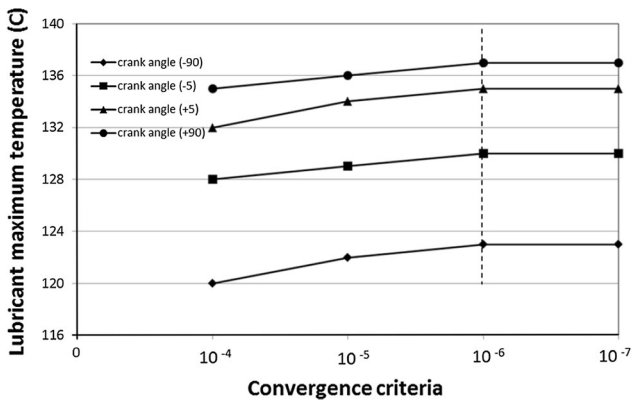

Fig. 18 Lubricant maximum temperature versus different convergence criteria for energy conservation

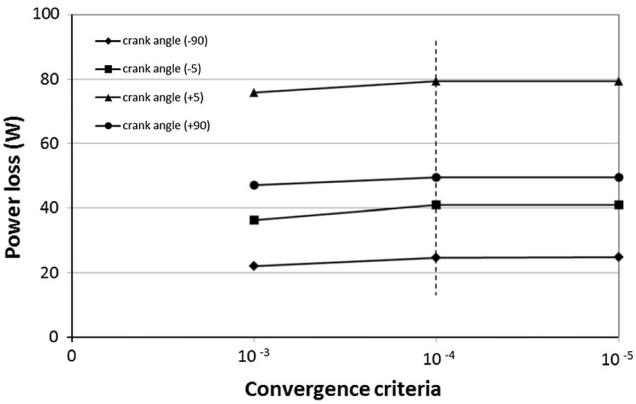

Fig. 19 Power loss versus different convergence criteria for mass and momentum conservation and the vapour volume fraction

References

1. Falkowski, A., McElwee, M., Bonne, M.: Design and development of the DaimlerChrysler 5.7L HEMI® engine multi-displacement cylinder deactivation system. SAE Technical Paper 2004 01-2106 (2004). doi:10.4271/2004-01-2106
2. Roberts, C.: Variable valve timing. SwRI Project No. 03.03271, Clean Diesel III Program (2004)
3. Wilcutts, M., Switkes, J., Shost, M., Tripathi, A.: Design and benefits of dynamic skip fire strategies for cylinder deactivated engines. SAE Int. J. Engines **6**(1), 278–288 (2013)
4. Vafaei, S., Menday, M., Rahnejat, H.: Transient high-frequency elasto-acoustic response of a vehicular drivetrain to sudden throttle demand. Proc. IMechE Part K: J. Multi-Body Dyn. **216**(1), 35–52 (2001)
5. Rahnejat, H.: Multi-body Dynamics: Vehicles, Machines and Mechanisms. Professional Engineering Publishing, Bury St Edmunds (1998)
6. Mohammadpour, M., Rahmani, R., Rahnejat, H.: Effect of cylinder deactivation on the tribo-dynamics and acoustic emission of overlay big end bearings. Proc. IMechE Part K: J. Multi-Body Dyn. **228**(2), 138–151 (2014)
7. Brewe, D.E., Ball, J.H., Khonsari, M.M.: Current research in cavitating fluid films. NASA Technical Memorandum 103184 (1990)
8. Swift, H.W.: The stability of lubricating films in journal bearings. Minutes Proc. **233**, 267–288 (1932)
9. Stieber, W.: Das Schwimmlager. Verein Deutscher Ingenieurre (VDI), Berlin (1933)
10. Skinner, S.: On the occurrence of cavitation in lubrication. Philos. Mag. Ser. 6 **7**(40), 329–335 (1904)
11. Dowson, D., Taylor, C.M.: Cavitation in bearings. Annu. Rev. Fluid Mech. **11**, 35–66 (1979)
12. Floberg, L., Jakobsson, B.: The Finite Journal Bearing Considering Vaporization, p. 190. Trans. Chalmers Univ. Tech, Goteborg (1957)
13. Olsson, K.: Cavitation in Dynamically Loaded Bearings, p. 308. Trans. Chalmers Univ. Tech, Goteborg (1965)
14. Coyne, J.C., Elrod, H.G.: Conditions for the rupture of a lubricating film, part 1: theoretical model. Trans. ASME J. Lubr. Technol. **92**, 451–456 (1970)
15. Coyne, J.C., Elrod, H.G.: Conditions for the rupture of a lubricating film, part 2: new boundary conditions for Reynolds' equation. ASME J. Lubr. Technol. Trans. **93**, 156–167 (1971)
16. Dowson, D., Taylor, C.M., Miranda, A.A.S.: The prediction of liquid film journal bearing performance with a consideration of lubricant film reformation part 1: theoretical results. Proc. IMechE J. Mech. Eng. Sci. **199**(2), 95–102 (1985)
17. Elrod, H.G.: A cavitation algorithm. Trans ASME J. Lubr. Technol. **103**, 350–354 (1981)
18. Dowson, D., Taylor, C.M., Miranda, A.A.S.: The prediction of liquid film journal bearing performance with a consideration of lubricant film reformation part 2: experimental results. Proc. IMechE J. Mech. Eng. Sci. **199**(2), 103–111 (1985)
19. Vijayaraghavan, D., Keith, T.G.: Development and evaluation of a cavitation algorithm. Tribol. Trans. **32**(2), 225–233 (1989)
20. Paydas, A., Smith, E.H.: A flow-continuity approach to the analysis of hydrodynamic journal bearings. Proc. IMechE J. Mech. Eng. Sci. **206**, 57–69 (1992)
21. Hirani, H., Athre, K., Biswas, S.: A simplified mass conserving algorithm for journal bearing under large dynamic loads. Int. J. Rotating Mach. **7**(1), 41–51 (2001)
22. Payvar, P., Salant, R.F.: A computational method for cavitation in a wavy mechanical seal. Trans. ASME J. Tribol. **114**, 199–204 (1992)
23. Xiong, S., Wang, Q.J.: Steady-state hydrodynamic lubrication modeled with the Payvar–Salant mass conservation model. Trans. ASME J. Tribol. **134**(3), 031703 (2012)
24. Giacopini, M., Fowell, M.T., Dini, D., Strozzi, A.: A mass-conserving complementarity formulation to study lubricant films in the presence of cavitation. Trans. ASME J. Tribol. **132**, 041702-1–041702-12 (2010)
25. Tucker, P.G., Keogh, P.S.: A generalized computational fluid dynamics approach for journal bearing performance prediction. Proc. IMechE Part J: J. Eng. Tribol. **209**(2), 99–108 (1995)
26. Dowson, D., Hudson, J.D., Hunter, B., March, C.N.: An experimental investigation of the thermal equilibrium of steadily loaded journal bearings. Proc. IMechE J. Mech. Eng. Sci. **181**(3B), 70–80 (1966–1967)
27. Boedo, S.: Practical Tribological Issues in Big End Bearings. Tribology and Dynamics of Engine and Powertrain, pp. 615–635. Woodhead Publishing, Cambridge (2010)
28. Mishra, P.C., Rahnejat, H.: Tribology of big-end-bearings. In: Rahnejat, H. (ed.) Tribology and Dynamics of Engine and Powertrain: Fundamentals, Applications and Future Trends, pp. 635–659. Woodhead Publishing Ltd, Cambridge (2010)
29. Rahnejat, H.: Multi-body dynamics: historical evolution and application. Proc. IMechE J. Mech. Eng. Sci. **214**(1), 149–173 (2000)
30. Thomson, W.T.: "Vibration Theory and Applications", 5th Impression. Prentice Hall Inc., Guildford, Surrey, UK (1976)
31. Rahnejat, H. (ed.): Tribology and Dynamics of Engine and Powertrain: Fundamentals, Applications and Future Trends. Elsevier. ISBN: 978-84569-361-9 (2010)
32. White, F.M.: Viscous Fluid Flow, 2nd edn. McGraw-Hill, New York (1991)
33. Singhal, A.K., Li, H.Y., Athavale, M.M., Jiang, Y.: Mathematical basis and validation of the full cavitation model. ASME FEDSM'01, New Orleans, LA (2001)
34. Ferron, J., Frene, J., Boncompain, R.: Study of the thermohydrodynamic performance of a plain journal bearing comparison between theory and experiments. J. Tribol. **105**(3), 422–428 (1983)
35. Shi, F., Wang, Q.J.: A mixed-TEHD model for journal-bearing conformal contacts—part I: model formulation and approximation of heat transfer considering asperity contact. Trans. ASME J. Tribol. **120**(2), 198–205 (1998)
36. Khonsari, M.M., Beaman, J.J.: Thermohydrodynamic analysis of laminar incompressible journal bearings. ASLE Trans. **29**(2), 141–150 (1986)
37. Dowson, D., Higginson, G.R.: A numerical solution to the elastohydrodynamic problem. J. Mech. Eng. Sci. **1**, 6–15 (1959)
38. Yang, P., Cui, J., Jin, Z.M., Dowson, D.: Transient elastohydrodynamic analysis of elliptical contacts. Part 2: thermal and newtonian lubricant solution. Proc. IMechE Part J: J. Eng. Tribol. **219**(187), 187–200 (2005)
39. Houpert, L.: New results of traction force calculations in elastohydrodynamic contacts. Trans. ASME J. Tribol. **107**, 241–248 (1985)
40. Gohar, R., Rahnejat, H.: Fundamentals of Tribology. Imperial College Press, London (2008). ISBN: 13 978-1-84816-184-9
41. Lee, P.M., Stark, M.S., Wilkinson, J.J., Priest, M., Lindsay Smith, J.R., Taylor, R.I., Chung, S.: The degradation of lubricants in gasoline engines: development of a test procedure to evaluate engine oil degradation and its consequences for rheology. Trib. Inter. Eng. Ser. **48**, 593–602 (2005)
42. Greenwood, J.A., Tripp, J.H.: The contact of two nominally flat rough surfaces. Proc. IMechE. J. Mech. Eng. Sci. **185**, 625–633 (1970–1971)

43. Teodorescu, M., Balakrishnan, S., Rahnejat, H.: Integrated tribological analysis within a multi-physics approach to system dynamics. Tribol. Interface Eng. Ser. **48**, 725–737 (2005)
44. Guangteng, G., Spikes, H.A.: An experimental study of film thickness in the mixed lubrication regime. Tribol. Ser. **32**, 159–166 (1997)
45. Greenwood, J.A., Williamson, B.P.: Contact of nominally flat surfaces. Proc. R. Soc. Lond. Ser. A **295**, 300–319 (1966)
46. Buenviaje, C.K., Ge, S.-R., Rafaillovich, M.H., Overney, R.M.: Atomic force microscopy calibration methods for lateral force, elasticity, and viscosity. Mater. Res. Soc. Symp. Proc. **522**, 187–192 (1998)
47. Styles, G., Rahmani, R., Rahnejat, H., Fitzsimons, B.: In-cycle and life-time friction transience in piston ring–liner conjunction under mixed regime of lubrication. Int. J. Engine Res. **15**(7), 862–876 (2014)
48. Eyring, H.: Viscosity, plasticity and diffusion as examples of reaction rates. J. Chem. Phys. **4**, 283–291 (1926)
49. Briscoe, B.J., Evans, D.C.B.: The shear properties of Langmuir–Blodgett layers. Proc. R. Soc. Ser. A: Math. Phys. Sci. **380**(177), 389–407 (1982)
50. Langmuir, I.: The constitution and fundamental properties of solids and liquids II, liquids 1. J. Am. Chem. Soc. **39**(9), 1847–1906 (1917)
51. Bowden, F.P., Tabor, D.: The Friction and Lubrication of Solids. Clarendon Press, Oxford (1950)
52. Manninen, M., Taivassalo, V., Kallio, S.: On the Mixture Model for Multiphase Flow. VTT Publications 288 Technical Research Centre of Finland (1996)
53. Wang, X.L., Zhu, K.Q.: Numerical analysis of journal bearings lubricated with micropolar fluids including thermal and cavitating effects. Tribol. Int. **33**, 227–237 (2006)
54. Morris, N., Rahmani, R., Rahnejat, H., King, P.D., Fitzsimons, B.: Tribology of piston compression ring conjunction under transient thermal mixed regime of lubrication. Tribol. Int. **59**, 248–258 (2013)

Proceedings of the ASME 2013 International Mechanical Engineering Congress and Exposition
IMECE2013
November 15-21, 2013, San Diego, California, USA

IMECE2013-62395

Cavitating Flow in Engine Piston Ring-Cylinder Liner Conjunction

Hamed Shahmohamadi
H.Shahmohamadi@lboro.ac.uk

Ramin Rahmani
R.Rahmani@lboro.ac.uk

Homer Rahnejat
H.Rahnejat@lboro.ac.uk

Paul King
P.D.King@lboro.ac.uk

Colin Garner
C.P.Garner@lboro.ac.uk

Wolfson School of Mechanical and Manufacturing Engineering, Loughborough University, Loughborough, LE11 3TU, Leicestershire, UK

ABSTRACT

The main function of piston compression ring is to seal the space between the piston and the liner, acting as slider bearing, subjected to reciprocating motion. The compression ring-cylinder liner conjunction has been extensively studied and it is responsible for a significant part of the total frictional parasitic power losses of an engine. Paradoxically, the required sealing function of the compressions ring can result in increased friction. Therefore, in order to improve engine efficiency, it is important to fundamentally understand and subsequently palliate some of these losses. Another problem in any slider bearing-type contact is lubricant film rupture and cavitation in the conjunctional outlet zone, reducing load carrying capacity and potentially leading to erosion damage.

A cavitation model presented in two-phase flow CFD analysis of the ring-bore contact under isothermal conditions. Liquid flow is modelled as a continuous phase and a dispersed phase, representing cavitation bubbles. Many of the fundamental physical processes assumed to take place in cavitating flows are incorporated into the model.

INTRODUCTION

Modern automotive engines are progressively smaller, faster and more efficient. This is partly due to the improved automotive control strategies and partly due to the better understanding of the physical phenomena governing various aspects of the IC engine [1].

The lubrication of the piston ring has been an important research topic for many years [2-5] because it is widely recognized that the interaction at the ring-cylinder wall interface has a significant contribution to engine friction, wear, oil consumption and power loss.

The piston ring pack in an internal combustion engine typically consists of three circular rings located in grooves in the piston. The primary function of the rings is to prevent high-pressure gases from leaking through the piston-liner interface, which would results in power losses [6]. Effective sealing is thus needed between the ring and the liner. However, without lubrication, the compression ring-liner conjunction would contribute to boundary interactions and large friction. Therefore, it is essential to be able to predict the conditions at the ring-cylinder wall interface. Another main objective of the piston ring-pack is to effectively distribute lubricant along the ring-liner interface, without allowing excessive oil to pass through and ingress into the combustion chamber.

Two models are predominantly used in hydrodynamic lubrication: the Reynolds model and the Elrod–Adams model [7]. The former, easier to implement numerically, though being non-conservative, gives reasonable predictions in many

cases and is thus still used in engineering practice. In the Elrod–Adams model, the JFO conditions proposed by Jacobson and Floberg [8] and Olsson [9] are applied at the cavitation boundary to enforce mass conservation. However, due to the highly non-linear nature of the problem, numerical implementations of this model are more prone to numerical instabilities [10]. The importance of using a conservative model has been shown by means of several numerical examples in [11, 12] for problems including transient effects and/or microtextures.

GOVERNING EQUATIONS

Figure 1 is a schematic representation of compression ring-liner conjunction along the ring axial face-width. The ring profile $h_s(x)$ is assumed to be parabolic with a maximum crown height of c and a face-width of b:

$$h_s(x) = \frac{cx^2}{(b/2)^2} \tag{1}$$

A high performance single cylinder V12 4-stroke naturally aspirated motocross motorbike engine is used in the current study (specifications are listed in Table 1).

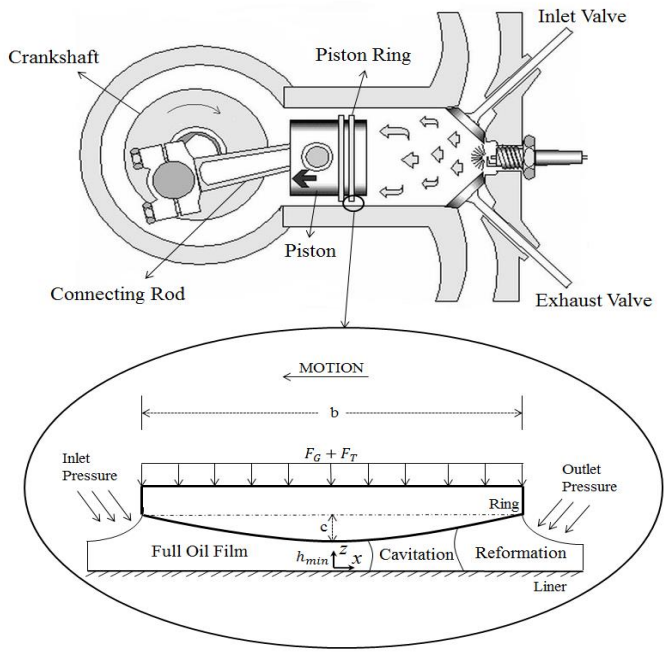

Fig.1: Piston ring–liner conjunction (power stroke)

Table1. Engine data

Parameters	Values	Units
Crank-pin radius, r	39.75	*mm*
Connecting rod length, l	138.1	*mm*
Bore nominal radius, r_0	44.52	*mm*
Ring crown height, c	10	μm
Ring axial face width, b	1.15	*mm*
Ring radial width, d	3.5	*mm*

As shown in Figure 1, in general, the contact region may be considered as comprising of three distinct regions: (i) full film (a coherent lubricant film region), (ii) film rupture and cavitation, and (iii) lubricant film reformation.

The general continuity and Navier-Stokes momentum equations for compressible viscous fluid flow are [13]:

$$\frac{D\rho}{Dt} + \rho\nabla.\vec{V} = 0 \tag{2}$$

$$\rho\frac{D\vec{V}}{Dt} = -\nabla p + \nabla.(\bar{\tau}_{ij}) + \vec{F} \tag{3}$$

where $\frac{D}{Dt}$ is the material derivation operator, ρ is the lubricant density, p is the pressure, $\bar{\tau}_{ij}$ is the tensor of viscous stresses and $\vec{F}$ is the body force field. In addition, $\vec{V} = u\hat{i} + v\hat{j} + w\hat{k}$ is velocity vector in which u is the component of velocity in the axial lubricant flow entrainment, v is that in side-leakage along the y-axis (which may reasonably be discarded as there is negligible side-leakage in the thin film ring-bore conjunction), and w is the z-component of velocity. The viscous stress tensor is given by:

$$\bar{\tau}_{ij} = \eta\left(\frac{\partial u_i}{\partial x_j} + \frac{\partial u_j}{\partial x_i} - \delta_{ij}\frac{2}{3}\nabla.\vec{V}\right) \tag{4}$$

where η is the lubricant viscosity and δ_{ij} is the Kronecher delta. As mentioned before, the present CFD analysis in this work is under isothermal conditions, hence, there is no need to solve energy equation.

One possibility in a CFD model is to evaluate fluid viscosity as a function of pressure along the liner and into the depth of the lubricant film. The latter is neglected in the conventional hydrodynamic

lubrication approaches which are based on Reynolds equation. The following boundary conditions are used along the axial x-direction of the contact (i.e. along the ring face-width)

$$p_h(-b/2) = p_L$$
$$p_h(+b/2) = p_U \quad (5)$$
$$p_h(x_c) = p_c$$

LUBRICANT RHEOLOGY

The lubricant bulk rheological properties including density and viscosity are affected by pressure [2]. The density–pressure relationship is [14]

$$\rho = \rho_0\left(1 + \frac{6.0\times10^{-10}(p - p_{atm})}{1 + 1.7\times10^{-9}(p - p_{atm})}\right) \quad (6)$$

in which p_{atm} is the atmospheric pressure. According to Gohar and Rahnejat [14], the dynamic viscosity of lubricant can be related to the variations in the pressure and temperature using Houpert's equation as follows:

$$\eta = \eta_0 \exp\left\{(\ln(\eta_0) + 9.67)\left[\left(1 + \frac{p - p_{atm}}{1.98\times10^8}\right)^Z - 1\right]\right\} \quad (7)$$

in which, η_0 is the lubricant dynamic viscosity at atmospheric pressure, and Z is constant independent of pressure and is defined below:

$$Z = \frac{\alpha_0}{5.1\times10^{-9}[\ln(\eta_0) + 9.67]} \quad (8)$$

where α_0 is constant at atmospheric pressure. Details of lubricant rheological parameters are given in Table 2.

Table2. Lubricant properties in 40°C

Parameters	Values	Units
Lubricant viscosity, η_0	0.05	kg/m-s
Lubricant density, ρ_0	833	kg/m^3
α_0	1×10^{-8}	m^2/N

EULER-EULER APPROACH: EULERIAN AND MIXTURE MODELS

The various phases are handled mathematically as interpenetrating continuity in the Euler-Euler approach. Since the volume of a phase remains unaffected by the other phases, the concept of phasic volume fraction is introduced. These volume fractions are assumed to be continuous functions of space and time, the sum of which equates to unity. Conservation equations for each phase are derived to obtain a set of equations, which have similar structure for all phases.

The Eulerian model [15] is the most complex of the multi-phase flow models. It solves a set of momentum and continuity equations for each phase. Coupling is achieved through pressure and inter-phase exchange coefficients. Momentum exchange between the phases is also dependent upon the type of mixture modeled.

The mixture model [16] solves for the mixture momentum equation and proposes relative velocities to describe the dispersed phases.

CAVITATION MODEL

During cavitation, the liquid-vapour mass transfer (evaporation and condensation) is governed by the vapour transport equation [17]:

$$\frac{\partial}{\partial t}(\alpha_v\rho_v) + \nabla.(\alpha_v\rho_v\vec{V}_v) = R_e - R_c \quad (9)$$

where ρ_v is the vapour density, $\vec{V}_v$ is the velocity vector of the vapour phase, R_e and R_c are mass transfer source terms, related to the growth and collapse of the vapour bubbles respectively. Singhal et al [18] assumed that the working fluid is a mixture of liquid and vapour and introduced a modified form of the above equation based upon vapour mass fraction, f_{mass} as:

$$\frac{\partial}{\partial t}(\rho_m f_{mass}) + \nabla.(\rho_m\vec{V}_v f_{mass}) = \nabla.(\Gamma\nabla f_{mass}) + R_e - R_c \quad (10)$$

where ρ_m is the mixture density and Γ is the diffusion coefficient. The mass transfer rate expressions are derived from the Rayleigh-Plesset equations, based on a limiting bubble size considerations (interface surface area per unit volume of vapour). These rates are functions of the instantaneous local pressure and are given as

for $p < p_c$:

$$R_e = C_e \frac{V_{ch}}{\sigma_s} \rho_l \rho_\upsilon \sqrt{\frac{2(p_c - p)}{3\rho_l}} (1 - f_{mass}) \qquad (11)$$

for $p > p_c$:

$$R_c = C_c \frac{V_{ch}}{\sigma_s} \rho_l \rho_\upsilon \sqrt{\frac{2(p - p_c)}{3\rho_l}} f_{mass} \qquad (12)$$

where the suffices l and υ denote the liquid and vapour phases respectively, V_{ch} is a characteristic velocity, σ_s is the surface tension coefficient of the liquid, p_c is the liquid cavitation pressure at the given temperature and C_e and C_c are empirical constants and are considered to be 50 and 0.01 in Kubota et al [19].

SIMULATION METHOD

A 2D simulation model is developed using the CFD package FLUENT 14.0. The pre-processor ANSYS Design Modeller and Meshing are used for grid generation. The geometrical nature of the problem examined here (the film thickness is very thin compared with the ring diameter and length) enforces the use of only quadrilateral cells. After conducting a grid sensitivity influence upon the predictions, forty divisions were used across the film depth and 1500 divisions along the ring contacting face-width. This provides a total number of cells of 60,000. Calculation of Reynolds number for the studied conditions shows that the flow is well within laminar regime. The operating pressure and vaporization (cavitation) pressure are set to the standard atmospheric pressure; i.e. 101325 Pa. The liner (bottom wall) is modelled as a "stationary wall". The ring (upper wall) is modelled as a "moving wall" with the speed obtained follow [14]

$$U(\varphi) = -r\omega \sin\varphi \left\{ 1 + \cos\varphi \left[\left(\frac{l}{r} \right)^2 - \sin^2 \varphi \right]^{-\frac{1}{2}} \right\} \qquad (13)$$

where φ is the crank-angle, l is the connecting rod length and r the crank pin radius.

Pressure inlet and outlet boundary conditions are used for the leading and trailing edges of the ring/liner contact. Therefore, when the piston undergoes upstroke motion, the inlet pressure is that of chamber given in Figure 2, whilst at the exit the crank-case pressure is assumed, which also is assumed to be the atmospheric pressure. On the other hand, for the down-stroke sense of the piston, the inlet pressure is set to that of the crank-case (atmospheric) pressure, whilst the outlet pressure is that of the combustion chamber.

The pressure-based Eulerian model [15] is chosen for the present analysis to compare with the Mixture model [16]. The velocity–pressure coupling is treated using the SIMPLE algorithm and the second-order upwind scheme is used for the momentum to reduce the discretisation-induced errors in the calculation process. For greater accuracy, a value of 10^{-6} is used for all residual terms.

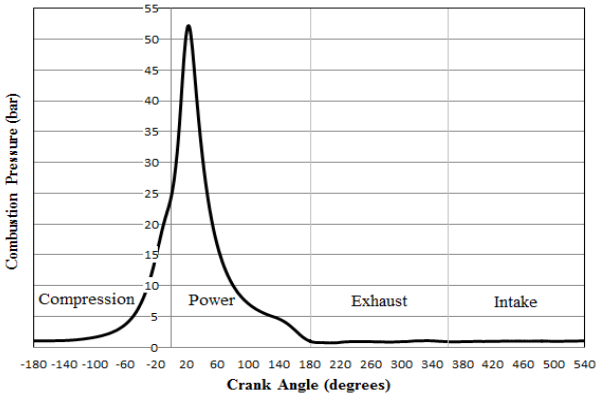

Fig. 2: Variation of chamber pressure with crank angle for engine speed of 1500 rpm

It is noted that the dynamic mesh concept based on force equilibrium is employed for variations in the minimum film thickness in the CFD analysis. In this method, the corresponding user-defined function (UDF) determines the desired position of the ring using the dynamic mesh technique. To achieve this, a smoothing mesh method is used with a convergence tolerance of 10^{-5}

RESULT

Vapour Volume Fraction

Figure 3 shows images of bubble formation induced by cavitation sequence between ring piston and liner in the crank angle of 90° (mid-span power stroke) at the engine motored speed of 1500 rpm.

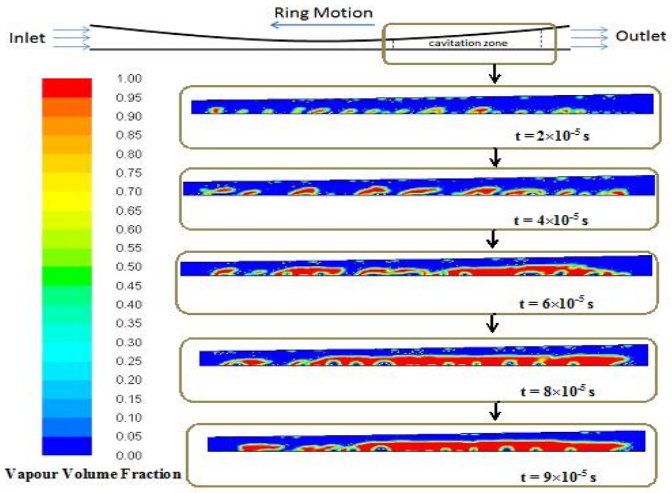

Fig.3: Cavitation-induced bubble formation sequence in the ring-liner conjunction at 1500 rpm

Figure 4(a) illustrates finger shaped bubbles in $xy-$plane (plan-view of contact) obtained experimentally as well as predicted results, Figure 4(b), in the $xz-$plane (into the depth of the conjunction in the cavitation region, also see Figure 1). The shape of bubbles in the cavitation zone is important due to their potential effect upon solid boundary erosion.

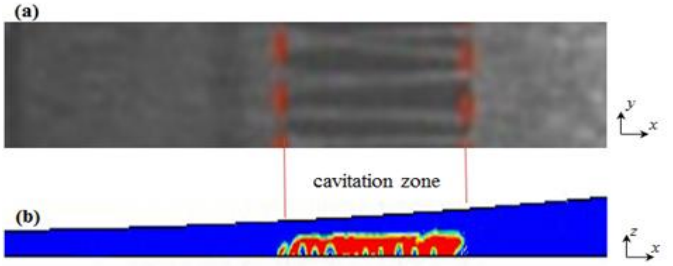

Fig.4: (a) Experimental result showing a plan-view of the cavitated finger shaped bubbles (the result has been obtained in City University lab: International Institute for Cavitation Research), (b) Predictions for vapour volume fraction into the depth of the lubricant film

Pressure Distribution

Figure 5 presents axial pressure profiles (along the ring face-width) at the piston crank angle of 90° (mid-span power stroke) at the engine motored speed of 1500 rpm. The predictions are made by three different methods: (I) Two-phase Eulerian model [15], (II) Two-phase Mixture model [16] and (III) The modified Reynolds equation using Elrod cavitation algorithm. Figure 5 shows good agreement between the Eulerian and the Elrod models. In addition, the rupture points (, x_c, from both methods coincide on each other. However, it can be seen that the reformation boundary in the Eulerian model commences earlier than for the Elrod model. Although there are differences in the locations of rupture and reformation points predicted by both of the Mixture and Elrod models, the length of cavitation zone remains almost the same for both. It should be noted that the position of rupture point and the length of cavitation zone both affect contact load carrying capacity, friction and consequent power losses. Larger cavitation region reduces the load carrying capacity, but can improve upon friction.

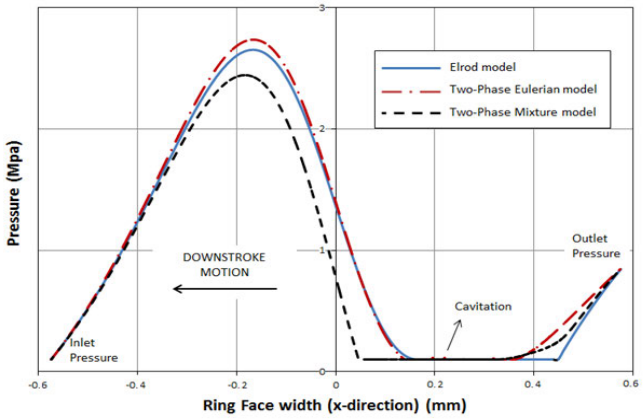

Fig.5: Axial ring-liner pressure profiles with three different predictive methods

CONCLUSION

A novel compartmental modelling framework has been investigated using CFD simulation in the Piston-ring conjunction. A combined Navier-Stokes and discrete dispersed phase Eulerian dynamics' model has been developed to predict cavitation and bubble formation in the piston compression ring-liner conjunction. Comparison of the obtained result for pressure distribution with the one obtained by Elrod model was analysed. The long finger shaped bubbles observed in experimental investigations are predicted by the current analysis.

NOMENCLATURE

b	ring axial face-width
c	crown height
d	ring thickness

f_{mass}	vapour mass fraction
g	ring end gap
h_m	minimum film thickness
l	connecting rod length
L	ring peripheral length
p_{atm}	atmospheric pressure
p_c	cavitation/lubricant vaporisation pressure
p	hydrodynamic pressure
r	crank-pin radius
r_0	nominal bore radius
R_e, R_c	mass transfer source terms
Re	Reynolds number
U	ring sliding velocity
$\vec{V}$	velocity vector
V_{ch}	characteristic velocity
x_c	oil film rupture point
Z	pressure-viscosity index

Greek Symbols

α_0	pressure/temperature–viscosity coefficient
φ	crank angle
η	lubricant dynamic viscosity
η_0	lubricant dynamic viscosity at atmospheric pressure
ρ	lubricant density
ρ_m	mixture density
ρ_0	lubricant density at atmospheric pressure
σ_s	surface tension coefficient
Γ	diffusion coefficient

ACKNOWLEDGEMENTS

The authors would like to express their gratitude to the Lloyds Registry Educational Foundation (LREF) for the financial support extended to this research. Thanks are also due to the Engineering and Physical Sciences Research Council for the Encyclopaedic Program Grant, from which some of the research are used in this paper.

REFERENCES

[1] Rahnejat H., Multi-body dynamics: vehicles, machines and mechanisms, *Professional Engineering Publishing, Bury St Edmunds, UK* and *SAE, Warrandale, PA, USA, 1998*

[2] Shahmohamadi H., Rahmani R., Rahnejat H., Garner C.P., King P.D., Thermo-Mixed Hydrodynamics of Piston Compression Ring Conjunction, *Tribology Letters, DOI: 10.1007/s11249-013-0163-5*

[3] Rahmani R., Theodossiades S., Rahnejat, H. and Fitzsimons B., "Transient elastohydrodynamic lubrication of rough new or worn piston compression ring conjunction with an out-of-round cylinder bore", *Proc. IMechE, Part J: J. Engng. trib., 226(4), 2012, pp. 284-305*

[4] Mishra P.C., Balakrishnan S. and Rahnejat H., "Tribology of compression ring-to-cylinder contact at reversal", *Proc. IMechE, Part J: J. Engng. Trib, 222(7), 2008, pp. 815-826*

[5] Mishra P.C., Rahnejat H. and King P.D., "Tribology of the ring—bore conjunction subject to a mixed regime of lubrication", *Proc. IMechE, Part C: J. Mech. Engng. Sci., 223(4), 2009, pp. 987-998*

[6] Morris N., Rahmani R., Rahnejat H., King P.D. and Fitzsimons, B., "The influence of piston ring geometry and topography on friction", *Proc. IMechE, Part J: J. Engng. trib., 2012, DOI: 10.1177/1350650112463534*

[7] Elrod HG, Adams M., A computer program for cavitation, Technical report 190, First LEEDS LYON symposium on cavitation and related phenomena in lubrication, I.M.E., 103 (1974) 354

[8] Jakobsson, B. and Floberg, L., "The Finite Journal Bearing Considering Vaporization," *Trans. of Chalmers University of Tech., Gothenburg. Sweden. (1957).*

[9] Olsson. K. O., "Cavitation in Dynamically Loaded Bearings," *Trans. Trans. of Chalmers University of Tech., Gothenburg. Sweden. (1965).*

[10] Kumar A, Booker J. A finite element cavitation algorithm. ASME Journal of Tribology, 113 (1991) 276–86

[11] Boedo S, Booker J. Cavitation in normal separation of square and circular plates. ASME Journal of Tribology, 117 (1995) 403–410

[12] Ausas R, Ragot P, Leiva J, Jai M, Bayada G, Buscaglia G. The impact of the cavitation model in the analysis of micro-textured lubricated journal bearings. ASME Journal of Tribology, 129 (2009) 868

[13] White F. M., "Viscous Fluid Flow", *McGraw-Hill, 2nd Edition, 1991*

[14] Gohar R. and Rahnejat H., Fundamentals of Tribology, *Imperial College Press*, *London, 2008*

[15] Cokljat D., Slack M. and Vasquez S. A., "Reynolds-Stress Model for Eulerian Multiphase", *Proceedings of the 4th International Symposium on Turbulence Heat and Mass Transfer*. *Begell House, Inc. 2003, 1047–1054*

[16] Manninen M., Taivassalo V. and Kallio S., "On the mixture model for multiphase flow", *VTT Publications 288 Technical Research Centre of Finland. 1996*

[17] Senocak I., Shyy W., "Interfacial dynamics-based modelling of turbulent cavitating Flows", Part-1: Model development and steady-state computations, *Int. J. Numer. Meth. Fluids, 44, 2004, pp. 975–995*

[18] Singhal A.K., Li H.Y., Athavale M.M., and Jiang Y., "Mathematical Basis and Validation of the Full Cavitation Model", *ASME FEDSM'01, New Orleans, Louisiana, 2001*

[19] Kubota A, Kato H, Yamaguchi H., "A new modelling of cavitating flows: a numerical study of unsteady cavitation on a hydrofoil section", *J. Fluid Mech., 240, 1992, pp. 59–96*